



Koester, Anna Magdalena (2021) *The spatial dynamics of insulin-regulated GLUT4 dispersal*. PhD thesis.

<http://theses.gla.ac.uk/82077/>

Copyright and moral rights for this work are retained by the author

A copy can be downloaded for personal non-commercial research or study, without prior permission or charge

This work cannot be reproduced or quoted extensively from without first obtaining permission in writing from the author

The content must not be changed in any way or sold commercially in any format or medium without the formal permission of the author

When referring to this work, full bibliographic details including the author, title, awarding institution and date of the thesis must be given

Enlighten: Theses

<https://theses.gla.ac.uk/>
research-enlighten@glasgow.ac.uk

The spatial dynamics of insulin-regulated GLUT4 dispersal

Anna Magdalena Koester

MSci, MRes

Thesis submitted in fulfilment of the requirements for the Degree of
Doctor of Philosophy

Institute of Molecular, Cell and Systems Biology

College of Medical, Veterinary and Life Sciences

University of Glasgow

January 2021

Abstract

Insulin regulates glucose homeostasis by stimulation of glucose transport into adipose and muscle tissues through the regulated trafficking of glucose transporter 4 (GLUT4). In response to insulin GLUT4 rapidly translocates from intracellular storage sites to the plasma membrane where it facilitates glucose uptake. Significant impairments in glucose transport and GLUT4 trafficking are a major hallmark of diabetes mellitus type II. Recent advances in light microscopy techniques enabled the study of GLUT4 dynamics in the plasma membrane and it was reported that the transporter was clustered in the basal state and insulin stimulation resulted in GLUT4 dispersal.

The main aim of this study was to develop a microscopy-based assay to study and quantify insulin-stimulated GLUT4 dispersal dynamics in the plasma membrane. Insulin-stimulated GLUT4 dispersal has only been observed in adipocytes and therefore we have chosen this model as a starting point to investigate the molecular mechanisms behind GLUT4 clustering and dispersal. We explored a range of cluster analysis methods to find the most suitable way to quantify GLUT4 clustering dynamics. Furthermore, this project aimed to optimise super resolution imaging in a variety of cell culture models to determine whether insulin-stimulated GLUT4 dispersal operates in skeletal and cardiac muscle and whether this process is affected by disease.

Using a range of approaches we showed that insulin results in GLUT4 translocation and dispersal within the plasma membrane of 3T3-L1 adipocytes. We found that AMPK activation attenuated insulin-stimulated glucose uptake in 3T3-L1 adipocytes and also GLUT4 dispersal. It was observed that cholesterol depletion resulted in increased glucose uptake rates and GLUT4 clustering. Knock down of the membrane-localised protein EFR3 that has previously been shown to be involved in glucose uptake resulted in disruption of GLUT4 dispersal in adipocytes. We also found that HeLa cells show similar insulin-stimulated GLUT4 dispersal as adipocytes and suggest that HeLa cells are a suitable experimental model for initial studies of GLUT4 trafficking and dispersal. Chronic insulin treatment was observed to induce a state of cellular insulin resistance in 3T3-L1 adipocytes and resulted in reduced GLUT4 translocation and a more clustered GLUT4 configuration for both basal and insulin-stimulated cells. This indicates that insulin resistance affects intracellular GLUT4 trafficking pathways as well as the organization of the transporter within the plasma membrane in adipocytes. Moreover, we found a negative correlation between adipocyte cell area and insulin-stimulated GLUT4 translocation.

We also report that insulin did not stimulate the reorganisation of the transferrin receptor in the plasma membrane of HeLa cells suggesting that insulin-stimulated GLUT4 dispersal did not originate from endosomal compartments in HeLa cells and that this observed effect may be specific for GLUT4. Finally, we observed that insulin did not affect GLUT4 distribution in the membrane of a commercially available model of skeletal muscle from healthy and diabetic donors. Sortilin is a sorting receptor involved in the formation of GLUT4 containing vesicles and levels of this protein were found to be reduced in skeletal muscle myotubes derived from a diabetic donor.

Finally, we discovered that insulin stimulated GLUT4 dispersal also operates in stem cell-derived cardiomyocytes and have investigated GLUT4 dispersal in a variety of in vitro models of cardiac muscle tissue.

Taken together, this thesis has detailed several novel findings regarding the regulation of GLUT4 clustering in adipose and muscle tissues. A robust assay to measure GLUT4 dispersal has been established and molecular mechanisms behind the observed GLUT4 clustering dynamics have been described in adipocytes. Furthermore GLUT4 clustering was characterised in several cell culture models of skeletal and cardiac muscle for the first time.

Table of contents

Abstract.....	ii
Table of contents	iv
List of tables	xi
List of figures	xii
Acknowledgements.....	xvii
Author’s declaration	xix
Definitions & abbreviations	xx
1. Introduction.....	1
1.1 Glucose homeostasis.....	1
1.2 Diabetes	3
1.2.1 Diabetes is a growing global healthcare burden.....	3
1.2.2 Complications	3
1.2.3 Causes	5
1.2.4 Treatment	5
1.3 Diabetic cardiomyopathy	6
1.3.1 Recognition of diabetic cardiomyopathy	6
1.3.2 Pathophysiology of diabetic cardiomyopathy.....	6
1.3.3 Impaired insulin signalling in diabetic cardiomyopathy	7
1.4 Glucose transport.....	8
1.4.1 Glucose transporters	8
1.4.2 Glucose transporter 4	9
1.4.3 GLUT4 intracellular trafficking overview.....	11
1.4.4 GLUT4 trafficking in muscle tissues.....	14
1.4.5 GLUT4 endocytosis.....	15
1.5 Insulin signalling	15
1.5.1 Mitogen-activated protein (MAP) kinase signalling pathway.....	16
1.5.2 Insulin receptor substrate (IRS) signalling pathway.....	16
1.5.3 Adaptor protein with pleckstrin homology and Src homology	17
domains (AP5) signalling pathway	17

1.5.4 Insulin signalling in muscle tissues	18
1.5.5 Insulin signalling defects in T2DM	19
1.6 GLUT4 in the plasma membrane.....	20
1.6.1 Total internal fluorescence microscopy reveals plasma membrane GLUT4 dynamics	21
1.6.2 The effect of insulin action on plasma membrane GLUT4 dynamics	23
1.7 Aims and hypothesis	26
2. Materials and Methods.....	29
2.1 Materials	29
2.1.1 Commercially derived cells.....	29
2.1.2 Primary cells.....	30
2.1.3 Plasmids.....	30
2.1.4 General materials and reagents	31
2.1.5 Solutions	36
2.1.6 Primary Antibodies and Nanobodies.....	38
2.1.7 Secondary Antibodies and Nanobodies.....	39
2.2 Cell Culture Methods	40
2.2.1 3T3-L1 fibroblast growth and maintenance.....	40
2.2.2 3T3-L1 adipocyte differentiation	40
2.2.3 HEK 293 and HeLa cell growth and maintenance	40
2.2.4 iPSC-CM growth and maintenance.....	40
2.2.5 Primary rabbit cardiomyocyte isolation	41
2.2.6 Primary rabbit cardiomyocyte maintenance	42
2.2.7 Neonatal rat cardiomyocyte isolation.....	42
2.2.8 Neonatal rat cardiomyocyte maintenance	43
2.2.9 Human skeletal muscle myoblast growth and maintenance.....	43
2.3 Super resolution microscopy methods	44
2.3.1 Coverslip preparation	44
2.3.2 Seeding cells onto coverslips.....	44
2.3.3 Infection of cells with HA-GLUT4-GFP adeno virus	44

2.3.4 Infection of cells with HA-GLUT4-GFP adeno-associated virus.....	45
2.3.5 Fixation of cells on coverslips.....	45
2.3.6 Immunofluorescence staining.....	45
2.3.7 Microscope setup.....	46
2.3.8 Image acquisition.....	47
2.3.9 Image reconstruction.....	47
2.3.10 GLUT4 localization density.....	47
2.3.11 GLUT4 cluster analysis.....	48
2.4 Glucose uptake assay.....	49
2.4.1 3T3-L1 adipocyte glucose uptake assay.....	49
2.4.2 Primary cardiomyocyte glucose uptake assay.....	49
2.4.3 Interpretation of glucose uptake assay results.....	50
2.5 Protein assays.....	50
2.5.1 Production of protein lysates.....	50
2.5.2 Bicinchoninic acid assay.....	50
2.5.3 Western immunoblotting.....	51
2.5.4 Densitometry.....	51
2.6 Molecular methods.....	51
2.6.1 Amplification of plasmid DNA.....	51
2.6.2 Transfection of mammalian cells with plasmid DNA.....	52
2.6.3 Generation of a novel TfR-GFP lentiviral plasmid.....	52
2.7 Confocal microscopy.....	52
2.8 Flowcytometry.....	53
2.8.1 GLUT4 translocation assay set up for HeLa cells.....	53
2.8.2 Preparation of HA-GLUT4-GFP HeLa cells for FACS analysis.....	53
2.8.3 GLUT4 translocation assay set up for adipocytes.....	54
2.8.4 Preparation of HA-GLUT4-GFP adipocytes for FACS analysis.....	54
2.8.5 Analysis of flowcytometry data.....	54
2.9 Statistical analysis.....	55
3. Stochastic optical reconstruction microscopy for the assessment of GLUT4 dispersal	56

3.1 Introduction.....	56
3.1.1 The diffraction limit of light	56
3.1.2 Super resolution microscopy	57
3.1.3 Stochastic optical reconstruction microscopy	58
3.1.4 Sample preparation.....	60
3.1.5 Cluster analysis.....	63
3.1.6 Hypothesis and Research Aims	69
3.2 Results.....	70
3.2.1 The effects of sample preparation on super resolution image quality.....	70
3.2.2 Automated computing of Ripley's K function analysis for the study of GLUT4 clustering	73
3.2.3 Bayesian cluster analysis.....	75
3.2.4 Cluster analysis with machine learning	77
3.2.5 Tessellation.....	80
3.2.6 Hierarchical density-based spatial clustering of applications with noise.....	81
3.2.7 Statistical analysis of spatial point pattern data in R	82
3.3 Discussion	84
3.3.1 Is my super resolution image a high-precision representation of the spatial organization of GLUT4 within the plasma membrane?	84
3.3.2 Image analysis is key to single molecule localization	85
3.3.3 Ripley's K function and its derivatives for GLUT4 cluster analysis	86
3.3.4 Machine learning for GLUT4 cluster analysis.....	88
3.3.5 Spatial point pattern analysis with Spatstat in R.....	89
4. Plasma membrane GLUT4 dispersal in adipocytes	93
4.1 Introduction.....	93
4.1.1. Insulin-stimulated GLUT4 dispersal in adipocytes.....	93
4.1.2 The effects of AMPK activation on adipocyte GLUT4 trafficking and dispersal	94
4.1.3 The effects of cholesterol depletion on adipocyte GLUT4 trafficking and dispersal.....	96
4.1.4 EFR3 and its potential role in GLUT4 clustering.....	97

4.1.5 HeLa cells as a tool to investigate GLUT4 trafficking	98
4.1.6 Hypothesis and research aims.....	99
4.2 Results.....	100
4.2.1 Insulin regulates GLUT4 dispersal on the plasma membrane of adipocytes..	100
4.2.2 AMPK activation regulates insulin-stimulated GLUT4 dispersal	104
4.2.3 Cholesterol depletion enhances basal GLUT4 clustering.....	110
4.2.4 EFR3 regulates insulin-stimulated GLUT4 dispersal.....	113
4.2.5 Insulin regulates GLUT4 dispersal in HeLa cells	114
4.3 Discussion	119
4.3.1 GLUT4 clustering in adipocytes.....	119
4.3.2 Does regulation of clustering underpin observed effects of AMPK activation on glucose transport?	120
4.3.3 Cholesterol depletion and GLUT4 dispersal.....	120
4.3.4 The role of EFR3 in insulin-stimulated GLUT4 dispersal	122
4.3.5 HeLa cells as a model system	123
5. Plasma membrane GLUT4 dispersal in cardiomyocytes	125
5.1 Introduction.....	125
5.1.1 Glucose transporters in the healthy heart	125
5.1.2 Insulin-independent stimuli of GLUT4 trafficking in the heart.....	126
5.1.3 Challenges of investigating GLUT4 trafficking in cardiac tissue models	126
5.1.4 Disease modelling in human induced pluripotent stem cells	128
5.1.5 Hypothesis and research aims.....	129
5.2 Results.....	130
5.2.1 Insulin does not regulate GLUT4 dispersal in neonatal rat ventricular myocytes	130
5.2.2 Primary cardiomyocytes are a challenging model for the investigation of GLUT4 dispersal in cardiac tissues	135
5.2.3 Insulin regulates GLUT4 dispersal in human induced pluripotent stem cell- derived cardiomyocytes (NCardia)	140
5.2.4 Differences in insulin-stimulated GLUT4 dispersal exist in human induced pluripotent stem cell-derived cardiomyocytes depending on their source.....	145

5.3 Discussion	148
5.3.1 GLUT4 clustering in neonatal ventricular cardiomyocytes.....	148
5.3.2 Investigation of GLUT4 dispersal in adult cardiomyocytes has several challenges.....	149
5.3.3 The promise of human induced pluripotent stem cell-derived cardiomyocytes	151
5.3.4 Conclusions and future directions	153
6. Plasma membrane GLUT4 dispersal in health and disease.....	155
6.1 Introduction.....	155
6.1.1 Skeletal muscle glucose uptake.....	155
6.1.2 Insulin resistance	156
6.1.3 Transferrin receptor trafficking	159
6.1.4 Hypothesis and research aims.....	161
6.2 Results.....	163
6.2.1 Insulin resistance reorganises plasma membrane GLUT4 clustering.....	163
6.2.2 Generation of a novel pCDH-TfR-GFP lentiviral vector to investigate the specificity of GLUT4 dispersal	167
6.2.3 GLUT4 dispersal in primary human skeletal muscle cells from healthy and diabetic donors.....	170
6.3 Discussion	180
6.3.1 Insulin resistance reorganises GLUT4 clustering.....	180
6.3.2 Is plasma membrane dispersal specific to GLUT4?.....	182
6.3.3 GLUT4 dispersal in primary human skeletal muscle cells from healthy and diabetic donors.....	183
6.3.4 Conclusions and future directions	185
7. Discussion	187
7.1 Summary of key findings	187
7.2 Current limitations and future directions	188
7.2.1 Super resolution microscopy as a tool to quantify membrane protein clustering dynamics	188
7.2.2 Insulin-stimulated plasma membrane GLUT4 dispersal in adipocytes.....	192

7.2.3 Plasma membrane GLUT4 dispersal in cardiac muscle	194
7.2.4 Plasma membrane GLUT4 dispersal in skeletal muscle	195
7.3 Conclusion	196
8. Appendices	198
8.1 Nanobody optimisation staining	198
8.2 Bayesian cluster analysis of GLUT4 distribution in the plasma membrane of induced pluripotent stem cell-derived cardiomyocytes	200
8.3 Optimisation of parameters for hierarchical density-based spatial clustering of applications with noise	202
8.4 Spatial analysis using spatstat	203
References	215

List of tables

Table 2.1 List of commercially obtained cells	29
Table 2.2 List of primary cells used	30
Table 2.3 List and description of plasmids	30
Table 2.4 List and description of primary antibodies	38
Table 2.5 List and description of secondary antibodies	39
Table 3.11 Summary of descriptive statistics for the Bayesian cluster analysis frequency distribution tables.....	77
Table 3.16 Summary of approaches for cluster analysis of GLUT4 dispersal.	91
Figure 4.1 Depiction of the chemical structure of 5-Aminoimidazole-4-carboxamide ribonucleotide (AICAR) and its mechanism of action.	95

List of figures

Figure 1.1 Schematic of glucose homeostasis.	2
Figure 1.2 Glucose transporter 4 structural features.	10
Figure 1.3 Schematic of intracellular GLUT4 trafficking.	13
Figure 1.4 Schematic of the insulin signalling cascade culminating in GLUT4 translocation to the plasma membrane.	17
Figure 1.5 The physical basis of epifluorescence and TIRF microscopy.	21
Figure 1.6 Schematic summary of the key events of GCV docking, priming and fusion occurring at the plasma membrane identified by imaging experiments.	26
Figure 1.7 Kinetic model of insulin-regulated recycling and spatial distribution of GLUT4 in the plasma membrane of adipocytes.	27
Figure 3.1 Principle of resolution.	57
Figure 3.2 Principle of stochastic optical reconstruction microscopy.	59
Figure 3.3 Schematic of the HA-GLUT4-GFP construct.	62
Figure 3.4 Schematic of the analysis of spatial point patterns with Ripley's L function.	64
Figure 3.5 Cluster analysis with machine learning.	66
Figure 3.6 Schematic of density-based spatial clustering of applications with noise. ...	67
Figure 3.7 TIRF and STORM images of surface GLUT4-GFP in basal and insulin-stimulated 3T3-L1 adipocytes stained with anti-GFP nanobodies.	72
Figure 3.8 Ripley's L function analysis of the effect of fixation on GLUT4 molecule distribution in the PM of 3T3-L1 adipocytes.	73
Figure 3.9 Ripley's L function analysis of GLUT4 clustering in basal and insulin-stimulated 3T3-L1 adipocytes.	74
Figure 3.10 Bayesian Cluster Analysis of GLUT4 molecules in the PM of basal and insulin stimulated 3T3-L1 adipocytes.	76
Figure 3.12 Cluster analysis with machine learning (CAML) to quantify GLUT4 clustering in 3T3-L1 adipocytes.	78
Figure 3.13 Cluster analysis with machine learning (CAML) to quantify GLUT4 clustering in 3T3-L1 adipocytes.	79
Figure 3.14 Creation of a Voronoï diagram followed by object segmentation with SR Tesseler for GLUT4 cluster analysis.	80
Figure 3.15 Hierarchical density-based spatial clustering of applications with noise analysis of basal and insulin-stimulated 3T3-L1 adipocytes.	82
Figure 3.16 Ripley's inhomogeneous L function of GLUT4 molecule clustering in 3T3-L1 adipocytes using spatstat in R.	83
Figure 4.2 Endogenous GLUT4 protein expression and insulin sensitivity in 3T3-L1 adipocytes.	100

Figure 4.3 Insulin-stimulated deoxyglucose uptake in 3T3-L1 adipocytes.	101
Figure 4.4 Confocal images of HA-GLUT4-GFP expressing 3T3-L1 adipocytes.	102
Figure 4.5 TIRF and STORM images of surface GLUT4 in basal and insulin-stimulated 3T3-L1 adipocytes.	103
Figure 4.6 Ripley's K-function analysis of GLUT4 clustering in basal and insulin-stimulated 3T3-L1 adipocytes.	104
Figure 4.7 AICAR and Insulin sensitivity in 3T3-L1 adipocytes.	105
Figure 4.8 AICAR- and insulin-stimulated glucose uptake in 3T3-L1 adipocytes.	106
Figure 4.9 Selective gating for quantification of insulin-stimulated GLUT4 translocation to the plasma membrane by flow cytometry in 3T3-L1 adipocytes.	107
Figure 4.10 Quantitative measurement of insulin-stimulated GLUT4 translocation to the plasma membrane by flow cytometry in 3T3-L1 adipocytes.	109
Figure 4.11 Ripley's K-function analysis of the effect of AMPK activation on GLUT4 clustering in basal and insulin-stimulated 3T3-L1 adipocytes.	110
Figure 4.12 Effect of cholesterol depletion on insulin sensitivity in 3T3-L1 adipocytes.	111
Figure 4.13 MBCD- and insulin-stimulated deoxyglucose uptake in 3T3-L1 adipocytes.	112
Figure 4.14 Ripley's K-function analysis of the effect of cholesterol depletion on GLUT4 clustering in basal 3T3-L1 adipocytes.	112
Figure 4.15 Ripley's inhomogeneous L function analysis of GLUT4 molecule clustering in EFR3 knock down basal and insulin-stimulated 3T3-L1 adipocytes using spatstat.	114
Figure 4.16 Selective gating for quantification of insulin-stimulated GLUT4 translocation to the plasma membrane by flow cytometry in HeLa cells.	115
Figure 4.17 Quantitative measurement of insulin-stimulated GLUT4 translocation to the plasma membrane by flow cytometry in HeLa cells.	116
Figure 4.18 TIRF and STORM images of surface GLUT4 in basal and insulin-stimulated HeLa cells.	117
Figure 4.19 Ripley's K-function analysis of GLUT4 clustering in basal and insulin-stimulated HeLa cells.	118
Figure 5.1 GLUT4 protein expression in HeLa cells infected with a commercial HA-GLUT4-GFP adenovirus.	130
Figure 5.2 Endogenous GLUT4 protein expression and insulin sensitivity in neonatal rat ventricular myocytes.	131
Figure 5.3 TIRF and STORM images of surface GLUT4 in basal and insulin-stimulated neonatal rat ventricular myocytes.	132
Figure 5.4 Localisation density in basal and insulin-stimulated neonatal rat ventricular myocytes determined by dSTORM imaging.	133

Figure 5.5 Ripley's L-function analysis of GLUT4 clustering in basal and insulin-stimulated neonatal rat ventricular myocytes.	134
Figure 5.6 Endogenous GLUT4 protein expression of isolated rabbit cardiomyocytes. .	135
Figure 5.7 Changes in endogenous GLUT4 protein expression of isolated rabbit cardiomyocytes over time.	136
Figure 5.8 Changes of insulin sensitivity in rabbit cardiomyocytes over time.....	137
Figure 5.9 Optimisation of substrates used in primary cardiomyocyte culture to attach cells to glass coverslips.....	138
Figure 5.10 Insulin-stimulated deoxyglucose uptake in rabbit cardiomyocytes.	138
Figure 5.11 Epifluorescence and TIRF images of HA-GLUT4-GFP cardiomyocytes.	139
Figure 5.12 TIRF and dSTORM images of HA-GLUT4-GFP cardiomyocytes.....	140
Figure 5.13 Endogenous GLUT4 protein expression of induced pluripotent stem cell-derived cardiomyocytes from two commercial sources.	140
Figure 5.14 Insulin sensitivity of induced pluripotent stem cell-derived cardiomyocytes from two commercial sources.	141
Figure 5.15 TIRF and STORM images of surface GLUT4 in basal and insulin-stimulated induced pluripotent stem cell-derived cardiomyocytes obtained from NCardia.	142
Figure 5.16 Localisation density in basal and insulin-stimulated induced pluripotent stem cell derived cardiomyocytes determined by dSTORM imaging.....	143
Figure 5.17 Ripley's L-function analysis of GLUT4 clustering in basal and insulin-stimulated induced pluripotent stem cell-derived cardiomyocytes from NCardia.....	144
Figure 5.18 TIRF and STORM images of surface GLUT4 in basal and insulin-stimulated induced pluripotent stem cell derived cardiomyocytes.	145
Figure 5.19 Localisation density in basal and insulin-stimulated induced pluripotent stem cell derived cardiomyocytes determined by dSTORM imaging.....	146
Figure 5.20 Ripley's L-function analysis of GLUT4 clustering in basal and insulin-stimulated induced pluripotent stem cell-derived cardiomyocytes from CDI.	147
Figure 6.1 Insulin-stimulated deoxyglucose uptake in control and chronic insulin-treated 3T3-L1 adipocytes.	163
Figure 6.2 Ripley's K-function analysis of the effect of chronic insulin treatment on GLUT4 clustering in basal and insulin-stimulated 3T3-L1 adipocytes.....	164
Figure 6.3 Localisation density in control and chronic insulin treated basal and insulin-stimulated 3T3-L1 adipocytes determined by dSTORM imaging.	165
Figure 6.4 GLUT4 localisation density as a function of cell area for basal and insulin-treated 3T3-L1 adipocytes determined by dSTORM imaging.	166
Figure 6.5 Comparison of GLUT4 localisation density in small and bigger basal and insulin-stimulated 3T3-L1 adipocytes determined by dSTORM imaging.	167
Figure 6.6 Generation of a novel pCDH-CMV-MCS-EF1-TfR-GFP DNA plasmid.	168

Figure 6.7 Transfection of HeLa cells with pCDH-CMV-MCS-EF1-TfR-GFP plasmid.....	169
Figure 6.8 Ripley's K-function analysis of TfR-GFP clustering in basal and insulin-stimulated HeLa cells.....	170
Figure 6.9 Bright field images of undifferentiated and differentiated HSMM derived from healthy and T2DM donors.	171
Figure 6.10 Confocal images HSMM stained for DAPI and desmin.	172
Figure 6.11 Confocal images HSMM stained for DAPI and endogenous GLUT4.....	174
Figure 6.12 TIRF and STORM images of surface GLUT4 in basal and insulin-stimulated HSMM from a healthy donor.	175
Figure 6.13 Ripley's K-function analysis of GLUT4 clustering in basal and insulin-stimulated HSMM.	176
Figure 6.14 Insulin sensitivity in differentiated healthy and T2DM HSMM.	177
Figure 6.15 Endogenous GLUT protein expression in differentiated and undifferentiated HSMM.....	178
Figure 6.16 Endogenous CHC17 and sortilin protein expression in differentiated and undifferentiated HSMM.	179
Figure 7.1 Summary of Ripley's K-function analysis of GLUT4 clustering in a range basal and insulin-stimulated cell types.	191
Supplemental Figure 8.1 Colocalization of HA-GLUT4-GFP with anti-GFP nanobody immunostaining in 3T3-L1 adipocytes.....	199
Supplemental Figure 8.2 Bayesian Cluster Analysis of GLUT4 molecules in the PM of basal and insulin stimulated iPSC-CM.	201
Supplemental Figure 8.3 Optimisation of hierarchical density-based spatial clustering of applications with noise analysis for 3T3-L1 adipocytes.....	202
Supplemental Figure 8.4 G function of GLUT4 molecule dispersal in 3T3-L1 adipocytes using spatstat in R.....	205
Supplemental Figure 8.5 F function of GLUT4 molecule dispersal in 3T3-L1 adipocytes using spatstat in R.....	206
Supplemental Figure 8.6 J function of GLUT4 molecule dispersal in 3T3-L1 adipocytes using spatstat in R.....	207
Supplemental Figure 8.7 Ripley's L function of GLUT4 clusters previously identified by tessellation in 3T3-L1 adipocytes.....	209
Supplemental Figure 8.8 GLUT4 clusters identified by tessellation in 3T3-L1 adipocytes summary statistics.	210
Supplemental Figure 8.9 GLUT4 clusters identified with Tessellation in 3T3-L1 adipocytes.....	211
Supplemental Figure 8.10 Ripley's L function of GLUT4 clusters previously identified with HDBSCAN in 3T3-L1 adipocytes using spatstat in R.	212

Supplemental Figure 8.11 HDBSCAN ROI Ripley's L-function of GLUT4 molecule dispersal in 3T3-L1 adipocytes using spatstat in R.213

Supplemental Figure 8.12 ROI localizations Ripley's L-function of GLUT4 molecule dispersal in 3T3-L1 adipocytes using spatstat in R.214

Acknowledgements

First and foremost, I would like to express my sincere gratitude to my primary supervisor, Gwyn, who has been one of the best supervisors a PhD student could wish for. This project would have not been possible without your expertise, positivity, engagement and kindness. I am very grateful that your door has always been open and you have provided me with continuous support and guidance. I want to thank you for listening to and helping me with the various challenges a graduate student faces and for going out of your way to support all my endeavours such as conferences, summer schools, research visits and academic jobs. I would like to thank my second supervisor Godfrey for his valued contribution and time to exchange inspirational ideas. A very special thanks goes out to my third supervisor Nikolaj whose motivation, recommendations and knowledge helped me to succeed in my project. I am grateful you always encouraged me to take initiative and make this project my own. Working with all of you was fantastic and I have learned so much thanks to you.

I want to thank Lab 241, the Smith lab and the Biomedical Interfaces at Glasgow lab for providing an inspirational working atmosphere and exchanges of knowledge and skills and making me feel a part of the team and always providing help if needed. It has been great fun to work with all of you and I want to especially thank my colleagues Silke, Peter, Shaun, Rachel, Laura, Paul, Emma, Marie, Beth, Eline, Alice, Bracy, Amy, Fatmah, Wandiya and Yazeed. I have been happy to see your faces every day! Weekly meetings provided a constant stimulus for reflection upon my work and helped me to find solutions to research problems on several occasions. I also want to thank the people working at SIPBS at the University of Strathclyde for helping me settle into a new research home in the final year of my PhD. Moreover, I want to thank all the amazing scientists from external institutions that took the time to engage with my research and teach me various aspects of super resolution microscopy. Especially Dave, Dylan, Leandro and Sebastian.

I am grateful for all the amazing friends I have found and that kept me sane throughout my PhD journey. All of you have listened to me, engaged in deep conversations with me, seen me laugh and cry, given me a place to stay when I needed it, fed me, inspired me to take on new hobbies, pushed me to pursue what I truly want and enlightened my life in ways you do not even know. Hiking and travelling have helped me to battle the inevitable challenges of postgraduate research and I am grateful for your company on all my adventures and forming unforgettable memories.

Von ganzem Herzen möchte ich meiner Familie danken, die mich auf meiner Reise stets begleitet hat. Ganz speziell möchte ich meiner Mama und meinem Papa danken. Mama, du hast mich zu einer selbstbewussten jungen Frau erzogen und mir beigebracht, dass ich alles werden kann was ich möchte. Deine Liebe und Fürsorge begleiten mich mein ganzes Leben und du hast mir während meiner Zeit als Doktorand und beim Schreiben dieser Arbeit besonders beigestanden. Papa, du hast immer an mich geglaubt und mir geholfen, mich darauf zu besinnen was im Leben wichtig ist. Du hattest immer ein offenes Ohr und gute Ideen. Deine Liebe und Gelassenheit haben mir besonders in schweren Zeiten Kraft gegeben.

I am very grateful to have you in my life Connor. Since I met you at the start of my PhD studies your love and support have accompanied me. You have been a great source of inspiration throughout this time of my life and I am grateful for all the fun memories we share. The flowers and little presents you have sent to the PhD office have put a smile on my face on many days!

Finally, I wish to thank the British Heart Foundation for providing me with generous funding and support of this project. The 4-year PhD programme was an amazing experience and learning opportunity that has paved the way for the rest of my career.

Author's declaration

I declare that the work presented in this thesis is my own, unless otherwise cited or acknowledged. It is entirely of my own composition and has not, in whole or in part, been submitted for any other degree.

Anna Magdalena Koester

January 2021

Definitions & abbreviations

2YT	2 Yeast Tryptone
AP	Adaptor protein
APS	Adaptor protein with Pleckstrin homology and Src homology 2 domains
AS160	Akt substrate of 160 kDa
ATP	Adenosine triphosphate
AVV	Adeno-associated virus
BMI	Body mass index
CAP	c-CBL-associated protein
CHO	Chinese hamster ovary
CVD	Cardiovascular disease
DAPI	4',6-diamidino-20-phenylindole
DM	Diabetic cardiomyopathy
DMEM	Dulbecco's Modified Eagle's Medium
DMSO	Dimethyl Sulfoxide
dSTORM	Direct stochastic reconstruction microscopy
DTT	Dithiothreitol
<i>E. coli</i>	<i>Escherichia coli</i>
EDTA	Ethylenediaminetetraacetic acid
EGFP	Enhanced Green Fluorescent Protein
EGTA	Ethylene glycol-bis(2-aminoethylether)- <i>N,N,N',N'</i> -tetraacetic acid
ER	Endoplasmic Reticulum
FCS	Foetal Calf Serum
FFA	Free fatty acid
GAP	GTPase-Activating Protein
GCV	GLUT4 containing vesicles
GFP	Green Fluorescent Protein
GLUT	Glucose Transporter
GLUT4	Glucose transporter type IV
HA	Haemagglutinin
HEPES	4-(2-hydroxyethyl)-1-piperazineethanesulfonic acid
HF	Heart failure
IBMX	3-isobutyl-1-methylxanthine
IF	Immunofluorescence
iPSC-CM	Induced pluripotent stem cell derived cardiomyocytes
IR	Insulin receptor

IRAP	Insulin-Responsive Aminopeptidase
IRS	Insulin Receptor Substrate
IRV	Insulin responsive vesicles
LV	Left ventricle
MEA	Mercaptoethylamine
MOI	Multiplicity of infection
NA	Numerical Aperture
NCS	Newborn Calf Serum
PAGE	Polyacrylamide gel electrophoresis
PBS	Phosphate buffered saline
PBST	Phosphate buffered saline with Tween
PCA	Protocatechuic acid
PCD	Protocatechuic dioxygenase
PDK1	Phosphoinositide-dependent kinase 1
PFA	Paraformaldehyde
PI	Phosphoinositide
PI3K	Phosphoinositide 3-kinase
PI4P	Phosphatidylinositol 4-phosphate
PIK	Phosphoinositide kinase
PIP3	Phosphatidylinositol 3-phosphate
PKB	Protein kinase B
PM	Plasma membrane
PSF	Point spread function
ROI	Region of interest
SD	Standard deviation
SDS	Sodium dodecyl sulphate
SEM	Standard error of the mean
SIM	Structured illumination microscopy
SMLM	Single molecule localization microscopy
T2DM	Type II diabetes mellitus
TAE	Tris-acetate EDTA
TfR	Transferrin receptor
TGN	Trans-Golgi network
TIRF	Total internal reflection fluorescence
TIRFM	Total internal reflection fluorescence microscopy
VAMP	Vesicle-Associated Membrane Protein
v/v	Units volume per unit volume
w/v	Units weight per unit volume

1. Introduction

1.1 Glucose homeostasis

Glucose is the most abundant monosaccharide (simple sugar) with the molecular formula $C_6H_{12}O_6$ that serves as the primary source of energy for life (Urry et al., 2017). It is produced by plants and algae during photosynthesis from carbon dioxide and water using the energy supplied by sunlight. Its naturally occurring form is D-glucose and most of it is stored in the form of polysaccharides. In humans and animals glucose is metabolised by an oxidative process known as glycolysis. Glucose is enzymatically broken down to form adenosine triphosphate (ATP) that provides energy for all cellular activities (Urry et al., 2017).

Glucose homeostasis is key to survival and long-term health due to the central role of glucose as a universal source of energy for cell function (Urry et al., 2017). Circulating blood sugar levels are monitored and several mechanisms exist to react to changes and maintain levels within narrow limits, 4-6 mM in healthy humans (Urry et al., 2017). After a meal glucose is absorbed from the gut and blood glucose levels spike considerably. To avoid the effects of chronic hyperglycaemia (high blood sugar) it is essential to lower post-prandial blood glucose. Glucose homeostasis is primarily achieved by two glucoregulatory hormones of the body with opposing actions (Figure 1.1). Insulin and glucagon are peptide hormones that are produced by specialised cells in the islets of Langerhans of the pancreas (Brelje et al., 1989; Brissova et al., 2005). Glucagon is released from α -cells when blood glucose levels are low and is considered the body's main catabolic hormone, raising the concentration of glucose and fatty acids in the bloodstream (Urry et al., 2017). Glucagon mainly acts on hepatocytes in the liver by binding to the G protein-coupled glucagon receptor in their plasma membrane. In response to glucagon hepatocytes convert stored glycogen into glucose through glycogenolysis. When glycogen stores are depleted glucagon stimulates the liver and kidney to synthesize additional glucose by gluconeogenesis. Furthermore glucagon inhibits glycolysis so that glycolytic intermediates can be used for gluconeogenesis (Urry et al., 2017).

In contrast insulin is released from β -cells in response to high blood glucose levels and considered the body's main anabolic hormone. Its main action is to lower blood glucose levels by signalling to peripheral tissues to store excess glucose (Levine and Goldstein, 1958). Insulin binds to the tyrosine kinase insulin receptor (IR) to inhibit hepatic glucose production and catalyse glucose uptake by adipose and muscle tissues (Park and Johnson, 1955). Glucose is converted to glycogen in liver and muscle tissues and to triacylglycerols in adipose tissue which is essential for energy storage.

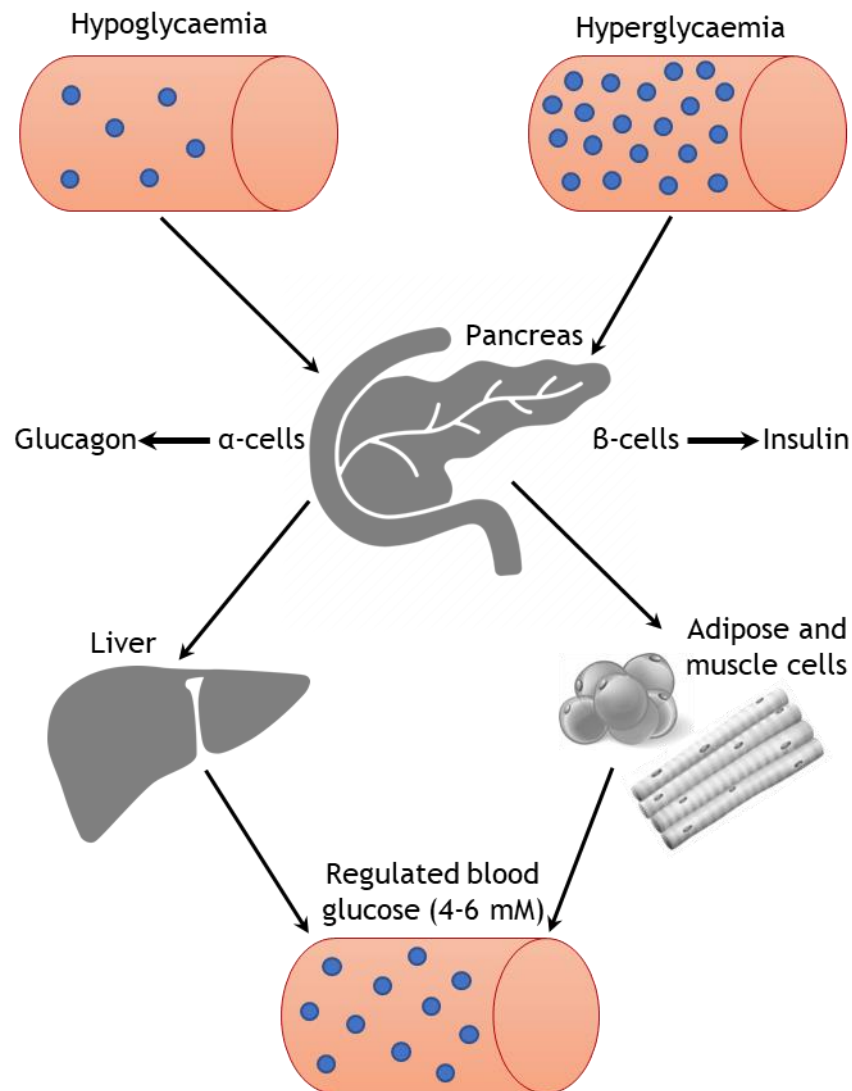


Figure 1.1 Schematic of glucose homeostasis.

Regulation of blood glucose levels occurs through the release of the two opposing peptide hormones glucagon and insulin from the α -cells and β -cells of the pancreatic islets respectively. Low blood glucose (hypoglycaemia) triggers the release of glucagon into the blood stream. Glucagon binds to its receptor in hepatocytes which activates signalling pathways that lead to the breakdown of glycogen into glucose (glycogenolysis) and the synthesis of glucose through gluconeogenesis. Insulin is secreted in response to increased blood glucose levels (hyperglycaemia). Upon binding to its receptor on muscle and adipose cells signalling pathways inducing cellular glucose uptake are triggered. In hepatocytes insulin stimulates storage of glucose in the form of glycogen through glycogenesis.

1.2 Diabetes

1.2.1 Diabetes is a growing global healthcare burden

Diabetes mellitus is a lifelong metabolic disorder characterised by high blood glucose levels due to relative lack of insulin or insulin resistance (WHO, 2013). In 2014 the WHO estimated that 422 million individuals were living with diabetes worldwide (WHO, 2016). The global prevalence of diabetes has sharply risen among adults from 4.7% in 1980 to 8.7% in 2014 with similar rates among women and men (WHO, 2016). It is predicted that the incidence of the condition is steadily on the rise. Between 2000 and 2016 a 5% increase in premature mortality attributed to diabetes was reported. In 2019 diabetes caused 4.2 million deaths worldwide, making it the 7th leading cause of death (IDF, 2019). Diabetes is prevalent around the globe but it occurs more often in developed countries. However, in recent years the greatest increase in rates has been recorded in low- and middle-income countries in Africa and Asia (Danaei et al., 2011; Ogurtsova et al., 2017). The disease and its complications impose a large economic burden on patients and their families, health care systems and national economies through medical costs and loss of productivity. The global economic burden of diabetes was estimated at 673 billion US dollars in 2015 and is expected to increase significantly in the next decades (Bommer et al., 2018; Ogurtsova et al., 2017).

In the UK 4.5 million people are estimated to live with diabetes of which 24,000 are predicted to die prematurely (Diabetes UK, 2014). The costs of diabetes to the NHS were estimated at 23.7 billion in 2010 with 9.8 billion in direct costs and 13.9 billion in indirect costs (Hex et al., 2012). This accounts for approximately 10% of the annual NHS budget which is expected to rise to 17% by 2035 (Hex et al., 2012). Mitigation of the national and global effects of diabetes is a primary goal as prevalence, deaths and health expenditure continue to rise.

1.2.2 Complications

Complications of diabetes have a dramatic effect on quality of life and can result in long-term disability (WHO, 2013). Generally, they can be grouped into acute and chronic complications. Diabetic ketoacidosis (DKA) and the hyperglycaemia hyperosmolar state (HHS) develop rapidly and are dangerous medical emergencies (IDF, 2019). DKA is caused by low insulin levels. The liver is stimulated to turn fatty acids to ketone as an energy source resulting in the accumulation of ketone bodies in the blood. As a consequence the blood's pH is lowered which can result in hypotension, shock, and death if not treated appropriately. HHS is caused by dramatically elevated blood glucose levels resulting in water being osmotically drawn out of cells. The increase in

blood osmolarity and loss of water leads to dehydration and electrolyte imbalances. Hypoglycaemia is naturally rare in diabetic patients but can be caused by a range of diabetic treatments. Without urgent medical treatment DKA, HSS and hypoglycaemia can result in unconsciousness known as diabetic coma.

Chronic hyperglycaemia is highly toxic for the body and over time leads to serious damage of blood vessels and the tissues they supply. Microangiopathy is the damage to small blood vessels such as arterioles and capillary beds causing chronic complications within target organs. Endothelial cells lining the blood vessels absorb more glucose and produce more glycoproteins which leads to thickening and weakening of the vessel basement membrane. As a result the small vessels start to leak and slow blood flow. Reduced supply of oxygen and nutrients results in severe organ damage. Diabetic nephropathy is the chronic loss of kidney function that culminates in kidney failure (Haller et al., 2017). Diabetic retinopathy is a medical condition that arises from damage to the retina and is the leading cause of blindness in the developed world (Duh et al., 2017). The development of microangiopathy correlates closely with neuronal dysfunction because neurons and nerves are not sufficiently supplied with blood. The loss of function of nerves is known as diabetic neuropathy and affects the whole body (Feldman et al., 2019). However, one of the most common pathologies associated with diabetes is diabetic foot caused by advanced peripheral nerve dysfunction (Pendsey, 2010). A combination of dysfunctional motor, autonomic, and sensory components of the nervous system result in anatomic foot deformities, skin breakdown, susceptibility to infection and ulceration (Pendsey, 2010). The loss of sensation in the affected foot causes that patients are unaware of the insult to their feet and the condition progressively worsens. As a result treatment is delayed and often only leaves amputation as the only remaining option (Pendsey, 2010).

Apart from affecting small vessels hyperglycaemia has a detrimental effect on the large vessels of the body. In the Framingham Heart Study a strong positive correlation between diabetes and the incidence of cardiovascular disease was established for the first time (Kannel and McGee, 1979). Today it is known that diabetic patients have an elevated risk of developing a specific form of pre-mature, accelerated atherosclerosis (Madonna et al., 2018). Atherosclerosis is characterised by inflammatory remodelling of the arterial vascular wall that leads to accumulation of plaques and narrowing of the vessel lumen (van Varik et al., 2012). Enlargement of atherosclerotic plaques results in either rupture or stenosis. The complete obstruction of blood flow and prevention of perfusion of the downstream tissue can lead to myocardial ischaemia in the heart and stroke in the brain. Both are immediately life-threatening conditions. Furthermore,

arterial remodelling increases arterial stiffness which promotes pathological hemodynamic patterns for instance hypertension which is a strong independent risk factor for many cardiovascular diseases. Diabetic macroangiopathy and its complications are the number one cause of death in the diabetic patient population.

1.2.3 Causes

Diabetes mellitus is divided into three main types known as type I, type II and gestational. Type I diabetes mellitus is defined by the loss of insulin-producing pancreatic β -islet cells resulting in insulin deficiency (WHO, 2013). The majority of cases result from an auto-immune response in which a T cell-mediated attack culminates in the loss of β -islet cells. Type I accounts for 10% of diabetes mellitus cases and it is mostly attributed to genetic factors affecting otherwise healthy individuals (Todd et al., 2007; WHO, 2013). In contrast, type II diabetes mellitus (T2DM) is characterized by insulin resistance sometimes occurring in combination with relatively reduced insulin secretion. Insulin resistance is the inability of the body's tissues to respond adequately to insulin stimuli and decrease blood glucose concentration. T2DM is the most common type of diabetes making up 90 % of cases (WHO, 2013). Genetic factors have been identified for making people more susceptible to the development of T2DM (Florez et al., 2003; Gerich, 1998) but the condition is primarily associated with life style factors. The underlying genetic mechanisms are complex, multifaceted and still poorly understood but numerous studies reported that lifestyle factors associated with weight gain and the development of obesity increase the risk of T2DM. Particularly lack of physical activity, a poor diet rich in saturated fatty acids and high glycaemic index carbohydrates, stress and smoking are strong environmental risk factors (Dendup et al., 2018; Kolb and Martin, 2017; Uusitupa, 2002). Gestational diabetes is a condition in which high blood sugar levels are developed during pregnancy and resembles type II diabetes (McIntyre et al., 2019). The condition can improve or disappear after giving birth.

1.2.4 Treatment

Treatment strategies for the management of diabetes generally focus on monitoring and maintaining blood glucose levels within the appropriate range which can be achieved by several means. Injection of insulin is the first line treatment option for type I diabetes mellitus (IDF, 2019). T2DM is a more heterogeneous, multifactorial condition and treatment consists of a mixture of lifestyle interventions, management of cardiovascular risk factors and normalization of blood glucose (Ripsin et al., 2009). Lifestyle modification strategies are the most widely used treatment for T2DM and were

shown to elicit long-lasting positive effects on disease progression in small subject groups (Haw et al., 2017). Nevertheless, the education, implementation and sustainability of behaviours needed for ongoing self-management is difficult to establish for individual patients in the global context (Franz et al., 2015). The currently available pharmacological interventions focus on the treatment of symptoms rather than the actual cause (Haw et al., 2017). The global rise in the prevalence of diabetes and soaring mortality rates lead to the conclusion that the current treatment options for the condition are limited and insufficient. Diabetes research is vital to enhance our understanding of the underlying pathophysiology of diabetes and develop novel treatment strategies that address the underlying cause.

1.3 Diabetic cardiomyopathy

1.3.1 Recognition of diabetic cardiomyopathy

The close link between T2DM and the development of cardiovascular disease (CVD) has been long established (Leon and Maddox, 2015). The Framingham Heart Study reported that the incidence of heart failure (HF) in T2DM is increased 2.4-fold in men and 5-fold in women (Kannel et al., 1974). Moreover, HF clinical outcomes are significantly more detrimental for T2DM patients compared to the normal population and HF incidence ranges from 19% - 26% (Rydén et al., 2000; Shindler et al., 1996; Thrainsdottir et al., 2005). It has been found that T2DM has direct adverse effects on the myocardium in the absence of other cardiac risk factors such as coronary artery disease, valvular disease, hypertension and dyslipidaemia. In 1972 diabetic cardiomyopathy (DCM) was firstly described after post-mortem examination of 4 T2DM patients who manifested HF without any signs of coronary artery or valvular disease (Rubler et al., 1972). DCM is a clinical condition of ventricular dysfunction that is not directly attributable to other confounding CVD risk factors. It affects approximately 12% of T2DM patients and its prevalence rises in parallel with the global increase in T2DM (Trachanas et al., 2014). T2DM leads to different structural and functional modifications in the myocardium emerging from metabolic alterations caused by hyperglycaemia, hyperlipidaemia and insulin resistance (Lorenzo-Almorós et al., 2017). The functional phenotype of DCM manifests itself in stages over time.

1.3.2 Pathophysiology of diabetic cardiomyopathy

The first clinically asymptomatic stage of DCM is characterised by increased myocardial stiffness and fibrosis. During this stage early diastolic filling is reduced, atrial filling is increased and left ventricle (LV) end-diastolic pressure is elevated (Westermeyer et al., 2016). Several studies using Doppler echocardiography to investigate the prevalence of

LV diastolic dysfunction highlight that this pathology is common in T2DM patients and DCM (Boyer et al., 2004; Poulsen et al., 2010; Zahiti et al., 2013). Over time a range of adaptive processes occur that result in structural remodelling of the diabetic heart to compensate for loss of functional capacity during the initial stage of disease progression (Walker et al., 2016). The second stage of DCM is defined by LV hypertrophy, cardiac remodelling and advanced diastolic dysfunction. Clinical studies found that diabetics had a significantly increased LV wall thickness compared to healthy controls (Devereux et al., 2000; Lee et al., 1997; Shang et al., 2016; Walker et al., 2016). The pathological LV hypertrophy is associated with an increased cardiomyocyte volume due to collagen deposits and activation of mitogen-activated protein kinase (MAPK) and calcium signalling pathways resulting in cell death (Bernardo et al., 2010). These molecular changes culminate in reduced cardiac contractile capacity (Bernardo et al., 2010). During the second stage of DCM clinical symptoms of HF with normal ejection fraction develop. Further disease progression leads to systolic dysfunction coexisting with diastolic dysfunction and decreased myocardial compliance culminating in HF with reduced ejection fraction.

1.3.3 Impaired insulin signalling in diabetic cardiomyopathy

Studies indicate that abnormal insulin signalling is a key contributor in the development of DCM and changes in GLUT4 expression and trafficking precede pathological structural and functional changes of the myocardium (Jia et al., 2018). Mice with cardiomyocyte-restricted deletion of insulin receptors (CIRKO) showed a decrease in cardiac glucose uptake and an increase in cardiac reactive oxygen species production and mitochondrial dysfunction (Bugger et al., 2012). Insulin receptor substrates function as essential signalling intermediates downstream of the activated insulin receptor to regulate cell metabolism. Heart-specific double knock out of insulin receptor substrate genes 1 and 2 in mice resulted in cardiac apoptosis and fibrosis and exhibition of features of HF for instance impaired energy metabolism gene expression of the myocardium (Qi et al., 2013). Moreover in CIRKO mice impaired insulin action was shown to contribute to oxidative stress and mitochondrial dysfunction (Boudina et al., 2009). Myocardial biopsies from T2DM patients were reported to have reduced insulin signalling and GLUT4 expression and translocation (Cook et al., 2010). This highlights the importance of further studies investigating insulin action in the myocardium.

1.4 Glucose transport

1.4.1 Glucose transporters

Glucose transport from the blood stream into cells is mediated by 14 tissue-specific members of the glucose transporter (GLUT) family (Mueckler and Thorens, 2013). GLUTs are membrane proteins that facilitate transport of glucose and related hexoses across cell plasma membranes. GLUT1 was the first facilitative GLUT identified to catalyse glucose uptake into erythrocytes in 1985 (Mueckler et al., 1985). The molecular cloning of GLUT1 subsequently led to the identification of homologue genes and discovery of four more facilitative GLUTs (GLUT2-5) (Joost and Thorens, 2001). Only in recent years more GLUT-like sequence fragments were identified in homology searches of gene databases from various genome projects. With this strategy seven new members of the GLUT family were identified sharing significant similarity with GLUT1 (Joost and Thorens, 2001). GLUTs are encoded by the SLC2 genes and composed of approximately 500 amino acids and can be divided into three classes based on sequence similarities (Deng and Yan, 2016). All members of the GLUT family contain 12 membrane-spanning α -helices with intracellular N- and C-termini, seven conserved glycine residues, two conserved tryptophan residues and two conserved tyrosine residues (refer to figure 1.2 for GLUT structural features). Class I facilitative GLUTs are glucose-specific GLUTs represented by GLUT1-4 and GLUT14 with specific glutamine residues on helix 5 and STSIF-motifs in loop 7. Class II comprises the fructose-specific GLUT5 and the related GLUTs 7, 9 and 11 with a characteristic lack of tryptophan in helix 10. Class III are the structurally atypical GLUT6, 8, 10, 12, 13 characterised by a shorter extracellular loop 1 lacking a glycosylation site (Mueckler and Thorens, 2013). One or more GLUTs are present in all cells of the body and although structurally very similar GLUT isoforms differ in tissue and cellular distribution, substrate specificity and transport kinetics (Kahn, 1992). Class I GLUTs are most well-characterised whereas the functions of GLUTs in class II and III are not clearly defined at present. The first comprehensively studied GLUT was GLUT1 which is highly abundant in erythrocytes and the blood-brain barrier (Kasahara and Hinkle, 1977; Mueckler et al., 1985). GLUT3 is a high-affinity isoform and referred to as the “neuronal GLUT” and also highly expressed in brain tissue. The brain is dependent on a continuous and constant supply of its main energy substrate glucose and therefore the GLUTs in the brain are mainly located in the abluminal membranes of brain cells (Duelli and Kuschinsky, 2001). GLUT2 is the major GLUT expressed in hepatocytes and able to catalyse bidirectional flow of glucose in fed and fasting states (Thorens and Mueckler, 2010). GLUT2 is a low-affinity isoform that facilitates glucose uptake for glycolysis and glycogenesis and glucose release during gluconeogenesis. GLUT4 is the predominant isoform that mediates insulin-regulated glucose transport

into adipose tissue, skeletal and cardiac muscle (Bell et al., 1993). GLUTs catalyse glucose transport through an ATP-independent, facilitative diffusion mechanism. Crystal structures for GLUT1, 3 and 5 have only become available recently and suggest that GLUTs transport glucose down its concentration gradient according to a model of alternate conformation (Holman, 2020). It is predicted that the membrane spanning domains are built from replicated trimer substructures that move relative to each other. GLUTs expose a substrate binding site toward the outside of the cell and substrate binding results in a conformational change that closes the cleft towards the external side and alternately opens a cleft to the internal side of the membrane to release the substrate on the other side (Holman, 2020). Glucose transporters in the heart specifically are discussed separately in section 5.1.1. Since its discovery GLUT4 (James et al., 1988) has been the subject of numerous investigations and received more attention than any other membrane transport protein (Thorens and Mueckler, 2010). GLUT4 plays a key role in glucose homeostasis and its dysregulation in several prevalent insulin-resistant disease states makes it an important study target that will also be addressed in this thesis.

1.4.2 Glucose transporter 4

In the early 1980s pioneering work in the Cushman (Cushman and Wardzala, 1980), Kono (Suzuki and Kono, 1980) and Jenrenaud (Wardzala and Jeanrenaud, 1981) laboratories revealed that insulin causes translocation of glucose transport units from an intracellular storage site to the PM in adipocytes (Thorens and Mueckler, 2010). In 1988 the production of a monoclonal antibody (mAb 1F8) against a GLUT residing in microsomes of primary adipocytes enabled the identification of a unique, insulin-regulatable GLUT isoform known as GLUT4 today (James et al., 1988). In resting cells no protein was detectable through immunoblotting in the plasma membrane fraction of the adipocytes but upon insulin stimulation an increase in cell surface labelling was evident. This experiment provided the first evidence for the existence of GLUT4 translocating from an intracellular location to the cell surface in response to insulin (James et al., 1988). The SLC2A4 gene encoding GLUT4 was cloned (Birnbaum, 1989; James et al., 1989) and mapped (Bell et al., 1989) in the following year. It shares ~65% sequence identity with the SLC2A1 gene encoding GLUT1 referred to as HepG2 GLUT at the time (Bell et al., 1989). Structurally GLUT4 shares basic similarities with other GLUTs (Mueckler and Thorens, 2013). However, GLUT4 has some unique differences in the amino acid arrangement of its primary sequence (Figure 1.2) supporting its specific functions and playing a role in the kinetics of endo- and exocytosis (Huang and Czech, 2007). Genetically engineered mouse models with enhanced or ablated GLUT4 expression support the idea that GLUT4 plays a central role in whole body metabolism.

The homozygous fully GLUT4-deficient knock-out mouse displays a range of compensatory mechanisms ensuring its survival and is therefore less informative (Katz et al., 1995). Heterozygous GLUT4^{+/-} mice with decreased GLUT4 expression in adipose and muscle tissues have increased levels of blood glucose and insulin, reduced muscle glucose uptake, hypertension, and diabetic pathologies comparable to human patients in their heart and liver (Stenbit et al., 1997). Overexpression of GLUT4 in heterozygous GLUT4^{+/-} mice prevents the development of insulin insensitivity and the diabetic phenotype showing that GLUT4 is a key player in glucose homeostasis (Tsao et al., 1999). Transgenic mice overexpressing GLUT4 selectively in either adipocytes (Shepherd et al., 1993) or muscle cells (Tsao et al., 1996) showed enhanced *in vivo* glucose tolerance and basal and insulin-stimulated glucose transport. Selective GLUT4 depletion in both adipose (Abel et al., 2001) and muscle tissues (Zisman et al., 2000) results in insulin resistance and glucose intolerance. Targeted GLUT4 gene disruption in specific tissues using cre-lox recombination in mice was found to strongly affect other tissues metabolically which is surprising especially regarding adipocytes that only account for a small fraction of body glucose disposal (Abel et al., 2001; Zisman et al., 2000).

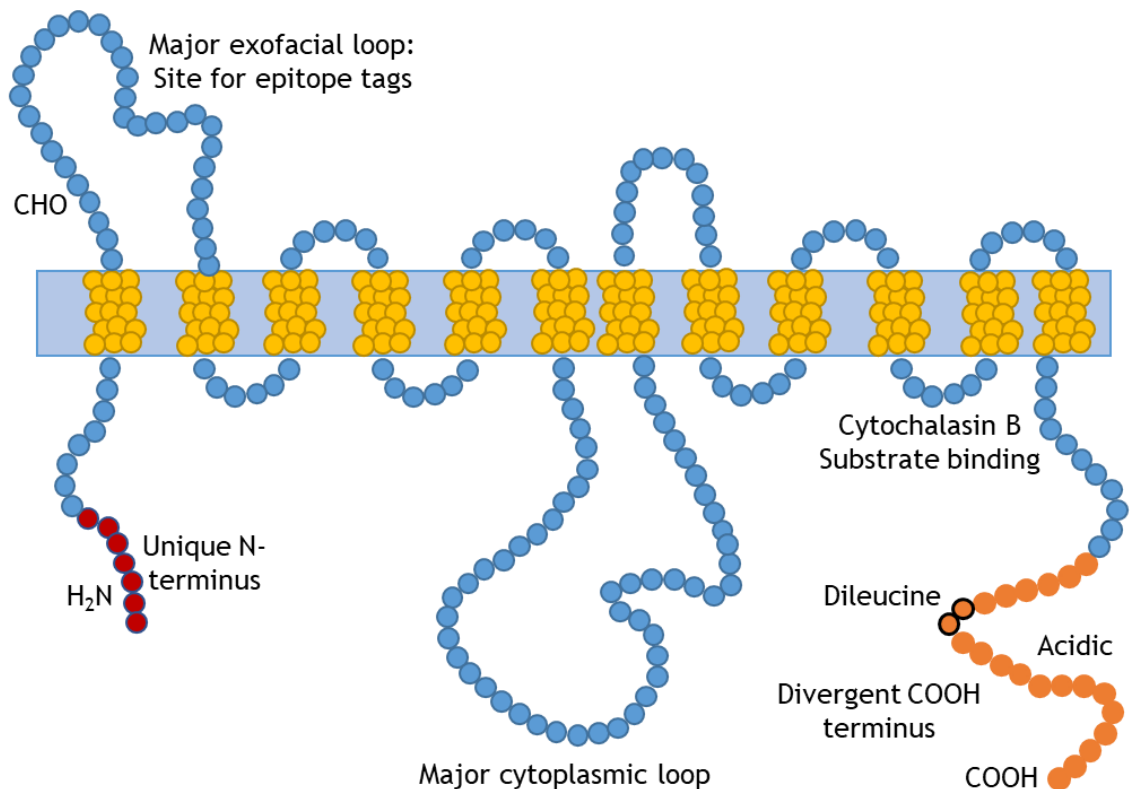


Figure 1.2 Glucose transporter 4 structural features.

The affinity of GLUT4 for insulin is strongly linked to its unique sequences found in the H₂N and C-termini. GLUT4 shares basic structural similarities with other members of the GLUT family but its H₂N contains a F₅QQI motif that interacts with adaptor proteins important for endocytosis. The C-terminal end contains a double leucine and an acidic TELEY motif that regulate the intracellular distribution of GLUT4 (adapted from (Huang and Czech, 2007)).

1.4.3 GLUT4 intracellular trafficking overview

In the following, a nomenclature will be defined to discuss GLUT4 intracellular trafficking appropriately. In the absence of insulin, GLUT4 populates tubules and vesicles throughout the cell. Multiple names are used in the field of GLUT4 traffic to identify/define intracellular GLUT4-containing vesicles. For clarity, the names used in this thesis and the meaning I ascribe to them are given below:

GSC All intracellular vesicles and tubules that contain GLUT4 - hence the ***GLUT4 Storage Compartment*** - this includes GLUT4 in endosomes, the *trans*-Golgi network and the compartment targeted by CHC22 in humans. IRVs are regarded as a separate compartment. The GSC is likely comprised of multiple sub-compartments (Kandror and Pilch 2011; Bogan 2012; Kioumourtzoglou et al. 2015).

IRV ***Insulin-Responsive Vesicles***: That population of vesicles derived from the GSC that respond acutely to insulin by mobilisation to the cell surface. IRV are formed from donor membranes that are likely a sub-domain of the *trans*-Golgi network and/or recycling endosomes. The general view is that these vesicles are depleted of endosome or Golgi markers.

In this thesis, I will use IRV to represent any GLUT4-containing vesicle that approaches the PM in response to insulin. '***GLUT4 containing vesicle***' will be used when the nature of the GLUT4-containing structure is ambiguous or ill-defined.

Vesicle exocytosis is vital for the delivery of intracellular material to the extracellular space and governed by signalling pathways that regulate and coordinate proteins associated with the vesicle trafficking machinery (Leto and Saltiel, 2012). Several membrane proteins are known to cycle between the membrane and intracellular loci known as the endosomal cycle (Rea and James, 1997). Selective retrieval of GLUT4 from the PM occurs either through clathrin-mediated endocytosis or other pathways that proceed independently of clathrin in adipose and muscle tissues (Doherty and McMahon, 2009). Clathrin-independent endocytotic pathways require specialised lipid domains such as cholesterol with or without participation of caveolin (Antonescu et al., 2008, 2009). Kinetic and morphological analysis of GLUT4 sequence mutants have largely contributed to the understanding of GLUT4 endocytosis and sorting (Rea and James, 1997). GLUT4 contains a unique N-terminal phenylalanine residue in addition to dileucine and acidic motifs in its COOH terminus (Figure 1.2). It was shown that the dileucine motif L₄₈₉ / L₄₉₀ present in the GLUT4 C-terminus is critical for GLUT4 sorting and intracellular sequestration (Verhey and Birnbaum, 1994). Replacement of the

dileucine motif with alanine substitutions did not inhibit GLUT4 internalisation but slowed basal GLUT4 intracellular retention after insulin withdrawal indicating that L₄₈₉/L₄₉₀ is not the only endocytosis motif (Blot and McGraw, 2008). The C-terminus acidic cluster TELEYLGP motif (498-505) is important for the sequestration of GLUT4 from endosomal compartments to specialised vesicles that can fuse with the PM (Blot and McGraw, 2008). Replacing 12 amino acids in the GLUT4 C-terminus with the same sequence found in human GLUT3 creates chimeras that remain stuck in the endosomal cycle (Shewan et al., 2000). The F₅QQI sequence plays a critical role in GLUT4 sequestration from endosomes and ablation of the sequence results in inhibition of GLUT4 recycling after insulin stimulation and the targeting of GLUT4 to late endosomes/lysosomes where it is degraded (Palacios et al., 2001). GLUT4 molecules are stable proteins with a half-life of 48 hours and will undergo multiple rounds of recycling before being degraded (Sargeant and Pâquet, 1993). Complex interactions between numerous proteins regulate the subcellular localization of GLUT4 and its translocation to the plasma membrane in response to insulin stimulation, a process known as GLUT4 trafficking (Leto and Saltiel, 2012). In contrast to other GLUT family members, GLUT4 is not always present in the PM. In the basal state the majority of GLUT4 is sequestered in intracellular tubulo-vesicular structures. The investigation of the intracellular distribution of GLUT4 in rat adipose tissue with immunolocalization and electron microscopy revealed that 99 % of GLUT4 was located in small vesicles near the *trans*-Golgi reticulum and tubulo-vesicular structures in the cytoplasm whereas only 1 % of total GLUT4 were located in the PM under basal conditions (Slot et al., 1991a). Insulin stimulation resulted in an increase of total GLUT4 in the PM to 40 %. A later study confirmed the existence of a population of small vesicles in the neuro-endocrine cell line PC12 transfected with rat GLUT4 (Herman et al., 1994). It was found that GLUT4-containing vesicles did not colocalise with the transferrin receptor (TfR), a marker of recycling endosomes, indicating the presence of a distinct class of intracellular GLUT4 storage vesicles beyond the endosomal system (Herman et al., 1994). Another study using subcellular fractionation of 3T3-L1 adipocytes reported that 40 % of GLUT4-positive vesicles colocalised with TfR whereas 60 % of GLUT4-positive vesicles were TfR-negative confirming the existence of a specialized intracellular compartment involved in GLUT4 trafficking (Livingstone et al., 1996). In 1997 the compartment was referred to as GLUT4 storage compartment and the GLUT4-positive, TfR-negative vesicles named GLUT4 storage vesicles (Rea and James, 1997); the latter are now more usually referred to as IRVs (see above). Biochemically, several proteins have been identified as markers of GSC by subcellular fractionation and immunofluorescence analysis. Both vesicle-

associated membrane protein 2 (VAMP2) and insulin-regulated aminopeptidase (IRAP) have been reported to colocalise with insulin-responsive GLUT4-containing vesicles (Martin et al., 1996; Subtil et al., 2000). Furthermore sortilin-1, low-density lipoprotein receptor-related protein 1 and the tethering protein TUG have been reported to localise with GLUT4 in the GSC (Jedrychowski et al., 2010; Shi and Kandror, 2005; Yu et al., 2007). It was proposed that 40-50 % of GLUT4 is retained in the endosomal cycle whereas 50-60 % is distributed in the *trans*-Golgi network and IRVs (Martin et al., 1996; Zeigerer et al., 2002). The current model of GLUT4 trafficking is that GLUT4 is distributed between the two intracellular pools that are in dynamic communication with one another (Zeigerer et al., 2002). The simplified fundamental concept of GLUT4 trafficking depicted in figure 1.3 is that GLUT4 is internalised into a general endosomal system from which it can enter a specific cycle where it is targeted to the *trans*-Golgi network to be sorted into insulin-responsive IRVs that translocate to the PM upon insulin stimulation.

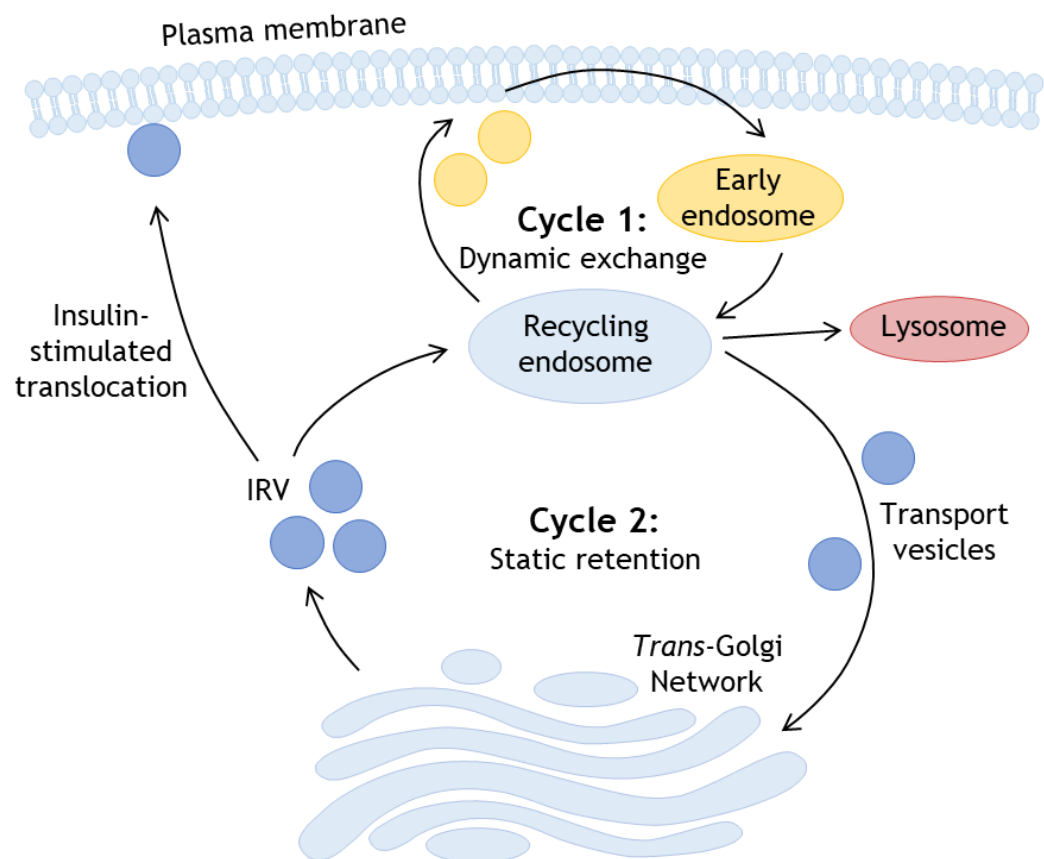


Figure 1.3 Schematic of intracellular GLUT4 trafficking.

GLUT4 is sequestered intracellularly in the GLUT4 storage compartment (GSC) which includes cycle-1 and cycle-2. GLUT4 is sorted into insulin responsive vesicles (IRV) which translocate to the plasma membrane upon insulin stimulation. After endocytosis GLUT4 enters the endosomal pathway (cycle 1). During cycle 1 GLUT4 can either be returned to the PM, targeted to lysosomes to be degraded or sequestered into IRV via the *trans*-Golgi network. The static retention model describes a specialised sorting cycle (cycle 2) in which GLUT4 continuously cycles through the *trans*-Golgi network and recycling endosome until insulin stimulates rapid translocation to the PM.

1.4.4 GLUT4 trafficking in muscle tissues

Similarly to adipocytes GLUT4 is mostly retained within intracellular GSC and excluded from the cell surface in resting skeletal muscle fibres. In rat muscle it was observed that 23 % of GLUT4 was present in large structures for instance multivesicular endosomes located in the *trans*-Golgi network and 77 % was associated with small tubulovesicular structures (Ploug et al., 1998). Several studies investigating skeletal muscle in living mice employing novel confocal imaging techniques have demonstrated that insulin as well as contractions induce GLUT4 translocation to the plasma membrane proper known as sarcolemma and its extensions known as t-tubular membranes (Lauritzen et al., 2006, 2008, 2010). Quantitative analysis of imaging data revealed that insulin stimulation increased GLUT4 labelling 7-fold and contraction 9-fold in the sarcolemma of rat muscle fibres. The two stimuli combined resulted in a 14-fold increase in GLUT4 labelling indicative of an additive effect (Ploug et al., 1998). Furthermore, insulin stimulation increased GLUT4 labelling 15-fold and contraction 20-fold in the t-tubules of the muscle fibres with both stimuli resulting in a 30-fold increase (Ploug et al., 1998). Due to the additive nature of insulin- and contraction-induced glucose transport it was proposed that two different pools of GLUT4 exist in skeletal muscle in rodents that are recruited by distinct mechanisms. These processes are more difficult to demonstrate in human subjects due to technical and ethical constraints. Nevertheless several studies showed that both insulin and contraction stimulate recruitment of GLUT4 to the plasma membrane and increase glucose transport in human skeletal muscle (Goodyear et al., 1996; Gumà et al., 1995; Kennedy et al., 1999). Skeletal muscle glucose transport is further described in section 6.1.1.

The transport of glucose across the sarcolemma is facilitated by GLUT4 in fully differentiated cardiomyocytes similarly to adipose and skeletal muscle tissues (Slot et al., 1991b). In the resting state GLUT4 is located in intracellular tubulovesicular structures that comprise at least two distinct populations (Fischer et al., 1997). The first pool contains predominantly GLUT4 and low levels of GLUT1 and secretory carrier membrane proteins (SCAMPs) whereas the second pool is enriched with GLUT1 and SCAMPs and contains less GLUT4. In isolated rat cardiac myocytes insulin treatment resulted in GLUT4 depletion from both pools and GLUT1 and SCAMPs depletion from the second pool (Fischer et al., 1997). Insulin withdrawal was observed to result in re-entry of GLUT1 and GLUT4 to the specific pools they translocated from. Glucose transporters in the healthy heart are further described in section 5.1.1.

1.4.5 GLUT4 endocytosis

The protein clathrin plays a fundamental role in endocytosis and the formation of coated vesicles in the cytoplasm for intracellular trafficking (Pearse, 1976). In the basal state GLUT4 was reported to be present on clathrin-coated vesicles from the PM and the *trans*-Golgi network indicating that clathrin also plays a role in intracellular GLUT4 retention (Robinson et al., 1992). Another study observed that GLUT4 colocalised with clathrin lattices and appeared to be continually retrieved from the PM through the clathrin pathway in the basal state (Chakrabarti et al., 1994). Insulin treatment decreased the concentration of GLUT4 in PM-derived clathrin coated vesicles specifically by 60%. It was hypothesised that insulin has a direct effect on GLUT4 endocytosis via the described mechanism (Chakrabarti et al., 1994). Later it was found that GLUT4 retention occurs via two different pathways dependent on either cholesterol or clathrin adaptor protein complex-2 (AP-2) (Blot and McGraw, 2006). In the basal state 80% of GLUT4 was observed to be internalised by a cholesterol-dependent mechanism independent of AP-2. Insulin stimulation was observed to inhibit the cholesterol-dependent pathway and shift GLUT4 internalization towards an AP-2-dependent pathway in adipocytes (Blot and McGraw, 2006).

However, comparison of the time courses of tracer-tagged GLUT4 redistribution under basal and insulin-stimulated conditions in 3T3-L1 adipocytes revealed that endocytosis rate constants were only 30% slower following insulin stimulation (Yang and Holman, 1993). Moreover, it was found that insulin increased GLUT4 exocytosis rate constants significantly indicating that insulin stimulation had a minimal effect on GLUT4 endocytosis compared to substantial effects on exocytosis (Yang and Holman, 1993).

1.5 Insulin signalling

After a meal the β -cells of the pancreas sense the sudden increase in blood glucose levels and release insulin. Binding of insulin to the membrane-bound insulin receptor (IR) initiates a complex intracellular signalling cascade that culminates in translocation of GLUT4 to the PM within minutes (Figure 1.4). Insulin binds to the two IR α -subunits resulting in auto-phosphorylation of the two internal-facing IR β -subunits activating the receptor intrinsic tyrosine kinase activity (Lee and Pilch, 1994). Following activation of the IR tyrosine kinase binding sites for several protein signalling partners containing Src-homology 2 (SH2) and phosphotyrosine-binding domains become available (De Meyts, 2000). Various intracellular signalling cascades are coordinated by either insulin receptor substrates (IRS) or adapter protein with a pleckstrin homology and an SH2 domain (APS) following interaction with the IR. Insulin causes a variety of metabolic and

mitogenic effects in several tissues. Insulin signalling in cardiac tissues is described in section 6.1.2 specifically.

1.5.1 Mitogen-activated protein (MAP) kinase signalling pathway

The mitogen-activated protein (MAP) kinase signalling pathway mediates the mitogenic actions of insulin resulting in cellular proliferation and gene transcription (Boucher et al., 2014). After ligand binding Shc proteins are recruited and phosphorylated. This results in phosphorylation of Grb2 and binding of son-of-sevenless (SOS) proteins. The membrane-bound Ras is switched from its GDP-bound form to its active GTP-bound form by SOS resulting in interaction with Raf. Raf stimulates MEK1 and 2 leading to activation of the MAP kinases ERK1 and 2. Phosphorylated ERK controls cell proliferation, differentiation, gene expression and cytoskeletal reorganisation (Boucher et al., 2014).

1.5.2 Insulin receptor substrate (IRS) signalling pathway

The best studied insulin signal transduction pathway is coordinated by the IRS-1, -2, -3 and -4 proteins that mediate varying pathways resulting in the metabolic actions of insulin (Figure 2.4). IRS-1 and -2 are most abundant in insulin sensitive tissues and the key mediators. In adipose and muscle tissues the activated IR tyrosine kinase phosphorylates IRS-1 resulting in the recruitment of phosphatidylinositol-3-kinase (PI3K) (Backer et al., 1992). Experimental inhibition of either IRS-1 or PI3K results in an impairment of insulin-stimulated glucose transport in adipocytes suggesting that these proteins are key intermediates of insulin signalling (Clarke et al., 1994; Quon et al., 1994). PI3K promotes the formation of the lipid second messenger phosphatidylinositol (3,4,5) trisphosphate (PIP3) from phosphatidylinositol (4,5)bisphosphate (PIP2) at the inner leaflet of the PM. PIP3 recruits phosphoinositide dependant kinase 1 (PDK1) and protein kinase B (Akt) to the cell surface where Akt is activated by phosphorylation (Kohn et al., 1996). Akt activation results in activation of numerous downstream targets regulating lipid and glycogen synthesis, gluconeogenesis, and glucose transport (Boucher et al., 2014). In this thesis the main focus will be put on insulin's actions on regulating glucose transport. Pharmacological Akt activation in 3T3-L1 adipocytes engineered to express a rapidly drug-inducible Akt2 system showed that Akt2 activation alone results in a GLUT4 translocation response comparable to insulin stimulation (Ng et al., 2008). Therefore, Akt2 is regarded as another key intermediate in the IRS insulin signalling pathway governing glucose transport. Akt activation leads to phosphorylation of its main target Akt substrate of 160 kDa (AS160). AS160 contains a GTPase-activating protein (GAP) domain that inhibits GTP loading and activation of downstream effectors. In adipocytes the key target of AS160 is Rab10. Phosphorylation of AS160 by Akt results in

the relief of AS160 inhibition of GAP activity and allows GTP loading of Rab10. This process activates the Rab10 protein and culminates in IRV translocation to and fusion with the PM (Sano et al., 2007). IRV fusion with the PM is driven by SNARE proteins which are present as monomers on incoming and target cell membranes. The v-SNARE protein VAMP2 assembles irreversibly with the two t-SNARE proteins syntaxin4 and SNAP23 situated on the target membrane and fusion of the proximate lipid bilayers is established through thermodynamic melting (Bryant and Gould, 2011).

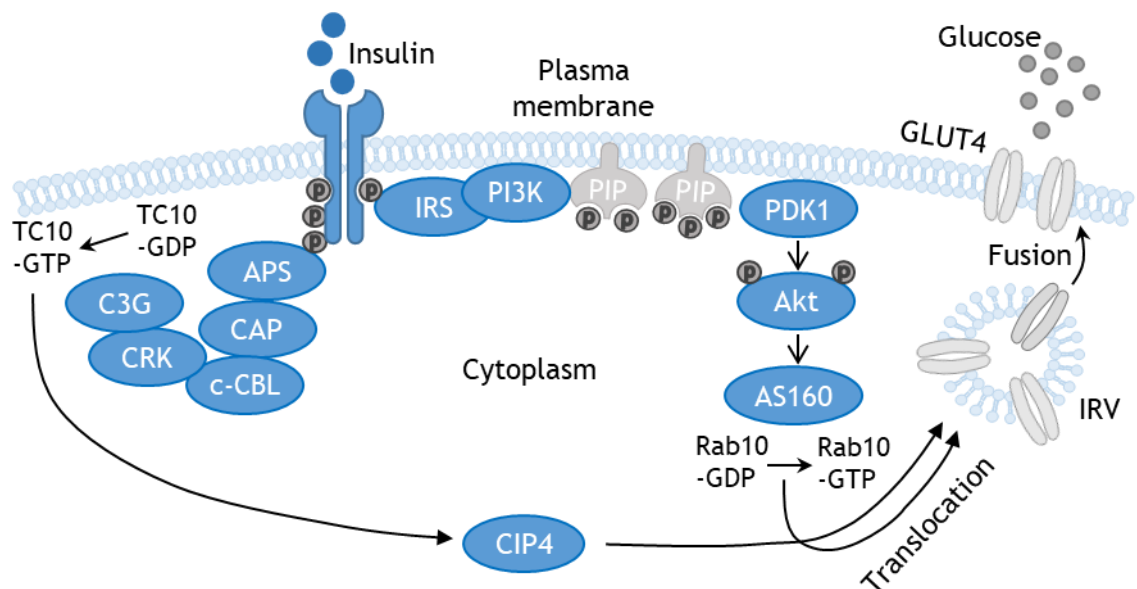


Figure 1.4 Schematic of the insulin signalling cascade culminating in GLUT4 translocation to the plasma membrane.

Insulin binds to its receptor which results in autophosphorylation leading to activation of the IRS and APS signalling pathways. IRS recruits PI3K which promotes formation of PIP3 at the PM. In response PDK1 and Akt are recruited to the cell surface and activated. AS160 is phosphorylated which results in the relief of AS160 inhibition of GAP activity and allows GTP loading of Rab10. This activates the Rab10 protein and culminates in GLUT4 translocation. The APS signalling branch is less well characterised but activation results in recruitment of TC10-GTP, which binds to CIP4 aiding GLUT4 translocation.

1.5.3 Adaptor protein with pleckstrin homology and Src homology domains (APS) signalling pathway

Several studies proposed that the APS interacts with the IR kinase and that this signalling branch contributes to GLUT4 translocation in 3T3-L1 adipocytes (Isakoff et al., 1995; Wiese et al., 1995). However, the APS signalling branch is less well characterised than the previously described IRS branch (Figure 2.4). Studies suggest that APS activation recruits c-CBL associated protein (CAP) which associates with c-Cbl in 3T3-L1 adipocytes and Chinese hamster ovary (CHO) cells to allow for c-Cbl tyrosine phosphorylation (Ahmed and Pillay, 2003; Ahmed et al., 2000; Liu et al., 2002; Wakioka et al., 1999). The CAP/Cbl complex recruits the guanine nucleotide exchange factor (GEF) C3G along with Crk in the caveolin-enriched lipid rafts. The activated GEF assists

in the exchange of GDP for GTP in the small effector G protein TC10. The activated TC10 binds to Cdc42-interacting protein 4 (CIP4) aiding GLUT4 translocation independently of the PI3-kinase pathway (Liu et al., 2002, 2003). Many studies investigate insulin signalling and GLUT4 translocation in adipocytes but currently less is known about cardiac and skeletal muscle tissues.

1.5.4 Insulin signalling in muscle tissues

As previously discussed insulin signalling can be transduced along different metabolic pathways containing several points of regulation and signal divergence. Further complexity is added by the expression of multiple tissue-specific isoforms of insulin signalling substrates and protein kinases (Taniguchi et al., 2006). The insulin signalling cascade resulting in GLUT4 translocation in muscle tissues is only fragmentarily understood. In skeletal muscle the small GTPases Rab8 and Rab14 have been identified to be activated instead of Rab10 downstream of AS160 (Ishikura et al., 2007; Sun et al., 2010). Furthermore, the Rab GTPase activating protein TBC1D4 has been described as a key component of the insulin signalling axis whereas its TBC1D1 paralog has been identified to contribute to contraction-induced GLUT4 translocation in skeletal muscle (Taylor et al., 2008). SNARE proteins are responsible for docking with and fusion to the PM and in skeletal muscle the actin skeleton has been identified to significantly contribute to insulin-stimulated GLUT4 translocation (Chiu et al., 2011; JeBailey et al., 2004; Ueda et al., 2010). The Rho family GTPase Rac1 has been proposed to play a critical role in insulin-stimulated GLUT4 translocation in skeletal muscle (Ueda et al., 2010). Ectopic expression of activated Rac1 in combination with insulin stimulation caused GLUT4 translocation in mice whereas insulin-dependent GLUT4 translocation was significantly decreased in Rac1-knockout mice (Ueda et al., 2010). In general it is assumed that contractions stimulate GLUT4 translocation through molecular pathways distinct from insulin stimulation. Nevertheless, in their distal parts the insulin- and contraction-induced molecular pathways converge involving a number of similar signalling molecules.

As is the case in adipose and skeletal muscle tissue, the binding of insulin to its receptor induces autophosphorylation and increases tyrosine kinase activity for IRS proteins in cardiac muscle. In the heart IRS1 and IRS2 are the most abundant isoforms and required to activate PI3K to catalyse the generation of PIP3 (Riehle and Abel, 2016). In isolated cardiomyocytes it has been observed that Akt2 is required for insulin-stimulated glucose uptake independent of Akt1 (DeBosch et al., 2006a). Therefore in the heart Akt2 mediates the metabolic effects of insulin whereas Akt1 governs somatic growth of cardiomyocytes (Bae et al., 2003; DeBosch et al., 2006b). Akt phosphorylates TBC1D4

and inactivates its GTPase-activating function and thereby enables the activation of Rab proteins. In skeletal muscle a protein from the same family, TBC1D1, plays a similar role but does not seem to be expressed in cardiomyocytes (Montessuit and Lerch, 2013). The specific Rab proteins involved in cardiac insulin signalling need to be investigated further. Only Rab11 has been consistently reported to contribute to insulin-stimulated GLUT4 translocation in the myocardium (Kessler et al., 2000; Uhlig et al., 2005). Rab4a may also participate in GLUT4 vesicle trafficking (Dransfeld et al., 2000).

1.5.5 Insulin signalling defects in T2DM

A major hallmark of T2DM is significantly reduced insulin-mediated glucose transport into fat and muscle tissues (Dutka et al., 2006; Hu et al., 2018b; Szablewski, 2017). This impairment is associated with a range of molecular defects at one or several levels of the insulin signalling cascade. The first step of the insulin signalling cascade is IR autophosphorylation leading to activation of its intrinsic tyrosine kinase activity. In insulin-resistant rodent models it was observed that insulin-induced phosphorylation of the IR beta subunit was significantly decreased compared to controls (Kadowaki et al., 1984; Le Marchand-Brustel et al., 1985). However in skeletal muscle samples of diabetic human subjects only modest impairments of IR autophosphorylation were reported (Maegawa et al., 1991; Nolan et al., 1994). In adipocytes from human diabetic subjects decreased numbers of IR and IR binding were reported (Kolterman et al., 1981; Sinha et al., 1987) alongside a significant decrease in insulin-induced tyrosine kinase activity (Freidenberg et al., 1987; Sinha et al., 1987). Taken together these studies show that alterations of insulin receptor functionality contribute to the development of T2DM but significant differences exist between tissues. Phosphorylation of IRS proteins provides docking sites for SH2 domain containing molecules and activates PI3K which mediates the further transmission of the insulin signal. Numerous independent studies have reported that IRS1 tyrosine phosphorylation is diminished on several sites in skeletal muscle and adipocytes from T2DM patients (Björnholm et al., 1997; Bouzakri et al., 2003; Danielsson et al., 2005; Goodyear et al., 1995; Krook et al., 2000). The role of insulin-induced PI3K activation resulting in formation of PIP3 at the PM has been extensively investigated *in vitro* and alterations of PI3K in the context of T2DM are only fragmentarily understood *in vivo* (Fröjdö et al., 2009). Some groups reported impaired activation of PI3K in human diabetic subjects but paradoxically unaltered Akt activation downstream (Beeson et al., 2003; Kim et al., 1999, 2003). Furthermore, the impairment of insulin-induced activation of Akt in the development of T2DM in skeletal muscle is currently debated. Some studies reported reduced Akt phosphorylation in T2DM patients (Cozzone et al., 2008; Meyer et al., 2002) whereas other studies observed no differences between T2DM and control subjects (Cusi et al., 2000; Kim et al., 1999).

The reports regarding impaired activation of Akt in adipocytes from T2DM patients are more consistent (Carvalho et al., 2000; Rondinone et al., 1999). Reduced insulin-stimulated phosphorylation of Akt was reported in these cells in combination with reduced glucose uptake (Carvalho et al., 2000; Rondinone et al., 1999). However, it is important to note that how modest changes in signalling translate to impaired insulin action has been questioned (Tan et al., 2015). In addition to impaired insulin signalling, defects in GLUT4 trafficking have been suggested to contribute to the progression of T2DM and are described in section 6.1.2. There is emerging evidence that insulin action influences GLUT4 dynamics in the PM and dysregulation of this newly described process might be another impairment contributing to the development of insulin resistance.

1.6 GLUT4 in the plasma membrane

Since the discovery of the GLUT4 protein in 1988 GLUT4 signalling pathways have been extensively studied (Klip et al., 2019). Biochemical approaches have revealed that insulin stimulates a complex signalling cascade culminating in GLUT4 translocation from intracellular storage vesicles to the PM where the channel becomes available for glucose uptake (Birnbaum, 1989; James et al., 1988). Relatively little is known about GLUT4 dynamics within the PM itself. The discovery of green fluorescent protein (GFP) and the ability to use it as a marker for protein localization fundamentally altered the scope of which questions could be addressed by cell biologists (Tsien, 1998). In 1994 GFP was successfully expressed in *E. coli* and only two years later GFP-tagged GLUT4 was used to visualise the dynamics of insulin-stimulated GLUT4 translocation in living CHO cells (Dobson et al., 1996). Shortly after the same group managed to express GLUT4-GFP in 3T3-L1 adipocytes and observed GLUT4 translocation in response to insulin for the first time (Powell et al., 1999). Two years later another group inserted an additional hemagglutinin (HA) tag into the first exofacial loop of the GLUT4-GFP fusion protein and expressed it in rat adipocytes (Dawson et al., 2001). This was the first time that intracellular GLUT4 could be distinguished from GLUT4 that fused with the PM using confocal microscopy (Dawson et al., 2001). These studies laid the foundation for all future studies using microscopy to investigate GLUT4 dynamics and HA-GLUT4-GFP has become the most prevalent genetically modified variant of GLUT4 used to study all aspects of GLUT4 dynamics over time. The development of light microscopy and recent emergence of novel high-resolution live cell microscopy techniques facilitated the study of GLUT4 regulation and behaviour in close proximity to the PM. The key studies in this relatively novel field will be described in the following.

1.6.1 Total internal fluorescence microscopy reveals plasma membrane GLUT4 dynamics

Total internal reflection fluorescence (TIRF) microscopy has been a valuable tool in the study of PM GLUT4 dynamics (Jiang et al., 2008; Li et al., 2004; Lizunov et al., 2005, 2013a; Stenkula et al., 2010). TIRF microscopy is an elegant method that allows the selective visualisation of fluorescent proteins within a thin optical section of the biological sample (Ambrose, 1956). In general, refraction of light when it encounters the interface between two media with different refractive indexes (RI) leads to the confinement of a proportion of the light to the higher RI medium. A laser beam that passes through a medium and hits this interface is either refracted upon entering the second medium or reflected at this interface (Figure 1.5). This physical phenomenon is dependent on the incident angle of the laser beam and the specific RI of the two media.

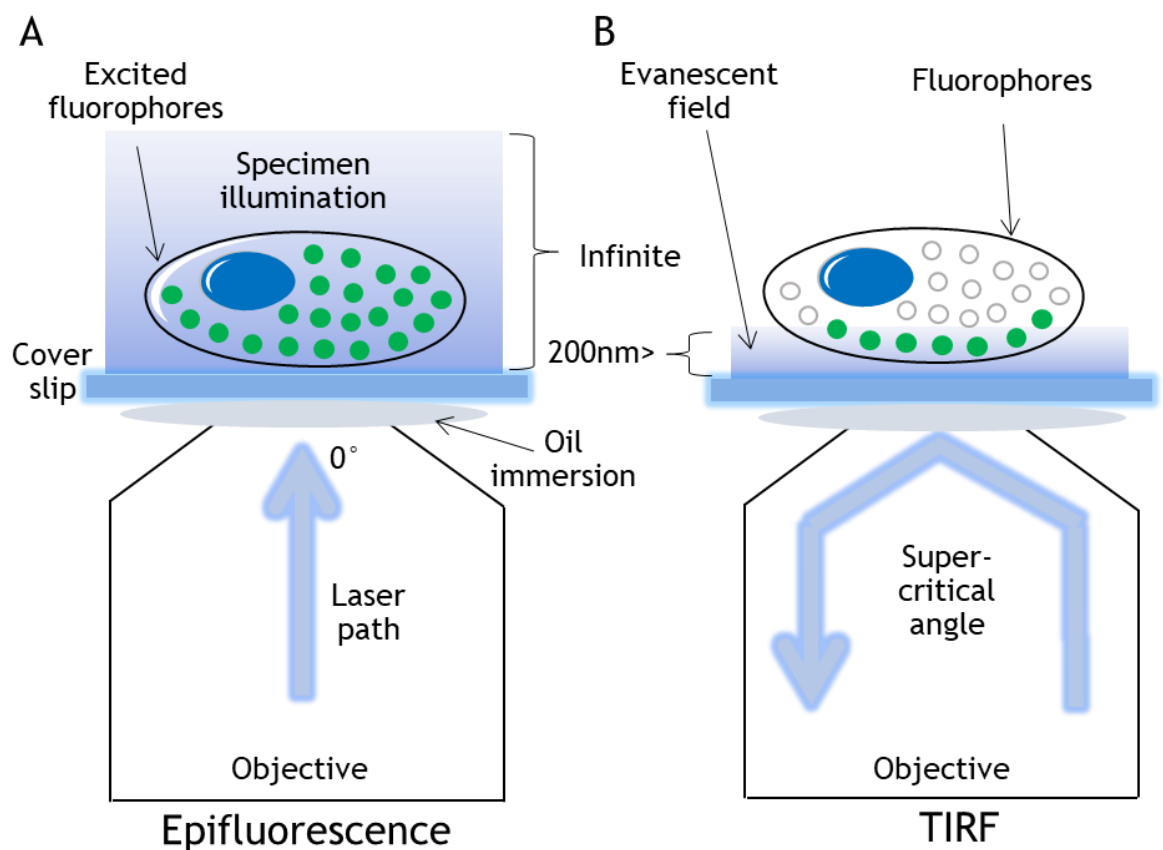


Figure 1.5 The physical basis of epifluorescence and TIRF microscopy.

Schematic showing the cover-slip-sample interface (Mattheyses et al., 2010). (A) During epifluorescence illumination the laser beam travels directly through the cover-slip-sample interface and as a consequence excites all fluorophores indicated by the green colour. (B) During TIRF illumination the laser beam enters the sample from the right at an incidence angle that is larger than the critical angle and is reflected off the cover-slip-sample interface on the left side. An evanescent field is generated on the opposite side of the interface penetrating the sample $<200\text{nm}$. Only fluorophores within this evanescent field are excited.

At oblique angles greater than what is known as the 'critical angle' the light beam is totally reflected in a transparent solid substance with high RI for instance a cover slip (Axelrod, 1981). This generates a highly restricted electromagnetic field called the 'evanescent wave' that propagates in parallel to the liquid-solid interface. The intensity of the evanescent wave decays exponentially with perpendicular distance and thus extends only 200-300 nanometres into the sample to excite fluorophores in close proximity (Axelrod, 1981).

The first study taking advantage of TIRF microscopy allowed investigation of the three-dimensional mobility of single GLUT4 containing vesicles labelled with EGFP-fused GLUT4 in live 3T3-L1 adipocytes (Li et al., 2004). The exponential decay of the evanescent wave in the TIRF microscope was used to study GLUT4 containing vesicles that approach the PM as these presented with increased fluorescence intensity the closer they moved towards the interface. This property was used to track the vertical movement of GLUT4 containing vesicles specifically (Li et al., 2004). Most GCV moved repeatedly up and down in the TIRF-zone indicating that these GLUT4 containing vesicles were not docked to the PM. Moreover, it was observed that GLUT4 containing vesicles moved as if restricted within a cage within a 160 nm radius laterally suggesting the presence of an intracellular tethering matrix (Li et al., 2004). How these GLUT4 containing vesicles relate to IRVs or the GSC is not certain, reflecting the difficulty in resolving the GSC into distinct vesicle types.

Without insulin similar behaviour of GLUT4 containing vesicles rapidly moving along the PM has been observed by applying time-lapse TIRFM to primary rat adipocytes (Lizunov et al., 2005). Under basal conditions GLUT4 containing vesicles were described to move along predefined trajectories along the entire PM periodically stopping and loosely tethering to the PM indicating presence of a microtubule network. Insulin stimulation resulted in a drastic reduction of GLUT4 containing vesicles movement indicating immobilization of these vesicles at the PM (Lizunov et al., 2005). TIRFM has enhanced our understanding of how GLUT4 containing vesicles interact with the PM and enabled detection of single GLUT4 containing vesicles and quantification of tethering and fusion in 3T3-L1 (Jiang et al., 2008; Li et al., 2004) and primary adipocytes (Lizunov et al., 2005, 2009).

1.6.2 The effect of insulin action on plasma membrane GLUT4 dynamics

As previously described insulin stimulation resulted in tethering of mobile GLUT4 containing vesicles to the PM (Lizunov et al., 2005). In the basal state the spatial distribution of GLUT4 containing vesicles near the plasma membrane was reported to be uniform whereas insulin stimulation resulted in targeting of GLUT4 containing vesicles to specific regions of the PM in rat adipocytes. This result could indicate either tethering of GLUT4 containing vesicles in these areas prior to fusion as hypothesised in the study (Lizunov et al., 2005) or the movement of GLUT4 containing vesicles into relatively static PM regions. In the PM of primary mouse adipocytes clathrin which is fundamental for exocytosis has been found to be localised in large immobile patches (Bellve et al., 2006). In adipocytes dual-colour TIRFM revealed that insulin stimulation resulted in colocalization of GLUT4 and clathrin (Huang et al., 2007). In the basal state colocalization was observed to a smaller extent indicating that insulin promotes accumulation of GLUT4 in clathrin-coated regions of the PM (Huang et al., 2007). In contrast to this finding, a more recent study distinguishing between intracellular and PM GLUT4 reported that surface-exposed HA-GLUT4 only colocalised with ~10% in basal and insulin-stimulated adipocytes (Stenkula et al., 2010). The majority of GLUT4 colocalized with clathrin was found in intracellular compartments and clathrin was hypothesised to be important for GLUT4 endocytosis from existing clusters (Stenkula et al., 2010).

Reversible GLUT4 containing vesicles docking, priming and fusion are the key steps occurring at the PM but it remains unclear which steps are directly regulated by insulin action (Bai et al., 2007). Time-lapse images of 3T3-L1 adipocytes expressing EGFP-GLUT4 were acquired in TIRF mode and thousands of fusion events were analysed with a novel computational method to address how insulin signalling affects what presumably reflect IRV trafficking pathways (Bai et al., 2007). EGFP-GLUT4 approaching the PM were characterised by an increase in fluorescence intensity and appearance of a fluorescent spot. Docking events were characterised by the mentioned fluorescent spot remaining static in the field of view for a defined time period and fusion of IRV was characterised by dispersion of the fluorescence signal post docking. A decrease of fluorescence after docking indicated vesicle undocking without fusion (Bai et al., 2007). Detailed quantitative kinetic analysis revealed that insulin stimulation resulted in an 8-fold increase in fusion rate and a 2-fold increase in docking rate. The mean dwell time defined as the period of time the IRV remained in the docked state decreased by 30%. The PI3K inhibitor wortmannin was reported to decrease the docking rate significantly indicating that this step relies on PI3K action (Bai et al., 2007). This study showed for

the first time that insulin regulates IRV fusion whereas docking is regulated by PI3K and its downstream effector AS160 (Bai et al., 2007).

pH-dependent GFP variants known as pHluorins have become valuable tools for the non-invasive tracking of cell surface proteins during exocytosis and endocytosis (Ashby et al., 2004). IRAP co-localises with GLUT4 and can be labelled with pHluorin on its luminal c-terminus. Prior to fusion pHluorin is located in the acidic lumen of the IRV where it is non-fluorescent at a pH < 6.0. Once the IRV fuse with the plasma membrane pHluorin will be exposed to the extracellular medium where it is fluorescent at a pH of 7.4 and provides a high contrast signal for identification of fusion events (Chen and Lippincott-Schwartz, 2015). Tagging GLUT4 containing vesicles with pHluorin is an elegant way to visualise fusion events without ambiguity. The development of a novel dual-coloured probe to monitor GLUT4 translocation as well as prefusion behaviour of GLUT4 containing vesicles advanced the elucidation of the underlying molecular processes even further (Jiang et al., 2008). In this study IRAP was not only tagged with pHluorin on its luminal end but also with the red fluorescence protein Tdimer2 on its cytosolic end (Jiang et al., 2008). The pH-insensitive Tdimer2 is visible at all times in the red channel and used to monitor pre-fusion behaviour. The combination of both dyes allowed reliable quantification of docking, priming and fusion events in living 3T3-L1 cells based simply on an abrupt fluorescence increase. For the first time the fusion rate constant of single adipocytes was estimated and a 40-fold insulin-stimulated increase in GLUT4 fusion events was reported. A dysfunctional mutant of the RabGAP AS160, known as AS160-4P, inhibited IRV docking but not fusion suggesting that AS160 is essential for IRV docking and probably not involved in processes downstream of IRV docking. Furthermore, a mode of fusion similar to the 'kiss-and-run' mode of fusion observed in synaptic vesicles has been observed for IRV that preserved the integrity of vesicles and permitted fast local vesicle internalisation (Jiang et al., 2008). These studies confirmed that GLUT4 molecules are distributed non-homogeneously within the PM but it remains unclear how insulin regulates spatial dynamics of GLUT4 organization in the PM.

By labelling GLUT4 containing vesicles of 3T3-L1 adipocytes with VAMP2-pHluorin another study also reported 'kiss-and-run' events and GLUT4 containing vesicles fusing with the PM briefly before being endocytosed again (Xu et al., 2011). The first study reported that in the basal state 15% of fusion events were 'kiss-and-run' (Jiang et al., 2008) whereas the second study observed almost 40% (Xu et al., 2011). Insulin stimulation resulted in a significant decrease in observed 'kiss-and-run' fusion events to 5% total (Xu et al., 2011). Insulin stimulation resulted in fusion pore expansion but shortening of fusion pore duration (Xu et al., 2011). This study highlights that insulin has

a direct impact on IRV fusion pores. To summarise, in adipocytes GLUT4 containing vesicles/IRVs approach the PM where they dock and a fusion pore opens up (Figure 1.6). The fusion pore can either close and the vesicle undock in the 'kiss and run' mode or the vesicle can fuse entirely with the PM. The first event is more common during the basal state whereas in the insulin-stimulated state the latter event is more common resulting in GLUT4 dispersal in the PM (Figure 1.6).

Impaired tethering and fusion of GLUT4 containing vesicles has been associated with T2DM (Lizunov et al., 2013b). Adipocytes isolated from human subjects with varying BMI and peripheral insulin sensitivity were transfected with fluorescently labelled GLUT4 and imaged using TIRFM (Lizunov et al., 2013b). Under basal conditions there was no observed difference in GLUT4 containing vesicles trafficking to and fusion with the PM and total PM GLUT4 levels of cells derived from different donors. This finding indicates that basal GLUT4 trafficking mechanisms were not affected by obesity or insulin resistance. However, insulin-stimulated GLUT4 trafficking was significantly impaired in states of insulin resistance. Insulin stimulation in cells derived from healthy subjects increased GLUT4 containing vesicles tethering and fusion 3-fold and this resulted in an increase in total cell-surface GLUT4. With decreasing levels of donor insulin sensitivity GLUT4 containing vesicles tethering and fusion decreased accompanied by a decrease in total PM GLUT4 (Lizunov et al., 2013b).

Recently, a new line of investigation has emerged that suggests that insulin does not only affect intracellular GLUT4 trafficking but the distribution of the transporter in the PM itself after the fusion event (Stenkula et al., 2010). A study combining multi-colour TIRF and wide field microscopy investigated GLUT4 organization and its relationship with insulin-regulated GSC recycling in rat adipocytes transfected with HA-GLUT4-GFP (Stenkula et al., 2010). It was observed that two distinctive populations of GLUT4 molecules exist in the PM: relatively stationary clusters and freely diffusible monomers. In the basal state most GLUT4 molecules within the TIRF zone appeared as stationary clusters with the amounts of GLUT4 molecules localized in clusters and being dispersed being roughly equal. Insulin stimulation resulted in a 4-fold increase in the amount of dispersed monomers and a 2.5-fold increase in the number of clusters (Stenkula et al., 2010). The total amount of GLUT4 translocated to the PM upon insulin-stimulation corresponded to the increase in insulin-stimulated glucose uptake and therefore indicates that both GLUT4 populations were functional glucose transporters. Moreover, two distinct types of GLUT4-vesicle exocytosis were identified: fusion-with-release events dispersed GLUT4 within the PM whereas fusion-with-retention events (previously described as 'kiss-and-run') retained GLUT4 molecules at the fusion site (Figure 1.6). In

the basal state 95% of events observed were fusion-with-retention and insulin led to a 60-fold increase in fusion-with-release events within 2-3 min (Stenkula et al., 2010). This study identifies GLUT4 dispersal in the PM as a potential key aspect of insulin action. However, this aspect of insulin action lacks mechanistic detail. Currently it is unknown what mediates formation of GLUT4 clusters or GLUT4 dispersal in response to insulin stimulation.

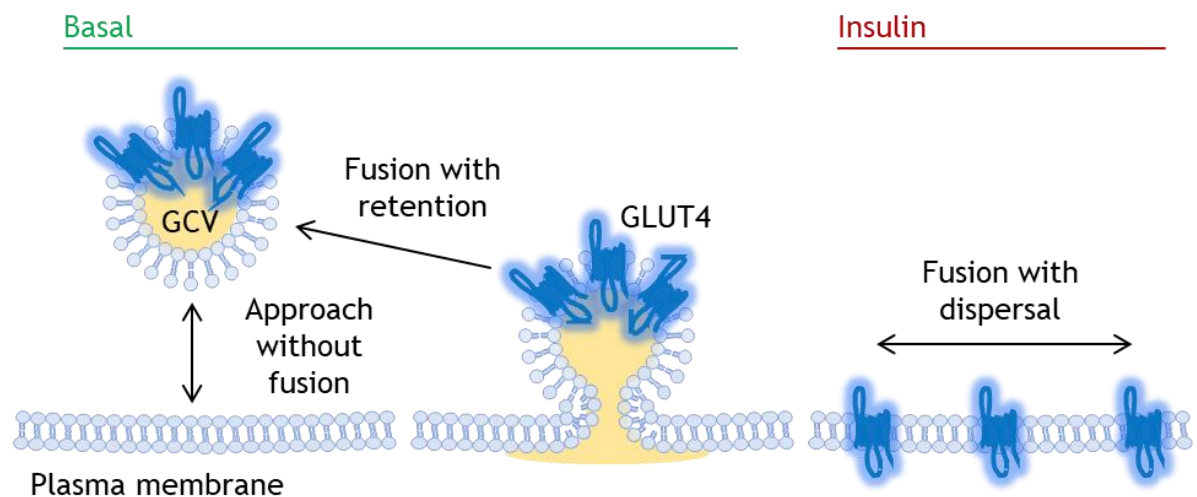


Figure 1.6 Schematic summary of the key events of GCV docking, priming and fusion occurring at the plasma membrane identified by imaging experiments.

In the basal state GCV either approach the plasma membrane and dock without fusion or dock with opening of a fusion pore before retreating in a kiss-and-run like fashion. This process was recently described as fusion with retention and ensures that the majority of GLUT4 remains sequestered intracellularly in the absence of insulin. Insulin stimulation triggers an increase of GCV delivery to the PM. GCV fully fuse and disperse GLUT4 across the entirety of the PM. Insulin stimulation results in a shift from fusion with retention to fusion with dispersal (Stenkula et al., 2010).

1.7 Aims and hypothesis

Since the discovery of the insulin-responsive GLUT4 in 1988 numerous mechanistic studies have laid the foundations for our understanding of how insulin regulates glucose uptake in muscle and fat (Klip et al., 2019). Various effects of insulin action on GLUT4 trafficking have been identified over the years and dysfunction has been associated strongly with the development of T2DM. Currently there is no cure for T2DM and prevalence is globally on the rise. In recent years it has been reported that insulin does not only regulate GLUT4 translocation from intracellular stores but also affects the distribution of GLUT4 in the PM (Stenkula et al., 2010). In the basal state GLUT4 appears in clusters whereas insulin was reported to disperse GLUT4 in adipocytes (Figure 1.7). In the basal state fusion with retention was found to result in the creation of *de novo* GLUT4 clusters at the PM. Internalisation of GLUT4 is hypothesised to be restricted to these clusters. Insulin stimulation resulted in an increase of overall fusion

events and dispersal of GLUT4 monomers (Stenkula et al., 2010). This observation resulted in the development of a novel kinetic model of GLUT4 trafficking in which clustered and monomeric GLUT4 co-exist and insulin regulates the amount of GLUT4 in each of these distinct pools (Figure 1.7). The underlying mechanisms of GLUT4 dispersal remain unresolved but are of great therapeutic interest.

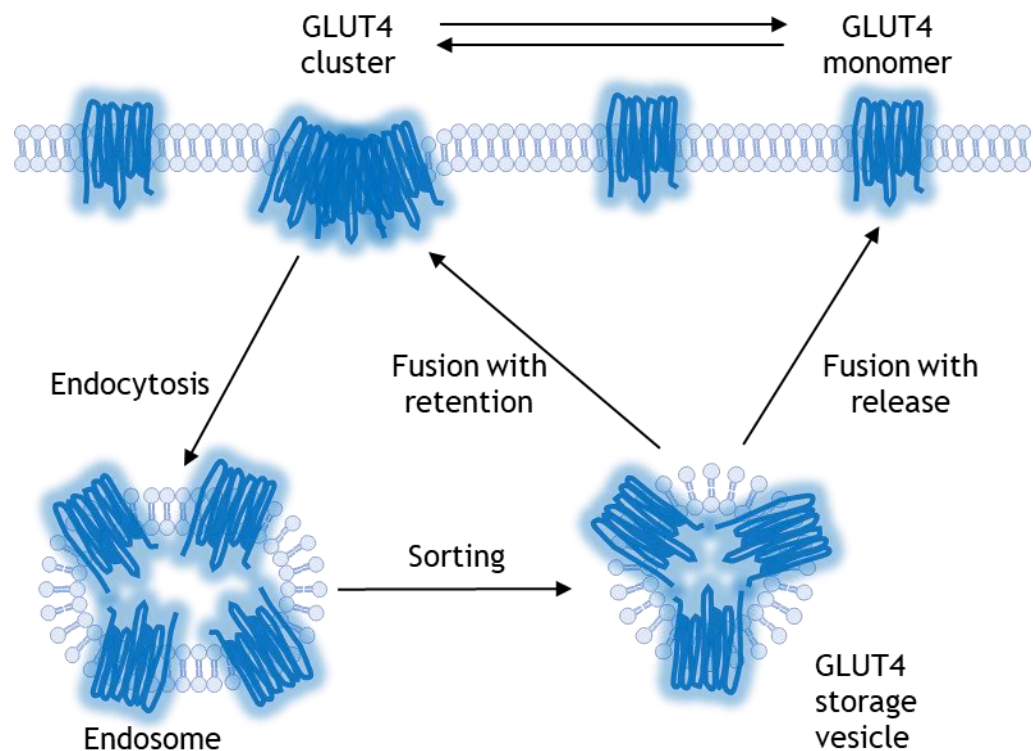


Figure 1.7 Kinetic model of insulin-regulated recycling and spatial distribution of GLUT4 in the plasma membrane of adipocytes.

Schematic model of insulin-regulated GLUT4 recycling among GLUT4 storage vesicles, endosomes, and GLUT4 monomers and clusters found in the plasma membrane of 3T3-L1 adipocytes. GLUT4 molecules are assumed to be cycling among four quasi-compartments. In the basal state clusters play a key role in regulation of the recycling of GLUT4 between the PM and intracellular pools as endocytosis is restricted to clusters. Insulin stimulation releases GLUT4 monomers diffusely into the PM (adapted from (Stenkula et al., 2010)).

The key aim of this project was to develop a microscopy-based assay to study and quantify insulin-stimulated GLUT4 dispersal dynamics in the PM. Super resolution microscopy is a relatively young field that provides the opportunity to visualise individual GLUT4 molecules and quantify their spatial relationships. Insulin-stimulated GLUT4 dispersal has only been observed in adipocytes and therefore we have chosen this model as a starting point for our investigation. Firstly, we aimed to optimise super resolution imaging in our lab and hypothesised that insulin stimulation would shift GLUT4 distribution in the PM from a clustered to a more dispersed state in line with the current literature (Gao et al., 2017; Lizunov et al., 2013a; Stenkula et al., 2010). Super

resolution imaging is rapidly evolving and persistently engages cell biologists with new challenges. One of these challenges is the generation of big data sets and interpretation of results. Here, we also aimed to explore a range of cluster analysis methods to find the most suitable way to quantify GLUT4 clustering and dispersal dynamics in response to various stimuli (Chapter 1). Moreover, we investigated the underlying molecular mechanisms of this dispersal in adipocytes, in particular the role of AMPK, cholesterol and EFR3 (Chapter 2).

Patients suffering from T2DM commonly develop DCM that culminates in heart failure. The link between T2DM and CVD has long been established but relatively little is known about the underlying molecular mechanisms of DCM and treatment options are limited. One of the biggest challenges of cardiovascular science is the identification of appropriate *in vitro* models. Thus, we aimed to optimise super resolution imaging in a variety of cardiac cell culture models to research whether insulin-stimulated GLUT4 dispersal exists in the myocardium. This is the first investigation of GLUT4 spatial patterning at the single molecule level in cardiac tissues and will provide new insights into the spatial organisation of GLUT4 in the PM of cardiac muscle (Chapter 3).

Next we aimed to investigate different aspects of GLUT4 trafficking and dispersal in health and disease (an introduction to GLUT4 trafficking in diabetes will be provided in Chapter 4). We aimed to characterise how insulin resistance affects GLUT4 dispersal in adipocytes. We hypothesised that chronic insulin treatment would result in a state of cellular insulin resistance and attenuation of insulin-stimulated GLUT4 dispersal could be the underlying cause (Chapter 4). Furthermore, we aimed to investigate whether the observed mechanism of PM dispersal is specific to GLUT4. Therefore, we performed experiments to investigate the spatial patterning of TfR on the cell surface (Chapter 4).

Finally, we aimed to characterise GLUT4 dispersal in a cell culture model of human skeletal muscle for the first time (Chapter 4). We also aimed to investigate the expression of several proteins involved in the GLUT4 trafficking cascade to gain insights into underlying molecular processes.

2. Materials and Methods

2.1 Materials

2.1.1 Commercially derived cells

Identity	Origin
3T3-L1 fibroblasts P/N: CL-173	American Tissue Culture Collection, Manassas, Virginia, USA
HeLa P/N: CCL-2	American Tissue Culture Collection, Manassas, Virginia, USA
HEK 293FT P/N: CRL-1573	American Tissue Culture Collection, Manassas, Virginia, USA
HSMM P/N: CC-2580	Lonza Bioscience, Basel, Switzerland
D-HSMM P/N: CC-2901	Lonza Bioscience, Basel, Switzerland
iPSC-CM (Cor.4U) P/N: Ax-B-HC02-1M	NCardia (Axiogenesis), Cologne, Germany
iPSC-CM (iCell Cardiomyocytes ²) P/N: CMC-100-012-000.5	FujiFilm Cellular Dynamics International (CDI), Wisconsin, USA
5-alpha Competent <i>E. coli</i> P/N: C2987I	Thermo Fisher Scientific, UK
Stbl3 competent <i>E. coli</i> P/N: C737303	Thermo Fisher Scientific, UK

Table 2.1 List of commercially obtained cells

2.1.2 Primary cells

Identity	Origin
New Zealand White Rabbits	Male, 2.5-3.2 kg, approximately 20 weeks old, in collaboration with the Godfrey Smith Laboratory, University of Glasgow
Wistar rat neonates	Male, 1-2 days old, gifted by George Baillie Laboratory, University of Glasgow
C57BL/6 mice	Male, 12 weeks old, Biological Procedures Unit, University of Strathclyde

Table 2.2 List of primary cells used

2.1.3 Plasmids

Identity	Origin
pCDH-CMV-MCS-EF1-HA-GLUT4-GFP	Lentiviral plasmid containing the gene sequence for GLUT4 tagged with green fluorescent protein and hemagglutinin; generated by Silke Morris in house (Morris et al., 2020)
pEGFP-N1-Flag-TfR-GFP	Plasmid for cloning and expression of FLAG-GFP tagged transferrin receptor, generated and gifted by Jennifer Lippincott-Schwartz Laboratory, USA (Patterson and Lippincott-Schwartz, 2002)
pCDH-CMV-MCS-EF1-TfR-GFP	Generated in this project, described in section 6.2.2

Table 2.3 List and description of plasmids

2.1.4 General materials and reagents

This list summarises key materials used in this project with corresponding suppliers and product numbers (P/N) in all cases possible.

Axiogenesis, NCardia, Leiden, The Netherlands

Cor.4U® Culture medium for maintenance containing FBS (P/N: Ax-MHC250)

Cor.4U® BMCC serum free medium (P/N: Ax-M-BMCC250)

BioRad Laboratories Ltd, Hemel Hemstead, Hampshire, UK

Precision Plus Protein™ All Blue Standards (P/N: 1610373)

Cellular Dynamics International, Wisconsin, USA

iCell Cardiomyocytes2 Maintenance Medium (P/N: CMM-100-120-001)

iCell Cardiomyocytes2 Plating Medium (P/N: CMM-100-110-001)

Corning Incorporated, Maine, USA

6 well polystyrene TC-treated cell culture plate (P/N: 3516)

12 well polystyrene TC-treated cell culture plate (P/N: 3513)

24 well TC-treated cell culture plate (P/N: 3524)

75cm² Polystyrene Cell Culture Flask (P/N: 430641U)

96 well clear flat bottom polystyrene TC-treated microplates (P/N: 3596)

Electron Microscopy Sciences, Hatfield, PA, USA

CoverWell™ Modular Hybridization System (P/N: 70327-05)

Fisher Scientific UK Ltd., Loughborough, Leicestershire, UK

2-[4-(2-hydroxyethyl)-1-piperazine] ethanesuphonic acid (HEPES)

Bovine Serum Albumin (P/N: BP9702-100)

D-Glucose anhydrous (P/N: G/0500/53)

Ethanol (P/N: 10680993)

Glycerol (P/N: G/0650/17)

Glycine (P/N: 10061073)

Immu-Mount (P/N: 10662815)

Pierce™ Micro BCA™ Protein Assay Kit (P/N: 23225)

RPMI Media 1640 (P/N: 21875091)

Tris(hydroxymethyl)aminoethane Base (Tris Base)

Formedium, Norfolk, UK

Agar (P/N: AGA02)

Tryptone (P/N: TRP02)

Yeast Extract Powder (P/N: YEA02)

Gibco by Life Technologies, ThermoFisher Scientific, Paisley, UK

Dulbecco's Modified Eagle Medium (1x) 0 g/L D-Glucose (P/N: 11966025)

Dulbecco's Modified Eagle Medium (1x) 1 g/L D-Glucose (P/N: 11885084)

Dulbecco's Modified Eagle Medium (1x) 4.5 g/L D-Glucose (P/N: 41965039)

Dulbecco's Phosphate Buffered Saline (1x) (P/N: 14190094)

Dulbecco's Phosphate Buffered Saline, calcium, magnesium (P/N: 14040141)

Fetal Bovine Serum (FBS) (P/N: 10500064)

Horse Serum, heat inactivated, New Zealand origin (P/N: 16050130)

L-Glutamine 200mM (100x) (P/N: 25030024)

Lipofectamine® 2000 transfection reagent (P/N: 11668019)

Medium 199, Earle's Salts (P/N: 11150059)

MEM Non-Essential Amino Acids Solution (100X) (P/N: 11140-050)

Newborn Calf Serum (P/N: 16010159)

OPTI-MEM (1X) Reduced Serum Medium (P/N: 31985062)

Penicillin-Streptomycin (Pen-Strep) (10,000U/mL) (P/N: 15140122)

0.05% Trypsin-EDTA (P/N: 25300054)

Lonza Bioscience, Basel, Switzerland

SkGM™-2 Skeletal Muscle Cell Growth Medium-2 BulletKit™ (P/N: CC-3245)

ReagentPack™ Subculture Reagents: Trypsin/EDTA, trypsin neutralizing solution, and HEPES buffered saline solution (P/N: CC-5034)

Marienfeld Laboratory Glassware, Lauda-Koenigshoefen, Germany

Coverglass, high precision (1.5H), diameter - 24mm (P/N: 0117640)

Melford Laboratories Ltd., Chelsworth, Ipswich, UK

Dithiothreitol (DTT) (P/N: MB1015)

Merck, Darmstadt, Germany

Sodium dihydrogen phosphate (NaH₂PO₄) (P/N: 106342)

New England Biolabs, Massachusetts, USA

CutSmart Buffer 10x (P/N: B7204S)

KasI restriction enzyme (P/N: R0544S)

NheI restriction enzyme (P/N: R0131S)

NotI restriction enzyme (P/N: R0189S)

SOC Outgrowth Medium (P/N: B9020S)

T4 DNA Ligase (P/N: M0202S)

10X T4 DNA Ligase Reaction Buffer (P/N: B0202S)

Pall Life Sciences, Portsmouth, UK

BioTrace NT Nitrocellulose Transfer Membrane 0.2µm pore thickness (P/N: 66485)

Perkin Elmer, Massachusetts, USA

Deoxy-D-glucose, 2-[1,2-3H (N)] (P/N: NET328A001MC)

Ultima Gold Liquid Scintillation Counting Cocktail (P/N: 6013326)

Promega, Wisconsin, USA

Blue/Orange DNA Loading Dye, 6X (P/N: G1881)

FuGENE HD Transfection Reagent (P/N: E2311)

1kb DNA ladder (P/N: G5711)

Wizard Plus SV Minipreps DNA Purification Systems (P/N: A1330)

Qiagen, Hilden, Germany

Nuclease-Free water (P/N: 129115)

QIAfilter Plasmid Midi and Maxi Kits

Roche Diagnostic Ltd., Burgess Hill, UK

Complete™ Protease Inhibitor Cocktail Tablets (P/N: 11697498001)

Sartorius, Gottingen, Germany

Minisart 0.2 µm pore size syringe filter (P/N: 16534K)

Severn Biotech Ltd., Worcestershire, UK

Acrylamide Bis-Acrylamide Stock Solution, 30% Acrylamide (w/v) Ratio 37.5:1

(P/N: 20-2100-10)

Sigma-Aldrich Ltd., Gillingham, Dorset, UK

Ampicillin Sodium Salt (P/N: A0166)
Bromophenol Blue (P/N: B0126)
(±)-Carnitine hydrochloride (P/N: C9500)
Creatine (P/N: C0780)
Cysteamine (MEA) (P/N: M9768)
Cytochalasin B from *Drechslera dematioidea* (P/N: C6762)
2-Deoxy-D-glucose (P/N: D8375)
Dexamethasone (P/N: D4902)
Dimethyl sulphoxide (DMSO) (P/N: D2650)
Dulbecco's Phosphate Buffered Saline (DPBS) with MgCl₂ and CaCl₂ (P/N: D8662)
Dulbecco's Modified Eagle's Medium/Ham's Nutrient Mixture F12 (P/N: 51445C)
Ethylenediaminetetracetic acid (EDTA) (P/N: E6758)
Ethidium Bromide Solution (P/N: E1510)
Fibronectin from bovine plasma (P/N: F1141)
Gelatine from cold water fish skin (P/N: G7041)
Goat serum (P/N: G9023)
HEPES (P/N: H3375)
Insulin from porcine pancreas (P/N: I5523)
3-isobutylmethylxanthine (IMBX)
Isopropanol (P/N: I9516)
Laminin from Engelbreth-Holm-Swarm murine sarcoma basement membrane (P/N: L2020)
Magnesium sulphate (MgSO₄) (P/N: M3409)
Methyl-β-cyclodextrin (P/N: C4555)
N,N,N',N'-Tetramethylethylenediamine (TEMED) (P/N: T9281)
Palmitic acid (P/N: P0500)
Paraformaldehyde powder (P/N: 158127)
Ponceau S (P/N: P3504)
Protease from *Streptomyces griseus*, Type XIV (P/N: P5147)
Taurine (P/N: 86329)
3,3',5-Triiodo-L-thyronine sodium salt (P/N: T6397)
Triton X-100 (P/N: T9284)
Troglitazone (P/N: T2573)
Trypan Blue Solution (0.4%) (P/N: T8154)
TWEEN 20 (P/N: P7949)
Wash-N-Dry™ coverslip rack (P/N: Z688568-1EA)

ViraQuest Inc. Iowa, USA

HA-GLUT4-GFP Adeno virus

HA-GLUT4-GFP Adeno associated virus

VWR International Ltd., Lutterworth, Leicestershire, UK

Glacial Acetic Acid (P/N: 36289.AE)

Calcium chloride (CaCl₂) (P/N: 190464K)di-Sodium hydrogen phosphate anhydrous (Na₂HPO₄) (P/N: 102494C)

Ethanol absolute (P/N: 20821.330)

Magnesium chloride hexahydrate (P/N: 25108.260)

Potassium chloride (KCl) (P/N: 26764.260)

Sodium chloride (NaCl) (P/N: 27810.295)

Sodium dodecyl sulphate (SDS) (P/N: 442444H)

Worthington Biochemical Corporation, Lakewood, NJ, USACollagenase from *Clostridium histolyticum*, Type 1 (P/N: CLS-1)**Toronto Research Chemicals, Ontario, Canada**

5-Aminoimidazole-4-carboxamide-1-β-D-ribofuranoside (AICAR)

2.1.5 Solutions

2x Laemmli Sample Buffer (LSB)	100mM Tris, HCl pH 6.8, 4% (w/v) SDS, 20% (v/v) glycerol, 0.2% (w/v) bromophenol blue, 100 mM DTT
2YT	1.5% (w/v) Tryptone, 1% (w/v) Yeast Extract 0.5% (w/v) NaCl, (Autoclaved prior to use)
ADS buffer	120 mM NaCl, 20 mM HEPES, 1 mM Na ₂ PO ₄ , 5 mM glucose, 5.4 mM KCl, 1.8 mM MgSO ₄ , pH 7.4
Basic Krebs Solution	130 mM NaCl, 5 mM HEPES, 4.5 mM KCl, 0.4 mM NaH ₂ PO ₄ , 3.5 mM MgCl ₂ , 10 mM glucose, 140 μM CaCl ₂ , pH 7.4
Calcium solutions	Basic Krebs solution supplemented with either 100 μM, 200 μM, 500 μM, 1 mM or 1.8 mM CaCl ₂
Immunofluorescence buffer	0.2 % (w/v) Fish skin gelatin 0.1 % (v/v) goat serum in PBS
Krebs-Ringer-Phosphate (KRP) Buffer	136 mM NaCl, 5 mM sodium phosphate buffer (NaH ₂ PO ₄ -Na ₂ HPO ₄ ·7H ₂ O, pH 7.4), 4.7 mM KCl, 1 mM MgSO ₄ , 1 mM CaCl ₂ , pH 7.4
LB Broth	1% (w/v) Tryptone, 0.5% (w/v) Yeast Extract 1% (w/v) NaCl (autoclaved prior to use)
PBS	140mM NaCl 3mM KCl, 1.5mM KH ₂ HPO ₄ , 8mM Na ₂ HPO ₄ , pH 7.4
PBS-T	140mM NaCl 3mM KCl, 1.5mM KH ₂ HPO ₄ , 8mM Na ₂ HPO ₄ , 0.1% (v/v) Tween-20
PFA solution	4% (w/v) paraformaldehyde in PBS; pH 7.5

Ponceau S	0.2% (w/v) Ponceau S, 1% (v/v) acetic acid
Quenching buffer	50 mM NH ₄ Cl in PBS
RIPA Buffer	50mM Tris, HCl pH8, 150mM NaCl, 2mM MgCl ₂ , 1% Triton X-100, 0.5% sodium deoxycholate (w/v), 0.1% (w/v) SDS, 1mM DTT, 1x Protease Inhibitor Cocktail Tablet
SDS-PAGE running buffer	25mM Tris, 190mM glycine, 0.1% (w/v) SDS
SDS-PAGE transfer buffer	25 mM Tris-HCl, 192 mM glycine, 20% (v/v) ethanol
STORM imaging buffer	PBS, 50mM MEA, pH 8
TAE buffer	40 mM Tris, 1 mM EDTA, pH 7.4
TBS	20 mM Tris-HCl, 137 mM NaCl, pH 7.5
TBS-T	20 mM Tris-HCl, 137 mM NaCl, pH 7.5, 0.1% (v/v) Tween-20

2.1.6 Primary Antibodies and Nanobodies

Antigen	Working dilution	Description	Source
Acetyl-CoA Carboxylase	1:2000 in 3% BSA in TBS-T	Rabbit, monoclonal	Cell Signalling (P/N: 3676)
CHC17	1:1000 in 3% BSA in TBS-T	Mouse, monoclonal	R&D systems (P/N: AF6784)
CLTCL1 / CHC22	1:1000 in 3% BSA in TBS-T	Rabbit, monoclonal	LifeSpan BioSciences (P/N: C803540)
Desmin	1:1000 in 5% BSA/2 % goat serum in PBS	Rabbit, polyclonal	AbCam (P/N: 15200)
GAPDH	1:80,000 in 1% milk in PBS-T	Mouse, monoclonal	Ambion (P/N: 4300)
GFP	1:10 in 5% BSA/2 % goat serum in PBS	Camelid nanobody conjugated with AF647	Nanotag Biotechnologies (N0301)
GFP	1:1000 in 3% BSA in TBS-T	Rabbit, polyclonal	Badrilla (P/N: A010-pGFP-50)
GLUT1	1:1000 in 1% milk in PBS-T	Rabbit, polyclonal	AbCam (P/N: 652)
GLUT4	1:2000 in 5% milk in PBS-T	Rabbit, polyclonal	AbCam (P/N: 654)
GLUT8	1:1000 in 1% milk in PBS-T	Rabbit, polyclonal	AbCam (P/N: 191269)
GLUT12	1:1000 in 1% milk in PBS-T	Rabbit, polyclonal	AbCam (P/N: 191298)
HA tag	1:125 in 5 % BSA/2 % goat serum in PBS	Mouse, monoclonal	Invitrogen (P/N: 26183-A647)
HA tag	1:200 in 5 % BSA in PBS	Mouse, monoclonal	BioLegend (P/N: 901503)
Pan Akt	1:2000 in 3% BSA in TBS-T	Mouse, monoclonal	Cell Signalling (P/N: 2920)
Phospho-Acetyl-CoA Carboxylase	1:2000 in 3% BSA in TBS-T	Rabbit, monoclonal	Cell Signalling (P/N: 11818)
Phospho-Akt	1:1000 in 3% BSA in TBS-T	Rabbit, monoclonal	Cell Signalling (P/N: 4058)
Rab10	1:1000 in 3% BSA in PBS-T	Rabbit, monoclonal	Cell Signalling (P/N: 4262)
Rab14	1:1000 in 3% BSA in PBS-T	Rabbit, monoclonal	AbCam (P/N: 40938)
Sortilin	1:1000 in 3% BSA in PBS-T	Rabbit, monoclonal	Cell Signalling (P/N: 20681)

Table 2.4 List and description of primary antibodies

2.1.7 Secondary Antibodies and Nanobodies

Antigen	Working dilution	Description	Source
Rabbit IgG (Western blotting)	1:5000-10,000, in 1% milk in PBS-T	IRDye 680LT Donkey anti Rabbit IgG	LI-COR Biosciences (P/N: 925 68023)
Mouse IgG (Western blotting)	1:5000-10,000, in 1% milk in PBS-T	IRDye 680LT Donkey anti Mouse IgG	LI-COR Biosciences (P/N: 925 68070)
Mouse IgG (Western blotting)	1:5000-10,000, in 1% milk in PBS-T	IRDye 800CW Donkey anti Mouse IgG	LI-COR Biosciences (P/N: 925 32210)
Mouse IgG (Flowcytometry and imaging)	1:300-1:1000 in 3% BSA/2 % goat serum in PBS	Goat anti-Mouse IgG, Secondary Antibody, Alexa Fluor Plus 647	Invitrogen (P/N: A32728)
Mouse nanobody (Imaging)	1:10 in 3% BSA/2 % goat serum in PBS	Camelid nanobody fused to one molecule of AlexaFluor 647	Nanotag Biotechnologies (P/N: 1202- At647N-S)

Table 2.5 List and description of secondary antibodies

2.2 Cell Culture Methods

2.2.1 3T3-L1 fibroblast growth and maintenance

Wild-type 3T3-L1 murine fibroblasts and cells expressing HA-GLUT4-GFP previously generated in the laboratory were cultured in Dulbecco's Modified Eagle Medium (DMEM) supplemented with 10% (v/v) Newborn Calf Serum (NCS) at 37°C under 10% CO₂. Cells were fed every second day. Cells were passaged and frozen down as described (Laidlaw, 2018).

2.2.2 3T3-L1 adipocyte differentiation

Differentiation into mature adipocytes was initiated 2 days post confluence and lasted for 8 days. Day 0 medium consisted of DMEM supplemented with 10% (v/v) Fetal Calf Serum (FCS), 0.5 mM 3-isobutyl-1-methylxanthine (IBMX), 1 µM insulin, 0.25 µM dexamethasone, and 1nM troglitazone. 3 days after differentiation media was changed to Day 3 medium containing DMEM supplemented with 10% (v/v) FCS, 1µM insulin and 1nM troglitazone. On day 6 media was replaced with Day 6 medium containing DMEM supplemented with 10% (v/v) FCS. Cells were fully differentiated after Day 8 and used from 9-12 days post differentiation. Media was changed every second day after day 6 with DMEM supplemented with 10% (v/v) FCS.

2.2.3 HEK 293 and HeLa cell growth and maintenance

Wild-type HEK 293 and HeLa cells and HeLa cells expressing HA-GLUT4-GFP that were previously generated in the laboratory were cultured in DMEM supplemented with 10% (v/v) FCS and 1% (v/v) glutamine at 37°C under 5% CO₂. Media was changed every other day until cells were ready for passage or use.

2.2.4 iPSC-CM growth and maintenance

2.2.4.1 Plating of Axiogenesis iPSC-CM

Cryopreserved induced pluripotent stem cell derived cardiomyocytes (iPSC-CM) were sourced commercially from Axiogenesis and transferred to liquid nitrogen for storage upon receipt. Approximately 3 h before plating 25mm diameter glass coverslips were placed into 6-well tissue culture plates and coated with 500 µL fibronectin diluted 1:100 in PBS supplemented with MgCl₂ and CaCl₂ that resulted in a final concentration of 2 µg/cm². Moreover, Cor.4U® Culture Media was transferred to a 50 mL tube and pre-warmed to 37°C. Cor.4U® iPSC-CM were removed from liquid nitrogen storage and transferred directly to a 37°C water bath for 1-2 min. The vial was transferred into the laminar flow cabinet once the frozen cell suspension detached from the bottom and only a small ice clump was visible. The cells were carefully transferred to the pre-warmed media in a drop-wise manner to avoid heat shock. To avoid cell clumping the

tube was constantly and gently agitated by hand. Subsequently, 10 μ l of the cell suspension was mixed with the same amount of 0.4 % trypan blue and applied to a Neubauer haematocytometer to count viable and dead cells. The percentage of total cell viability was determined; typically >80% of cells were viable. Plating density ranged from 100,000 - 200,000 living cells per well. 12 h post seeding a media change was conducted to remove dead cells and DMSO. The media was replaced every other day.

2.2.4.2 Plating of CDI iPSC-CM

iCell iPSC-CM were obtained from CDI and stored in liquid nitrogen upon receipt. Prior to plating dishes were coated with fibronectin as described above. For plating cells a vial was removed from liquid nitrogen storage and placed into a 37°C water bath for 3 min. The contents of the vial were transferred into an empty sterile 50 mL falcon tube and the vial was rinsed with CDI plating medium which was then added dropwise to the cells. An additional 3 mL of plating medium was added afterwards to reach a final volume of 5 mL of cell suspension. A live cell count was performed using a haematocytometer as described in the previous section. CDI iPSC-CM were plated at a density of 200,000 cells per well for imaging experiments. Finally, plating medium was replaced with pre-warmed (37°C) CDI maintenance medium approximately 4 h post-plating.

2.2.4.3 Maintenance of Axiogenesis and iCell CDI iPSC-CM

Both Axiogenesis and iCell CDI iPSC-CM were kept in a sterile humidified incubator at 37°C and 5% CO₂ and maintenance media was replaced every 24 h. Typically cells were cultured 7 (+/- 1) days post plating for both imaging experiments and obtaining protein lysates. Cells were allowed to recover from cryopreservation and only used once they presented with a stable contractile phenotype. Cells were transfected with Ad-HA-GLUT4-GFP 3-4 days after plating and used for experiments once expression of fluorescent protein was visible under a microscope 48-72 h later.

2.2.5 Primary rabbit cardiomyocyte isolation

Septal cardiomyocytes were isolated from adult male New Zealand white rabbits (2-2.5kg) by standard enzymatic dissociation (Kettlewell et al., 2009). Animals were anaesthetised by administration of an intravenous injection of sodium pentobarbital (100mg/kg) containing 1.000 IU of heparin. The heart was excised in accordance with the United Kingdom Animals (Scientific Procedures) Act 1986 and conformed to the Guide for the Care and use of Laboratory Animals (NIH publication no. 85-23, revised 1985). The aorta was rapidly cannulated and perfused retrogradely in a Langendorff system at a perfusion rate of 25 ml min⁻¹ (37°C) with Krebs solution. The solution was then switched to Krebs containing 0.05 mM Ca²⁺, 1.4 mg ml⁻¹ type 1 collagenase and 0.1

mg ml⁻¹ type XIV protease for 15 min. Finally, perfusion was changed to a 1% bovine serum albumin 0.075 mM Ca²⁺ Krebs solution. The digested septum was removed from the cannula, cut into small pieces and agitated in 0.125 mM Ca²⁺ solution for 1 h. Subsequently, the cardiomyocytes were re-suspended in a series of Krebs solution containing (mM) 0.25, 0.5 and 1 Ca²⁺.

2.2.6 Primary rabbit cardiomyocyte maintenance

Cardiomyocytes were cultured in Medium 199 (M199) supplemented with 1% penicillin/streptomycin (v/v), 1mM glutamine, 5mM carnitine, 5mM creatine and 5mM taurine. Media was changed every other day.

2.2.7 Neonatal rat cardiomyocyte isolation

Neonatal rat cardiomyocytes were isolated from 1-2 day old Sprague-Dawley rats by standard enzymatic dissociation. Animals were anaesthetised by administration of an intraperitoneal injection of Euthatal. Hearts were excised in accordance with the United Kingdom Animals (Scientific Procedures) Act 1986 and placed directly into a 5 cm dish containing ice-cold ADS buffer. Atrial and aortic tissue was removed by dissection and the hearts were squeezed gently to remove residual ventricular blood and transferred to a new 5 cm dish with fresh ice-cold ADS buffer. Hearts were cut up into 1mm³ sized pieces before being transferred into a 50 mL tube. The heart tissue was left to settle and the supernatant ADS buffer was aspirated. Collagenase buffer consisting of 0.03% (w/v) collagenase and 0.06% (w/v) pancreatin was added and the tissue was incubated in a shaking water bath at 37°C for 5 min. During the first step of the serial enzymatic digestions pericardial collagen was removed. Afterwards the collagenase buffer was replaced with fresh buffer and the heart tissue subjected to 20 min digestions 4-5 times. The heart tissue was allowed to settle after each digestion and the supernatant was removed and added to a sterile 15 mL tube containing 500 µL NCS to terminate the digestion. Tubes were centrifuged at 1500 x g or 5 min and pellets were resuspended in 2 mL NCS. Tubes were kept at 37°C until subsequent digestions were completed. After the last digestion cells were pooled and centrifuged at 1500 x g for 5 min and then resuspended in Day 1 medium (M1) containing 80% (v/v) DMEM and 20% (v/v) M199 supplemented with 10% (v/v) horse serum, 5% (v/v) NCS, 1% (v/v) L-glutamine and 1% (v/v) penicillin/streptomycin. At this stage, the cells were a mixed culture comprised mainly of fibroblasts and neonatal rat cardiomyocytes. To purify remove fibroblasts, a pre-plating step was carried out. 10 mL of the cell suspension were plate per 10 cm culture dish and incubated for 2 h at 37°C. Fibroblasts adhere to the culture dish whereas neonatal rat cardiomyocytes do not and thus remain in suspension. The suspension containing the neonatal rat cardiomyocytes was removed and transferred to a 50 mL tube. Culture dishes were washed with M1 medium to collect

all cardiomyocytes. Cells were centrifuged at 1250 rpm for 5 min and resuspended in fresh M1. Cells were seeded at a density of 400,000 cells per well of a 6 well plate containing cleaned coverslips that were previously coated with 1 $\mu\text{g}/\text{cm}^2$ laminin. Cells were incubated at 37°C with 5% CO₂.

2.2.8 Neonatal rat cardiomyocyte maintenance

After 24 h of culture in M1, neonatal rat cardiomyocytes were washed twice with ADS M1 was replaced with Day 2 medium (M2) containing 80% (v/v) DMEM and 20% (v/v) M199 supplemented with 5% (v/v) horse serum, 0.5% (v/v) NCS, 1% (v/v) L-glutamine and 1% (v/v) penicillin/ streptomycin. Before virus infection, the cells were left in the incubator for at least two h. The cells were incubated at 37°C with 5% CO₂ and the medium changed every other day.

2.2.9 Human skeletal muscle myoblast growth and maintenance

Cryopreserved human skeletal muscle myoblasts (HSMMs) were from Lonza Bioscience (Switzerland). Two batches from either a healthy (HSMM) or a diseased (D-HSMM) donor were used. Closely matches samples of age, weight etc were not available. HSMM were obtained from a healthy Caucasian female, age 19 years, weight 70 kg and smoking (Lot #0000629287). D-HSMM were obtained from a T2DM Caucasian female, age 85 years, weight 66 kg and non-smoker (Lot #00002192060). The following data were also supplied by the manufacturer and matched for both cell types: no history of heart disease or hypertension, cell passage 2, cell count 700,000, ATP quantity 25 and doubling time 20 h. Myoblasts were maintained in SkGM™-2 Basal Medium with SkGM™-2 SingleQuots™ supplements containing human epidermal growth factor, dexamethasone, l-glutamine, foetal bovine serum, and gentamicin/amphotericin-B at 37°C in 5% CO₂ atmosphere. A reagent pack containing trypsin-EDTA solution, HEPES-buffered saline and trypsin-neutralizing solution was also obtained from the manufacturer. Cells were passaged at 50-70 % confluence to avoid spontaneous myotube formation. Cells were seeded at 3,500 cells/cm² for maintenance and at 10,000 cells/cm² one day before initiation of differentiation for experiments. Myoblast cells were differentiated by switching the medium to DMEM:F12 supplemented with 2% horse serum. Growth and differentiation media were changed every other day. HSMMs were grown for 5 days before preparing lysates for protein analysis or imaging experiments.

2.3 Super resolution microscopy methods

2.3.1 Coverslip preparation

High performance (\varnothing 24mm; thickness 1.5mm) glass coverslips were placed into a Wash-N-Dry coverslip rack and sequentially submerged in 0.1M NaOH and 0.1% (v/v) Decon-90 for two min in each solution with constant sonication in a sonicating water bath. Coverslips were washed by submerging them into 1L of deionised water 3 times. Coverslips were submerged in 100% ethanol and 100% acetone for 2 min with constant sonication in a sonicating water bath and the washing step was repeated. Coverslips were placed into 100% ethanol and transferred to the laminar flow hood. Lab tissue was soaked in ethanol and coverslips were placed on top and were left to dry under UV light for at least 30 min. Once all coverslips were washed and the tissue was dry each coverslip was removed individually with tweezers and placed into a 6 well plate. The 6 well plates including the coverslips were sealed with cling film and stored at 4°C until use.

2.3.2 Seeding cells onto coverslips

Coverslips were cleaned as described previously and removed from 4°C storage 30 min prior to cell seeding to adjust to room temperature. Cells were added as described in the passaging methods for each individual cell type. HeLa cells were seeded and 3T3-L1 fibroblasts differentiated on the glass coverslips without any previous coating steps. Primary rabbit cardiomyocytes and neonatal rat cardiomyocytes were seeded onto coverslips coated with laminin (1 $\mu\text{g}/\text{cm}^2$). Laminin was slowly thawed on ice and suspended to the desired concentration in PBS. Glass coverslips were covered with coating solution and incubated for three h at 37°C. The coating solution was removed and primary rabbit cardiomyocytes (~100,000 cells/well) and neonatal rat cardiomyocytes (~300,000 cells/well) were seeded directly. iPSC-CM were seeded onto coverslips coated with fibronectin (2 $\mu\text{g}/\text{cm}^2$). Fibronectin was suspended in DPBS with Ca^{2+} and Mg^{2+} and coverslips were covered in coating solution for two h at 37°C. The coating solution was removed and iPSC-CM (~200,000 cells/well) were seeded as described before.

2.3.3 Infection of cells with HA-GLUT4-GFP adeno virus

Viral gene transfer was the preferred method for expressing the HA-GLUT4-GFP construct in the cell models for this study. HeLa and 3T3-L1 cell lines stably expressing HA-GLUT4-GFP were previously generated in the laboratory (Morris et al., 2020). Primary rabbit cardiomyocytes and neonatal rat cardiomyocytes were seeded onto glass coverslips as described (section 2.3.2). Primary rabbit cardiomyocytes were infected with a commercially produced HA-GLUT4-GFP adenovirus with a multiplicity of infection

(MOI) of 100 in cell culture media 4 h after seeding. Virus containing media was removed after 24 h and replaced with fresh culture media. The cells were incubated for another 24 h to give the protein 48 h overall to be expressed. Neonatal rat cardiomyocytes were infected with HA-GLUT4-GFP adeno virus at 40MOI in cell culture medium 24 h after isolation. Media was removed after 24 h and replaced with fresh culture media. The cells were incubated for another 24 h. CDI iPSC-CM were infected with HA-GLUT4-GFP adeno virus at 50MOI and HSMM were infected with virus at 500MOI. Transfection was assessed before fixation by checking the GFP signal through an epifluorescence microscope.

2.3.4 Infection of cells with HA-GLUT4-GFP adeno-associated virus

Axiogenesis iPSC-CM were seeded onto glass coverslips as previously described. 12 h after plating and removal of the freezing media cells were infected with 150MOI of HA-GLUT4-GFP adeno-associated virus (AVV) in serum-free Opti-MEM. The Opti-MEM containing the AVV was removed and replaced with fresh culture media after 24 h. Cells were left to express the HA-GLUT4-GFP protein for another 72 h. Transfection was assessed before fixation by checking the GFP signal through an epifluorescence microscope.

2.3.5 Fixation of cells on coverslips

Cells were serum-starved for 2 h prior to fixation. Cells were placed on ice to stop all reactions and washed with ice cold PBS 3 times. Coverslips were fixed with 4% (w/v) paraformaldehyde (PFA) in PBS overnight at 4°C. The samples were quenched with 50mM NH₄Cl in PBS for 10 min at room temperature and washed with PBS. Samples were stored at 4°C and stained prior to imaging experiments.

2.3.6 Immunofluorescence staining

2.3.6.1 Anti-HA conjugated antibody stain

Samples were incubated in blocking solution containing 2% (w/v) BSA with 5% (v/v) goat serum in PBS for 30 min. Afterwards cells were incubated with a conjugated anti-HA antibody coupled to Alexa Fluor 647 at a concentration of 8 mg/mL (1:125 dilution) in blocking solution for 1 h in the dark. Samples were then washed with PBS for 10 min 3 times on an orbital shaker. Cells were stored at 4°C no longer than a week before imaging.

2.3.6.2 Anti-GFP nanobody stain

Samples were stained with FluoTag®-Q anti-GFP nanobody according to manufacturer's instructions. Samples were permeabilised and blocked with immunofluorescence (IF) buffer containing 0.1% (v/v) Triton X-100/PBS supplemented with 10% (v/v) goat serum

for 15 min on an orbital shaker. Samples were treated with 0.5 μ M FluoTag®-Q anti-GFP nanobody (1:10 dilution) coupled to Alexa Fluor 647 in IF buffer for 1h. Samples were then washed with PBS for 10 min 3 times on an orbital shaker. Cells were stored at 4°C no longer than a week before imaging.

2.3.6.3 Anti-HA primary antibody with secondary nanobody stain

Samples were blocked with 10% (v/v) goat serum in PBS for 30 min. Samples were incubated in primary mouse anti-HA antibody at a concentration of 8 mg/mL (1:125 dilution) in 10% (v/v) goat serum in PBS for 1 h. Samples were washed with PBS 3 times before treatment with 0.5 μ M FluoTag®-X2 anti-Mouse nanobody (1:10 dilution) coupled to Alexa Fluor 647 in 10% (v/v) goat serum in PBS for 1h. Samples were then washed with PBS for 10 min 3 times on an orbital shaker. Cells were stored at 4°C no longer than a week before imaging.

2.3.7 Microscope setup

The dSTORM image sequences were acquired on a Zeiss Elyra PS. 1 system with ZEN Black software. The commercial system comes with all components necessary for SMLM image acquisition with a resolution of 20-30 nm in the x/y and 50-80 nm in the z-axis. Optical systems alignment is a prerequisite for accurate localization of molecules at nanometre precision. Firstly, the objective phase plate needs to be aligned with the condenser annulus of the microscope. To achieve this bright-field illumination was switched on and an objective removed to place a clear glass slide into the transillumination pathway. Another glass slide was placed into the sample holder on the microscope stage. The “stage alignment” tool was selected in the software window and displayed the objective rear focal plane with the misaligned objective phase plate and condenser annulus light cones. The X- and Y-bolts on the stage enabled the adjustment of the position of the condenser annulus light cone with respect to the fixed objective phase plate. When the two annuli were centred, the ideal illumination of the specimen was ensured. Secondly, chromatic shifts between different colour channels were corrected with the “Channel alignment” tool. The 100x 1.46 alpha Plan-Apochromat DIC M27 Elyra objective was selected and a fluorescent bead sample placed on the stage and the eye piece used to focus on it. A bead calibration file was created in the acquisitions tab which includes a z-stack of images with the activation of the 405 (50mW), 488 (200mW), 561 (200mW) and 642 (150mW) HR Diodes. Next the channel alignment transformation table was obtained in the processing tab of the software. The “channel alignment” tool was selected and the previously obtained bead calibration file chosen as input image. Running the “channel alignment” tool resulted in all colour channels being properly aligned and produced a transformation table that was saved.

2.3.8 Image acquisition

Coverwell modular hybridisation chambers were glued onto glass slides. Cold dSTORM imaging buffer containing 50mM mercaptoethylamine (MEA) in PBS (pH=8) was pipetted into the chamber and coverslips with the fixed and stained samples were vacuum-sealed onto the chambers to avoid oxygen entry. The dSTORM imaging buffer was stored on ice during the imaging session in case it was needed at a later stage. The dSTORM image sequences were acquired in TIRF configuration using a 100x 1.46 oil-immersion alpha Plan-Apochromat DIC M27 Elyra TIRF objective with a BP 420 - 480/BP 495 - 550/LP 650 emission and MBS 405/488/642 excitation multi-band filter set. Samples were illuminated with 647 nm laser light at 100% (150mW). Images were recorded on an Andor iXon 897 EMCCD camera using a centred 256 × 256 pixel region at 30 ms per frame for 10,000 frames and an electron multiplier gain of 200 and pre-amplifier gain profile 3.

2.3.9 Image reconstruction

The dSTORM data were processed using the freely available Image J plugin ThunderSTORM (Ovesný et al., 2014). ThunderSTORM is a comprehensive platform for analysis of SMLM data including several different localisation methods and processing tools. The image reconstruction parameters chosen are lined out in the following: pre-detection wavelet filter (B-spline, scale 2, order 3), initial detection by local maximum with 8-connected neighbourhoods (radius 1, threshold at two standard deviations of the F1 wavelet), and sub-pixel localisation by integrated Gaussian point-spread function (PSF) and maximum likelihood estimator with a fitting radius of 3 pixels. The first pass detected localisations were filtered according to the following criteria: an intensity range of 300 - 5000 photons, a sigma range of 50 - 250, and a localisation uncertainty of less than 25 nm. Subsequently, the filtered data set was corrected for sample drift using cross-correlation of images from 5 bins at a magnification of 5. Repeated localisations, such as can occur from dye re-blinking, were reduced by merging points which re-appeared within 20 nm and 1 frame of each other.

2.3.10 GLUT4 localization density

Localization density of GLUT4 molecules in the PM was determined using the Image J plugin LocFileVisualizer_v1.1 (van de Linde, 2019). Briefly, csv files previously generated using ThunderSTORM were opened and the Image J polygon selection tool was used to draw around the outline of each cell. Area and mean intensity grey value were measured for each individual cell. Graphpad prism was used to prepare a list containing all cells and their mean intensity values were normalised against the corresponding cell area and plotted in a graph.

2.3.11 GLUT4 cluster analysis

GLUT4 cluster analysis was carried out using several approaches which are described in detail in the introduction to Chapter 1 of this thesis (see section 3.1.6).

2.3.11.1 SR Tesseler

Ripley's K function analysis was carried out using SR Tesseler software (Levet et al., 2015). The software version 1 and its dependencies and external libraries were downloaded from Github (<https://github.com/flevet/SR-Tesseler>). Ripley's K function analysis was carried out according to the SR Tesseler manual (section 3.1.6.1). In brief, csv files were imported into the SR Tesseler interface and minimum, maximum and step radius chosen before the K function was automatically calculated. Furthermore, Voronoï diagrams were calculated on the GLUT4 localization data using SR Tesseler. The density factor was set to 2 and objects were created automatically by the software based on the Voronoï diagrams. Object (cluster) information was exported as an excel file.

2.3.11.2 Bayesian cluster analysis

For Bayesian GLUT4 cluster analysis R (<https://cran.r-project.org/>) and RStudio (<https://www.rstudio.com/>) were installed (Griffié et al., 2016). Additionally the two R libraries "splancs" and "igraph" were installed using the R Studio interface. Firstly, experimental data sets were appropriately formatted for analysis, working directories created and regions of interest defined. Folders were created for each cell and the files provided for the analysis placed into these folders (formatting.R, get_histograms.m, run.R, internal.R, postprocessing.R, simulate.R, formatting_params.txt, sim_params.txt, Coord.txt and config.txt files). Four regions of interest were chosen for each cell that were 3 μm x 3 μm in size. Secondly, the code for cluster analysis provided as a download was run in R Studio (processing 45 min per ROI). Lastly, a postprocessing step was carried out to generate cluster descriptors for each ROI. Theories of the Bayesian approach for cluster analysis can be found in section 3.1.6.2.

2.3.11.3 Cluster analysis with machine learning

Python scripts for cluster analysis with machine learning was obtained from Gitlab (<https://gitlab.com/quokka79/caml>). Firstly, a provided script was used to create a JSON file that contained all important information about the data set (Williamson et al., 2020). In the following the Data Preparation script was run that measured all distances between individual GLUT4 molecule localizations (see section 3.1.6.3). In the next step the data points and distances are evaluated with a previously generated model. In this project the previously generated model KRIRK0 was used. Furthermore, David Williamson who is the author of the software also prepared a specific model trained on GLUT4 localization data named Q3VHAP.

2.3.11.4 Density-based spatial clustering of applications with noise

Python scripts for the hierarchical density-based spatial clustering of applications with noise algorithm were downloaded from Github (<https://github.com/scikit-learn-contrib/hdbscan>). A script was written in collaboration with Marie Cutiongco that applied the HDBSCAN algorithm automatically to GLUT4 localizations using the Python integrated development environment Spider. Clusters were determined for whole cells and ROIs of 8 μm x 8 μm size. A detailed description of how the algorithm operates can be found in section 3.1.6.5.

2.3.11.5 Spatial statistics

The complete spatstat package version 1.64-1 was downloaded from the comprehensive R archive network website (<https://cran.rproject.org/web/packages/spatstat/index.html>). Spatial statistics analysis of GLUT4 localization data was carried out in collaboration with Marie Cutiongco and based on the book published by the software authors (Baddeley et al., 2016). Refer to section 3.1.6.6 for a detailed account of the calculations that were carried out in this project.

2.4 Glucose uptake assay

2.4.1 3T3-L1 adipocyte glucose uptake assay

3T3-L1 fibroblasts were differentiated into mature adipocytes in 12 well plates as previously described. Cells were rendered quiescent for 2 h in serum-free medium and then washed twice with pre-warmed Krebs-Ringer-Phosphate (KRP) buffer containing 136 mM NaCl, 20 mM, 5 mM sodium phosphate buffer ($\text{NaH}_2\text{PO}_4\text{-Na}_2\text{HPO}_4\cdot 7\text{H}_2\text{O}$, pH 7.4), 4.7 mM KCl, 1 mM MgSO_4 , 1 mM CaCl_2). All glucose uptake experiments were performed with 3 technical replicates per group. The buffer was removed and the cells were incubated with or without 100nM insulin in KRP buffer at 37°C for 30 min. Subsequently, an aliquot of [3H]-2-deoxy-d-glucose in KRP buffer was added (0.25 uCi/well; 50 μM final concentration) and incubated at 37 °C for 10 min. Half of the samples were incubated with 10 μM of cytochalasin B (CB), a mycotoxin which inhibits facilitative glucose uptake in the cells and serves as a measure for background in this assay. After that, the cells were rinsed carefully with ice-cold PBS 3 times, air dried and lysed with 1% (v/v) Triton 100x (1mL/well). The radioactivity in the sample was measured using liquid scintillation counting.

2.4.2 Primary cardiomyocyte glucose uptake assay

Primary rabbit cardiomyocytes were plated in 96-well plates and on experiment day the plate was transferred to a hotplate at 37°C and washed with pre-warmed KRP buffer only once to avoid the disturbance of the cells. Subsequently, cells were incubated for

30 min with all combinations of 100 μ L KRP +/- 40 μ M CB +/- 860 nM insulin, in triplicate, as previously described (section 2.4.1). 100 μ L of 10 μ Ci/ml of [3H]-2-deoxy-d-glucose in KRP buffer supplemented with 100 μ M 2-deoxy-d-glucose was added and cells were incubated at 37 $^{\circ}$ C for 30 min. Termination of the procedure was initiated by pipetting off the solution and washing the wells with ice-cold PBS once. Cells were lysed and suspended in scintillation fluid as previously described and radioactivity was measured.

2.4.3 Interpretation of glucose uptake assay results

At minimum 3 replicates were obtained from each glucose uptake experiment for 4 experimental conditions. Firstly, the raw data were plotted and visually inspected for outliers and abnormalities. In the rare event that a data point would be lower than its associated CB value exclusion of the data point was justified as this is a strong indicator of measurement error. The mean CB values for +/- insulin conditions was calculated and subsequently these values were subtracted from each data point for the corresponding condition. These background corrected data are reported in all of the figures included in this project. Final graphs were plotted and statistical comparisons made between conditions using GraphPad Prism.

2.5 Protein assays

2.5.1 Production of protein lysates

Rabbit cardiomyocytes were left to sediment in a tube for 20 min. The supernatant was removed and the tube was placed on ice. RIPA buffer was applied to the cells and samples were homogenised using a tissue grinder and left to incubate on ice for 20 min. The grinding was repeated twice and the samples centrifuged at 12470 x g at 4 $^{\circ}$ C for 5 min to separate the insoluble material from the lysate. Lysates were stored at -20 $^{\circ}$ C until required. For cells on plasticware, cells were washed 3 times with cold PBS and placed on ice. Protein was extracted by applying Laemmli Sample Buffer on ice for 20 min. Samples were centrifuged at 12470 x g at 4 $^{\circ}$ C for 5 min and stored at -20 $^{\circ}$ C until used.

2.5.2 Bicinchoninic acid assay

When appropriate a bicinchoninic acid assay (BCA) assay was performed for the colorimetric detection and quantitation of protein concentration. Protein standards with bovine serum albumin (BSA) concentrations between 25 - 2,000 μ g/mL were prepared and 25 μ L of each standard and the experimental sample were mixed with 200 μ L working reagent supplied by the manufacturer. Further dilutions were prepared of protein standards and experimental samples diluted 1:1 in distilled water to make sure that the samples would fall into the range of the BSA standards. The mixtures were

pipetted into a microplate in duplicate and incubated at 37°C for 30 min. A microplate reader was used to measure the absorbance at 562 nm.

2.5.3 Western immunoblotting

Polyacrylamide resolving gels were cast manually in the laboratory using Biorad mini-Protean III equipment. The final percentage of acrylamide was determined by the size of the protein but was usually at 10 %. Protein samples were thawed and boiled at 95°C for 5 min or heated to 65°C for 10 min when probing for GLUT4. BioRad Precision Plus Protein Standards All Blue Markers was used as molecular weight ladder. Samples were usually electrophoresed at 100V for approximately 2 h and subsequently transferred onto Nitrocellulose membrane. Membranes were stained with Ponceau solution to check correct transfer of proteins prior to immunolabelling. Nitrocellulose membranes were blocked in 5% (w/v) BSA or milk powder in PBS-T for 30 min at room temperature, then incubated with primary antibody at 4°C overnight. The next day membranes were washed in PBS-T three times for ~5 min before incubation with appropriate secondary antibodies at room temperature for 1 h. After washing, the blots were visualised with a LI-COR Odyssey-SA.

2.5.4 Densitometry

Scanning of nitrocellulose membranes was performed with a resolution of 100 µm and high quality composite images of 2 channels of excitation/emission were obtained. Images were imported into Image Studio Lite software (Version 5.2) provided by LI-COR. In the analysis window a box was drawn around each protein band of interest and the automatically background corrected mean pixel intensity was measured. Mean pixel intensities of proteins of interest were normalised against GAPDH protein intensities to adjust values for the amounts of protein that were loaded.

2.6 Molecular methods

2.6.1 Amplification of plasmid DNA

Several plasmids had to be amplified in volume during this project for subsequent aims and a general description of this process is provided in this section. All steps were performed in semi-sterile conditions on a bench top under a flame using sterile equipment. Plasmid DNA was transformed into Stbl 3 or 5- α *E. Coli* cells. 1 µL of plasmid DNA was incubated with 50 µL of competent cells in an Eppendorff tube on ice for 30 min. The cells were heat shocked at 42°C for 45 s and placed on ice for another 2 min. In the following 300 µL of SOC medium was added and the mixture was shaken in a 37°C incubator for 45 min. Cells were plated on antibiotic selection agar plates and incubated overnight at 37°C. Additionally, untransformed *E. Coli* cells were plated on an antibiotic selection plate (negative control) and one plate without antibiotic selection

marker (positive control) for each experiment. Success of the transformation protocol was assessed the following day by observation of bacterial growth on appropriate plates only. A single colony was scraped off the plate using a P20 sterile pipette tip and placed into a tube containing 5 mL 2YT medium. The culture was placed into a shaker at 37°C during the day (~ 8 h). The small culture was then transferred into a big flask containing 100 mL 2YT medium which was rigorously shaken at 37°C overnight (~ 16 h). The following day a commercially obtained Maxi Prep kit was used to extract the plasmid DNA from the cells. A NanoDrop spectrophotometer was used to determine the concentration of the new DNA preparation.

2.6.2 Transfection of mammalian cells with plasmid DNA

HeLa cells were plated in 6-well plates for imaging experiments and preparation of protein lysates. At 50-70 % confluency cells were transfected with the transfection reagent Lipofectamine 2000 and plasmid DNA. As indicated in figure legends several concentrations of Lipofectamine 2000 and DNA were used for optimisation during this project. Usually 8 µL Lipofectamine 2000 plus 2.5 µg DNA in 500 µL Opti-MEM were prepared for each well of a 6-well plate. 8 µL Lipofectamine 2000 and 2.5 µg DNA were added to 250 µL Opti-MEM respectively and incubated for 5 min. Thereafter, the two solutions were mixed thoroughly and incubated for 20 min before application to the well plate containing the HeLa cells. Opti-MEM containing either Lipofectamine 2000 or plasmid DNA were prepared to serve as controls for each experiment. Cells were incubated at 37°C and 5% CO₂ with the reagents for 4 h and then medium was switched back to normal maintenance medium. Cells were used for experiments exactly 48 h post transfection.

2.6.3 Generation of a novel TfR-GFP lentiviral plasmid

To generate a plasmid suitable for the development of a lentivirus the TfR-GFP gene sequence had to be subcloned from the pEGFP-N1-Flag-TfR-GFP plasmid into the pCDH backbone of the pCDH-CMV-MCS-EF1-HA-GLUT4-GFP plasmid. This was achieved using a NotI/NheI double digest of both the original TfR-GFP plasmid and the pCDH backbone. After purification and ligation using standard procedures, single putative positive colonies were amplified and DNA purified using commercial mini-prep plasmid kits according to the manufacturer's instructions. The DNA was digested with the same restriction enzymes to confirm that the backbone (pCDH) and insert (TfR-GFP) were of the correct molecular size. Once this was achieved the newly generated plasmid was transformed into Stbl 3 *E. Coli* and amplified in volume for future use.

2.7 Confocal microscopy

Cells were seeded onto ø 12mm and 24mm coverslips and fixed when 70-80 % confluent as described in section 2.3.2 and 2.3.5 respectively. Between all steps of the protocol

samples were washed with PBS 3 times. After fixation quenching buffer was applied for 10 min and immunofluorescence buffer was used for blocking for a minimum of 30 min. Cells were stained with primary and secondary antibodies specified in table 2.4 and 2.5. Coverslips were mounted onto clean glass slides using Immu-Mount non-fluorescent anti-fading medium and left to dry overnight. Samples were imaged using a 40x or 63x objective lens on a Zeiss LSM 800. Images were processed using Image J.

2.8 Flowcytometry

2.8.1 GLUT4 translocation assay set up for HeLa cells

Flow cytometry is a powerful multiparameter laser-based technology for assaying GLUT4 translocation in a high throughput fashion. Firstly, this technique was optimised in HeLa cells as they are a highly homogenous cell population. Wild-type and unstained HeLa cells stably expressing HA-GLUT4-GFP were used as experimental controls. Detection thresholds for HeLa cells were set at 150,000 SSC-A (side scatter area) and 250,000 FSC-A (forward scatter area). Log intensities of scattered light and fluorescence (FITC, 488 nm excitation/515-545 nm emission; APC, 635 nm excitation/650-670 nm emission) were collected for 20,000-30,000 cells from the control samples. HeLa cells in culture contain healthy cells and some cellular debris. Data collection thresholds were set based on FSC and SSC profiles to omit small light scattering debris and machine noise from the analysis. A first elliptical gate was set to identify the HeLa cell population. Fluorescence detector gains were set so that background autofluorescence in noninfected cells was collected in the first log decade of the detector range. A second elliptical gate was drawn to separate cells expressing the HA-GLUT4-GFP (GFP-positive) construct from cells that did not express the construct (GFP-negative).

2.8.2 Preparation of HA-GLUT4-GFP HeLa cells for FACS analysis

HA-GLUT4-GFP HeLa cells were seeded into 6 well plates (~300,000 cells/well) 24 h pre-analysis. On the experiment day cells were serum-starved for two h and half of the HA-GLUT4-GFP HeLa cell samples were stimulated with 1 μ M insulin for 40 min at 37°C. The plates were then placed on ice where all subsequent steps were performed with use of ice-cold solutions. Surface GLUT4 was stained for using the HA-tag. Cells were incubated with labelling medium containing primary anti-HA antibody at a concentration of 1:200 in DMEM with 10% (v/v) FCS for one h. Cells were washed 3 times with PBS and incubated in labelling medium containing 1:300 secondary antibody conjugated with AlexaFluor® 647 for one h. Cells were washed with PBS and gently dissociated with collagenase type I (2 mg/ml (w/v)) in PBS supplemented with 0.5mM EDTA and 10% (v/v) FCS at 37°C for 10 min. Samples were diluted in PBS and gently filtered through a 100 μ m cell strainer to remove clumps of cells and analysed on a BD™

LSR II flow cytometer. Events of 50,000 cells were collected for each experimental condition.

2.8.3 GLUT4 translocation assay set up for adipocytes

Subsequently, this GLUT4 translocation assay was optimised in 3T3-L1 adipocytes. Mature adipocytes were differentiated from 3T3-L1 fibroblasts and therefore presented as a more heterogeneous cell population in culture. Differentiated 3T3-L1 adipocytes in culture contain fully differentiated adipocytes, nondifferentiated fibroblasts and necrotic cells that died during differentiation. Wild-type and unstained HA-GLUT4-GFP adipocytes were used as experimental controls. Detection thresholds for 3T3-L1 cells were set at 250,000 SSC-A (side scatter area) and 250,000 FSC-A (forward scatter area). Log intensities of scattered light and fluorescence (FITC, 488 nm excitation/515-545 nm emission; APC, 635 nm excitation/650-670 nm emission) were collected for 20,000-30,000 cells from the control samples. For the analysis of adipocytes an elliptical gate was applied to the FSC and SSC resulting in analysis of only adipocytes and exclusion of any residual fibroblasts and cellular debris. 3T3-L1 adipocytes expressing the HA-GLUT4-GFP construct were separated from cells that did not express the construct using a threshold gate in SSC and FITC.

2.8.4 Preparation of HA-GLUT4-GFP adipocytes for FACS analysis

HA-GLUT4-GFP 3T3 L1 fibroblasts were seeded into 12 well plates and differentiation into mature adipocytes was initiated 10 days prior to the experiment as previously described. On the experiment day cells were serum-starved for two h and half of the HA-GLUT4-GFP 3T3 L1 adipocyte samples were stimulated with 100 nM insulin for 40 min at 37°C. The plates were then placed on ice where all subsequent steps were performed with use of ice-cold solutions. Surface GLUT4 was stained for using the HA-tag. Cells were incubated with labelling medium containing primary anti-HA antibody at a concentration of 1:200 in DMEM with 10% (v/v) FCS for one h. Cells were washed 3 times with PBS and incubated in labelling medium containing 1:300 secondary antibody conjugated with AlexaFluor® 647 for one h. Cells were washed with PBS and gently dissociated with collagenase type I (2 mg/ml (w/v)) in PBS supplemented with 0.5mM EDTA and 10% (v/v) FCS at 37°C for 10 min. Samples were diluted in PBS and gently filtered through a 100 µm cell strainer to remove clumps of cells and analysed on a BD™ LSR II flow cytometer. Events of 50,000 selectively gated GFP-positive HA-GLUT4-GFP 3T3 L1 adipocytes were collected for each experimental condition.

2.8.5 Analysis of flowcytometry data

The flow cytometric data were analysed using Flowjo v8 software (BD, USA). Briefly, for both fibroblasts and adipocytes FITC mean fluorescence was determined for GFP-positive and GFP-negative cells. To control for autofluorescence and non-specific

staining FITC fluorescence values for GFP-negative cells were subtracted from FITC fluorescence values of GFP-positive cells. Mean values were determined for APC and FITC fluorescence and the HA/GLUT4 ratio calculated by dividing the fluorescence intensity of the APC (HA signal, GLUT4 located in the PM) by the fluorescence intensity of the FITC (GFP signal, total intracellular GLUT4). The HA/GLUT4 ratio was expressed as fold change between conditions.

2.9 Statistical analysis

Throughout this project, GraphPad Prism (version 7) was used for the appropriate statistical analysis of experimental data. Most frequently an unpaired t-test or one-way ANOVA was deemed appropriate and the level of significance was set at $p < 0.05$. Full details are contained within figure legends.

3. Stochastic optical reconstruction microscopy for the assessment of GLUT4 dispersal

3.1 Introduction

3.1.1 The diffraction limit of light

The optical resolution of an imaging system is defined as the ability to resolve detail within the sample and depends on the minimum distance at which two points can be distinguished as individuals (Nollmann and Georgieva, 2015). Throughout history resolving power has been enhanced to a certain extent by careful design of lenses and optics. Nevertheless, any optical microscope has a finite resolution rooted in the fundamental physical laws governing light diffraction referred to as the ‘diffraction limit’. Fluorophores are point sources of light that emit photons diffracted by the optical components of the imaging system and appear as regularly spaced rings known as Airy disks at the detector unit (Figure 3.1). The point spread function (PSF) is the three-dimensional representation of the Airy disk in the image plane and is unique for each imaging system (Nollmann and Georgieva, 2015). The numerical aperture (NA) of the objective defines its performance and is dependent on the amount of photons that can be collected and the refractive index of the immersion medium. Fluorescence microscopy objectives typically have an NA ranging between 0.2 to 0.95 for air objectives and 0.85 to 1.4 for oil objectives. The physicist Ernst Abbe was the first to empirically define the resolution of an optical microscope (Abbe, 1873) as

$$d = \lambda/2NA$$

The smallest resolvable distance d between two PSFs is the wavelength of the observed light λ divided by two times the NA of the objective. The visible spectrum of light ranges from 400 to 750 nm and a typical oil immersion objective has an NA of 1.4 resulting in a maximum resolution of 200-300 nm for a standard microscope (Figure 3.1). Many subcellular structures and processes remain elusive due to the diffraction limit and novel imaging techniques are required to enhance the limit of resolution and so further our understanding.

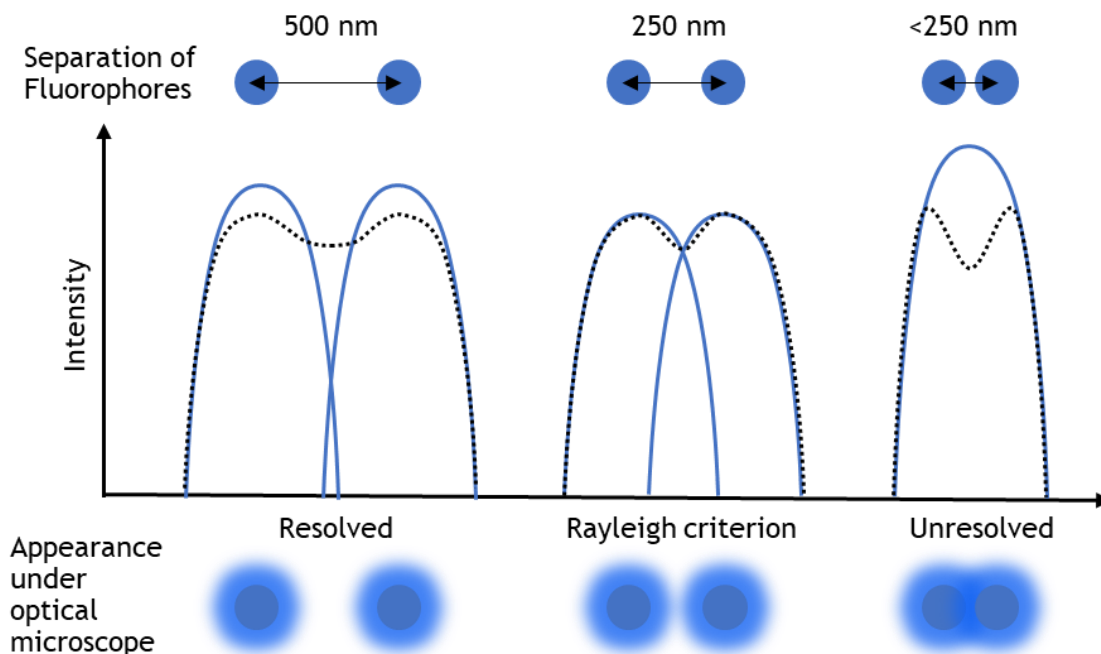


Figure 3.1 Principle of resolution.

Monochromatic light passed through a small circular aperture results in the appearance of circular intensity profiles known as Airy discs. Plotting the signal intensity of this point source of light on a graph it appears as peaks. The Rayleigh criterion is defined as the smallest possible separation between two light sources that can be resolved into separate objects. Adapted from (Thorley et al., 2014).

3.1.2 Super resolution microscopy

In the 1990s Eric Betzig, Stefan Hell and William Moerner came up with different ideas on how to circumvent the physical barriers of the diffraction limit (Betzig et al., 1991; Dickson et al., 1997; Hell and Wichmann, 1994). This was the beginning of the field of super resolution microscopy resulting in the award of the Nobel Prize in Chemistry in 2014 (Thorley et al., 2014). The term super resolution microscopy encompasses several techniques that can be divided in two major groups known as deterministic and stochastic super-resolution. The work described in this thesis employs a stochastic super-resolution approach.

Stochastic super resolution microscopy techniques take advantage of the chemical complexity and temporal behaviour of fluorophores which can be used to make closely situated fluorophores emit light at separate times. These techniques include all single molecule localization microscopy (SMLM) methods such as photo-activated localization microscopy (PALM) (Betzig et al., 2006; Hess et al., 2006) and stochastic optical reconstruction microscopy (STORM) (Heilemann et al., 2008; Rust et al., 2006). SMLM methods are able to temporally isolate single molecules from a group and take

advantage of our ability to localize these single molecules with nanometre precision resulting in the reconstruction of a final super-resolved image.

3.1.3 Stochastic optical reconstruction microscopy

Stochastic optical reconstruction microscopy has become one of the most widely used super resolution techniques for single molecule imaging (Rust et al., 2006). Subcellular structures can be selectively stained with fluorescent molecules which are either linked to an antibody as in immunolabelling or fused genetically to a target of interest. As in standard fluorescence microscopy a set of photons is collected from a molecule and becomes visible as a diffraction-limited PSF in the image plane of the microscope. The centre of this PSFs can be determined by fitting the observed emission profile to a geometrical Gaussian function in two dimensions (Figure 3.2). In this scenario the resolution is only limited by the precision with which the centre of a molecule can be localized and the overall number of localizations. The localization precision Δx can be approximated by

$$\Delta x = \sigma/\sqrt{n}$$

with σ being the standard deviation of the PSF and n being the number of photons collected. The more photons can be collected from a molecule the lower is the error in localizing the centre of this molecule.

Nevertheless, localization precision does not automatically translate to high resolution. Most structures and organelles in biological samples are densely populated with fluorophores with several fluorescent molecules sharing the same volume of diffraction-limited space making single-molecule localization virtually impossible. SMLM methods take advantage of the possibility to switch fluorophores between a light and a dark state. A relatively sparse subset of fluorophores within a densely labelled sample is randomly switched on at an image frame. Subsequently signals of several subsets of activated fluorophores are collected over a series of imaging cycles and the molecule centres are localized with nanometre precision (Figure 3.2). The final result is a table of coordinates containing an accumulation of each individual molecule localization and a final image can be reconstructed from these coordinates with a resolution of up to 20 nm (Rust et al., 2006). The discovery that conventional commercially available fluorophores can be reversibly photo-switched without the presence of an activator dye has revolutionised the field of STORM (Heilemann et al., 2008). The simplified method using single-dye switching is called direct STORM (dSTORM) and is currently the method of choice in the wider scientific community.

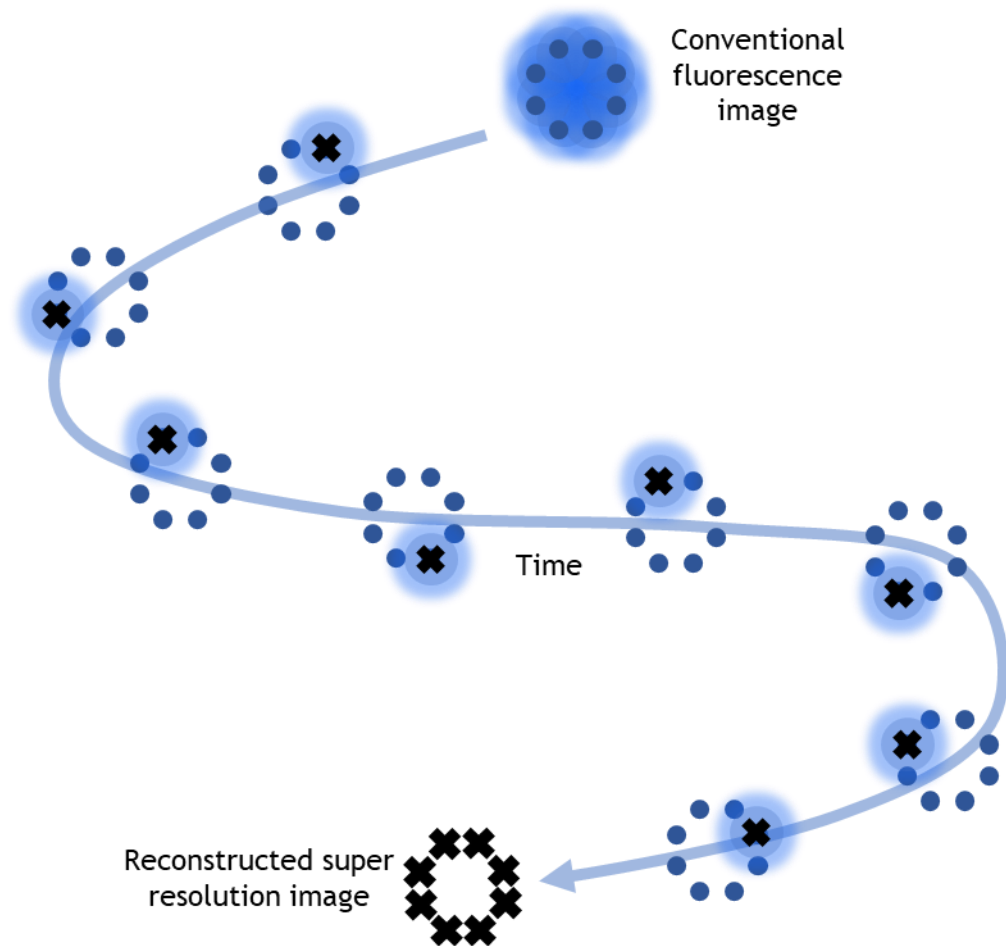


Figure 3.2 Principle of stochastic optical reconstruction microscopy.

A high density of fluorophores results in overlap of individual intensity profiles and limited resolution due to the Abbe diffraction limit. Selective activation of isolated fluorophores over a number of frames achieves temporal separation of the signals. Spatial separation is obtained by localization of molecules by fitting Gaussian curves onto the individual intensity profiles from each frame and a super resolved image with single molecule coordinates is reconstructed. Adapted from (Heilemann et al., 2008).

Photo-switches are all fluorescent molecules that can be switched between a light and a dark state by external means (Heilemann et al., 2008). Photoactivatable fluorophores transition from a dark to a light state in an irreversible manner. These molecules are activated, read-out and subsequently bleached and cannot be reactivated. PALM generally uses genetic fusion constructs to exogenously express photoactivatable fluorescent protein within biological samples. Photoactivation and photobleaching limit the fluorescence lifetime in this setup and continuous emission of the fluorophore between these states is desirable during image acquisition (Heilemann et al., 2008). In contrast, dSTORM makes use of antibodies tagged with organic dyes that can be reversibly switched from a fluorescent to a non-fluorescent state. Cycling between the light and dark states is enabled by electron transfer. High energy light of a short wavelength will excite a fluorescent molecule and promote an orbital electron within the molecule to transition from the ground state S_0 to a higher quantum state known as

the excited singlet state S_1 . After several nanoseconds the electron will relax back to the ground state and the stored energy will be released as an emitted photon (Heilemann et al., 2008). This emitted fluorescent light has a longer wavelength than the absorbed light and the difference between the excitation and emission energy is termed the Stokes shift. Excitation of an electron to a higher energy state can be accompanied by a change of spin state of the electron which is then called intersystem crossing to the excited triplet state T_1 . When the electron has changed its spin state it cannot quickly relax back to its ground state because the re-emission involves quantum-mechanically complex energy state transitions and therefore phosphorescence is the delayed emission of absorbed radiations. To stabilise fluorescence emission during SMLM and generate long-lasting off-states before reactivating a fluorescent molecule the triplet state and therefore phosphorescence need to be quenched (Heilemann et al., 2008). Adding reducing agents with thiol groups for instance MEA have been shown to successfully quench the triplet state and thus retain the electron in the dark state (Olivier et al., 2013). Molecular oxygen can oxidise the fluorescent molecule so it can return to its ground state. This molecular mechanism can be induced for several cycles and this is how efficient photo-switching is achieved in SMLM techniques. The optimal photo-switching rate, at which the activated subset of fluorophores in each frame are further apart than the diffraction limit can be determined by varying the laser intensity, thiol, and oxygen concentration (Olivier et al., 2013).

dSTORM is widely used among the state-of-the-art super resolution microscopy techniques as it offers many advantages. The use of a wide range commercially available standard fluorescent probes which can be used to label virtually any structure have hugely increased the popularity of dSTORM in recent years (Heilemann et al., 2008). Furthermore, the experimental setup only requires a standard confocal microscope with sufficiently powerful lasers which is readily available in most laboratories around the world. Sample preparation is time-efficient, inexpensive and easy to execute without specialist training. DSTORM also offers one of the best resolutions down to ~20 nm which makes it more powerful in resolving molecular details compared to deterministic super resolution microscopy methods.

3.1.4 Sample preparation

Increased resolution gives rise to various new technical issues that must be addressed in order to obtain faithful and high quality super resolution images (Leyton Puig et al., 2016). Both sample preparation and appropriate imaging conditions are key to successful SMLM experiments. Sample preparation starts with fixation of the structure of interest. Electron microscopy experiments have shown that different fixatives affect

cellular structures differently and buffers can also impact on fixation.

Paraformaldehyde (PFA) and glutaraldehyde (GA) are crosslinking fixatives and usually preferred to ethanol, methanol and acids (Leyton Puig et al., 2016). Both PFA and GA bind amino groups preserving the location of structures within the cell. The 4 % PFA solution has been the standard fixative for immunostaining of fluorescence microscopy samples for many decades (Richter et al., 2018). PFA does not change the tertiary structure of target proteins and their epitopes remain available for antibody binding. Nevertheless, studies have reported various problems with PFA fixation, including morphological changes, loss of epitopes, mis-localization of target proteins and slow and incomplete fixation (Melan, 1994; Schnell et al., 2012; Tanaka et al., 2010). GA alleviates these problems by crosslinking proteins more strongly (Smith and Reese, 1980). However, GA introduces free aldehyde groups into the fixed sample leading to alterations in tertiary protein structure. This makes epitopes unrecognizable for antibodies and interferes negatively with immunostaining. Mixtures of PFA and GA result in efficient fixation with reduction of the lateral mobility of molecules but can reduce the efficiency of immunostaining by blocking antibody access to epitopes (Tanaka et al., 2010). Therefore, it is crucial to find a balance between strong fixation with accurate morphology preservation and good quality immunostaining with reliable antibody binding. Fixation artefacts may be negligible in conventional microscopy but need to be taken into consideration to avoid drawing the wrong conclusions about biological processes from SMLM data.

Antibody staining of endogenous GLUT4 protein has been unsuccessful in the visualisation of GLUT4 dynamics historically (personal communication). However, the availability of fluorescent tags revolutionised GLUT4 research and enabled visualisation of GLUT4 and quantification of GLUT4 translocation. The reporter construct HA-GLUT4-GFP is most widely distributed in the GLUT4 research community and its extensive use resulted in reliable characterisation (Figure 3.3). HA-GLUT4-GFP was found to display comparable translocation, localisation and recycling kinetics to endogenous GLUT4 (Dawson et al., 2001; Zeigerer et al., 2002). It was reported that only GFP-labelling of the GLUT4 C-terminus resulted in trafficking dynamics resembling endogenous GLUT4 and placement of the GFP-tag in different molecular locations resulted in undesirable GLUT4 trafficking defects (Dawson et al., 2001).

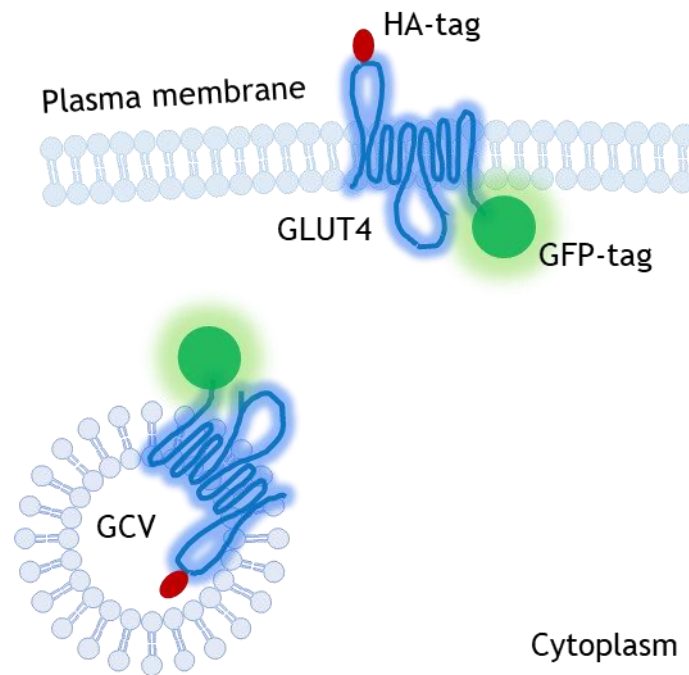


Figure 3.3 Schematic of the HA-GLUT4-GFP construct.

Cells expressing the HA-GLUT4-GFP construct are valuable for the quantification of GLUT4 translocation. Human GLUT4 protein is tagged with a hemagglutinin (HA)-tag on its first exofacial loop and a green fluorescent protein (GFP)-tag fused to its C-terminus. The GFP-fluorescence is directly proportional to the total amount of GLUT4 expressed. When GLUT4 fuses with the PM the HA-tag becomes exposed at the surface and binding of a fluorescently labelled antibody to the HA-tag in nonpermeabilized cells is proportional to the amount of GLUT4 that translocated to the PM.

In theory resolution of super resolution microscopy techniques can reach molecular scale. However, resolution is often limited by sample specific factors for instance the size of the fluorescent label (Huang et al., 2009). At high resolution common antibodies significantly limit how well the image reflects the actual structure by increasing the apparent size of visualised structures. Binding of primary and secondary antibody complexes was reported to increase the diameter of microtubules from 25 nm to about 60 nm using STORM imaging (Bates et al., 2007). Reducing the distance between the dye and fluorescent label, known as linkage error, can be achieved by genetic fusion of organic dye molecules to target proteins (Popp et al., 2007). However, genetic engineering and overexpression is time consuming and not appropriate for all experiments and therefore the use of labelled nanobodies as nanoscale detection tools has emerged recently (Beghein and Gettemans, 2017). Conventional heterotetrameric immunoglobulin- γ (IgG) antibodies are composed of two identical heavy (H)-chain and two identical light (L)-chain polypeptides (Padlan, 1994). The H-chain comprises four domains whereas the L-chain folds into two domains. In 1993 Hamers-Casterman and colleagues observed that in addition to conventional IgG antibodies camelids possess special H chain-only antibodies devoid of L-chains and lacking the first constant domain (CH1) which normally associates with the light chain (Hamers-Casterman et al., 1993).

H-chain antibodies contain a single variable N-terminal domain (VHH) with dimensions in the nanometer range (Ingram et al., 2018; Muyldermans, 2013). Nanobodies are engineered from H-chain antibodies and contain only the single monomeric VHH (Harmsen and De Haard, 2007). They have a molecular weight of 12-15 kDa and are much smaller than common antibodies (150-160 kDa) but have similar binding affinities and improved solubility (Beghein and Gettemans, 2017). Nanobodies can be equipped with a single strongly fluorescent organic dye molecule and significantly reduce fluorescent label linkage error by delivering fluorophores into close proximity of target proteins (Beghein and Gettemans, 2017). Moreover, their small size allows for binding of hidden intracellular epitopes. Recently several studies have reported the successful use of anti-GFP nanobodies that target genetically encoded green fluorescent fusion proteins for super resolution imaging applications (Chamma et al., 2016; Platonova et al., 2015; Ries et al., 2012). High affinity nanobodies have become commercially available, are cost-efficient and allow quantitative labelling because every nanobody can be linked to a single fluorescent molecule (Rothbauer et al., 2006). Nanobodies should always be explored as an alternative to conventional antibodies to avoid linkage error and localization bias in super resolution experiments.

3.1.5 Cluster analysis

Cluster analysis consists of several methods that can be used to classify a set of objects into a group or cluster that share similar properties compared to other sets of objects within a sample (Everitt et al., 2011). It can be achieved by a number of algorithms that vary in how clusters are detected and what is identified as a cluster. Clustering in biological samples can be regarded as a multi-objective optimization problem because the appropriate clustering algorithm and parameter settings depend on the specific sample and intended use of results (Everitt et al., 2011). Data pre-processing steps and model parameters such as distance function, density threshold or number of expected clusters often need to be modified and adjusted to each individual data set until the desired cluster segmentation can be achieved (Levet et al., 2015; Williamson et al., 2020).

The first aim of my research is to quantify GLUT4 clustering and statistically analyse the spatial point pattern generated during dSTORM experiments. To this end, several methods of cluster analysis were evaluated in this study and are described in this chapter. Information on GLUT4 clusters obtained through the use of each individual method was compared to information available from the literature (Gao et al., 2017; Lizunov et al., 2013a; Stenkula et al., 2010).

3.1.5.1 Ripley's K function and its derivatives

In 1976 the British statistician Brian Ripley developed a function to analyse the occurrence of point patterns over a given area of interest (Ripley, 1976). Ripley's K function enables researchers to investigate whether points of interest appear dispersed, clustered or randomly distributed within a sample. The K function is described as

$$K(r) = 1/n \left(\sum_{i=1}^n N_{pi}(r) \right) / A$$

with n being the number of points, N_{pi} being the number of points within a distance r and A being the area (Kiskowski et al., 2009). Ripley's K function is usually calculated at multiple distances to see how the point pattern distributions change with scale (Figure 3.4). Concentric circles are drawn around each point and the number of neighbours enclosed is counted and plotted against the radius resulting in a graph giving information about the spatial point distribution (Kiskowski et al., 2009).

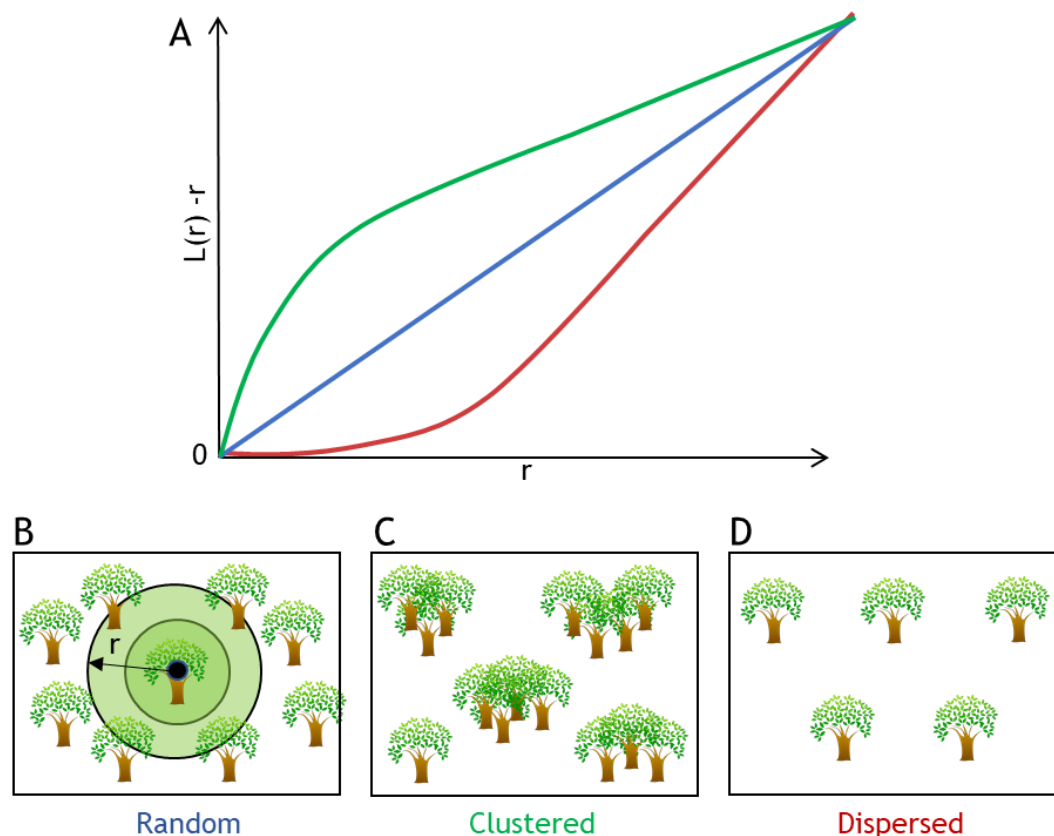


Figure 3.4 Schematic of the analysis of spatial point patterns with Ripley's L function.

The normalized Ripley's K function $L(r)$ is a spatial analysis method used to describe whether spatial point patterns in a given area of interest appear to be uniform (complete spatial randomness=CSR), clustered or dispersed. In this graphic $L(r)$ represents the counts of the number of neighbouring trees found within a given distance r of each individual tree. This number is compared to the number of trees that were expected to be found if all trees were distributed based on CSR (blue line). If the number of trees is bigger than that for CSR the distribution is clustered (green line) and if the number of trees is smaller the distribution is dispersed (red line). Adapted from (Lagache et al., 2013).

The variance stabilised L function is usually used in data analysis and defined as

$$L(r) = \sqrt{(K(r)/\pi)}$$

If the points of interest within a sample are randomly distributed the L function is a straight line (Kiskowski et al., 2009). If the points are more clustered the obtained L value plotted against r will be bigger than expected and when the points are more dispersed the L value will be smaller than expected. Ripley's K and L functions are the gold standard of spatial descriptive statistics and used to detect deviations from spatial homogeneities in many fields of biology. Furthermore, this analysis method is easy to carry out with freeware software packages and the least time consuming (Baddeley and Turner, 2005; Levet et al., 2015; Rubin-Delanchy et al., 2015).

3.1.5.2 Bayesian cluster analysis

In 2015 Dylan Owen developed a new specialist model-based Bayesian approach to analyse pointillist SMLM data sets (Rubin-Delanchy et al., 2015). SMLM raw data consist of a list of the x and y coordinates of all localised fluorophores that also contains an associated, estimated localization precision value for each of the points. Based on Ripley's K function the Bayesian cluster analysis evaluates molecular cluster assignment taking into account the localization precision for each localised molecule. Several cluster proposals are generated for the SMLM data points with variable spatial scales and thresholds and the model that approximates the spatial distribution of the data best is selected (Rubin-Delanchy et al., 2015). The Bayesian cluster analysis has been especially developed for analysis of SMLM data. It is more accurate and eliminates many of the shortcomings of Ripley's K function such as occurrence of edge effects and user-selected parameters that require some pre-existing information of the sample to be correct. However, the generation of thousands of cluster proposals is very time-consuming and requires more computing power and space for data storage.

3.1.5.3 Cluster analysis with machine learning

In 2018 a supervised machine-learning approach to cluster analysis was developed to convert SMLM point pattern data into a meaningful description of clustering (Williamson et al., 2020). Machine learning is a method of data analysis that provides computer systems with the ability to learn to perform specific tasks without being explicitly programmed (James et al., 2013). In supervised machine learning a function is learnt by mapping labelled input training data to desired output values (Figure 3.5). A supervised training algorithm analyses artificially simulated SMLM pointillist input data sets for which the spatial distribution output patterns are known and creates an inferred

function that can be used for mapping new real SMLM data sets (Williamson et al., 2020). The generated model firstly classifies point coordinates as clustered or non-clustered (Figure 3.5). In the next step this information is used to partition points into spatially similar cluster shapes (Williamson et al., 2020). This approach has the benefit of combining fast analysis with high precision and moreover it requires minimal parameter input and pre-existing information about the sample of interest.

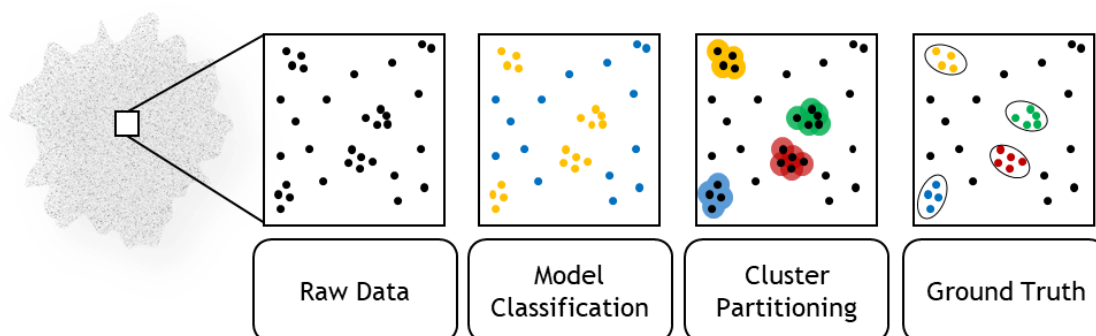


Figure 3.5 Cluster analysis with machine learning.

CAML uses raw data with spatial molecule coordinates of STORM experiments (black dots). Distances are measured from each point in the data set to its neighbouring points. The pattern of the distance values changes from points in dense regions (clusters) to points within a fields of randomly distributed points. Nearby-neighbour distances and distance-differences are used to classify as either clustered (yellow dots) or non-clustered (blue dots). The yellow clustered points are then assigned to spatially similar clusters around which a cluster shape is fitted (cluster partitioning). The model can be compared to the training data to determine the accuracy of the process (ground truth). Adapted from (Williamson et al., 2020).

3.1.5.4 Tessellation

In mathematics, Voronoï tessellation is the subdivision of space into numerous polygonal regions centred around a given set of objects in terms of Euclidian distance (Ju et al., 2011). In the simplest case, the objects are a finite amount of points in a plane called seeds. The polygonal regions provide detailed information about the neighbourhood surrounding the points. The Voronoï diagram can be built from single molecule coordinates and thus applied for cluster analysis of dSTORM data (Levet et al., 2015). Voronoï polygons are centred on individual localizations and their edges are equidistant from the two nearest seeds and perpendicular bisectors computed between them. Each polygon region is influenced by its corresponding seed, and characteristics such as polygon area or shape can be used to describe the molecular organization of the seeds (Levet et al., 2015). Regions with low molecular density are composed of large seeds whereas regions with higher molecular density are comprised of smaller and denser polygons. This is followed by the computing of an object segmentation process that selects polygons with parameters of interest in defined thresholds. Selected polygons are merged and object outlines defined. In 2015 the opensource software SR Tesseler

became available that allowed for automatic segmentation of biological data based on Voronoi tessellation (Levet et al., 2015). The software is time and cost efficient and user-friendly and was explored for the quantification of GLUT4 organization in the PM.

3.1.5.5 Density-based spatial clustering of applications with noise

The density-based spatial clustering of applications with noise (DBSCAN) has become one of the most common data clustering algorithms since its development in 1996 (Xu, 1996). Density-based clustering defines clusters as areas of higher density compared to the remainder of the data points (Figure 3.6). DBSCAN relies on a specific cluster model called "density-reachability" (Xu, 1996). Given a set of points it connects points with many nearby neighbours within certain distance thresholds. DBSCAN requires two parameters: the minimum amount of points needed to form a dense region (minPts) and epsilon (ϵ) determining the radius of a neighbourhood with respect to some point. Only points that satisfy a global density criterion are classified as clusters and clusters consist of these density-connected core points plus border points that lie within these points' range (Xu, 1996).

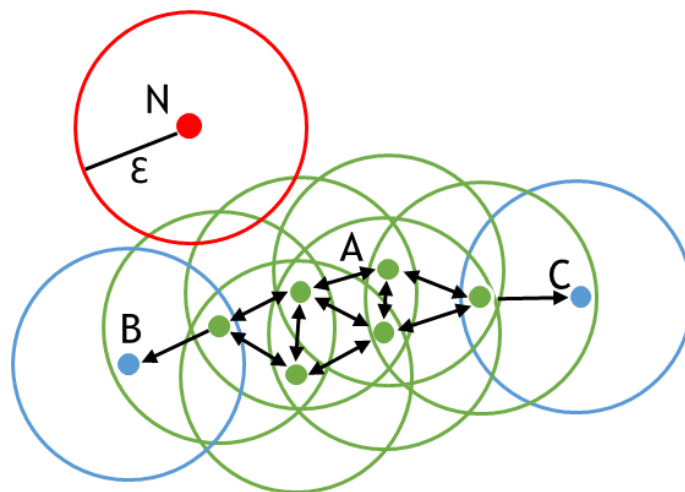


Figure 3.6 Schematic of density-based spatial clustering of applications with noise. DBSCAN divides datasets into n dimensions and forms n dimensional shapes around each point in the dataset and counts how many points fall within that shape. For this schematic minPts=4. The green points A are core points that contain at least 4 points (including the point itself) in their radius ϵ . DBSCAN counts this shape as a single cluster because each point is reachable from one another. The blue points B and C are border points because they lie within ϵ of core points. They are classed to belong to the cluster too. The red point N is an outlier because it is not a core point or directly reachable.

DBSCAN can identify arbitrary cluster shapes, requires minimum *a priori* parameter input and can be applied to big data sets and is therefore the most cited clustering algorithm in the scientific literature. Several extensions have been proposed over the years including hierarchical algorithm versions (Ankerst et al., 1999; Campello et al., 2013, 2015; Kriegel et al., 2011). Parametric algorithms summarize data with a set of

parameters of fixed size which makes their application less suited to complex data. Parametric models are fast and their results easily interpreted but they are constrained to a specific form and frequently the algorithms have a poor fit and do not match the underlying processes. HDBSCAN is a nonparametric algorithm that runs in Python and uses a density-based approach to find clusters making few implicit assumptions. HDBSCAN is an extension that performs DBSCAN over a range of ϵ values which allows to find clusters of varying densities and is more robust to parameter selection (Campello et al., 2015). We explored HDBSCAN as a method to evaluate GLUT4 clustering dynamics.

3.1.5.6 Spatial statistics

Spatstat is a package for analysing spatial point pattern data in the R programming language (Baddeley et al., 2016). The spatstat package supports a range of activities for instance exploratory data analysis, creation, manipulation and plotting of point patterns, parametric model fitting and simulation of point process models (Baddeley and Turner, 2005). Spatstat features a generic algorithm for fitting point process models to point pattern data. One of its biggest advantages is that the package can manage realistic data sets that are often inhomogeneous, contain sampling regions of arbitrary shape and additional covariate data (Baddeley and Turner, 2005). A big variety of empirical statistics are implemented in the spatstat package and can be generated and displayed. Ripley's K and L functions, the empty space function F, the nearest neighbour distance function G, pair correlation function g, and the J-function which expresses the combined estimates of the F and G functions (Baddeley et al., 2016).

Edge effects in spatial point pattern data are generated by choosing a defined sampling region which creates a bias by only studying points that fall into the specific region without knowing what occurs outside of the frame. There are several methods for correction of edge effects but the details of the techniques and their relative merits are not within the scope of this study. Spatstat automatically performs an edge correction and the developers state that the particular choice of edge correction technique is not critical (Baddeley et al., 2016). The summary functions generated by spatstat assume that a point process is stationary. In our experiment GLUT4 is sequestered intracellularly during the basal state and insulin stimulation results in translocation of the transporter to the PM leading to an increase in the total number of GLUT4. The 'inhomogeneous' versions of the summary functions have been proposed for the analysis of point pattern that are subject to special conditions with non-stationary underlying point processes, for instance when the intensity is gradually varying across the sampling window (Baddeley et al., 2016). Here we used the inhomogeneous versions of each of

the summary functions because GLUT4 clustering does not follow homogeneous patterns.

3.1.6 Hypothesis and Research Aims

The aim of this chapter was to find a reliable assay to study GLUT4 organization in the PM for application to several cell culture model systems. Using dSTORM to circumvent the resolution limit we hoped to be able to visualise individual GLUT4 molecules and quantify their spatial relationships in the PM as previously reported in the literature. Firstly, we aimed to establish dSTORM in our laboratory and optimised experimental procedures for instance sample preparation and imaging setup to achieve visualization of GLUT4 clusters comparable to the existing literature (Gao et al., 2017; Lizunov et al., 2013a; Stenkula et al., 2010). Secondly, we explored a wide range of cluster analysis methods to find the most suitable way to evaluate the molecular organization of GLUT4 and quantify clustering and dispersal dynamics in response to various stimuli using a single dataset to facilitate comparisons. We qualitatively assessed each computational cluster analysis method using the following predefined parameters: ease of use, requirement of *a priori* parameter input, time consumption, ease of interpretation of data output and information gained about GLUT4 clusters.

3.2 Results

3.2.1 The effects of sample preparation on super resolution image quality

One of the aims of this study was the visualization of GLUT4 at the single molecule level in 3T3-L1 adipocytes expressing HA-GLUT4-GFP. GLUT4 organization was investigated in this cell line previously (Gao et al., 2017) and thus it served as a control to optimise experimental protocols and obtain super resolution images of a comparable standard in this project. We explored a variety of protocols to establish dSTORM imaging in our laboratory. High-precision coverslips with an exceptionally accurate thickness ($170 \pm 5 \mu\text{m}$) were rinsed in 100 % ethanol and exposed to 30 min UV-light for sterilization prior to cell culture. Our first experiments had considerable background noise and imaging artefacts (data not shown) which were minimised by cleaning of coverslips by sonication in Decon 90™ Liquid Detergent, sodium hydroxide, ethanol and acetone. Furthermore, coverslips were exposed to 30 min of UV-light irradiation to eliminate autofluorescence originating from the coverslips themselves.

For staining we explored two commercially available anti-GFP VHH / nanobodies from Chromotek and Nanotag. For dSTORM experiments organic dyes with high photon yields, low on-off duty cycles and a large number of switching cycles are desirable. The Chromotek anti-GFP nanobody was coupled to Atto 647N which belongs to a new generation of fluorescent labels in the red spectral region ($\lambda_{\text{ex}} 644 \text{ nm}$; $\lambda_{\text{em}} 667 \text{ nm}$) with strong absorption, excellent quantum yield (0.65), high photostability and good solubility. We observed that the nanobody co-localized well with the GFP signal in the HA-GLUT4-GFP 3T3-L1 adipocytes at a concentration of 1:800 (Appendices Figure 8.1). The presence of dissolved oxygen is known to suppress blinking and fluorescent dyes. The solution to this problem is the addition of enzymatic oxygen-scavenging systems and chemicals that improve dye blinking. To make the Atto 647N dye photoswitch effectively during dSTORM experiments we used a buffer with the PCD/PCA oxygen scavenging system and COT, BME and MEA as reducing agents. We varied concentrations of the individual components until bright blinks were observed during dSTORM image acquisitions. Imaging buffers had to be prepared freshly before each imaging experiment which was very time consuming. Reconstructions calculated with the Image J plugin ThunderSTORM always showed a high amount of background noise and imaging artefacts so that the individual cells were not recognisable (Figure 3.7). We concluded that the use of Atto 647N in combination with an oxygen-scavenging buffer system did not yield satisfactory results for the visualization of individual GLUT4 molecules in 3T3-L1 adipocytes.

More recently nanobodies coupled to different fluorescent dyes have become commercially available. The Nanotag anti-GFP nanobody was coupled to Alexa Fluor 647 which proved to match all imaging criteria very well and has become the most used dSTORM dye during the past years. Alexa Fluor 647 is three times brighter than Atto 647N and this much brighter fluorescence signal results in improved single molecule localization. Another advantage is that the Chromotek nanobodies are randomly labelled with Atto 647N molecules and the Nanotag nanobodies have directly labelled sites with a choice of either 2 or 4 dye molecules per nanobody. At a concentration of 1:50 the nanobody co-localized well with the GFP signal but dSTORM imaging experiments required a dilution of 1:10 to yield satisfactory results (Appendices Figure 8.1). Figure 3.7 shows that the Nanotag anti-GFP nanobody diluted 1:10 resulted in reconstructions of 3T3-L1 cells with recognisable cell outlines. However, the images still had background noise and some imaging artefacts. The biggest advantage of using nanobodies is the less than 2 nm epitope-label displacement which reduces the linkage error significantly. However, the use of nanobodies resulted in lower quality reconstructions and GLUT4 molecule localization. This might be due to the fact that nanobodies bind to GFP and there are no nanobodies available that bind to the HA-tag. For the use of nanobodies samples always had to be subjected to permeabilization so that the GFP-tag is exposed. Staining for the GFP-tag will result in staining of GLUT4 in the PM and also in the vicinity of the PM, such as in vesicles undergoing endocytosis, or vesicles adjacent to but not yet fused with the PM. Only staining for the HA-tag in intact cells will result in targeting only GLUT4 molecules that have fused with the PM. Therefore, we decided to use a conjugated anti-HA antibody coupled to Alexa Fluor 647.

Next, we investigated the impact of fixation on super resolution microscopy results. We used 4 % PFA to fix our samples prior to experiments and also PFA supplemented with different concentrations of GA (Figure 3.8). Ripley's L function analysis of dSTORM images of cells fixed with PFA or PFA+GA yielded similar results. Therefore, applying GA as a supplement for stronger morphology preservation did not interfere with our imaging results. However, the manufacturer of the antibody that we finally decided to use for our imaging experiments advise against GA and therefore all samples were fixed with 4 % PFA.

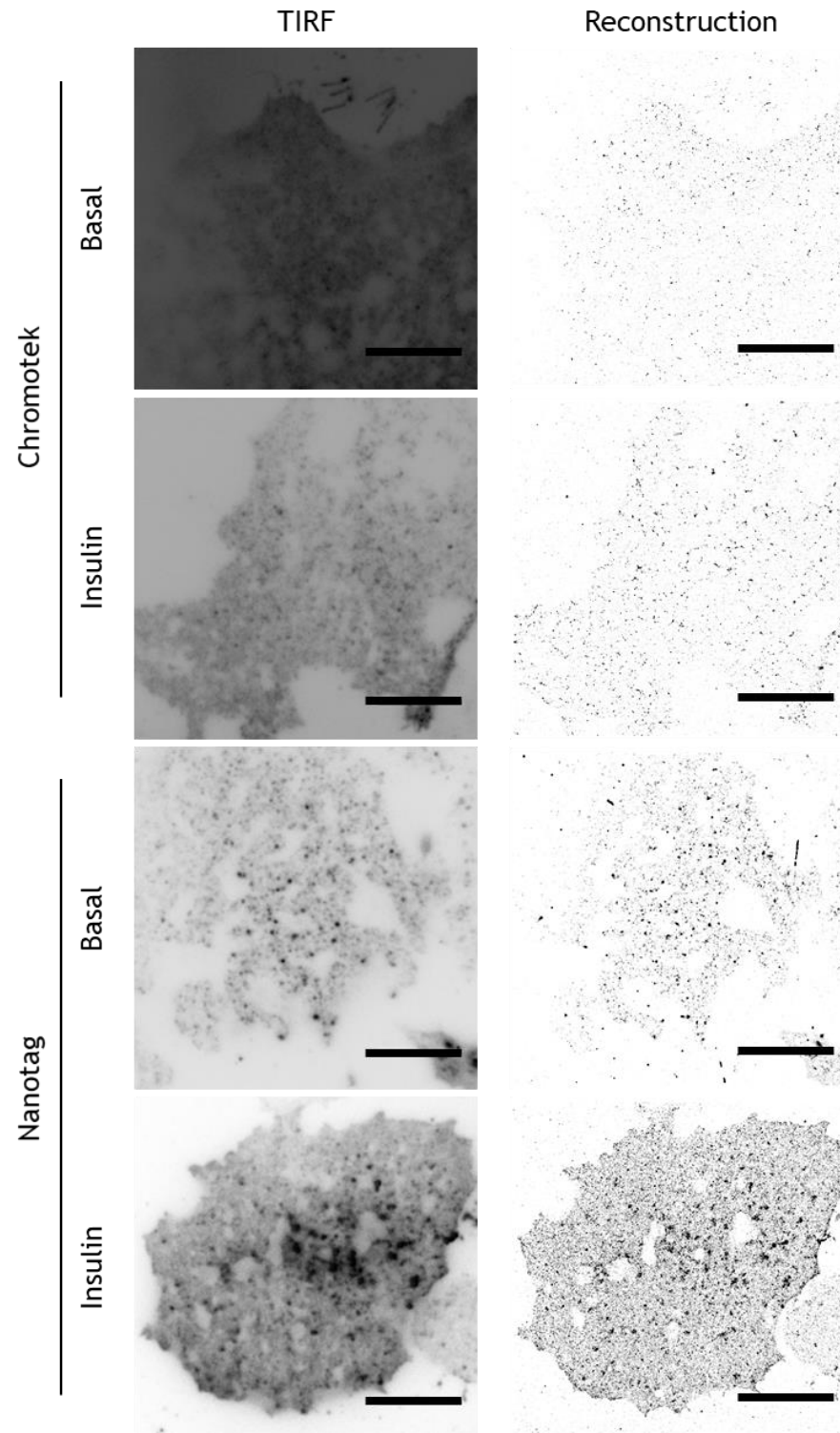


Figure 3.7 TIRF and STORM images of surface GLUT4-GFP in basal and insulin-stimulated 3T3-L1 adipocytes stained with anti-GFP nanobodies.

HA-GLUT4-GFP 3T3-L1 cells were serum-starved for 2 h prior and stimulated with 100 nM insulin for 20 min or left untreated. Cells were fixed and stained with two anti-GFP nanobodies (Chromotek/Nanotag as labelled) and images acquired on a Zeiss Elyra PS.1 (described in section 2.3). Reconstructions were calculated using ThunderSTORM. TIRF images (left) and scatterplots (right) of basal and insulin-stimulated 3T3-L1 adipocytes showing localizations of single GLUT4-GFP molecules. Scale bars 20 μm . This experiment was repeated several times with similar results.

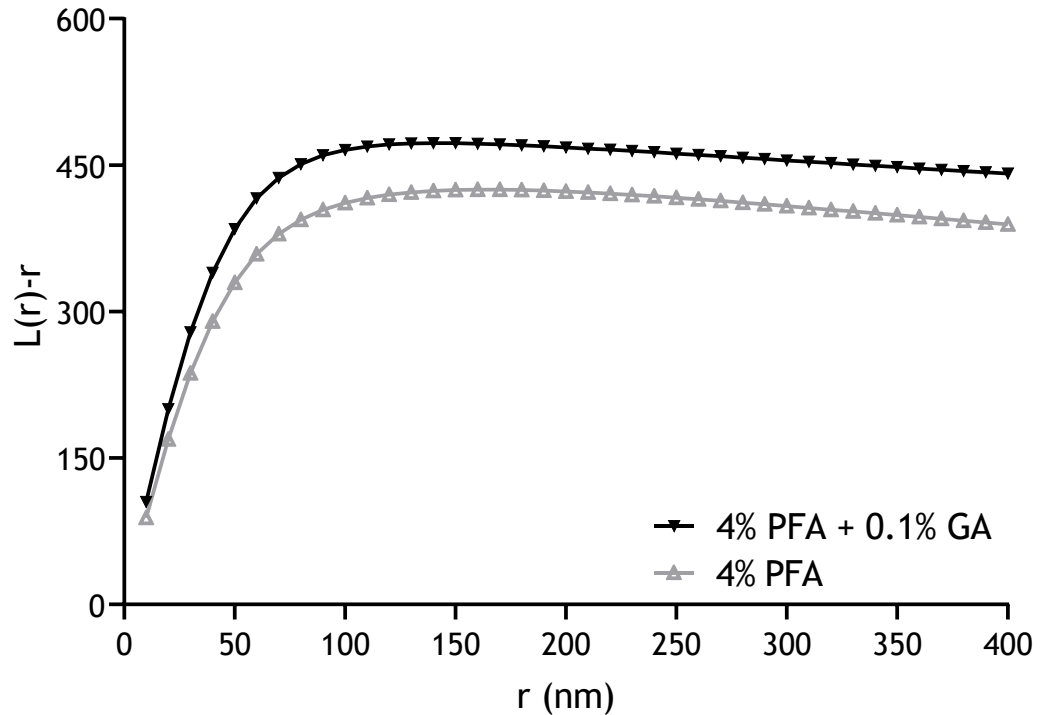


Figure 3.8 Ripley's L function analysis of the effect of fixation on GLUT4 molecule distribution in the PM of 3T3-L1 adipocytes.

Representative plot of Ripley's L function analysis of the clustering abilities of GLUT4 molecules in the PM of HA-GLUT4-GFP 3T3-L1 adipocytes. Cells were fixed with 4 % PFA or 4 % PFA supplemented with GA and stained for surface HA and dSTORM images acquired. GLUT4 molecule coordinates were obtained using ThunderSTORM and subjected to Ripley's L-function analysis using SR Tesseler with the minimum radius 10 nm, step radius 10 nm, and maximum radius 400 nm. $L(r)-r$ (y-axis) represents the clustering ability and r (x-axis) represents the radial scales of clustering. The presented data are means. The experiment was performed once for 4 % PFA (N=10 cells) and 4 % PFA + GA (N=10 cells) conditions. $p = 0.0047$ determined by two-tailed Student's t test.

3.2.2 Automated computing of Ripley's K function analysis for the study of GLUT4 clustering

We next aimed to investigate a range of cluster analysis methods for super resolution microscopy data and chose one representative 3T3-L1 adipocyte imaging data set to perform each method on (basal=8 cells; insulin=9 cells) to facilitate comparison. The first step of image analysis for SMLM was to localize each recorded emission of the individual GLUT4 single molecules and generate an output file that contains the complete x/y coordinates of millions of molecule localizations (van de Linde, 2019). There is a wide range of open source software available for localization and image reconstruction and we chose the Image J plug in ThunderSTORM for automated processing, analysis and visualization of our imaging data (Ovesný et al., 2014). ThunderSTORM is freely available and was chosen because it is heavily discussed in the community and cited in the literature as comprehensive and accurate. The imaging set was filtered to reduce background noise and imaging artefacts to include only high-

quality image reconstructions. This allowed careful evaluation of the results returned for each analysis method.

SR Tesseler is a framework for precise and automatic quantification of protein organization (Levet et al., 2015). The software is freely available and has a graphical user interface giving instant visual feedback of analysis results. SR Tesseler contains an algorithm for the automatic calculation of Ripley's L function. The experimentally obtained distribution of GLUT4 molecules is compared to a reference spatially uniform distribution. If for a given radius (r) the average number of localizations is bigger than the reference distribution the molecules are clustered (Levet et al., 2015). The software computes the value of r whilst maximising $L(r)$ and the minimum radius, step radius and maximum radius can be manipulated by the user (Figure 3.9). Figure 3.9 shows the results obtained by Ripley's L function analysis with SR Tesseler for basal and insulin-stimulated HA-GLUT4-GFP 3T3-L1 adipocytes stained with an anti-HA antibody. The graph shows that GLUT4 is more clustered in the basal condition and the molecules dispersed following insulin stimulation. This analysis method is very fast and allows to detect changes in GLUT4 clustering dynamics efficiently.

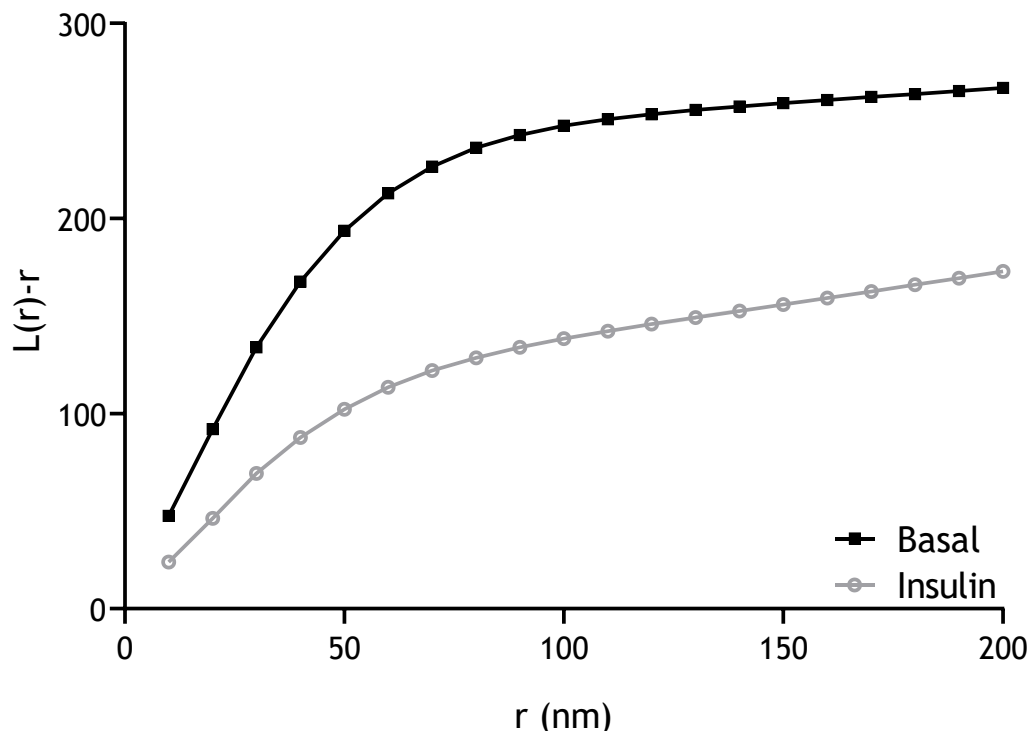


Figure 3.9 Ripley's L function analysis of GLUT4 clustering in basal and insulin-stimulated 3T3-L1 adipocytes.

Representative plot of Ripley's L function analysis of the clustering abilities of GLUT4 molecules in the PM of HA-GLUT4-GFP 3T3-L1 adipocytes. $L(r)-r$ (y-axis) represents the clustering ability and r (x-axis) represents the radial scales of clustering. The presented data are means. The experiment was performed once for basal ($N=10$ cells) and insulin-stimulated ($N=12$ cells) conditions. $p < 0.0001$ determined by two-tailed Student's t test.

However, the algorithm is very simplistic and lacks accuracy. Some limitations are that the experimental localizations are compared to a general reference distribution and inhomogeneous cluster distributions and background noise are confounding variables.

3.2.3 Bayesian cluster analysis

We investigated Bayesian cluster analysis as a method to quantify GLUT4 clusters in basal 3T3-L1 adipocytes and dispersal of the transporter in response to insulin. Four $3 \times 3 \mu\text{m}$ sized ROIs were chosen from each cell and the percentage of molecules in clusters, the number of clusters per ROI, the mean number of molecules per cluster, and the mean radius of clusters was determined for basal and insulin-stimulated cells. The individual data values of the obtained results were widely spread and frequency distribution bar graphs were prepared to give an overview of the distinct values (Figures 3.9). The majority of the ROIs chosen for basal cells showed that 50 % of molecules were found in clusters and fewer ROIs showed 30, 40, 60 or 70 % of molecules that were clustered (Figure 3.10 A). The majority of ROIs chosen from insulin-stimulated cells showed that 40 % of molecules were found in clusters and many of the other analysed ROIs showed 20 - 30 % of molecules in clusters indicating that GLUT4 molecules were less clustered and more dispersed after insulin-stimulation. In insulin-stimulated 3T3-L1 adipocytes the frequency distribution for the number of clusters per ROI was observed to shift towards the right indicating that more ROIs contained fewer clusters compared to basal cells (Figure 3.10 B). The average number of molecules per cluster was reduced after insulin stimulation suggesting that GLUT4 clusters decreased in size (Figure 3.10 C). This result was supported by the analysis of the mean cluster radius which was also reduced after insulin stimulation (Figure 3.10 D). Some ROIs showed clusters with very large radii after insulin stimulation which might be analysis artefacts and may represent dispersing clusters that appear larger because they are less compact. Descriptive statistics of the Bayesian cluster analysis frequency distribution are summarized in table 3.11. The Bayesian cluster analysis approach yielded results that enable quantification of insulin-stimulated GLUT4 dispersal in the PM of 3T3-L1 adipocytes as reported in the literature. A major drawback of this approach is that the analysis is slow and uses considerable computer time to process the data. We have also performed Bayesian cluster analysis in iPSC-CM (see Appendices section 8.2).

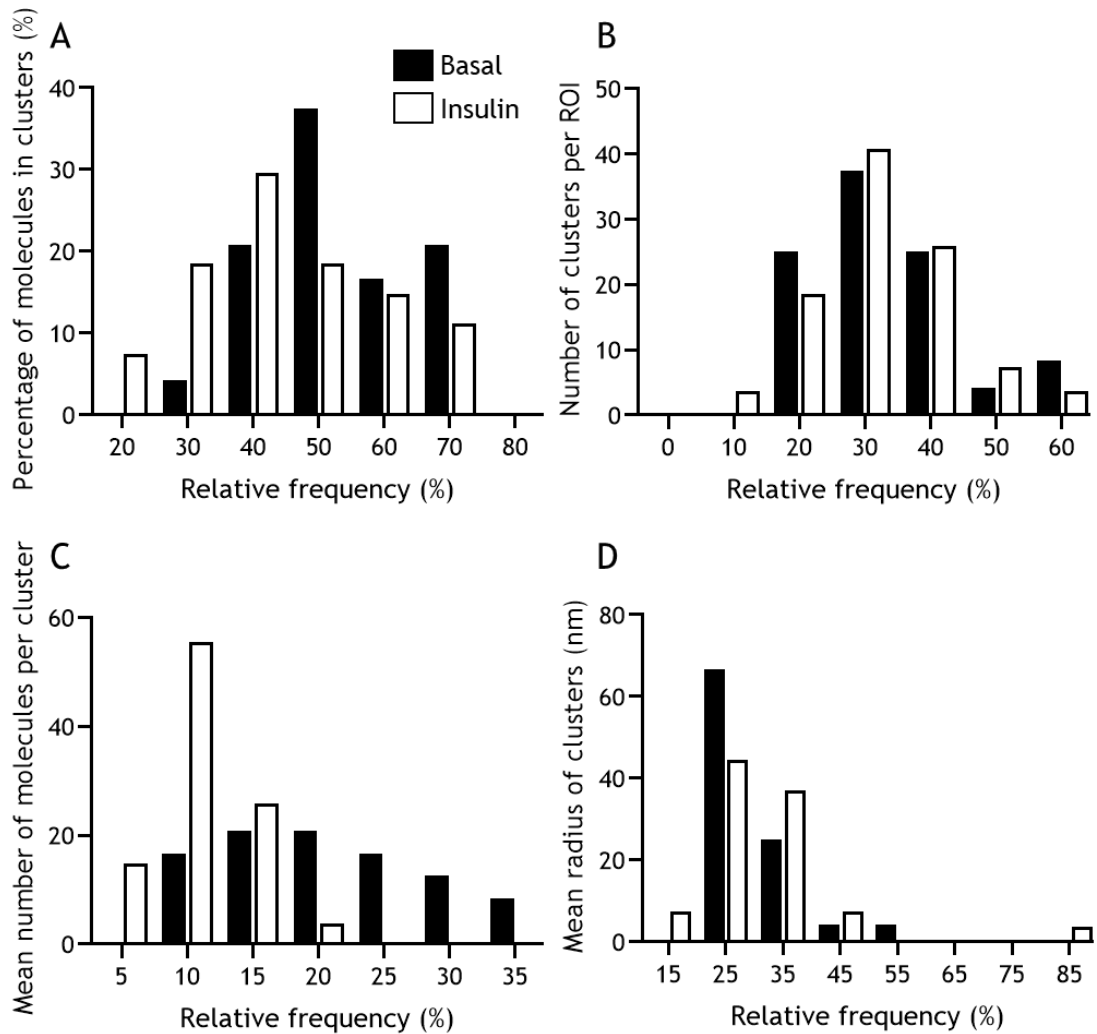


Figure 3.10 Bayesian Cluster Analysis of GLUT4 molecules in the PM of basal and insulin stimulated 3T3-L1 adipocytes.

GLUT4 molecule coordinates were subjected to Bayesian cluster analysis. Basal cells: black, $n = 8$; Insulin stimulated: white, $n = 9$. 4 ROIs of $3 \times 3 \mu\text{m}$ size per cell were analysed. Bar graphs shown are frequency distributions. (A) Percentage of molecules in clusters. (B) Number of clusters per ROI. (C) Mean number of molecules per cluster. (D) Mean radius of clusters. This experiment was repeated twice with similar results.

	A Basal	A Insulin	B Basal	B Insulin	C Basal	C Insulin	D Basal	D Insulin
Mean	32.58	31.3	52.82	44.73	20.56	21.26	29.70	31.65
STD	12.46	10.39	11.67	13.80	7.64	8.23	7.81	12.23
SEM	2.54	2.00	2.38	2.65	1.59	1.68	1.59	2.36
Low CI	27.31	27.18	47.89	39.27	17.25	17.78	26.40	26.81
Upper CI	37.84	35.41	57.75	50.19	23.86	24.74	33.00	36.49

Table 3.11 Summary of descriptive statistics for the Bayesian cluster analysis frequency distribution tables.

GLUT4 molecule coordinates were subjected to Bayesian cluster analysis. Basal cells n = 8; Insulin stimulated n = 9. 4 ROIs of 3x3 μm size per cell were analysed. This table is a summary of the frequency distribution bar graphs depicted in figure 3.10. (A) Percentage of molecules in clusters. (B) Number of clusters per ROI. (C) Mean number of molecules per cluster. (D) Mean radius of clusters. STD=Standard deviation, SEM=Standard error of the mean, Low CI=lower 95% confidence interval, Upper Ci= upper 95% confidence interval.

3.2.4 Cluster analysis with machine learning

Cluster analysis with machine learning (CAML) is a novel method of converting point pattern data into meaningful descriptions of clustering (Williamson et al., 2020). Keras is an open-source machine-learning framework for Python that was used to construct machine learning model configurations consisting of several layers defining the work flow and scripts used at different stages (Williamson et al., 2020). Firstly, we used a configured and trained model from the developers of CAML called KRIRK0. Training data were generated by a cell simulator and contained a broad range of different clustering scenarios with differences in overall point density, point density within each cluster, proportion of clustering and a maximum distance from a cluster seed (Williamson et al., 2020). KRIRK0 was trained using 500,000 points with an even mix of clustered and non-clustered values and completely spatially random data before validation against 100,000 different values. Performance was evaluated using novel simulated data and points were labelled accurately as clusters or non-clustered in 90 % of cases. Furthermore, we configured and trained a personally-specified model for GLUT4 clustering with the developers David Williamson and Dylan Owen (Kings College, London) named Q3VHAP. Q3VHAP was trained with input data from basal and insulin-stimulated cells labelled as clustered and non-clustered. We analysed our 3T3-L1 adipocyte data set with both models. A plot of the cluster area (nm^2) against points per cluster density distributions of the populations of basal and insulin-stimulated cells is shown in Figure 3.12. Most of the values for insulin-stimulated cells are within the lower ranges compared to basal

cells when evaluated by KRIRK0 (Figure 3.12 A). Q3VHAP analysis of the same data shows a different spread of the values (Figure 3.12 B). Values for cluster area and points per cluster are widely spread out for both basal and insulin-stimulated cells.

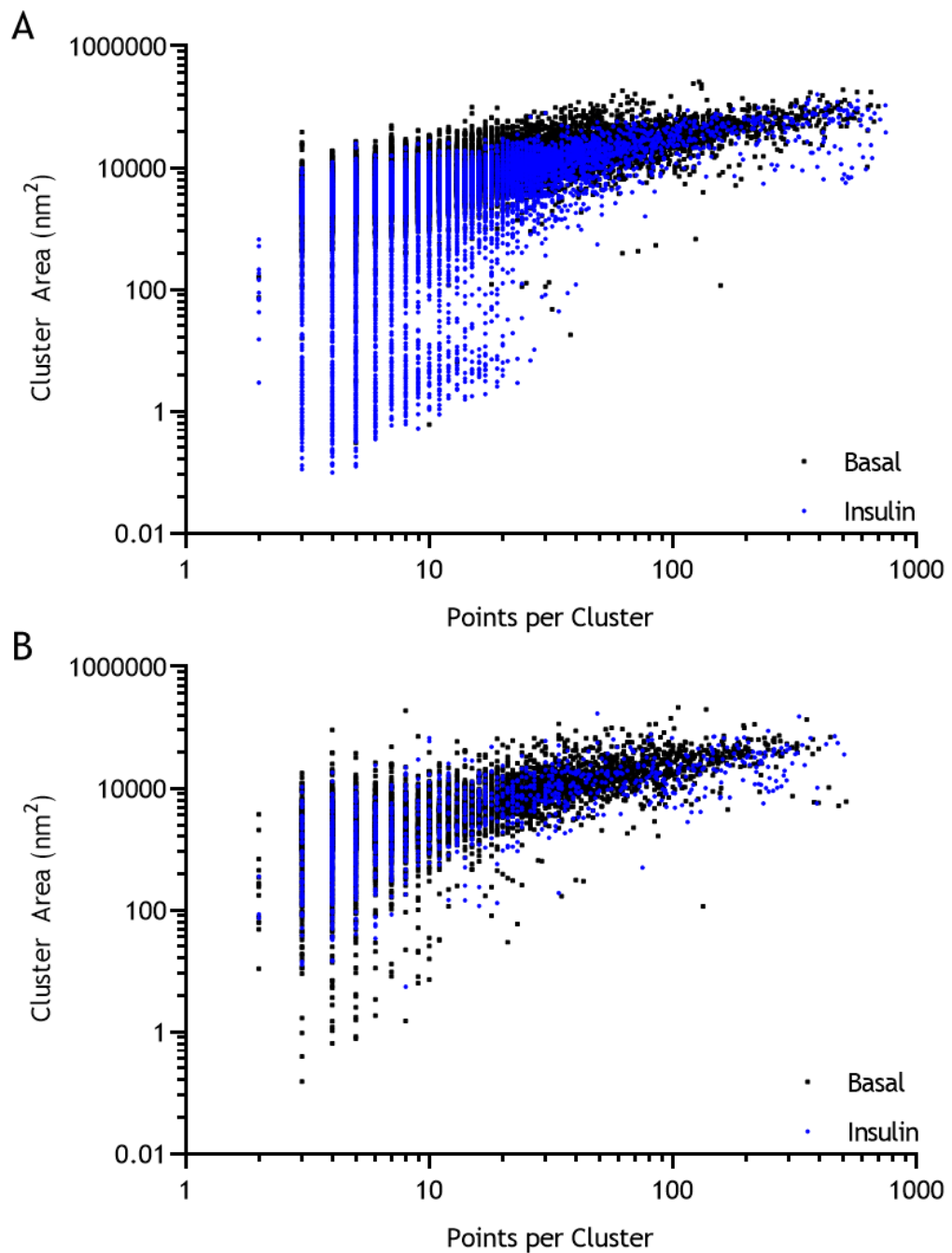


Figure 3.12 Cluster analysis with machine learning (CAML) to quantify GLUT4 clustering in 3T3-L1 adipocytes.

Cells were stimulated with 100 nM insulin for 20 min or left untreated before fixation and staining for surface HA. DSTORM images were acquired (see section 2.3) and reconstructions calculated using ThunderSTORM. Cluster analysis was performed with CAML. Representative plots of area of, and points contained by, individual clusters detected in HA-GLUT4-GFP 3T3-L1 which were either unstimulated (black circles) or stimulated with 100 nM insulin for 20 min (grey circles). (A) Cluster metrics from CAML (model KRIRK0) for dSTORM images. (B) Cluster metrics from CAML (model Q3VHAP) for dSTORM images.

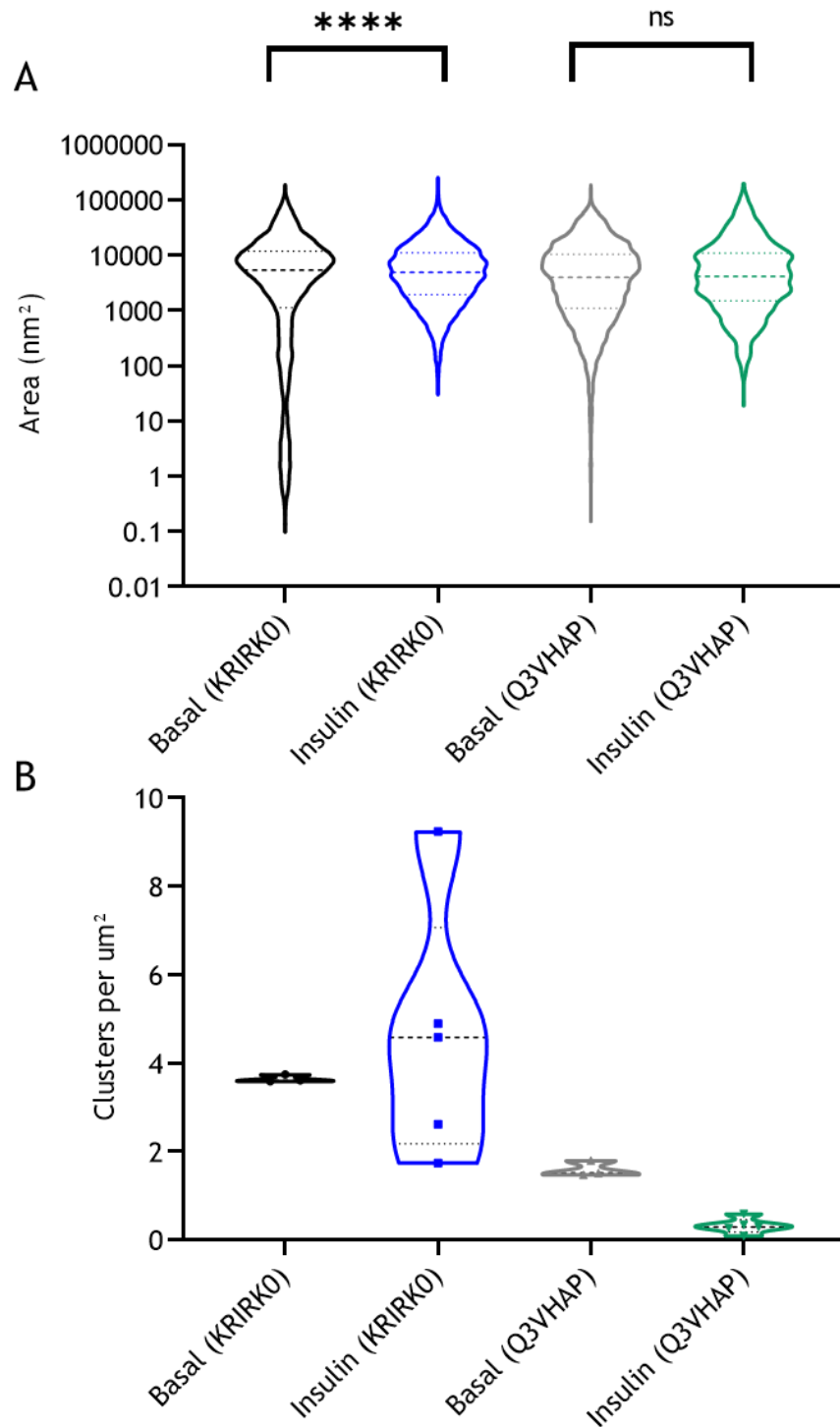


Figure 3.13 Cluster analysis with machine learning (CAML) to quantify GLUT4 clustering in 3T3-L1 adipocytes.

Cells were stimulated with 100 nM insulin for 20 min or left untreated before fixation and staining for surface HA. DSTORM images were acquired (see section 3.4) and reconstructions calculated using ThunderSTORM. Cluster analysis was performed with CAML. Representative plots of (A) cluster area (nm^2) and (B) clusters per μm^2 evaluated by two different CAML model configurations KRIRKO and Q3VHAP. $p < 0.0001$ (****); Dunn's multiple comparisons test between Basal (KRIRKO) vs. Insulin (KRIRKO).

Cluster area was significantly reduced and clusters per μm^2 were increased after insulin-stimulation compared to basal cells evaluated by KRIRK0 (Figure 3.13). When analysing the dataset with Q3VHAP cluster area increased after insulin stimulation clusters per μm^2 decreased (Figure 3.13).

3.2.5 Tessellation

Apart from containing a feature for the automatic calculation of Ripley's L function the SR Tesseler software is able to construct Voronoï diagrams from molecule localizations (Levet et al., 2015). Voronoï diagrams are useful for segmentation of dSTORM localizations and cluster analysis. For the construction of the Voronoï diagram and the following object segmentation the user needs to define parameters for instance density factors, minimum and maximum cluster area/number of localizations (Figure 3.14).

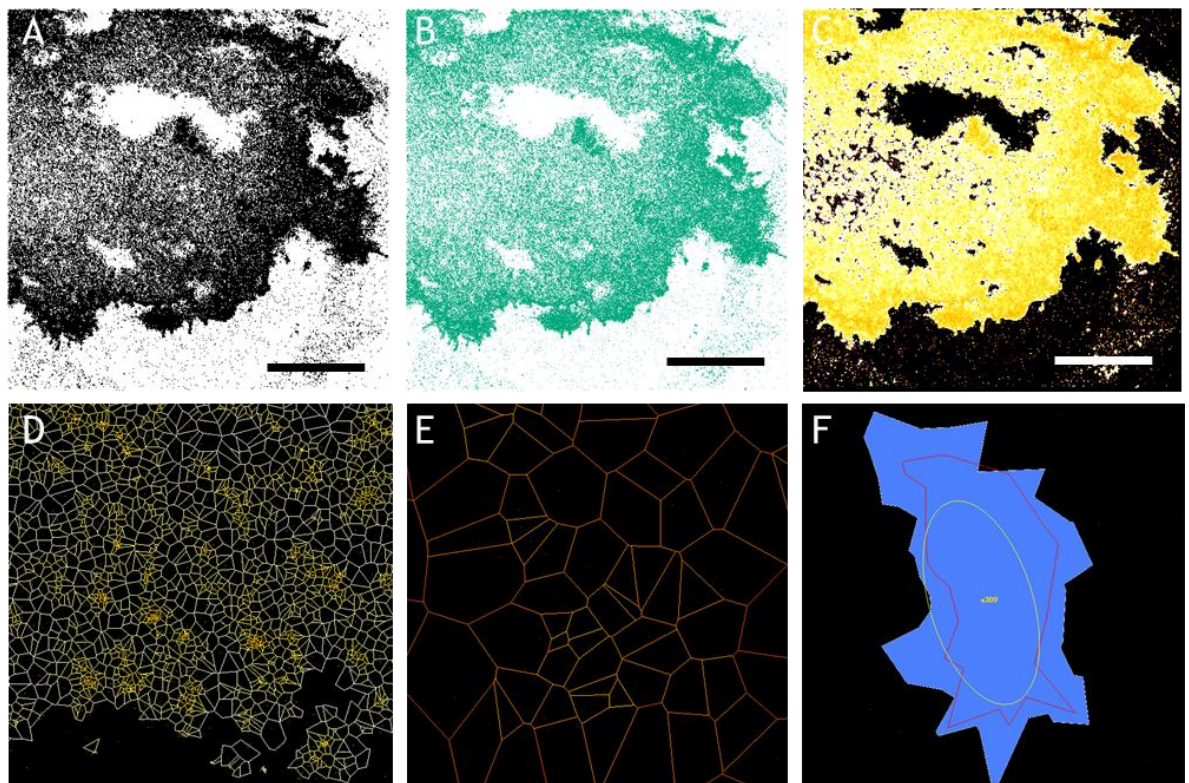


Figure 3.14 Creation of a Voronoï diagram followed by object segmentation with SR Tesseler for GLUT4 cluster analysis.

Cells were stimulated with 100 nM insulin for 20 min or left untreated before fixation and staining for surface HA. DSTORM images were acquired (see section 2.3) and reconstructions calculated using ThunderSTORM. GLUT4 coordinates were imported into SR Tesseler software. (A) Image of the imported GLUT4 coordinates of an insulin-stimulated 3T3-L1 cell in the graphical SR Tesseler user interface. (B) GLUT4 coordinates after an inbuilt filtering step. (C) Voronoï diagram created on the localizations of the cell shown in (A). (D) Magnification of the Voronoï diagram showing individual seeds surrounded by polygons. (E) Bigger magnification of polygons shown in (D). Dark orange colour depicts dense region with a cluster defined by neighbouring seeds. (F) Object segmentation of the cluster shown in (E). Scale bars 20 μm .

The advantage of this method is that the algorithm can create a Voronoi diagram of hundreds of thousands of localizations in a few seconds on a standard computer (Levet et al., 2015). Thus, clusters can be rapidly identified and further spatial point pattern analysis carried out quickly to quantify relationships between the identified clusters. This is discussed in 3.2.7 below.

3.2.6 Hierarchical density-based spatial clustering of applications with noise

Real world data sets often contain clusters of different sizes, with arbitrary shapes, with different densities, background noise and outliers. HDBSCAN identifies regions of the data that are denser than the surrounding space and considers these regions to be clusters with a higher probability. A cluster hierarchy is established on the probabilities of the underlying distributions resulting in robust identification of clusters of all shapes and sizes (Campello et al., 2013, 2015). The user can manipulate two variables known as minimum cluster size and minimum samples. Minimum cluster size describes the smallest size grouping that should be considered to form a cluster. The simplest explanation for what the parameter minimum samples describes is a measure of how conservative the clustering should be. The larger the value of minimum samples the more points will be considered to be noise and clusters will only be identified in progressively more dense areas. We explored HDBSCAN as a method to identify clusters of GLUT4 in dSTORM images of 3T3-L1 adipocytes. Firstly, we tried several parameters and observed how clustering changes in response (Appendices section 8.3). We chose minimum cluster size 5 and minimum samples 30 to get a good visualization of GLUT4 clustering in basal and insulin-stimulated 3T3-L1 adipocytes (Figure 3.15). In basal cells HDBSCAN identified several GLUT4 clusters and also dispersed GLUT4 molecules (Figure 3.15 A-C). After insulin-stimulation it can be observed that more GLUT4 clusters are visible in the PM and the presence of dispersed GLUT4 molecules is much higher (Figure 3.15 D-F). This result is in line with the current literature stating that about 50 % of GLUT4 molecules are clustered in the basal state and insulin stimulation induces an increase in GLUT4 clusters in the PM. Furthermore, insulin stimulation leads to the presence of significantly more GLUT4 monomers in the PM of 3T3-L1 adipocytes as seen in Figure 3.15 F. To quantify clusters identified through HDBSCAN further spatial point pattern analysis is necessary. This is discussed in 3.2.7 below.

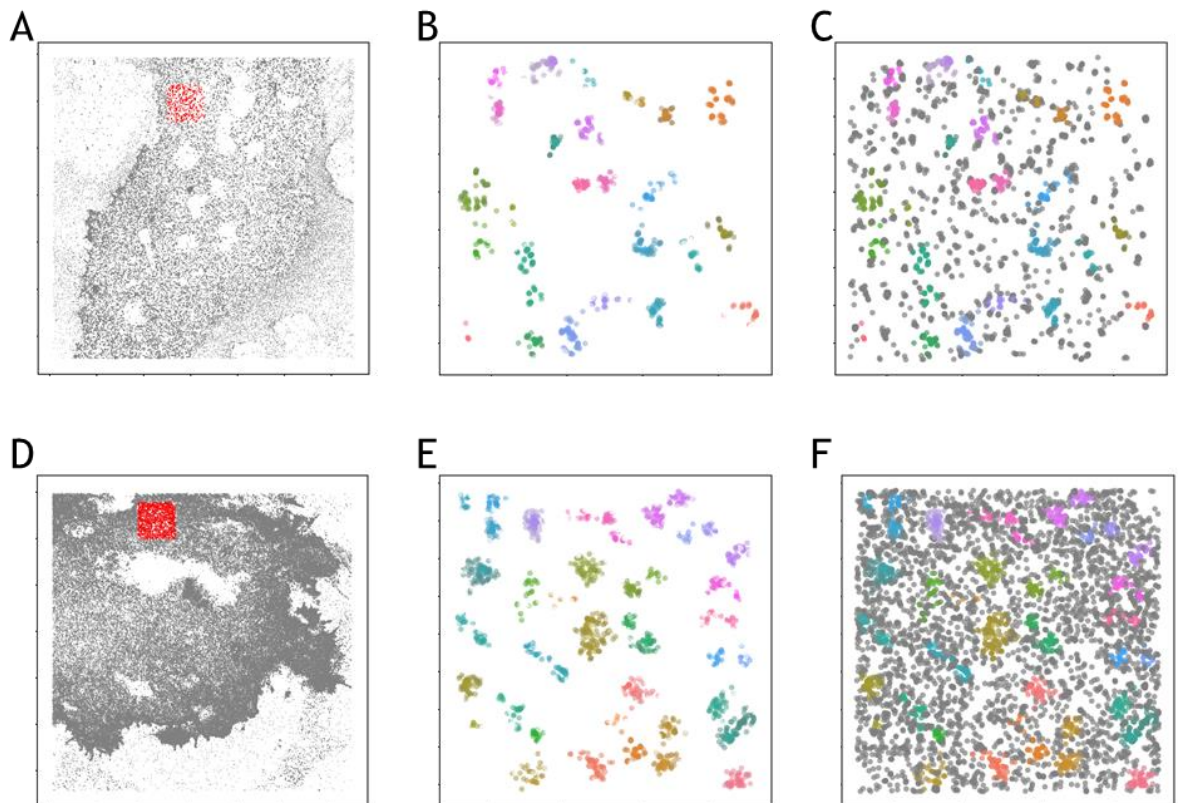


Figure 3.15 Hierarchical density-based spatial clustering of applications with noise analysis of basal and insulin-stimulated 3T3-L1 adipocytes.

Cells were stimulated with 100 nM insulin for 20 min or left untreated before fixation and staining for surface HA. DSTORM images were acquired (see section 3.4) and reconstructions calculated using ThunderSTORM. 6 ROI of $8\mu\text{m} \times 8\mu\text{m}$ were selected in Image J for each cell. GLUT4 molecule coordinates were processed using an HDBSCAN script written in house with Marie Cutiongco in Python. (A) GLUT4 molecule coordinates of a basal 3T3-L1 adipocyte. Image scale $51.2\ \mu\text{m}$. The red square highlights a representative ROI. (B) Coloured clusters identified in the chosen ROI of (A) by HDBSCAN $\text{min_cluster_size}=5$, $\text{min_samples}=30$. (C) Coloured clusters and grey non-clustered GLUT4 molecules in the ROI of (A). (D) GLUT4 molecule coordinates of an insulin-stimulated cell. Image scale $51.2\ \mu\text{m}$. (E) Colourful clusters identified in the chosen ROI of (D) by HDBSCAN. (F) Coloured clusters and grey non-clustered GLUT4 molecules in the ROI of (D).

3.2.7 Statistical analysis of spatial point pattern data in R

The spatstat package in R offers a number of options to statistically analyse spatial point pattern data. Here we explored some of them to quantify GLUT4 molecule distribution in the PM. The spatial analysis can be carried out using the raw localization data obtained from ThunderSTORM. However, localizations are numerous and some cells contain more than 1,000,000 localized GLUT4 molecules which limits time efficiency and requires considerable computational power. Therefore we also performed the analysis on previously identified clusters through the methods of tessellation and HDBSCAN. These two techniques already segment the data into clustered and non-clustered regions and reduce the size of the data set. The identified clusters can be

used to investigate spatial relationships time-efficiently with less computing power. Furthermore, ROI can be chosen to further reduce the data set.

Spatstat was used to compute an estimate for the edge-corrected inhomogeneous Ripley's L-function (Figure 3.16). It can be observed that the inhomogeneous L-function peaks at higher values for basal cells indicating a clustered distribution compared to insulin-stimulated cells. The same analysis was performed on ROI with conflicting results (Appendices 8.4).

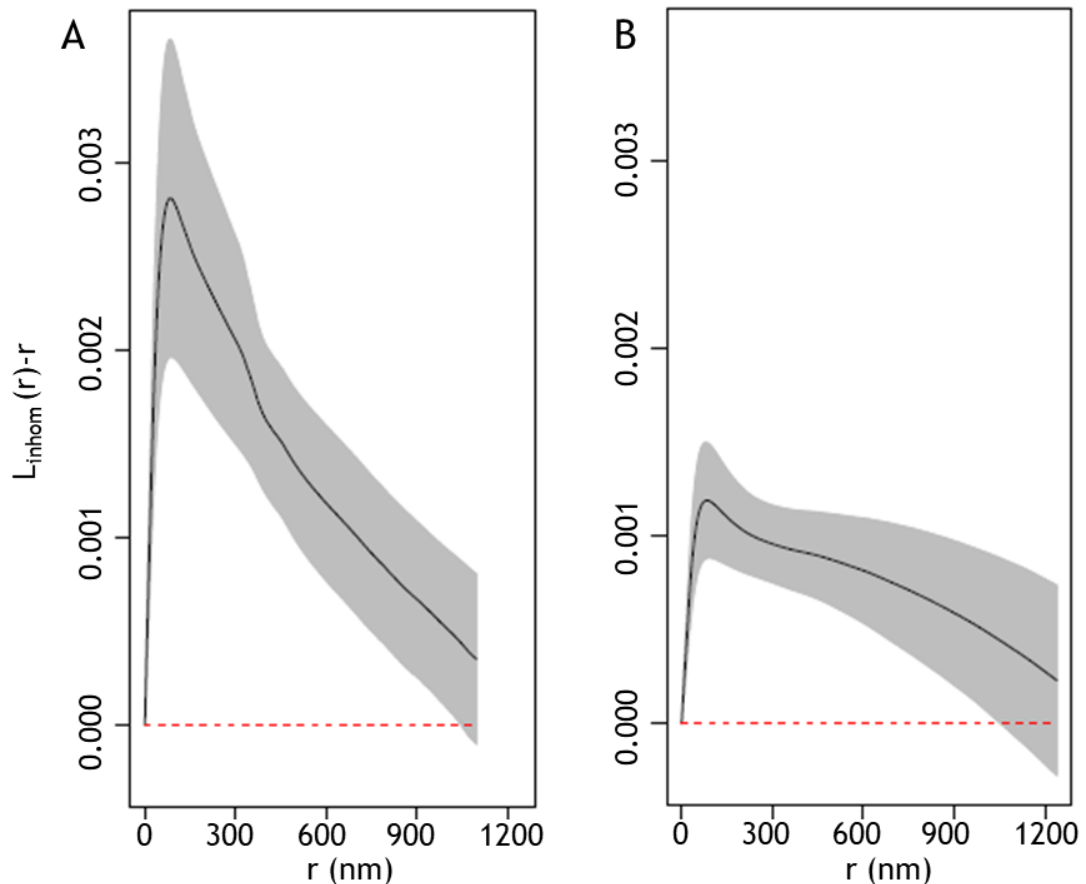


Figure 3.16 Ripley's inhomogeneous L function of GLUT4 molecule clustering in 3T3-L1 adipocytes using spatstat in R.

Representative plot of Ripley's inhomogeneous L function analysis of the clustering abilities of GLUT4 molecules in the PM of HA-GLUT4-GFP 3T3-L1 adipocytes. Cells were left untreated before fixation (panel A) or stimulated with 100 nM insulin for 20 min (panel B) then stained for surface HA. DSTORM images were acquired (see section 3.4) and reconstructions calculated using ThunderSTORM. GLUT4 coordinates were subjected to Ripley's inhomogeneous L function analysis using spatstat. The presented data are means (solid black lines). The grey shading indicates the global upper and lower envelopes which stand for the most extreme deviation from the theoretical L function at any distance r . The function is displayed as centred (red line). The experiment was performed for basal ($N=8$ cells) and insulin-stimulated ($N=9$ cells) conditions.

The edge-corrected inhomogeneous L-function generated with spatstat looks different than the one we received from the automatic analysis with SR Tesseler (Figure 3.9). The edge-corrected inhomogeneous L-function resembles more closely what has been

previously reported in the literature (Gao et al., 2017) and therefore this function describes GLUT4 clustering dynamics more accurately.

3.3 Discussion

3.3.1 Is my super resolution image a high-precision representation of the spatial organization of GLUT4 within the plasma membrane?

Super resolution microscopy has been one of the most significant developments in the life sciences over the last decades. The pace of innovation and accomplishment of this relatively young field has been very fast with novel methods for sample preparation, an innovative and breath-taking range of fluorescent labels, exciting new instruments and techniques for post-acquisition image analysis (Davis, 2009). However, many super resolution techniques rely on procedures that can result in the production of imaging artefacts leading to misinterpretation of biological information. One of the key questions always remains whether the experiments have been performed in such a way that the image reconstructions reflect underlying morphology and molecule locations accurately. Data quality assessment frequently relies on subjective comparison to prior published results or benchmarking against electron microscopy images.

One recent study quantitatively characterized the switching properties of 26 organic dyes and their impact on super resolution image quality (Dempsey et al., 2011). The two properties that are crucial to image quality are the amount of photons detected per switching event and its duty cycle which is the time a fluorophore is in the on state (Huang et al., 2010). Localization precision depends on the number of detected photons and therefore dyes with a high photon yield are desired. The maximum number of fluorophores that can be localized in an imaging area is inversely proportional to the duty cycle and therefore a low duty cycle is beneficial. Fluorescent dyes with high photon yield and low duty cycle result in high localization precision and molecule density and were used to successfully resolve an example structure (a nanoscopic ring-like object) (Dempsey et al., 2011). Experiments performed with dyes with low photon yields and/or high duty cycles obscured the ring-like structure. One central outcome of the study was that Alexa dyes were more suitable for dSTORM imaging than Atto dyes and that Alexa Fluor 647 requires thiol for photo switching (Dempsey et al., 2011). This result is in line with the results obtained in our study. We observed that we were unable to resolve the molecular distribution of GLUT4 using an anti-GFP nanobody coupled to Atto 647N. However, we were successful in obtaining high quality images with Alexa Fluor 647 as a label that closely resembled the super-resolved images of GLUT4 clustering in adipocytes previously published (Gao et al., 2017; Lizunov et al., 2013a).

In 2015 a study examined how different methods of sample preparation for SMLM affect clustering of the well-known mitochondrial import receptor subunit Tom20 (Whelan and Bell, 2015). It was reported that variations in fixative and antibody concentration alter the apparent clustering of Tom20 significantly. Fixation with a mixture of PFA and GA resulted in a lower degree of Tom20 clustering than previously reported. Staining with higher concentrations of primary and secondary antibody resulted in significantly enlarged clusters of Tom20 (Whelan and Bell, 2015). Another study investigated appropriate fixation and staining conditions using the transmembrane lymphatic vessel endothelial hyaluronan receptor 1 (LYVE-1) and CD44 as an example (Stanly et al., 2016). Even in resolution-limited confocal images it was apparent that different methods of fixation and immunostaining resulted in artefactual clustering of receptors in lymphatic endothelial cells. In this study use of PFA alone resulted in incomplete fixation and additional treatment with 0.2 % GA introduced reduction of mobility of the LYVE-1 (Stanly et al., 2016). Furthermore, using super-resolved STED imaging it was observed that fixation with PFA alone resulted in larger LYVE-1 cluster sizes. Immunostaining with a primary anti-LYVE-1 antibody and a secondary fluorescently tagged antibody resulted in a more punctate, clustered distribution of LYVE-1 indicative of antibody and not receptor clustering (Stanly et al., 2016). In our study fixation and staining procedures were optimised to reduce clustering image artefacts. Results from previous studies were taken into account and different mixtures of PFA and GA investigated for fixation of cells. Ultimately 4 % PFA had to be used for fixation in our study because we observed limitations in antibody binding. We also investigated antibodies and nanobodies for staining of GLUT4. The first anti-GFP nanobody coupled to Atto 647N did not have a high quantum yield or low duty cycle and therefore was not able to resolve the underlying distribution of GLUT4. Another anti-GFP nanobody coupled to Alexa Fluor 647 produced more high-quality images but we were unable to detect whether GLUT4 molecules had fused with the plasma membrane. GFP is not indicative of GLUT4 within the plasma membrane and no nanobodies are available for HA-staining. Therefore, we used a conjugated anti-HA Alexa Fluor 647 antibody for all future experiments.

3.3.2 Image analysis is key to single molecule localization

STORM provides sub-diffraction spatial high-resolution images and progress of the technique has been accompanied by the continuous and innovative development of image processing tools. In the last decade a large set of different data analysis tools and packages has become available (Sage et al., 2019; van de Linde, 2019). Packages are available in various programming languages for instance Python, Matlab, C, Java and IDL (Sage et al., 2019). In 1997 Image J was developed by Wayne Rasband as a platform-

independent and open-source image analysis software that allowed users to write their own macros to automate image processing steps or plugins to add new functionality (Schneider et al., 2012). Image J has a well organised graphical user interface and has become very popular with hundreds of downloadable plugins being available today.

In 2010 QuickPALM was the first available Image J plugin for single molecule localization (Henriques et al., 2010). The software detected the centroids of diffraction limited spots and was able to process image stacks in real time. Four years later ThunderSTORM was published with a variety of features (Ovesný et al., 2014). ThunderSTORM has many options for image filters and Gaussian fitting routines. The graphical user interface contains explanations on each of the settings making it the most comprehensive plugin (van de Linde, 2019). Furthermore, we studied PeakFit for localization of GLUT4 molecules which is part of the GDSC SMLM Image J plugin. Both ThunderSTORM and PeakFit performed very well in single molecule localization (Sage et al., 2019). Haar wavelet kernel (HAWK) processing is also available as a plugin in Image J (Marsh et al., 2018). HAWK is a preprocessing method for avoiding artefacts from high spot densities. The plugin separates fluorophores prior to localization and generates an image stack with increased frames with a lower density of emitters (Marsh et al., 2018). NanoJ-SQUIRREL is an image J-based analytical tool that has recently become available for the minimisation of super-resolution optical imaging artefacts (Culley et al., 2018). It compares diffraction-limited images and super resolution reconstructions and generates a quality score and quantitative map of super resolution defects. Researchers can obtain feedback on the quality of their super resolution images and optimise imaging parameters accordingly. The plug-in has been used in our study and parameters have been adjusted until quality scores were satisfactory (data not shown).

3.3.3 Ripley's K function and its derivatives for GLUT4 cluster analysis

Cluster analysis is the next step following single molecule localisation to understand the underlying spatial relationships of GLUT4 molecules. Cluster analysis is a multi-objective optimization problem and requires that many considerations have to be taken into account. In 2010 a study revealed that insulin stimulates GLUT4 dispersal within the PM of adipocytes for the first time using diffraction-limited TIRF microscopy (Stenkula et al., 2010). More recently GLUT4 dispersal was observed using dSTORM imaging and Ripley's K function for quantification of GLUT4 clusters (Gao et al., 2017). Ripley's K function has been employed in many fields including geography, economics and biomedical research (Ruan et al., 2019). Recently it has gained popularity for analysis of

protein clusters in the PM using SMLM. A study evaluated the accuracy of determining cluster size by Ripley's K function analysis in SMLM (Ruan et al., 2019). A modelled SMLM image was created with simulated clusters of 50 nm size. The average radius of clusters was calculated from the image using the point of maximum aggregation of $L(r)$ which equalled 63 nm. Thus the error was determined to be 25 %. It was concluded that Ripley's K function analysis may predict the cluster radius within a factor of 1.3 of actual radius but it was found to be essential to estimate the cluster radius by averaging data of at least ten cells (Ruan et al., 2019). Furthermore choosing small ROIs improved the accurate estimation of the cluster radius. In the following epidermal growth factor receptor (EGFR) clusters were successfully assessed in COS7 cells and cluster properties characterised with error normalization (Ruan et al., 2019).

Here we used an automated calculation of Ripley's K function with the open source software SR Tesseler (Figure 3.9). In the scientific community many laboratory groups seem to develop their own tools for the calculation of Ripley's K function and its derivatives. One paper studied the spatial organization of endoplasmic reticulum-plasma membrane (ER-PM) junctions in HeLa cells using PALM and SR Tesseler Ripley's K function analysis (Hsieh et al., 2017). The radius of maximal aggregation derived from Ripley's K function analysis was determined to estimate junctional size and the results were comparable to values obtained previously through electron microscopy (EM). Furthermore SR Tesseler was used to create Voronoï diagrams and segment ER-PM junctions. Morphological analysis of Voronoï diagrams resulted in values with equivalent diameter comparable to EM for junctional size (Hsieh et al., 2017). To further verify the results the group applied DBSCAN analysis to characterise ER-PM junctions and obtained similar results for the size of morphological features of the junctions after careful parameter selection (Hsieh et al., 2017). It was concluded that Ripley's K function analysis and object segmentation through tessellation with SR Tesseler made comparable estimations about the size of ER-PM junctions. Another study investigated the intracellular Ca^{2+} channels called inositol 1,4,5-trisphosphate receptors (IP3Rs) in the ER-PM in HeLa cells using dSTORM (Thillaiappan et al., 2017). Voronoï tessellation was successfully applied to study the distribution of EGFP-IP3R1s in endogenous clusters. SR Tesseler has also been applied to the study of plant plasma membrane protein dynamics (Gronnier et al., 2017) and G-protein-coupled receptors in pancreatic cancer cells (Jorand et al., 2016). The software developers validated their method on live neurons expressing GluA1-mEOS2, integrin- β 3-mEOS2 expressed in fibroblasts and tubulin-Alexa Fluor 647 in COS7 cells (Levet et al., 2015). SR Tesseler has been frequently cited in the literature and was the fastest approach we tested. The analysis provided a rapid and robust overview of GLUT4 clustering behaviour making it

particularly suitable for quick optimisation of experimental protocols. Ripley's K function analysis has a strong theoretical underpinning, but it does not generate key cluster descriptors for instance number of molecules per cluster or the number of clusters.

3.3.4 Machine learning for GLUT4 cluster analysis

Both the Bayesian cluster analysis approach and CAML were developed in the laboratory of Dylan Owen (Rubin-Delanchy et al., 2015; Williamson et al., 2020). The Bayesian cluster analysis proposes numerous cluster configurations and scores them against a generative model, which assumes Gaussian clusters overlaid on a spatially random background. In the following each point is scrambled by its localization precision (Rubin-Delanchy et al., 2015). The package generates interesting cluster descriptors such as the number of clusters, cluster radii and the percentage of molecules in clusters. These new Bayesian approaches were validated using simulated data sets and experimental data investigating T-cell synapses (Griffié et al., 2017, 2018). The accuracy of the Bayesian approach was very high and output results including key cluster descriptors were a great advantage. The biggest disadvantage of this method was that it was the most time-consuming taking 1-2 days for generating cluster proposals for four $3 \times 3 \mu\text{m}$ sized ROIs from one cell (Figure 3.10.1/2). The approach was declared suitable for analysis of final datasets but the length of the analysis was not realistic for optimisation of experimental protocols.

That is the reason why the same group explored a different approach of cluster analysis for SMLM datasets using a machine learning algorithm (Williamson et al., 2020).

Recently machine learning applications have become very popular in the field of biology and been used for classification of cellular images, genome analysis and drug discovery. A supervised machine-learning approach was developed to analyse large-scale datasets with inhomogeneities in clustering in a fast and accurate manner. CAML was downloaded with different models that were trained on a variety of simulated clustering data and then used to classify GLUT4 molecules into clustered or not clustered (Williamson et al., 2020). Cluster area, shape, and point-density were calculated using this method (Figure 3.12 and 13). The model has been designed carefully and performed cluster analysis with great accuracy shown through validation on simulated datasets and experimental datasets from T-cell synapses. Furthermore the approach has been compared to the Bayesian approach and performed with equal accuracy but much improved computation speed (Williamson et al., 2020). The code runs in Python and in principle the instructions and user interface are comprehensive. However, the code package was originally written for Linux and installing dependencies for the Python

environment on a Windows computer was not realistic for researchers without an extensive background in programming. A visit had to be arranged so that the developer of the machine learning approach installed the package on our Windows machines. Once the right dependencies were installed the analysis was carried out easily. The output contained numerous data files with tables which makes it difficult to summarise and interpret the obtained results. Our analysis showed that depending on the model that was used clustering was increased in basal or insulin-stimulated cells (Figure 3.12 and 13). We used a previously generated model and one that was personally trained that led to contradictory results. The previously generated model was generic and unable to identify GLUT4 clusters whereas the personally trained model performed better in identifying GLUT4 clusters in adipocytes specifically. CAML is advantageous because it does not need any parameter input prior to analysis. However, the machine learning approach only works if the model is trained appropriately and validated on datasets similar to the experimental ones.

In contrast to supervised machine learning algorithms unsupervised machine learning algorithms can classify data correctly based on finding some commonality in their features that can be used to predict classes of new data without training. HDBSCAN can classify clusters of different sizes, with arbitrary shapes, with different densities, background noise and outliers. After careful parameter selection HDSCAN produced striking visual representations of GLUT4 clusters in basal and insulin-stimulated cells (Figure 3.15). However, spatial analysis of previously identified HDBSCAN clusters yielded conflicting results. Parameter selection was very difficult for GLUT4 clusters because they have great inhomogeneity and different descriptions of GLUT4 clustering were found in the literature (Gao et al., 2017; Lizunov et al., 2013a; Stenkula et al., 2010).

3.3.5 Spatial point pattern analysis with Spatstat in R

The spatstat package in the R language provides the broadest range of capabilities for analysis of spatial point pattern data. The package comes with extensive documentation focused on researcher's practical needs explaining statistical principles, practicalities and helping with scientific interpretations of the results (Baddeley and Turner, 2005; Baddeley et al., 2016). This analysis was the most extensive performed as part of this chapter and was carried out in collaboration with Marie Cutiongco (University of Glasgow). Methods for spatial correlation such as the K and L function and of spacing such as the G, F and J function were used to quantify GLUT4 clustering dynamics (see Appendices). We performed spatial analysis on GLUT4 localizations, GLUT4 localizations with ROI, previously identified clusters by tessellation, previously identified clusters by

HDBSCAN and previously identified clusters by HDBSCAN with ROI (see Appendices). Spatial analysis on GLUT4 localizations themselves yielded an estimate of $L(r)$ (Figure 3.16) which was increased for basal cells indicative of GLUT4 clustering that was comparable to the results found in the literature (Gao et al., 2017) used as baseline validation in this study. This analysis was edge corrected and accounted for inhomogeneity in intensity caused by increased GLUT4 translocation in insulin-stimulated samples. Raw GLUT4 localizations were not confounded by pre-processing and definition of arbitrary clustering parameters. Both tessellation and HDBSCAN required parameter input prior to cluster analysis and these were selected by trial and error. However, a disadvantage of performing spatial statistics on raw localizations is that it is majorly time-consuming. Identifying clusters before spatial analysis greatly reduces datasets and thus computation times. Spatstat also offers the option to perform a variety of hypothesis tests and simulation envelopes. Normally spatial statistics summary functions are compared to an arbitrary Poisson process to determine whether data are clusters, random or dispersed. Simulation envelopes can be generated to assess the goodness-of-fit of a point process model to a particular set of point pattern data (Baddeley et al., 2016). We tried to perform Monte Carlo simulations to model the probability of different outcomes of $L(r)$ and $K(r)$. Unfortunately, the university has a traditional IT structure and no infrastructure to perform analysis of big data. As we performed our simulations they continuously crashed, and we were not able to obtain results with our small analysis computing clusters.

Table 3.16 gives an overview of all methods that were explored for GLUT4 cluster analysis in this chapter. Each method has its inherent advantages and disadvantages. We have carefully considered our experimental design and extensively optimised protocols to be able to investigate GLUT4 dispersal in the following chapters in a range of model cells. Here we compared visual representations of GLUT4 clustering with information available from the existing literature and successfully generated super-resolved images of GLUT4 clustering dynamics in adipocytes. Furthermore we have ruled out fixation artefacts and antibody linkage error to visualise GLUT4 clusters at molecular scale. A wide range of image processing methods has been applied for super resolution imaging and was qualitatively assessed using predefined parameters. Each cluster analysis approach yielded different information on spatial GLUT4 clustering dynamics. The most time-consuming methods Bayesian cluster analysis and cluster analysis with machine learning have provided detailed descriptors of GLUT4 clustering. However it is important to take into consideration that use of dSTORM as a method (fixation and use of antibodies) introduces problems for direct quantification of protein clusters (discussed in detail in section 7.2.1).

Method	Parameter input	Accuracy	Time consumption	Comprehensiveness	Data Interpretation
Ripley's K with SR Tesseler	Calculation of function on molecule localizations	Over simplified; no ROI; no corrections	Very fast analysis (min for each cell)	Easy to use without additional expertise	Easy interpretation of curve progression
Bayesian cluster analysis	Generating cluster proposals based on uncertainty value	Great accuracy in identifying clusters; on ROI	Very slow (1-2 days for each cell)	Very income-prehensive; code included errors	Data output as cluster metrics with ease of interpretation
Machine learning (CAML)	Supervised training to identify clusters	Accuracy comparable to Bayesian approach but highly sensitive to training	Slow (measuring nearest neighbour distances between points)	Difficult to use; code written for use in Linux not Windows	Data output are tables with numbers; difficult to group amount of data
Tessellation SR Tesseler	Creation of a Voronoi diagram for object segmentation	Needs arbitrary parameter input - not accurate	Fast	Easy to use	Data output needs to be analysed further
HDBSCAN in python	Density based approach	Needs arbitrary parameter input - not accurate	Fast	Easy to use but requires coding	Data output needs to be analysed further
Spatstat in R	Broad range of spatial statistics tools	Corrections and simulations with high Accuracy	Slow	Easy to use but requires coding	Generates a vast amount of data and comes with explanations

Table 3.16 Summary of approaches for cluster analysis of GLUT4 dispersal.

This table provides an overview of all analysis methods explored in this chapter to investigate insulin-stimulated GLUT4 dispersal in 3T3-L1 adipocytes.

We reached the conclusion that automated Ripley's K function analysis is a valuable tool to summarise spatial dependence over a range of distances and indicates changes in GLUT4 clustering dynamics. It has been the fastest approach we tested and hence will be used for future analysis throughout this thesis. In this chapter we have come to appreciate its limitations and these will be kept in mind for future experiments. The most accurate methods for cluster analysis were also the most time-consuming. These will be employed for analysis of a small subset of data for publication in peer-reviewed journals.

4. Plasma membrane GLUT4 dispersal in adipocytes

4.1 Introduction

4.1.1. Insulin-stimulated GLUT4 dispersal in adipocytes

Recently, experimental evidence has emerged that as well as stimulating GLUT4 translocation, insulin also affects the distribution of GLUT4 in the PM itself. Diffraction-limited TIRFM has been used to observe that in the basal state a majority of GLUT4 molecules appears in relatively stationary clusters whereas insulin stimulation promotes dispersal of the transporter into freely diffusible monomers in primary adipocytes (Stenkula et al., 2010).

The emergence of super resolution microscopy techniques (Betzig et al., 2006; Hess et al., 2006; Rust et al., 2006) followed by their application by cell biologists paved the way to obtain structural and dynamic information on length scales of vesicle trafficking and understand the relationship between the functional state of GLUT4 and its mobility in the PM. A follow-up study by the same group aimed to investigate GLUT4 cluster retention and the molecular dynamics guiding GLUT4 exchange in the PM and how these processes are affected by the presence of insulin (Lizunov et al., 2013a). Isolated adipocytes were transfected with a newly developed photo switchable HA-GLUT4-EOS probe that undergoes a shift from green to red fluorescence when illuminated with UV irradiation. Controlling UV exposure allowed activation of a small subset of expressed HA-GLUT4-EOS and to monitor vesicular movements within the PM through TIRFM. The results suggest that insulin had three effects that contributed to the shift of GLUT4 molecules within the PM from a clustered to a more dispersed state. Firstly it was found that insulin shifted the fraction of dispersed GLUT4 upon delivery, secondly insulin increased the dissociation of GLUT4 monomers from clusters and lastly insulin decreased the rate of GLUT4 endocytosis (Lizunov et al., 2013a). It was proposed that GLUT4 confinement in clusters is a novel kinetic mechanism of how insulin regulates glucose homeostasis.

Most recently, STORM was used to reveal the insulin-resistance-regulated reorganization of GLUT4 on the PM at the single molecule level (Gao et al., 2017). 3T3-L1 adipocytes stably expressing HA-GLUT4-GFP stained with an anti-HA antibody were imaged to analyse the spatial patterning of GLUT4 within the PM and how this is influenced by insulin resistance. Results showed that PM GLUT4 distribution was non-homogenous and that GLUT4 molecules formed clusters or monomers in normal 3T3-L1 adipocytes and in insulin-resistant adipocytes. In line with the previous studies Ripley's K function spatial

analysis revealed that GLUT4 molecules were less clustered after insulin stimulation (Gao et al., 2017). Insulin resistance in 3T3-L1 adipocytes increased GLUT4 clustering and insulin stimulation only led to small changes in clustering due to the reduced insulin sensitivity of the cells.

4.1.2 The effects of AMPK activation on adipocyte GLUT4 trafficking and dispersal

The enzyme 5' adenosine monophosphate-activated protein kinase (AMPK) is highly evolutionarily conserved from yeast to humans and plays a vital role in cellular energy homeostasis. AMPK can sense cellular energy levels and its activation largely results in increased glucose and fatty acid uptake and oxidation (Winder and Hardie, 1999). The enzyme is a heterotrimeric protein complex that consists of an α , a β , and a γ subunit with specific roles (Hardie et al., 1998). AMPK is able to sense shifts in the adenosine monophosphate (AMP): adenosine triphosphate (ATP) ratio through its γ subunit that contains four Cystathionine beta synthase (CBS) domains. These four CBS domains form two Bateman domains that act as binding sites for AMP. Once an AMP nucleotide binds to a Batman domain the binding affinity of the second Bateman domain increases. The binding of AMP to both Bateman domains of the γ subunit induces a conformational change resulting in the exposure of the catalytic domain located on the α subunit. AMPK becomes activated when phosphorylation occurs in this catalytic domain at the threonine-172 residue by an upstream AMPK kinase (Hawley et al., 1996). AMPK influences numerous metabolic processes and has been described to serve as a metabolic master switch (Winder and Hardie, 1999).

Numerous studies observed an increase in glucose uptake in response to insulin and contraction in skeletal muscle (Barnard and Youngren, 1992; Goodyear and Kahn, 1998; Hayashi et al., 1997). Both insulin-stimulated and contraction-induced glucose uptake are regulated by GLUT4 translocation from intracellular stores to the PM and the transverse tubules but use different signalling mechanisms and probably involve distinct GLUT4 intracellular pools (Richter and Hargreaves, 2013). AMPK is thought to be involved in contraction-stimulated glucose transport (Richter and Hargreaves, 2013).

5'-aminoimidazole-4-carboxamide ribonucleotide (AICAR) is a nucleoside that is taken up and accumulated inside the cell where it is converted to the monophosphorylated form ZMP (Figure 4.1). ZMP acts as an AMP analogue and directly activates AMPK by binding to the AMPK γ subunit resulting in activation of the complex as previously described (Kim et al., 2016). ZMP does not influence the intracellular AMP:ATP ratio or oxygen uptake like many other AMPK activators (Corton et al., 1995). ZMP has a lower

potency for the γ subunit compared to AMP resulting in requirement of high effective concentrations (Gruzman et al., 2009). As an AMP analog AICAR/ZMP activates other AMP-dependent enzymes for instance fructose-1,6-bisphosphatase, 6-phosphofructo-2-kinase and glycogen phosphorylase that may result in off-target effects (Gruzman et al., 2009). In animal models of diabetes and diabetic patients AICAR treatment was reported to exhibit several antidiabetic effects (Kim et al., 2016). Other highly specific AMPK activators include A-769662 and compound 911. However these compounds have a molecular mechanism of AMPK activation that is not fully elucidated (Gruzman et al., 2009). AMPK activation via AICAR mimics contraction signalling in skeletal muscle experimental systems and has a dual effect to stimulate glucose transport and increase fatty acid oxidation (Merrill et al., 1997). It was hypothesised that AMPK activation following the increasing energy demands of contracting muscles increases availability of fatty acids and glucose (Merrill et al., 1997). Ongoing studies within the field provided further evidence that AICAR stimulates glucose uptake into skeletal muscle in the absence of insulin and that this effect is additive with insulin stimulation (Hayashi et al., 1998). Moreover it was established that skeletal muscle glucose uptake stimulated by AICAR is caused directly by translocation of GLUT4 to the PM (Kurth-Kraczek et al., 1999).

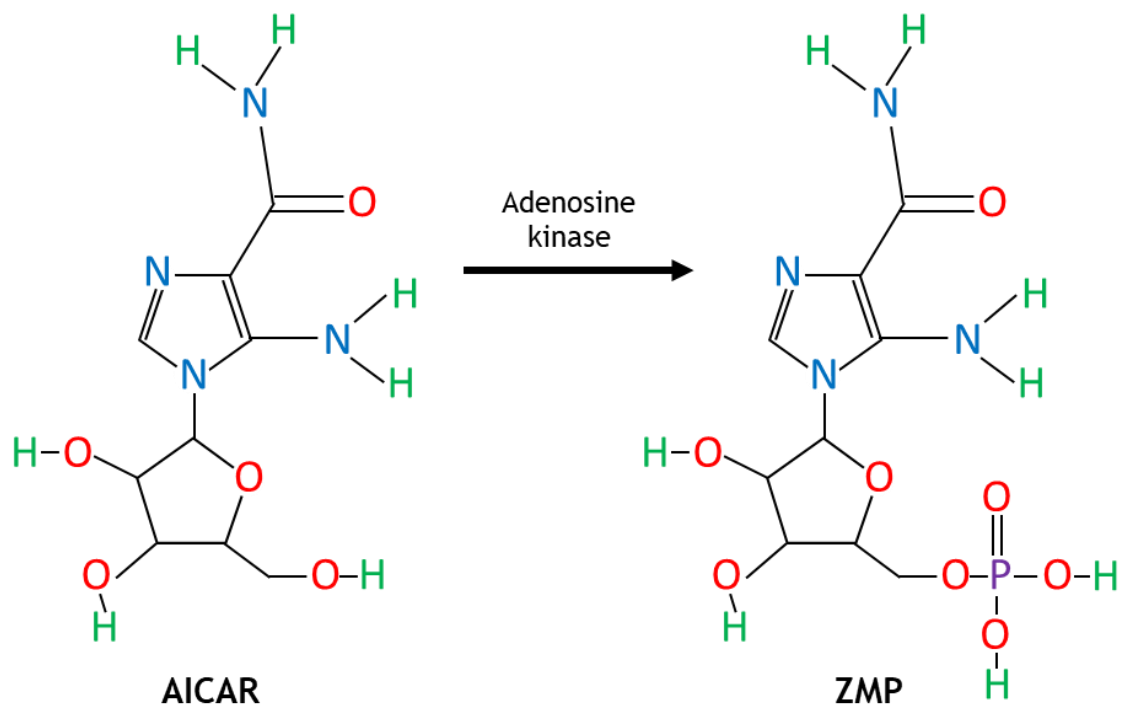


Figure 4.1 Depiction of the chemical structure of 5-Aminoimidazole-4-carboxamide ribonucleotide (AICAR) and its mechanism of action.

AICAR is taken up into cells by adenosine transporters and phosphorylated by adenosine kinase to AICAR monophosphate (ZMP). ZMP is an AMP-mimetic that binds to site 3 on the AMPK γ subunit similarly to AMP and allosterically activates the entire AMPK complex.

The role of the AMPK cascade and effects of AICAR on adipocyte glucose uptake remained undefined for numerous years. A study conducted in 2000 was the first to report that AICAR stimulates AMPK activity in a time- and dose-dependent manner in 3T3-L1 adipocytes and increased glucose transport by 2-fold (Salt et al., 2000). Surprisingly it was reported that AICAR reduced insulin-stimulated glucose transport and also inhibited insulin-stimulated GLUT4 translocation. In contrast to skeletal muscle in which AMPK activation stimulates glucose uptake to provide ATP as a fuel in adipocytes AMPK activation inhibits insulin-stimulated glucose uptake to conserve ATP in scenarios of cellular stress (Salt et al., 2000). The observation that AMPK activation has different effects on glucose uptake in skeletal muscle and adipose tissues led to the hypothesis that the mode of AMPK activation must involve different signalling pathways or modulation of the same pathway. One of the aims of this chapter is to ascertain whether AMPK activation modulates the dispersal GLUT4 translocation within the PM.

4.1.3 The effects of cholesterol depletion on adipocyte GLUT4 trafficking and dispersal

Cholesterol is a type of lipid that is a vital structural component of all cell membranes and required for membrane formation and maintenance. Cholesterol composes invaginated caveolae and clathrin-coated pits that play roles in endocytosis and thus cholesterol itself functions in intracellular transport and cell signalling (Hailstones et al., 1998). Investigations of the function of cholesterol in endocytosis frequently use methyl- β -cyclodextrin to deplete the PM from cholesterol and observe the resulting effect (Hailstones et al., 1998; Parpal et al., 2001; Shapira et al., 2018). Using immunogold electron microscopy and immunofluorescence microscopy it was observed that insulin receptors are localised in cholesterol-rich regions of the PM in isolated rat adipocytes (Gustavsson et al., 1999). Cholesterol removal with cholesterol oxidase or β -cyclodextrin was observed to attenuate insulin receptor signalling and replenishment with exogenous cholesterol reversed the effect of the observed insulin signalling attenuation in adipocytes (Gustavsson et al., 1999). Furthermore, cholesterol depletion with β -cyclodextrin was observed to decrease insulin-stimulated glucose transport in 3T3-L1 and isolated rat adipocytes (Parpal et al., 2001). It was shown that cholesterol depletion had neither an effect on the access to or affinity of insulin for its receptor nor the autophosphorylation of the receptor itself. But it was observed that cholesterol depletion inhibited tyrosine phosphorylation of insulin receptor substrate-1 and protein kinase B and therefore affected downstream targets of insulin signalling (Parpal et al., 2001); similar results were reported by others (Nystrom et al., 1999). Confocal fluorescence microscopy revealed that cholesterol depletion resulted in an insulin-

independent rise in the amount of GLUT4 within the PM of 3T3-L1 adipocytes (Shigematsu et al., 2003). Cholesterol replenishment reversed the observed effect. It was reported that GLUT4 endocytosis was impaired and that the rise in surface GLUT4 was due to decreased GLUT4 endocytosis (Shigematsu et al., 2003). Taken together these findings suggest that there is a relationship between cholesterol, insulin signalling and GLUT4 translocation and further studies are needed for characterisation.

4.1.4 EFR3 and its potential role in GLUT4 clustering

The EFR3 membrane protein is conserved from yeast to mammals and a genetic screen of the *Saccharomyces cerevisiae* yeast strain has shown that the protein potentially plays a role in regulation of GLUT4 within the PM (Wieczorke et al., 2003). In *Saccharomyces cerevisiae* EFR3 has been found to bind to YPPI and form a complex that is required to recruit Stt4 to the PM to form phosphoinositide kinase (PIK) clusters (Baird et al., 2008; Wu et al., 2014). Specifically EFR3 is thought to be the membrane-anchoring component that associates with the PM through palmitoylation of its N-terminus (Baird et al., 2008; Wu et al., 2014). The mammalian homologue Stt4 is phosphatidylinositol 4-kinase type III α (PI4KIII α) which functions in the metabolic conversion of PIP₂ (Nakatsu et al., 2012). Phosphatidylinositols are glycerophospholipids that are phosphorylated at different sites and play numerous fundamental roles in several signalling pathways in the trans-Golgi network, endosomes, and the PM (Falkenburger et al., 2010). PI3K is found in late endosomes and plays a role in insulin signalling and PI4K is found in the *trans*-Golgi network and GSC where it catalyses the formation of PI4P and generates PI4P pools in the PM (Tan and Brill, 2014).

Previous work in our laboratory has found that overexpression of EFR3 results in increased GLUT4 translocation and glucose uptake in 3T3-L1 adipocytes and that siRNA targeting EFR3 inhibited insulin-stimulated glucose transport by ~80% (Laidlaw, 2018). Inhibition of PI4KIII α with phenylarsine oxide or knockdown of PI4KIII α with siRNA was found to inhibit glucose uptake indicating that the observed effect of EFR3 overexpression is consistent with effects via PI4KIII α (Laidlaw, 2018). Because PI4K is PM associated, it was hypothesised that insulin signalling has an effect on the EFR3 machinery by activating PI4KIII α in adipocytes. We hypothesise that activation of PI4KIII α phosphorylates PI in the PM and PI4P is formed and as a result GLUT4 clusters are dispersed within the PM. This process prevents GLUT4 from being endocytosed and thus increases glucose uptake. To further test this hypothesis electroporation was used to knock down EFR3 in 3T3-L1 adipocytes (Laidlaw, 2018; Morris, 2020). STORM imaging experiments and Ripley's K-function cluster analysis with SR Tessler showed that insulin-stimulated GLUT4 dispersal was inhibited by EFR3 knock down in 3T3-L1

adipocytes (Morris, 2020). The previously chosen analysis method using SR Tesseler is easy and fast but to publish these findings we have re-analysed the existing EFR3 knock out STORM imaging data with the thorough but time-consuming spatial point pattern analysis tool spatstat (described in sections 3.1.4.6 and 3.2.7).

4.1.5 HeLa cells as a tool to investigate GLUT4 trafficking

Because of difficulties associated with over-expression of genes in primary cells it has proven challenging to study GLUT4 trafficking *in vivo* and in human tissues (Bryant and Gould, 2020). A prevalent view in the field is that insulin-stimulated GLUT4 translocation is a property that is highly specific to adipose and muscle tissues and that the larger an observed insulin response in a model system the more physiologically relevant it is (Bryant and Gould, 2020). Studies conducted in primary rat adipocytes and the murine 3T3-L1 cell line report 10 to 30-fold increases in GLUT4 translocation and glucose uptake in response to insulin stimulation which represents a huge magnitude of change (Sato et al., 1993; Yang et al., 1996). The argument that the larger the insulin response of an experimental model the more physiologically relevant it is may be flawed and does not necessarily correlate with our current knowledge of human glucose metabolism (Bryant and Gould, 2020). Studies using human adipocytes and muscles frequently report insulin-stimulated changes in GLUT4 translocation of 2 to 3-fold much smaller effects compared to rodent adipocytes (Kashiwagi et al., 1983; Kozka et al., 1995).

Heterologous expression of GLUT4 can be achieved in a range of model cell systems. Studies of GLUT4 trafficking in *Saccharomyces cerevisiae* revealed that this model organism shares several common features of GLUT4 trafficking with adipose and muscle tissues (Kasahara and Kasahara, 1997; Shewan et al., 2013; Wieczorke et al., 2003). GLUT4 is sequestered intracellularly in yeast and can be mobilised to the surface in response to an environmental cue (Shewan et al., 2013). Furthermore the same molecular machinery regulating GLUT4 trafficking exists in yeast and other eukaryotic cells indicating that the proteins regulating GLUT4 developed before the evolution of GLUT4 itself. Fibroblasts, HeLa and CHO cells were reported to translocate GLUT4 to the PM in response to insulin stimulation further supporting that GLUT4 trafficking is not limited to insulin-responsive tissues in the classical sense (Haga et al., 2011; Lampson et al., 2000).

Recently a study characterised GLUT4 trafficking in HeLa cells expressing an HA-GLUT4-GFP construct compared to 3T3-L1 adipocytes (Morris et al., 2020). This study was partly carried out in our lab and it was shown that insulin stimulation induced

translocation of HA-GLUT4-GFP in both cell types with similar kinetics and with activation of a similar trafficking machinery. However the observed GLUT4 translocation effect was in order of 2 to 3-fold and thus significantly smaller than the effect observed in adipocytes of magnitude 10 to 20-fold (Morris et al., 2020). The machinery and capacity of HeLa cells to traffic GLUT4 is not equally as developed as in adipose tissues but their response seems more similar to the response observed in human tissues. On this basis, we propose that HeLa cells are a valid, experimentally tractable human model system (Bryant and Gould, 2020) to further our understanding of GLUT4 trafficking and PM dispersal.

4.1.6 Hypothesis and research aims

The aim of this chapter was to investigate and quantify surface GLUT4 spatial patterning at the single molecule level in adipocytes using dSTORM. We aimed to optimise dSTORM imaging in our lab and hypothesised that insulin stimulation would shift GLUT4 distribution in the PM from a clustered to a more dispersed state in line with the current literature.

Subsequently we aimed to investigate some of the underlying molecular mechanisms of the process in particular the relationship between AMPK activation and GLUT4 clustering. We hypothesised that AMPK activation attenuates insulin-stimulated glucose transport by attenuating insulin-stimulated GLUT4 dispersal.

We sought to ascertain whether cholesterol depletion using methyl- β -cyclodextrin modulated GLUT4 dispersal in the PM.

Finally, given the similarities between GLUT4 trafficking in adipocytes and HeLa cells, we aimed to investigate GLUT4 dispersal in response to insulin stimulation in HeLa cells for the first time.

4.2 Results

4.2.1 Insulin regulates GLUT4 dispersal on the plasma membrane of adipocytes

As a starting point for our study we assessed GLUT4 protein expression and insulin sensitivity of differentiated 3T3-L1 adipocytes from our lab by western immunoblotting (Figure 4.2). 3T3-L1 cells demonstrated a high endogenous expression of GLUT4 protein seen in figure 4.2 A. They also showed insulin-stimulated phosphorylation of Akt as expected (Tan et al., 2015), consistent with these cells exhibiting a robust insulin response.

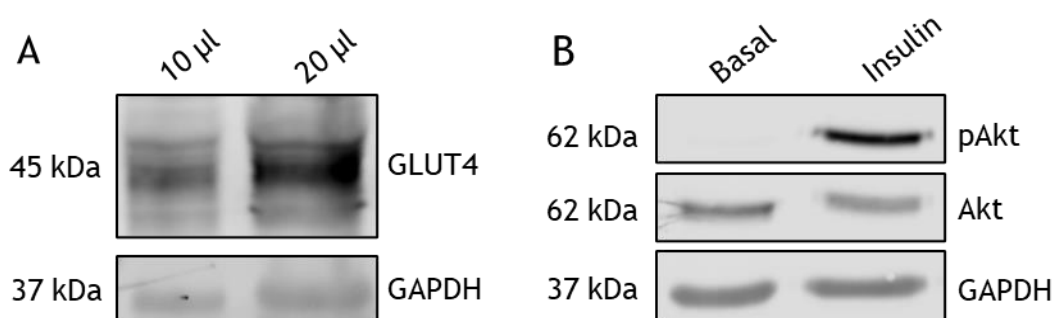


Figure 4.2 Endogenous GLUT4 protein expression and insulin sensitivity in 3T3-L1 adipocytes.

3T3-L1 adipocytes were differentiated as previously described and protein expression was assessed by western immunoblotting. (A) 10 µl and 20 µl of sample were loaded. Blots were incubated with anti-GLUT4 or anti-GAPDH (as a loading control) as labelled. (B) Cells were treated with or without 100 nM insulin for 20 min as indicated. Blots were incubated with anti-Akt or anti-phospho Akt (p-Akt). Blots were visualised with a LI-COR Odyssey-SA system; data from a typical experiment is shown.

We investigated glucose uptake in 3T3-L1 adipocytes using ^3H labelled 2-deoxyglucose to find the optimal conditions for insulin stimulation in this cell type (Figure 4.3). The glucose analog 2-deoxyglucose is taken up into the cells where it is phosphorylated and cannot be metabolised further. The compound gets trapped in the cells and a scintillation counter is used to measure radioactivity which directly corresponds to the amount of 2-deoxyglucose taken up by the cells. 3T3-L1 adipocytes were left untreated or stimulated with 100 nM insulin for 5, 10 and 20 min and significant increases in glucose uptake were observed for all durations of insulin stimulation ($p > 0.0001$; as determined by one-way ANOVA). As has been previously reported, insulin stimulated deoxyglucose transport ~10-fold, and was maximal 20 min after insulin addition; this was therefore chosen as duration of stimulation for all future experiments. In another experiment the dose-dependence of insulin stimulated deoxyglucose transport was examined in 3T3-L1 adipocytes (Figure 4.3 B). Based on this, 100 nM insulin was chosen as concentration for all future experiments.

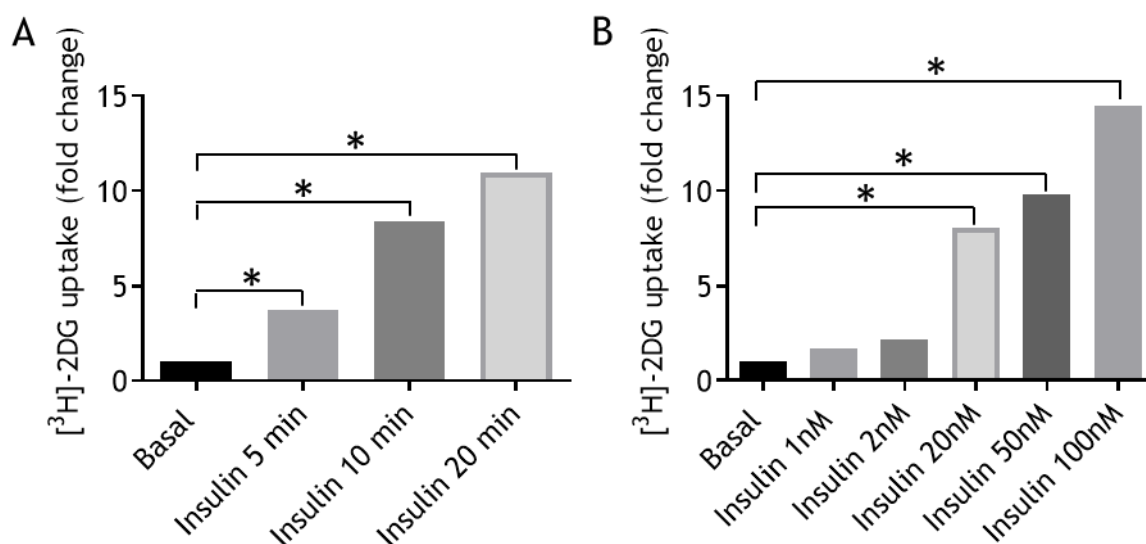


Figure 4.3 Insulin-stimulated deoxyglucose uptake in 3T3-L1 adipocytes.

2-deoxyglucose uptake was measured as described (section 2.4.1). 3T3-L1 adipocytes were incubated in serum-free medium for 2 h prior to experiments. Cells were washed with KRP and treated (A) for a range of time points with 100 nM insulin or (B) with a range of insulin concentrations for 20 min followed by a 5 min uptake of 2-deoxyglucose at 37°C. Basal glucose uptake rates were typically of the order of 600 counts per min/well. The data displayed represent fold changes of insulin stimulation from one experiment conducted in triplicate. Data from a representative experiments is shown. $p < 0.0001$ indicated by *; determined by one-way ANOVA.

Imaging experiments were performed on 3T3-L1 cells stably expressing an HA-GLUT4-GFP construct previously generated in the lab. Representative confocal images of HA-GLUT4-GFP adipocytes in figure 4.4 show that unstimulated cells had a strong GLUT4-GFP signal visible inside the cells (green arrows). HA-staining at the PM was elevated in insulin-stimulated adipocytes indicated by a strong ring formation around the majority of cells (blue arrows). Furthermore GLUT4-GFP was localised to the PM in insulin-stimulated 3T3-L1 cells and co-localised with the HA-stain (yellow arrows) which is representative of the majority of GLUT4 molecules having translocated from intracellular stores to the PM.

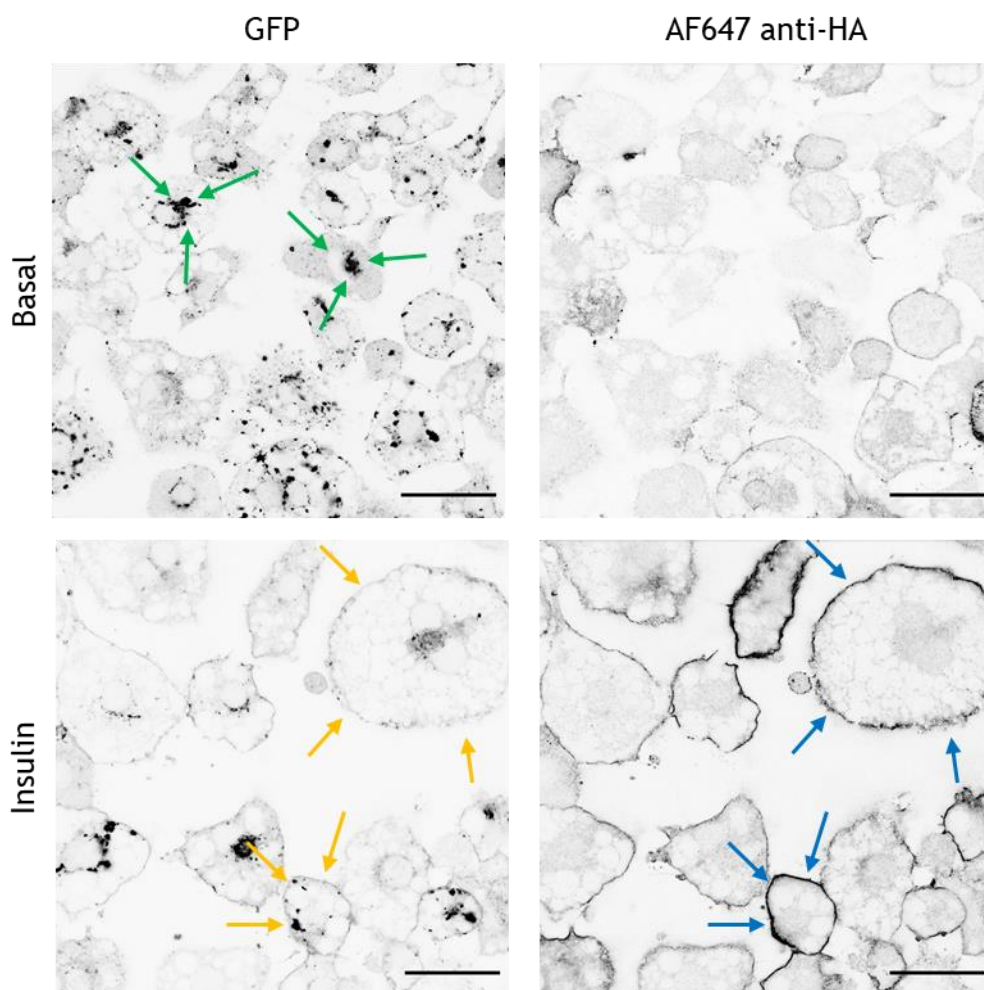


Figure 4.4 Confocal images of HA-GLUT4-GFP expressing 3T3-L1 adipocytes. Representative confocal images of 3T3-L1 adipocytes expressing HA-GLUT4-GFP (see section 2.7). The upper panel shows non-stimulated (basal) cells and the lower panel shows cells stimulated with 100 nM insulin for 20 min. Images on the right show GLUT4-GFP and images on the left show HA-tag GLUT4 staining. Displayed are grayscale images with inverted LUTs. Scale bars=30 μ m. Data are representative of many experiments of this type performed by multiple users in the Gould lab over 5 years.

To observe the molecular distribution and quantify the spatial patterning of GLUT4 within the PM with nanometre precision HA-staining was carried out in HA-GLUT4-GFP 3T3-L1 adipocytes and dSTORM images acquired. For the acquisition of dSTORM images adipocytes were screened in TIRF mode (Figure 4.5 A and D) and only cells that were big and rounded and adipocyte-like were chosen and fibroblast-like phenotypes were avoided. The vast majority of cells exhibited adipocyte-like morphology and contained lipid droplets (seen in figure 4.4). Representative TIRF images show selectively excited diffraction-limited GLUT4-GFP in close proximity to the plasma membrane with elimination of background fluorescence originating from out of focus GLUT4-GFP (Figure 4.5 A and D). Reconstructed dSTORM images of HA-GLUT4-GFP adipocytes show clearly visible single GLUT4 molecules as well as clusters within the PM (Figure 4.5 B and E). The spatial pattern of GLUT4 molecules was difficult to assess by eye but magnifications

of the reconstructed images as seen in figure 4.5 for a (C) basal and (F) insulin-stimulated cell show that the density of GLUT4 molecules and clusters at the cell surface was increased in insulin-stimulated adipocytes.

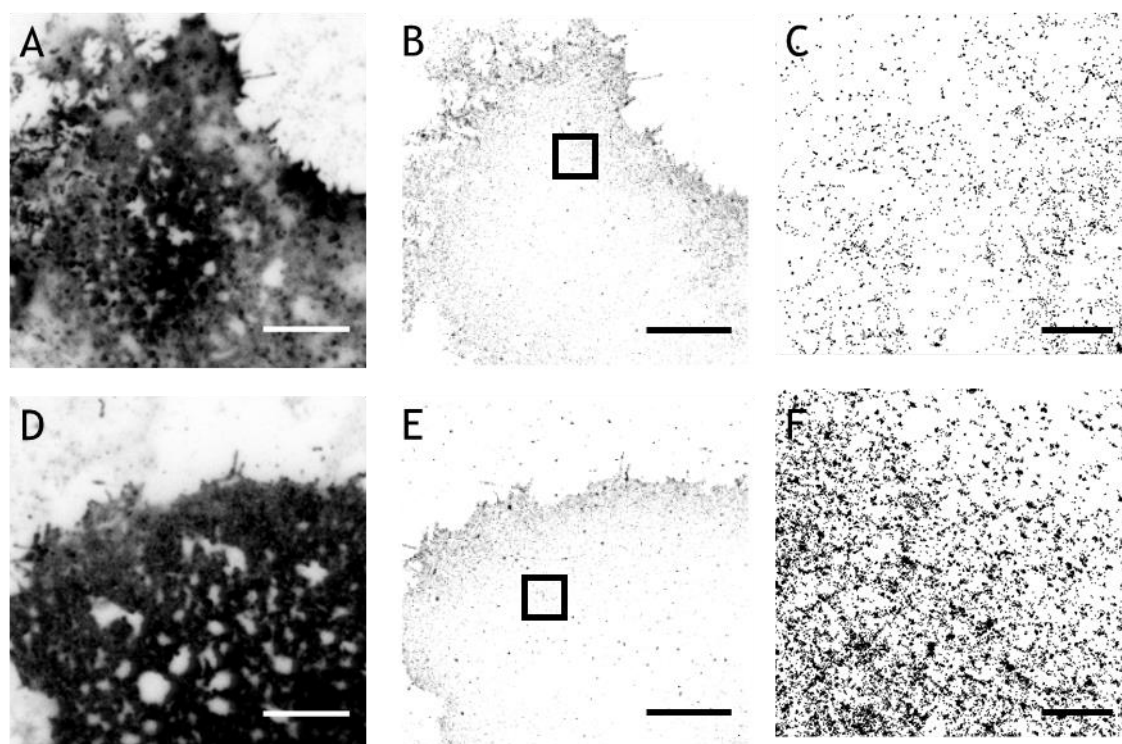


Figure 4.5 TIRF and STORM images of surface GLUT4 in basal and insulin-stimulated 3T3-L1 adipocytes.

HA-GLUT4-GFP 3T3-L1 cells were incubated in serum-free medium for 2 h prior to the experiment and stimulated with 100 nM insulin for 20 min or left untreated. Cells were fixed and stained for surface HA and dSTORM images acquired on a Zeiss Elyra PS. 1 (described in section 2.3). Reconstructions of raw images were calculated using the ImageJ plugin ThunderSTORM. (A) Representative TIRF image of a basal 3T3-L1 adipocyte. (B) Representative scatterplot of a basal cell showing localisations of single GLUT4 molecules. (C) Magnified section of image B. (D) Representative TIRF image of an insulin-stimulated cell. (E) Representative scatterplot of an insulin-stimulated cell showing localisations of single GLUT4 molecules. (F) Magnified section of image D. Scale bars 10 μm (A, B, D, E) and 1 μm (C and F). This experiment was repeated 5 times with similar results.

Ripley's K-function analysis was carried out to quantify changes in GLUT4 dispersal in the PM of basal and insulin-stimulated adipocytes. Ripley's L-function is normalised against the radius and plotting values from randomly distributed points results in an expected straight line $L(r)$. If the observed $L(r)$ is bigger than the expected $L(r)$ it indicates that the points in the sample are more clustered and if the observed $L(r)$ is smaller than the expected $L(r)$ it indicates that the points in the sample are more dispersed. Figure 4.6 shows the averaged $L(r)$ functions for basal and insulin-stimulated cells from three independently performed experiments. The observed $L(r)$ peaked at higher clustering values for GLUT4 on the PM of untreated adipocytes compared to

insulin-stimulated cells with a significant difference (section 2.3.10). This indicates that GLUT4 on the plasma membrane was less clustered in response to insulin-stimulation.

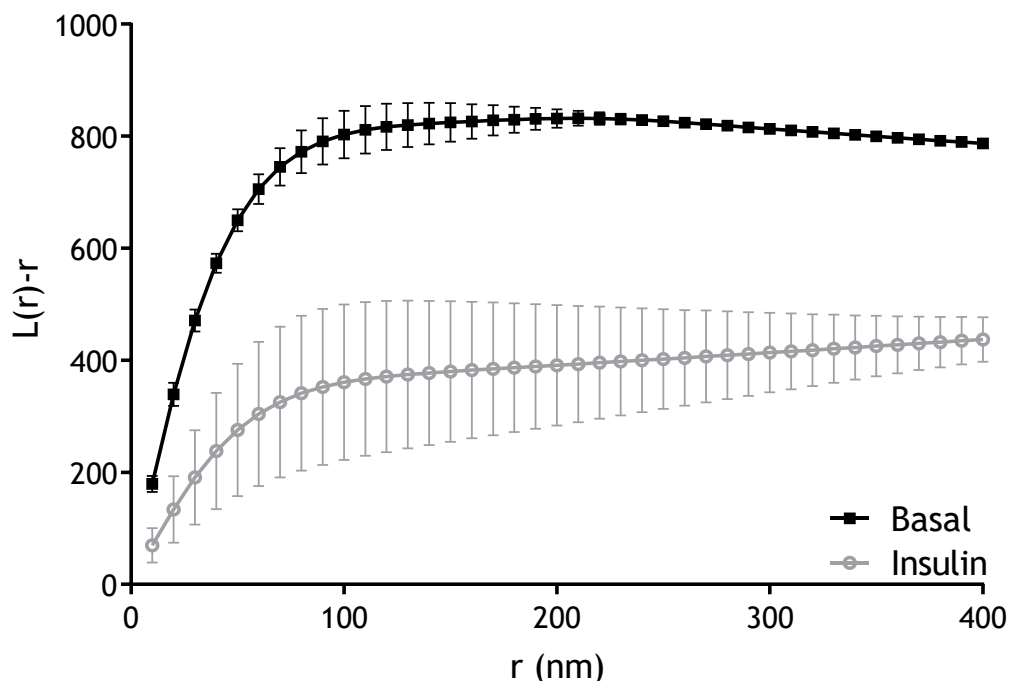


Figure 4.6 Ripley's K-function analysis of GLUT4 clustering in basal and insulin-stimulated 3T3-L1 adipocytes.

Representative plot of Ripley's K function analysis of the clustering abilities of GLUT4 molecules in the PM of HA-GLUT4-GFP 3T3-L1 adipocytes. Cells were serum-starved for 2 h prior to the experiment and stimulated with 100 nM insulin for 20 min or left untreated. Cells were fixed and stained for surface HA and dSTORM images acquired. GLUT4 molecule coordinates were obtained using ThunderSTORM and the obtained localization data was subjected to Ripley's K-function analysis using SR Tessler with the minimum radius 10 nm, step radius 10 nm, and maximum radius 400 nm. $L(r)-r$ (y-axis) represents the clustering ability and r (x-axis) represents the radial scales of clustering. The presented data are mean \pm SD. The experiment was performed independently 3 times for basal (N=19 cells) and insulin-stimulated (N=20 cells) conditions. $p < 0.0001$ determined by two-tailed Student's t-test.

4.2.2 AMPK activation regulates insulin-stimulated GLUT4 dispersal

AMPK is activated pharmacologically by AICAR which accumulates inside cells as its monophosphorylated form ZMP. Activated AMPK is known to phosphorylate and inactivate acetyl-CoA carboxylase (ACC). In our study we firstly confirmed this effect by determining phosphorylation of ACC by western immunoblotting (Figure 4.7). Total ACC protein and phosphorylated ACC (pACC) protein expression were examined. pACC levels increased in cells treated with 2 mM AICAR or a combination of 2 mM AICAR and 100 nM insulin. These results mirror an increased accumulation of ZMP and AMPK activity following 2 mM AICAR stimulation for 1 h (Figure 4.7). We also assessed levels of

phosphorylated and total Akt in response to 100 nM insulin stimulation and 2mM AICAR treatment. There was no phosphorylated Akt protein detected in basal samples. AICAR stimulation modestly elevated pAkt levels whereas insulin induced a strong pAkt signal, as expected. These data are similar to that reported by others in the field (Salt et al., 2000).

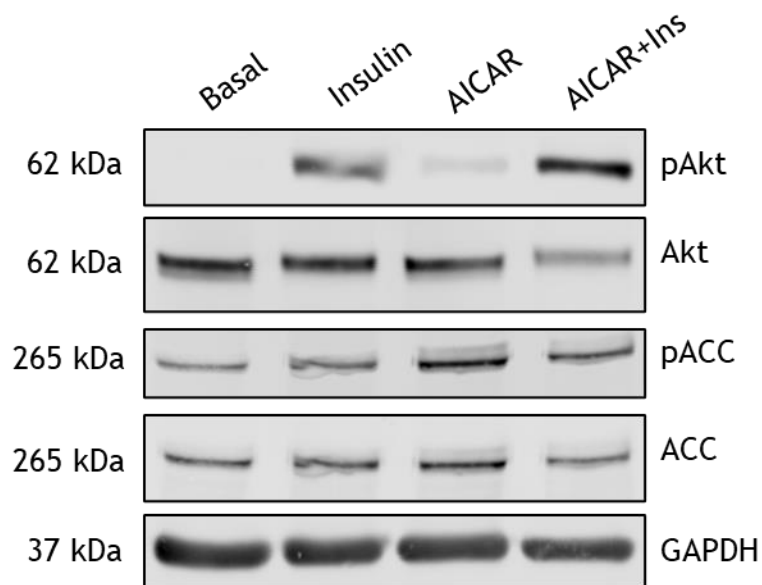


Figure 4.7 AICAR and Insulin sensitivity in 3T3-L1 adipocytes.

3T3-L1 adipocytes were serum-starved for 2 h prior to experiments and left untreated ('Basal') or treated with 2mM AICAR for 1 h ('AICAR'), insulin for 20 min ('Insulin') or both ("AICAR + Ins'). Cells were lysed and equal amounts of protein lysates were separated on SDS-PAGE and immunoblotted using the antibodies indicated on the right of the figure (see section 2.6 for details). Data from a typical experiment is shown.

We assessed the effect of AMPK activation on basal and insulin-stimulated glucose transport in 3T3-L1 adipocytes using ^3H labelled 2-deoxyglucose. Salt et al (2000) incubated cells with 500 $\mu\text{mol/l}$ AICAR and/or 10 nmol/l insulin for 1 h. Here we tested several concentrations and durations of AICAR stimulation (data not shown) and concluded that 2mM AICAR and 100 nM insulin stimulation for 1 h were most appropriate. A significant 6-fold increase in deoxyglucose uptake was observed following insulin stimulation with 100 nM for 1 h (Figure 4.8) compared to untreated adipocytes. Treatment of 3T3-L1 adipocytes with 2 mM AICAR for 1 h increased deoxyglucose uptake by 1.7-fold. These results suggest that AMPK activation itself had a modest effect on basal levels of glucose uptake in adipocytes, consistent with published data (Salt et al., 2000). AICAR treatment reduced insulin-stimulated glucose uptake by about 15% (Figure 4.8). This result indicates that there is a trend of AMPK activation attenuating insulin-stimulated glucose uptake in adipocytes.

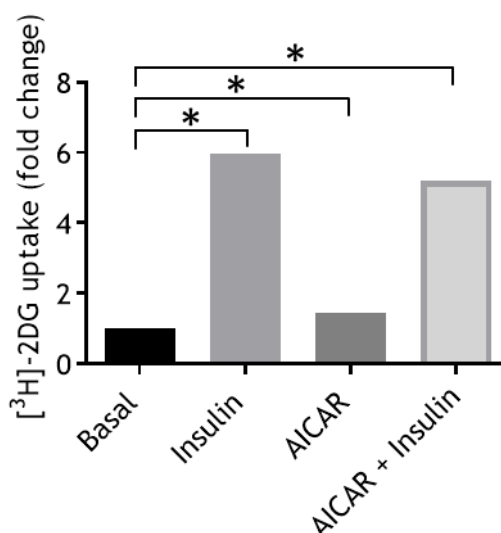


Figure 4.8 AICAR- and insulin-stimulated glucose uptake in 3T3-L1 adipocytes. Glucose uptake was measured using ³H labelled 2-deoxyglucose as outlined (section 2.4.1). 3T3-L1 adipocytes were incubated in serum-free medium for 2 h prior to experiments, washed with KRP and left untreated or were treated with 2 mM AICAR for 1h or 100 nM insulin for 1 h or both. This was followed by a 5 min uptake of 2-deoxyglucose at 37°C. Basal glucose uptake rates were typically of the order of 1500 counts per min/well. The data displayed represent fold changes of insulin stimulation from one experiment conducted in triplicate. Data from a representative experiment is shown. $p < 0.0001$ indicated by *; determined by one-way ANOVA.

Flow cytometry has emerged as a powerful technology for assaying GLUT4 translocation in a high throughput fashion. We analysed HA-GLUT4-GFP 3T3-L1 adipocytes treated with 100 nM insulin and 2 mM AICAR or both by flowcytometry to quantify effects on GLUT4 translocation in thousands of cells. Mature adipocytes were differentiated from 3T3-L1 fibroblasts and presented as a heterogeneous mixed population of cells containing residual fibroblasts, cellular debris and adipocytes of various sizes. In flowcytometry cells are suspended in a clear saline solution and funnelled to produce a single cell stream past a set of laser light sources. Light scatter is detected by two detectors. The parameter forward scatter is measured along the path of the laser whereas side scatter is detected at a ninety degree angle relative to the laser. Forward scatter allows for the discrimination of cells by size due to light diffraction around the cell. Side scatter gives information about the granularity of cells because intracellular structures cause the light to refract or reflect resulting in differences in signal. Selective forward versus side scatter gating was applied to identify adipocytes in the sample based on their size and granularity and to exclude any residual fibroblasts and cellular debris (Figure 4.9 A and B). Wild type 3T3-L1 adipocytes are auto-fluorescent in the GFP-channel and HA-GLUT4-GFP 3T3-L1 adipocytes do not express the GFP-positive construct in equal amounts and therefore GFP-fluorescence threshold gates were set to control for these confounding variables (Figure 4.9 C and D). The gates were set so that 98.7 % of wild type 3T3-L1 adipocytes were identified as completely GFP-negative

population (Figure 4.9 C). With these gates in place 54.1 % of unstained HA-GLUT4-GFP 3T3-L1 adipocytes were identified as GFP-positive population (Figure 4.9 D). HA-GLUT4-GFP 3T3-L1 adipocytes contain more GFP-positive cells than identified here but for this study the choice was made to carefully exclude auto-fluorescent and very dim cells from the analysis.

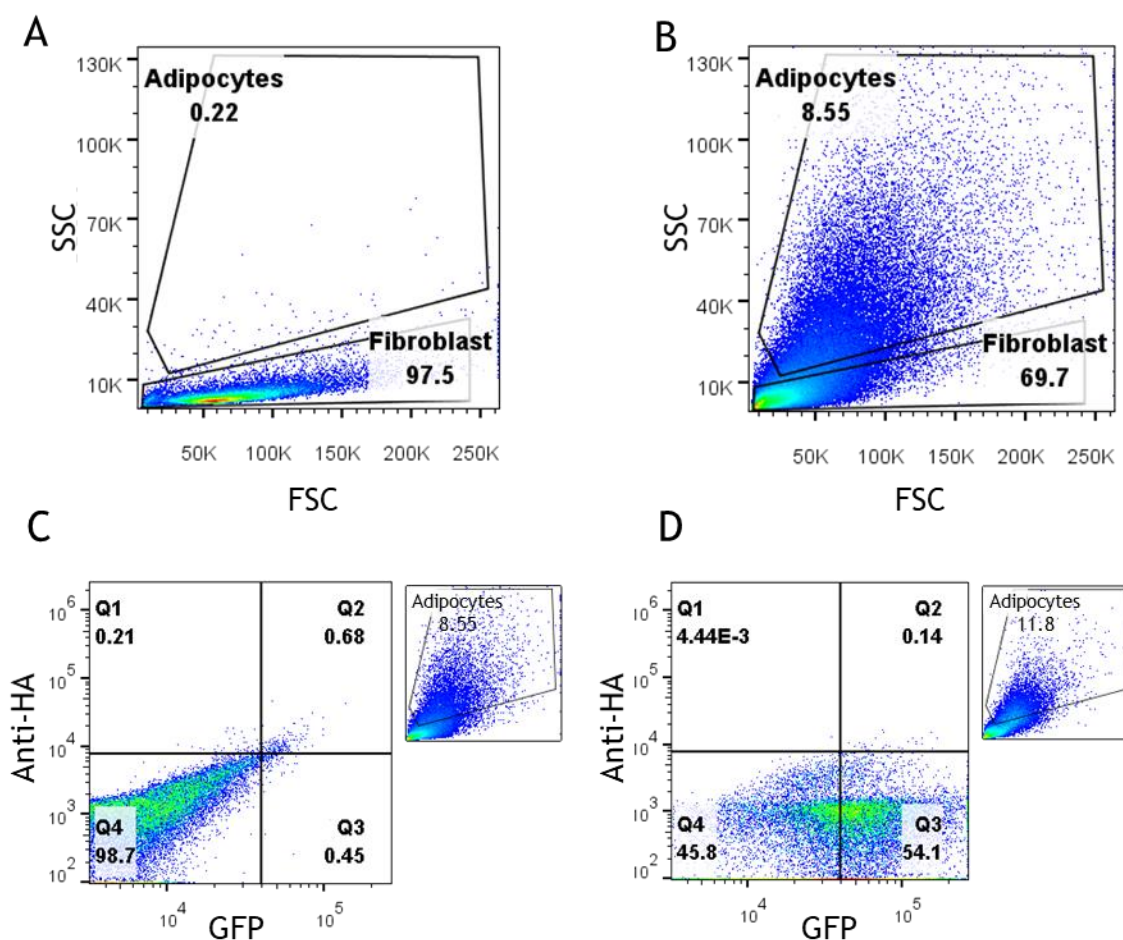


Figure 4.9 Selective gating for quantification of insulin-stimulated GLUT4 translocation to the plasma membrane by flow cytometry in 3T3-L1 adipocytes. Wild type and HA-GLUT4-GFP 3T3-L1 fibroblasts and adipocytes were washed and collagenase-digested and subsequently acquired on a BD LSR II™ and analysed using FlowJo® software as described (section 2.8). The collected light emissions are displayed as dual-colour fluorescence density plots. (A) SSC (side scatter) versus FSC (forward scatter) plot with a gate around 3T3-L1 fibroblasts and cellular debris. (B) SSC versus FSC plot with a gate around 3T3-L1 adipocytes. (C) Wild type adipocytes previously gated in B were subjected to another GFP-fluorescence threshold gate and identified as GFP-negative population. (D) HA-GLUT4-GFP 3T3-L1 adipocytes previously gated in B were subjected to another GFP-fluorescence threshold gate and identified as GFP-positive population. 30,000 cells per condition. Data from a typical experiment is shown.

In the following sample analysis 50,000 GFP-positive HA-GLUT4-GFP 3T3-L1 adipocytes were included for each condition and the experiment was performed two times independently. Adipocytes were left untreated, stimulated with 2 mM AICAR for 1 h or 100 nM insulin for 40 min or both and stained for the HA-epitope to quantify GLUT4

translocation using flowcytometry (Figure 4.10). In the basal state 5.39 % of HA-GLUT4-GFP adipocytes were GFP-positive and stained for surface HA-GLUT4 (Figure 4.10 C). Insulin stimulation lead to an 8-fold increase in surface HA-GLUT4 with an increase in fluorescence in 43.3 % of adipocytes (Figure 4.10 D). Treatment with 2 mM AICAR for 1 h resulted in a 1.4-fold change in GLUT4 translocation (Figure 4.10 E). Stimulation with 2 mM AICAR and insulin simultaneously resulted in a 9.4-fold increase in HA-epitope staining which is representative of GLUT4 translocation to the PM. These results indicate that AMPK activation slightly increases GLUT4 translocation from intracellular stores by itself and that AMPK activation attenuates insulin-stimulated GLUT4 translocation in 3T3-L1 adipocytes. These data are consistent with our own assays of deoxyglucose transport (Figure 4.8) and with (Salt et al., 2000).

Having established that our reagents and cells recapitulated published data on the effects of AICAR, we investigated the effect of AMPK activation on GLUT4 clustering in the PM of 3T3-L1 adipocytes (Figure 4.11). We performed Ripley's K-function analysis to investigate the effect of AMPK activation on the spatial patterning of membrane GLUT4 and data from two experiments are presented in figure 4.11. As previously reported the observed $L(r)$ peaked at significantly higher clustering values for GLUT4 on the PM of untreated adipocytes. There was no difference between untreated cells and cells treated only with 2 mM AICAR for 1 h and the $L(r)$ function followed a similar curve progression. Thus, AICAR treatment alone did not appear to modulate GLUT4 clustering. Our results indicate that insulin stimulation led to a more dispersed distribution of GLUT4 within the PM of adipocytes as previously observed. We also report for the first time that AMPK activation attenuated insulin-stimulated GLUT4 dispersal in 3T3-L1 adipocytes.

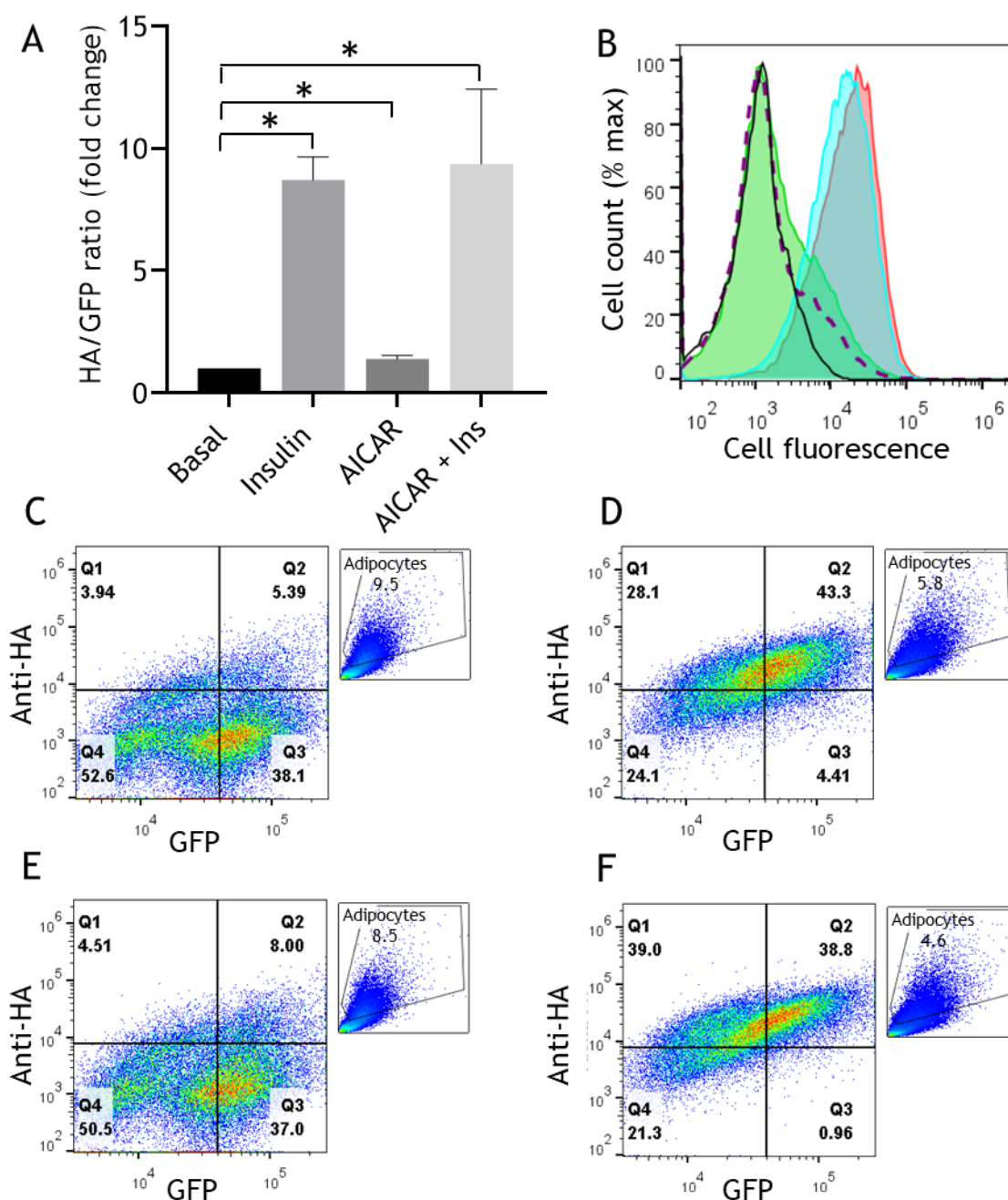


Figure 4.10 Quantitative measurement of insulin-stimulated GLUT4 translocation to the plasma membrane by flow cytometry in 3T3-L1 adipocytes.

3T3-L1 adipocytes were serum-starved 2 h prior to experiments and left untreated or stimulated with 2 mM AICAR for 1h or 100 nM insulin for 40 min or both. Cells were stained with anti-HA and in low serum medium on ice. Cells were washed and collagenase-digested and 50,000 events per condition acquired on a BD LSR II™ and analysed using FlowJo® software. The collected light emissions are displayed as histograms and density plots. (A) Quantification of HA/GFP fluorescence ratio (mean +SD; N=2). (B) Single parameter histogram showing number of cells as percentage of the whole population (y-axis) and fluorescence intensity of the HA-epitope stain. (C-F) Two-parameter dual colour fluorescence density plots displaying total GLUT4-GFP fluorescence vs HA-stain fluorescence for (C) untreated, (D) insulin-stimulated, (E) AICAR treated and (F) AICAR- and insulin-treated 3T3-L1 adipocytes. $p=0.0108$ indicated by *; determined by one-way ANOVA.

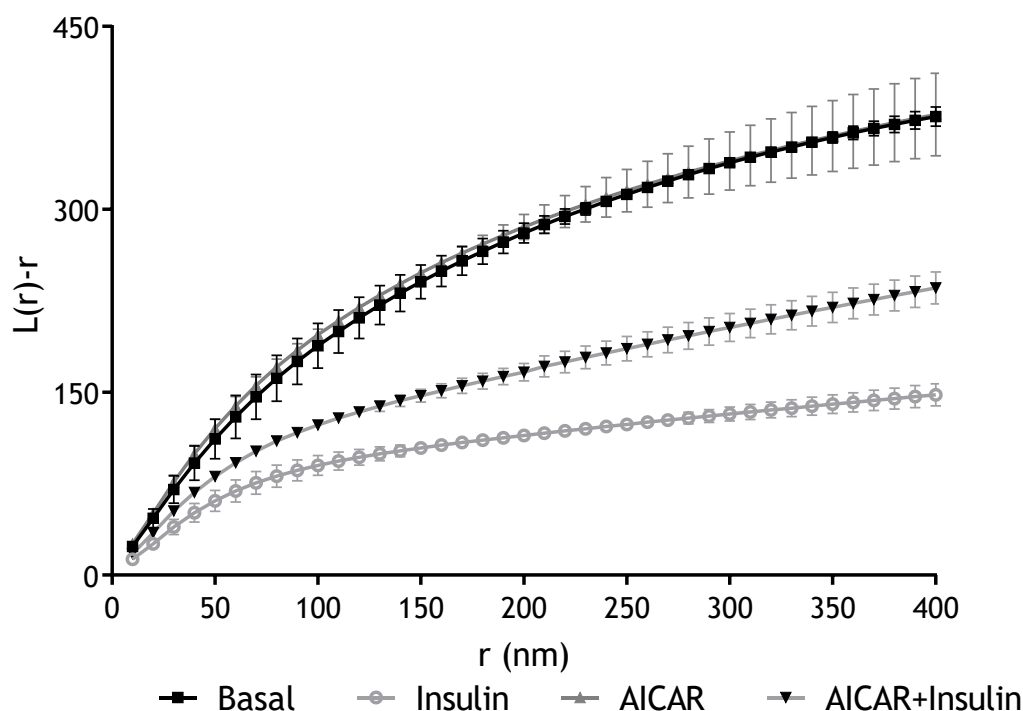


Figure 4.11 Ripley's K-function analysis of the effect of AMPK activation on GLUT4 clustering in basal and insulin-stimulated 3T3-L1 adipocytes.

Representative plot of Ripley's K function analysis of the clustering abilities of GLUT4 molecules in the PM of HA-GLUT4-GFP 3T3-L1 adipocytes. Cells were serum-starved for 2 h prior and stimulated with 100 nM insulin for 20 min, 2 mM AICAR for 1 h or both or left untreated. Cells were fixed and stained for surface HA and dSTORM images acquired. GLUT4 molecule coordinates were obtained using ThunderSTORM and subjected to Ripley's K-function analysis using SR Tesselator with minimum radius 10 nm, step radius 10 nm, and maximum radius 400 nm. $L(r)-r$ (y-axis) represents the clustering ability and r (x-axis) represents the radial scales of clustering. The presented data are mean \pm SD. The experiment was performed independently 3 times for basal (N=24 cells), insulin-stimulated (N=26 cells), AICAR-treated (N=26 cells) and AICAR- and insulin-treated (N=30 cells) conditions. $p < 0.0001$; determined by one-way ANOVA.

4.2.3 Cholesterol depletion enhances basal GLUT4 clustering

Studies have identified relationships between lipid rafts, caveolae, cholesterol, insulin signalling and GLUT4 translocation (Gustavsson et al., 1996, 1999; Nystrom et al., 1999; Parpal et al., 2001; Parton et al., 2002; Ros-Baro et al., 2001; Shigematsu et al., 2003; Yamamoto et al., 1998). We investigated whether GLUT4 clustering was associated with lipid rafts. We used methyl- β -cyclodextrin (MBCD) treatment which removes cholesterol from cultured cells and disrupts lipid rafts (Kabouridis et al., 2000). Firstly, we assessed whether MBCD treatment had an effect on insulin stimulation in 3T3-L1 adipocytes by assay of pAKT levels (Figure 4.12). Insulin stimulation led to a significant 47-fold increase in Akt phosphorylation (Figure 4.12 B) compared to untreated cells. Cells treated with 5 mM MBCD alone showed a 3.4-fold increase in pAkt signal. Furthermore, MBCD treatment resulted in a significant decrease of insulin-stimulated Akt phosphorylation by 50 %.

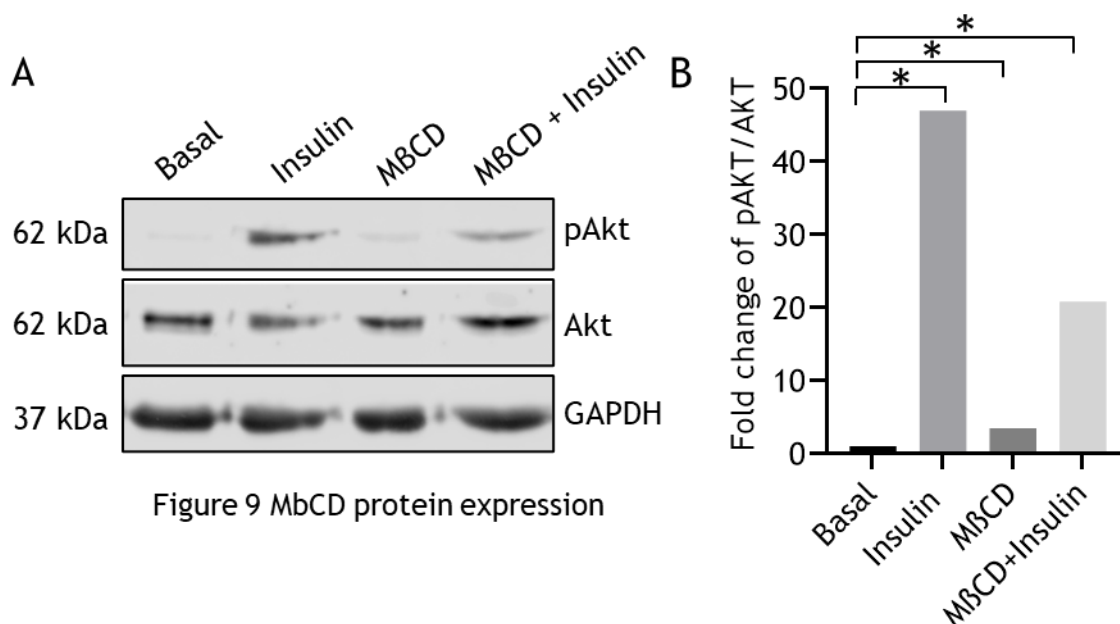


Figure 4.12 Effect of cholesterol depletion on insulin sensitivity in 3T3-L1 adipocytes.

3T3-L1 adipocytes were serum starved for 2 h and treated with 100 nM insulin for 20 min or 5 mM MBCD for 1 h or both or left untreated. (A) Equal amounts of protein were immunoblotted with antibodies indicated at the right of the figure. (B) Quantification of the immunoblot displayed in panel (A) performed via densitometry, expressed as the ratio of phosphorylated to total Akt. Data of a representative experiment is shown. $p < 0.05$ indicated by *; determined by one-way ANOVA.

Next we examined the effect of cholesterol depletion on glucose transport in 3T3-L1 adipocytes (Figure 4.13). Insulin stimulation with 100 nM for 20 min led to a significant 10-fold increase in glucose uptake in three independent experiments. Treatment of cells with 5 mM MBCD alone for 1 h also resulted in a significant 7-fold increase in glucose uptake compared to baseline levels (Figure 4.13). MBCD treatment leading to the depletion of cholesterol within the PM had a strong effect on basal glucose uptake in 3T3-L1 adipocytes.

We investigated the effect of cholesterol depletion on spatial GLUT4 patterning on the surface of adipocytes. Data from two independent experiments are shown in figure 4.14. As previously observed insulin stimulation for 20 min with 100 nM shifted the L(r) function towards smaller clustering values indicating that GLUT4 molecules in the sample were more dispersed. Treatment with 5 mM MBCD for 1 h resulted in a more curved L(r) compared to basal cells indicating a higher degree of GLUT4 clustering in this sample. Therefore cholesterol depletion increased surface GLUT4 clustering in adipocytes.

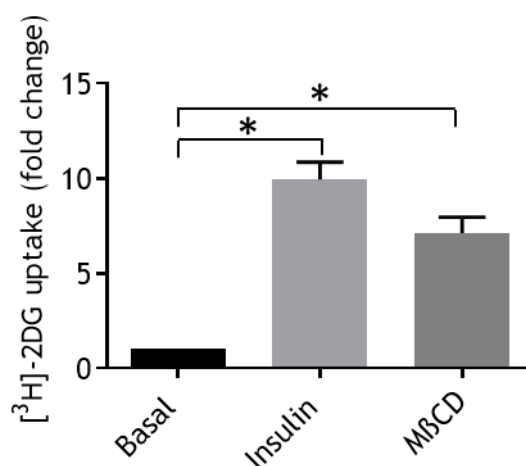


Figure 4.13 MBCD- and insulin-stimulated deoxyglucose uptake in 3T3-L1 adipocytes.

Deoxyglucose uptake was measured in 3T3-L1 adipocytes incubated in serum-free medium for 2 h. Cells were washed and treated with 5 mM MBCD for 1 h or 100 nM insulin for 20 min or both or left untreated followed by a 5 min uptake of 2-deoxyglucose at 37°C. Basal glucose uptake rates were of the order of 1000 counts per min/well. Data displayed represent fold changes from basal values from three experiments conducted in triplicate. $p < 0.0001$ indicated by *; determined by one-way ANOVA.

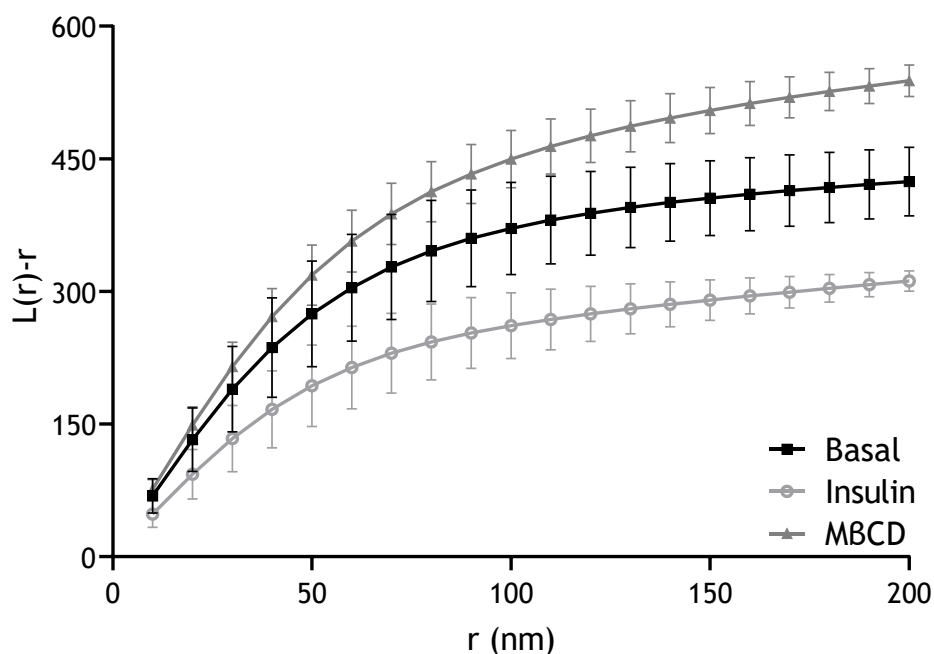


Figure 4.14 Ripley's K-function analysis of the effect of cholesterol depletion on GLUT4 clustering in basal 3T3-L1 adipocytes.

Representative plot of Ripley's K function analysis of the clustering abilities of GLUT4 molecules in the PM of HA-GLUT4-GFP 3T3-L1 adipocytes. Cells were serum-starved for 2 h and stimulated with 100 nM insulin for 20 min or 5 mM MBCD for 1 h or left untreated. Cells were fixed and stained for surface HA and dSTORM images acquired. GLUT4 molecule coordinates were obtained and subjected to Ripley's K-function analysis using SR Tesseler with minimum radius 10 nm, step radius 10 nm, and maximum radius 200 nm. $L(r)-r$ (y-axis) represents the clustering ability and r (x-axis) represents the radial scales of clustering. The presented data are mean \pm SD. The experiment was performed independently 2 times for basal (N=18 cells), insulin-stimulated (N=16 cells) and MBCD-treated (N=18 cells) conditions. $p < 0.0001$; as determined by one-way ANOVA.

4.2.4 EFR3 regulates insulin-stimulated GLUT4 dispersal

To assess the effect of EFR3 on insulin-stimulated GLUT4 dispersal in 3T3-L1 adipocytes electroporation was used to knock down the protein with 50 % efficiency and STORM imaging experiments were performed by Silke Morris (Morris, 2020). Previously, it was observed that protein levels of other GSC components were not affected by the electroporation procedure (Morris, 2020). Here existing imaging data were filtered (described in section 2.3.9) and Ripley's L-function analysis was carried out using the spatstat package in R with help of Marie Cutiongco (described in sections 2.3.11 and 3.1.4.6) to allow a more rigorous analysis of this dataset. During the analysis data were corrected for inhomogeneity of GLUT4 levels in the PM following insulin stimulation and edge corrections applied (see section 3.2.7). Figure 4.15 A shows that GLUT4 molecules appeared clustered in control basal cells and insulin stimulation shifted GLUT4 distribution to become more dispersed. EFR3 knock down did not affect GLUT4 clustering in the basal state but it was found that EFR3 knock down significantly attenuated insulin-stimulated GLUT4 dispersal in 3T3-L1 adipocytes (figure 4.15 B/C). This result is in line with the previously reported effect of EFR3 knock out on insulin-stimulated GLUT4 dispersal (Morris, 2020).

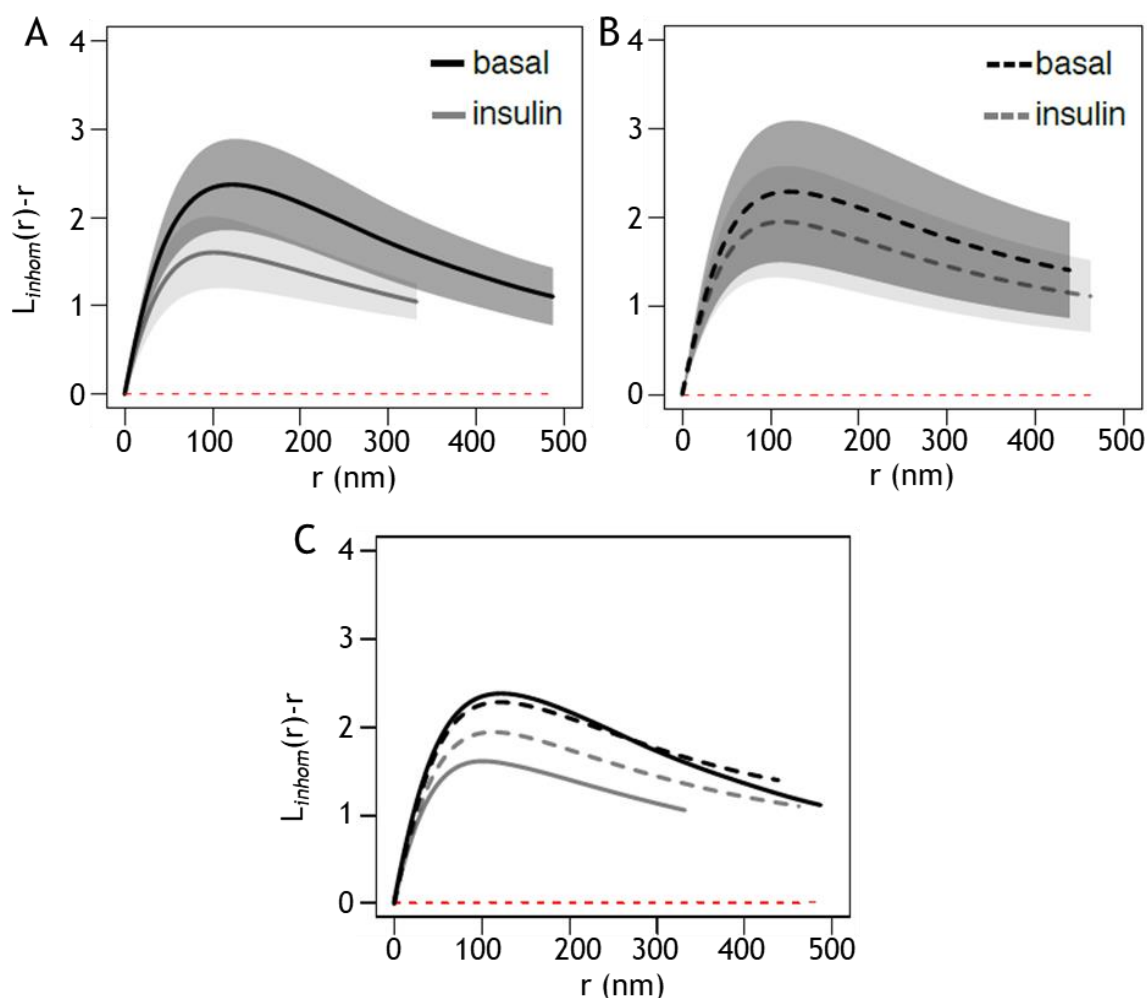


Figure 4.15 Ripley's inhomogeneous L function analysis of GLUT4 molecule clustering in EFR3 knock down basal and insulin-stimulated 3T3-L1 adipocytes using spatstat.

In HA-GLUT4-GFP 3T3-L1 cells EFR3 knock down was carried out as previously described (Morris, 2020). After 72h cells were serum-starved for 2h and stimulated with 100 nM insulin for 20min or left untreated. Surface HA-staining was performed and dSTORM images acquired and molecule coordinates obtained. Data subjected to analysis using spatstat described in 3.4.11. Representative graphs of Ripley's L-function for (A) control basal (N=40) and insulin-stimulated (N=35) cells. (B) EFR3 knock down basal (N=35) and insulin-stimulated (N=31) cells. (C) All experimental groups. The presented data are means; grey shading indicates the most extreme deviation from the theoretical L function at any distance r ; the function is displayed as centred (red line).

4.2.5 Insulin regulates GLUT4 dispersal in HeLa cells

Recently it has been shown that HeLa cells have comparable kinetics and orthologous GLUT4 trafficking mechanisms compared to 3T3-L1 adipocytes and offer a useful, human model system. HeLa cells traffic GLUT4 to the PM in response to insulin but the observed effect is much smaller compared to 3T3-L1 adipocytes. We used flowcytometry to quantify GLUT4 translocation in HeLa cells in a high throughput fashion. HeLa cells are highly homogenous in size but selective threshold gates were applied to distinguish GFP-positive HA-GLUT4-GFP HeLa cells from auto-fluorescent

GFP-negative wild type cells (Figure 4.16). Figure 4.16 B shows 79% of unstained HA-GLUT4-GFP HeLa cells were identified as GFP-positive.

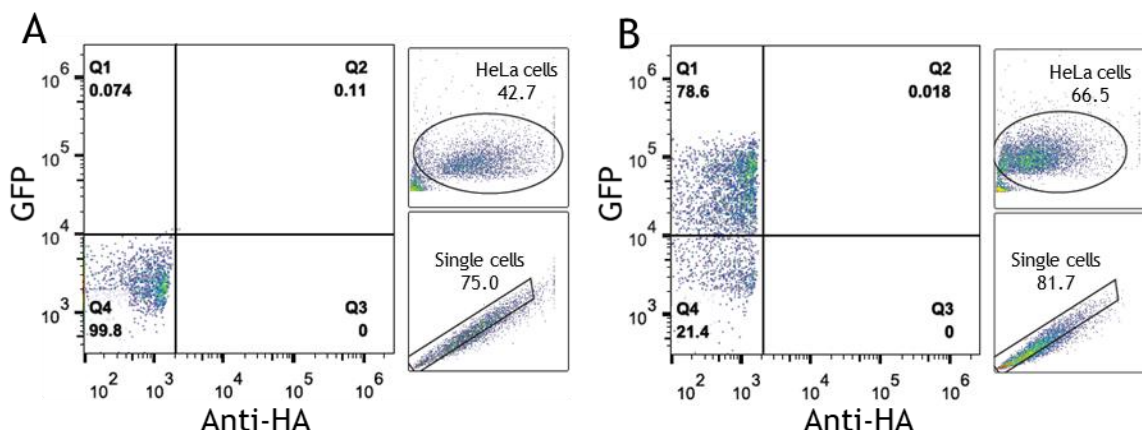


Figure 4.16 Selective gating for quantification of insulin-stimulated GLUT4 translocation to the plasma membrane by flow cytometry in HeLa cells.

Wild type and HA-GLUT4-GFP HeLa cells were washed and collagenase-digested and subsequently acquired on a BD LSR II™ and analyzed using FlowJo® software. The collected light emissions are displayed as dual-colour fluorescence density plots. (A) Wild type HeLa cells were subjected to a GFP-fluorescence threshold gate and identified as GFP-negative population. (B) HA-GLUT4-GFP HeLa cells were subjected to a GFP-fluorescence threshold gate and identified as GFP-positive population. N=1; 30,000 cells per condition.

In the following sample analysis 50,000 GFP-positive HA-GLUT4-GFP HeLa cells were included for each condition (Figure 4.17). A 1.3-fold increase in insulin-stimulated GLUT4 translocation was observed in HeLa cells (Figure 4.17 A). The shift in surface HA-epitope staining fluorescence intensity is most apparent in the fluorescence intensity histogram (Figure 4.17 B). The dual-colour fluorescence density plots show that there is a significant increase in surface HA-positive cells between the basal (Figure 4.17 C) and insulin-stimulated (Figure 4.17 D) conditions. This indicates that intracellular GLUT4 translocated to the PM where the HA-tag was exposed and stained. It should be noted that others have observed 2 to 3-fold increases in magnitude of translocation in this cell type (Morris et al., 2020), but we did not attempt to optimise the assay parameters here, and instead focussed upon GLUT4 dispersal.

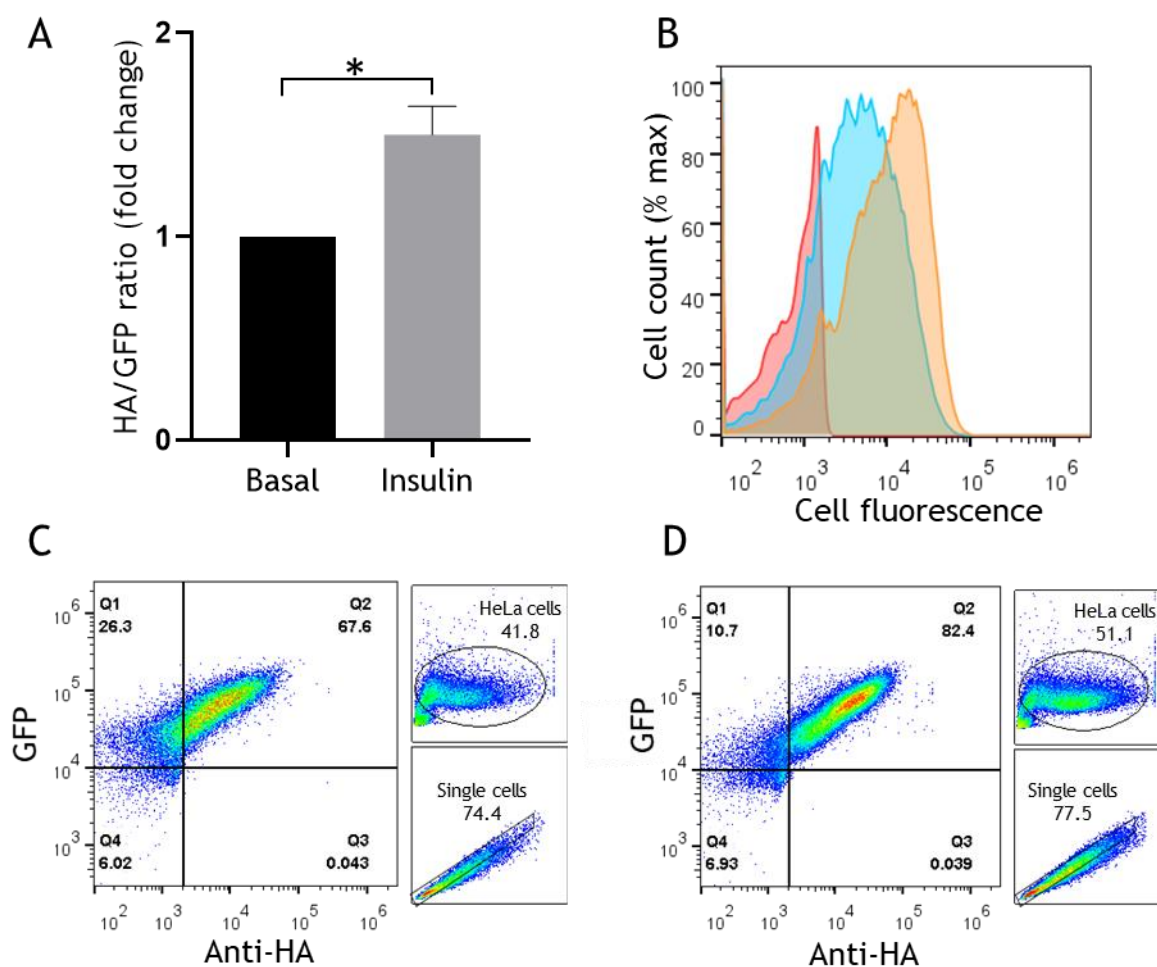


Figure 4.17 Quantitative measurement of insulin-stimulated GLUT4 translocation to the plasma membrane by flow cytometry in HeLa cells.

HeLa cells were incubated in serum-free medium 2 h prior to experiments. Cells were left untreated or stimulated with 1 μ M insulin for 20 min. Cells were stained with primary mouse anti-HA (1:200) and secondary anti-mouse Alexa-Fluor 647 (1:300) antibodies on ice. HeLa cells were washed and collagenase-digested and subsequently 50,000 events per condition acquired on a BD LSR II™ and analyzed using FlowJo® software. The collected light emissions are displayed as histograms and density plots. (A) Quantification of HA/GFP fluorescence ratio (mean+SD; N=2). (B) Single parameter histogram showing the number of cells as percentage of the whole population (y-axis) and the fluorescence intensity of the AF647 channel corresponding to the staining for the HA-epitope. Red=unstained, blue=basal and orange=insulin-stimulated cells. (C-D) Two-parameter dual colour fluorescence density plots displaying total GLUT4-GFP fluorescence vs AF647 fluorescence for (C) untreated and (D) insulin-stimulated HeLa cells. $p=0.0377$ indicated by *; determined by unpaired Student's t-test.

Having observed an insulin effect on translocation, we investigated GLUT4 dispersal in response to insulin stimulation. Representative TIRF images show selectively excited diffraction-limited GLUT4-GFP in close proximity to the plasma membrane with elimination of background fluorescence originating from out of focus GLUT4-GFP (Figure 4.18 A and D). Reconstructed dSTORM images of HA-GLUT4-GFP HeLa cells show clearly visible single GLUT4 molecules (Figure 4.18 B and E). Magnifications of the reconstructed images as seen in figure 4.18 for a (C) basal and (F) an insulin-stimulated

cell show that there are more GLUT4 molecules visible in response to insulin stimulation. This result confirms GLUT4 translocating to the PM at the single molecule level in HeLa cells similarly to 3T3-L1 adipocytes.

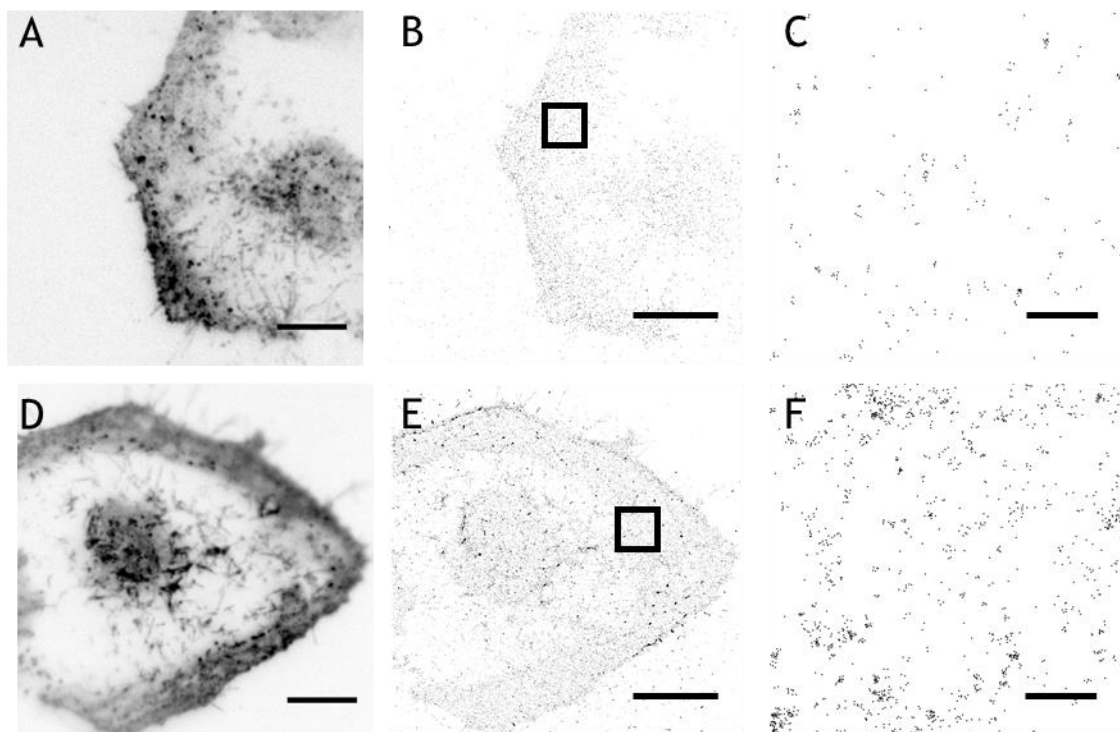


Figure 4.18 TIRF and STORM images of surface GLUT4 in basal and insulin-stimulated HeLa cells.

HeLa cells expressing HA-GLUT4-GFP were incubated in serum-free medium for 2 h prior to the experiment and stimulated with 1 μM insulin for 20 min or left untreated. Cells were fixed and stained for surface HA and dSTORM images acquired on a Zeiss Elyra PS. 1 (described section 2.3). Reconstructions of raw images were calculated using the ImageJ plugin ThunderSTORM. (A) Representative TIRF image of GLUT4-GFP in a basal HeLa cell (B) Representative scatterplot of a basal cell showing localisations of single GLUT4 molecules. (C) Magnified section of image A. (D) Representative TIRF image of a insulin-stimulated HeLa cell. (E) Representative scatterplot of an insulin-stimulated cell showing localisations of single GLUT4 molecules. (F) Magnified section of image E. Scale bars 10 μm (A, B, D, E) and 1 μm (C and F). This experiment was repeated twice with similar results.

We performed Ripley's K-function analysis of dSTORM images of untreated and insulin-stimulated HeLa cells. Data from two independent experiments are shown in figure 4.19. Insulin stimulation for 20 min significantly shifted the $L(r)$ function towards smaller clustering values indicating that GLUT4 molecules in the sample were more dispersed ($p=0.0028$; determined by two-tailed Student's t-test). Therefore insulin stimulation altered surface GLUT4 distribution significantly towards a more dispersed distribution. This is the first demonstration of GLUT4 dispersal in a cell type other than adipocytes; while compared to 3T3-L1 adipocytes the effect was of a much smaller magnitude, this result nevertheless supports the idea that insulin-stimulated GLUT4

dispersal is a replicable observation in other cell types, and adds weight to the idea that HeLa cells are a useful model system for the study of GLUT4 translocation (Bryant and Gould, 2020; Morris et al., 2020).

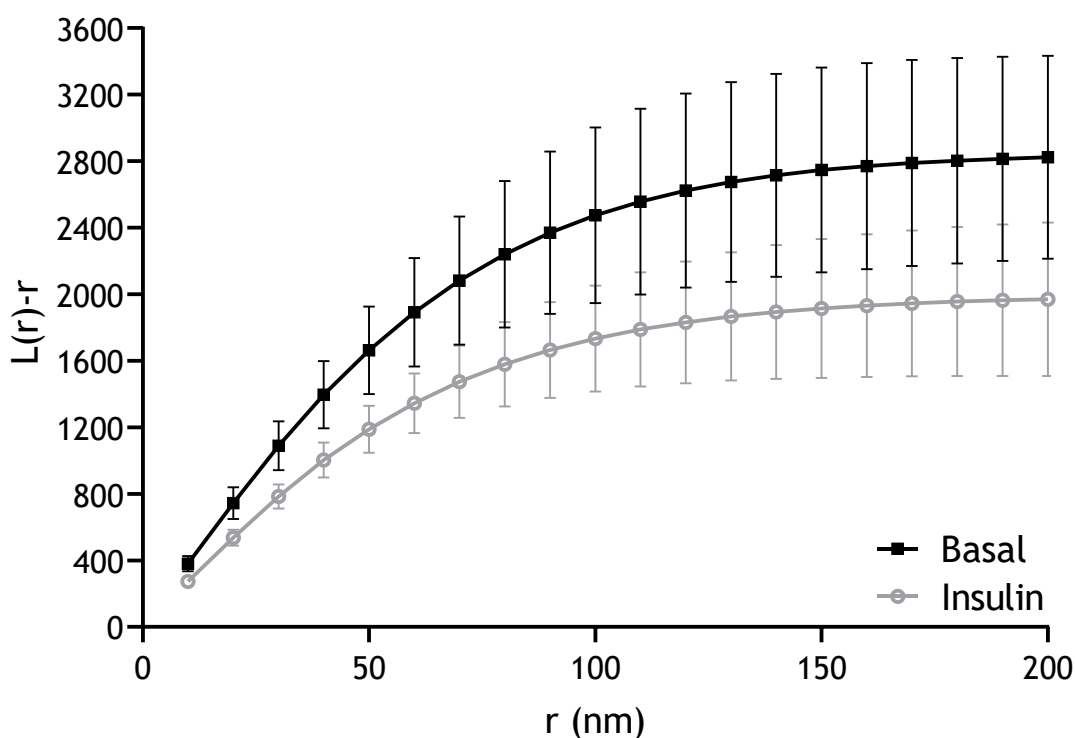


Figure 4.19 Ripley's K-function analysis of GLUT4 clustering in basal and insulin-stimulated HeLa cells.

Representative plot of Ripley's K function analysis of the clustering abilities of GLUT4 molecules in the PM of HA-GLUT4-GFP HeLa cells. Cells were serum-starved for 2 h prior to the experiment and stimulated with 1 μM insulin for 20 min or left untreated. Cells were fixed and stained for surface HA and dSTORM images acquired. GLUT4 molecule coordinates were obtained using ThunderSTORM and the obtained localization data was subjected to Ripley's K-function analysis using SR Tesseler with the minimum radius 10 nm, step radius 10 nm, and maximum radius 200 nm. $L(r)-r$ (y-axis) represents the clustering ability and r (x-axis) represents the radial scales of clustering. The presented data are mean \pm SD (N=2). The experiment was performed independently 2 times for basal (N=16 cells) and insulin-stimulated (N=16 cells) conditions. $p = 0.0028$; determined by two-tailed Student's t-test.

4.3 Discussion

4.3.1 GLUT4 clustering in adipocytes

The spatial and temporal organization of plasma membrane GLUT4 has been identified to play a key role in the regulation of cell metabolism (Stenkula et al., 2010). In 2010 it has been reported that insulin induces a burst of exocytosis that disperses GLUT4 directly within the PM. Some glucose transporter family members for instance GLUT1 are known to appear as oligomeric structures that influence their transport function (Zottola et al., 1995). However, GLUT4 has been thought to function as a monomer but an inhomogeneous distribution in the PM has been repeatedly observed (Gustavsson et al., 1996; Parton et al., 2002). Previous imaging studies have reported a punctate staining of GLUT4 (Lauritzen et al., 2008; Li et al., 2004; Lizunov et al., 2005). Stenkula et al were the first to identify the presence of GLUT4 clusters and monomers in the PM and quantify the relative amounts of GLUT4 in each state and how this was affected by insulin-stimulation in adipocytes (Stenkula et al., 2010). It was reported that clustered GLUT4 is internalised via recruitment of clathrin and clusters represent the molecular organization that functions as intermediate centre between GLUT4 delivery and reinternalization depending on insulin (Stenkula et al., 2010). Current kinetic models of GLUT4 trafficking propose a tightly regulated system of GLUT4 cycling between storage vesicles, intracellular compartments and the PM (Klip et al., 2019). Insulin has been reported to influence GLUT4 trafficking by interacting with several components of this system. It has been reported that insulin affects sorting and formation of storage compartments (Kandror and Pilch, 1994; Shi and Kandror, 2005), trafficking of GLUT4 towards the PM (Huang et al., 2007), intracellular untethering and PM tethering (Bai et al., 2007; Bogan et al., 2003), GLUT4 fusion and inhibition of endocytosis (Blot and McGraw, 2008). Insulin affects a large number of processes and now evidence is accumulating that one of the key actions of insulin is to regulate GLUT4 distribution within the PM (Gao et al., 2017; Lizunov et al., 2013a; Stenkula et al., 2010). As a consequence a new kinetic model containing 4 quasi-compartments has been proposed for GLUT4 cycling in adipocytes (Figure 1.7).

According to this model GLUT4 cycles between storage vesicles, endosomes and GLUT4 monomers and clusters within the PM (Stenkula et al., 2010). In this study we were able to quantify GLUT4 clustering and insulin-stimulated dispersal with the use of dSTORM (Figure 4.6) in line with the current literature. This then provided us with a mechanism to assess how clustering might underpin key aspects of glucose transport regulation.

4.3.2 Does regulation of clustering underpin observed effects of AMPK activation on glucose transport?

The molecular mechanisms of GLUT4 clustering have not been fully elucidated and in this study we investigated the effect of AMPK activation via stimulation with AICAR on GLUT4 clustering in 3T3-L1 adipocytes. Previous studies have shown that AICAR significantly attenuated insulin-stimulated glucose uptake and GLUT4 translocation. Based on these results we hypothesised that AMPK activation would affect insulin-stimulated GLUT4 dispersal within the PM. Here we report that AMPK activation had no effect on basal GLUT4 clustering but attenuated insulin-stimulated GLUT4 dispersal and shifted the molecular distribution of GLUT4 towards a more clustered state using super resolution microscopy (Figure 4.11). It has been suggested that AMPK is activated in response to cellular stress in adipocytes and inhibits the effects of insulin to conserve ATP levels (Salt et al., 2000). GLUT4 clusters have been described to function as hubs between GLUT4 exocytosis and endocytosis and the main site for GLUT4 internalization. In line with these two hypotheses it seems plausible that AMPK activation affects insulin signalling within the PM through preventing insulin-stimulated GLUT4 dispersal.

4.3.3 Cholesterol depletion and GLUT4 dispersal

Several studies have reported that cholesterol depletion increased the amount of PM GLUT4 and enhanced insulin-sensitivity, resembling the effect of AMPK activation in adipocytes (Chen et al., 2006; Liu et al., 2004; Pattar et al., 2006). Treatment of 3T3-L1 adipocytes with MBCD to deplete membrane cholesterol increased GLUT4 incorporation into the PM. This increase in plasma membrane GLUT4 in response to cholesterol depletion has been attributed to the inhibition of GLUT4 endocytosis (Ros-Baro et al., 2001; Shigematsu et al., 2003). It has been reported that 1 h of MBCD (2-20 mM) treatment of 3T3-L1 adipocytes resulted in a concentration-dependent decrease in the abundance of cholesterol (Parpal et al., 2001). Moreover, increased concentrations of MBCD were observed to inhibit insulin-stimulated glucose uptake especially at MBCD concentrations of 10 mM and above (Parpal et al., 2001). These results indicate that the extent of insulin stimulation on glucose transport was correlated to the abundance of cholesterol in the PM. In our study we incubated 3T3-L1 adipocytes in 5 mM MBCD for 1 h and reported a 7-fold increase in basal glucose transport in line with these findings (Figure 4.13).

The relationship of membrane cholesterol and GLUT4 clustering and dispersal is less well elucidated. Previously clathrin-coated pits and caveolae have been associated with the GLUT4 clustering in the plasma membrane. Multi-colour TIRF microscopy of the co-

localisation and interaction of clathrin and GLUT4 revealed that 25 % of clathrin and total amount of GLUT4-GFP were co-localized in the basal state and this increased to 30-40 % after insulin stimulation in 3T3-L1 adipocytes (Stenkula et al., 2010). However only 8 % of clathrin was found to be co-localized with surface-exposed HA-GLUT4 in the basal state and 11 % after insulin-stimulation. This difference between the total and surface-exposed GLUT4 co-localization with clathrin makes an accumulation of GLUT4 in clathrin-coated pits unlikely. Therefore GLUT4 clustering was not associated with accumulation in caveolar structures in primary rat adipocytes (Stenkula et al., 2010). Another study used dSTORM to study the association between maintenance of GLUT4 clusters and lipid rafts (Gao et al., 2017). The F⁵QQI motif on the N-terminal of GLUT4 has been associated with maintenance of GLUT4 clusters and was mutated to block the association between PM GLUT4 clusters and clathrin-coated pits. It was observed that the F⁵QQI motif mutation of GLUT4 promoted a more clustered distribution of GLUT4 under basal and insulin-stimulated conditions by itself. 3T3-L1 adipocytes with a F⁵QQI motif mutation were treated with 10 mM MBCD for 15 min to disrupt lipid rafts and an increase in GLUT4 density and dispersal of F⁵QQI-GLUT4 was observed under basal conditions (Gao et al., 2017). Previous studies have found that GLUT4 clustering was not associated with clathrin regulation (Lizunov et al., 2013a; Stenkula et al., 2010) and thus it was speculated that the F⁵QQI motif GLUT4 mutation increased amounts of plasma membrane GLUT4 via protein-protein interactions (Gao et al., 2017). There is evidence that cholesterol depletion and disruption of lipid rafts did not disrupt GLUT4 clustering (Lizunov et al., 2013a) whereas this study found that cholesterol depletion dispersed F⁵QQI -GLUT4 indicating a role for lipid rafts in GLUT4 clustering (Gao et al., 2017).

Our finding that cholesterol depletion resulted in increased basal glucose transport seems to contradict our finding that cholesterol depletion enhanced GLUT4 clustering. If GLUT4 clustering functionally diminishes glucose transport in adipocytes the more clustered GLUT4 configuration following cholesterol depletion should result in reduced glucose transport rates. However, the functional role of GLUT4 clustering could be linked to insulin action specifically and here the effect of cholesterol depletion on insulin-stimulated glucose transport and trafficking was not investigated. Basal glucose transport is maintained by GLUT isoform 1 (Calderhead et al., 1990). Another possibility is that in the presence of cholesterol GLUT4 clusters are readily endocytosed. Cholesterol depletion could interfere with this process resulting in increased glucose transport rates. Further studies are needed to elucidate the underlying mechanisms of the effects of cholesterol depletion on glucose transport and PM GLUT4 clustering. Furthermore, the debate of the role of lipid rafts in GLUT4 trafficking and PM

distribution is ongoing. Different methodologies of imaging and data analysis and incubation with different concentrations of MBCD can explain contradictions in findings and more studies are needed to establish the relationship between GLUT4 regulation and lipid rafts.

4.3.4 The role of EFR3 in insulin-stimulated GLUT4 dispersal

Previous work in our laboratory has characterised and discussed the role of EFR3 in insulin-stimulated GLUT4 trafficking (Laidlaw, 2018; Morris, 2020). Two homologues have been identified namely EFR3a and EFR3b (Bojjireddy et al., 2015) and it was found that adipocytes predominantly express EFR3a (Laidlaw, 2018). EFR3 was found to be localised to the PM in 3T3-L1 adipocytes and insulin stimulation had no effect on the distribution of the protein. This indicates that EFR3 plays a role in the dynamics of PM GLUT4 specifically (Laidlaw, 2018; Morris, 2020). Overexpression of EFR3 resulted in increased GLUT4 translocation and glucose uptake in response to insulin and overexpression of a dominant negative mutant inhibited the described effects (Laidlaw, 2018). Knock down of EFR3 resulted in significantly diminished insulin-stimulated glucose transport (Laidlaw, 2018). Knock down of EFR3 did not affect expression levels of other proteins participating in the GLUT4 trafficking machinery indicating that EFR3 acts independently. Insulin-stimulated GLUT4 dispersal was attenuated by EFR3 knock down indicating that EFR3 plays a significant role in GLUT4 clustering (Morris, 2020). As previously discussed EFR3 knock down also resulted in attenuating of insulin-stimulated glucose uptake and linking these results together this is an indirect indication that GLUT4 clustering controls insulin sensitivity in adipocytes. When GLUT4 is clustered in the basal state the ability of GLUT4 to transport glucose into the cell is diminished. This could be due to the conformation of GLUT4 clusters or the distribution of clusters itself in the PM and further experiments are necessary to link GLUT4 dispersal and glucose uptake responses directly (Morris, 2020).

In this study we reanalysed existing STORM raw data of control and EFR3 knock out conditions in basal and insulin-stimulated 3T3-L1 adipocytes. Previously, GLUT4 cluster analysis was performed with automated Ripley's K-function analysis using SR Tesseler (Morris, 2020). Advantages and disadvantages and why this method has been chosen for GLUT4 cluster analysis in this study have been described in detail in chapter 1. Spatial point pattern analysis with spatstat was used to reanalyse previously generated data sets for means of publication and L(r)-r curves generated using spatstat were comparable to those generated with SR Tesseler (Morris, 2020). In the context of this study the reanalysis of existing STORM imaging data of EFR3 knock down in 3T3-L1 cells

has most importantly validated the use of Ripley's K-function analysis with SR Tesseler for other imaging data sets.

4.3.5 HeLa cells as a model system

The HeLa cell line has been derived from cervical cancer cells and is durable, highly prolific, easily genetically manipulated, cheap to obtain, of human origin and has led to significant scientific research advances since its discovery (Masters, 2002). Recently, the cells have been compared to 3T3-L1 adipocytes and it was reported that they have comparable kinetics and orthologous GLUT4 trafficking mechanisms (Morris et al., 2020). In this study we reported that GLUT4 translocated to the PM and dispersed within the PM in HeLa cells in response to insulin. The observed response was quantitatively less pronounced than the one observed in 3T3-L1 adipocytes. Much of our current knowledge of GLUT4 trafficking has been established by the interpretation of data from a variety of model systems. In the 1960s and 1970s primary rat adipocytes were the model of choice until the murine 3T3-L1 cell culture line was developed in 1975 (Green and Kehinde, 1975; Green and Meuth, 1974). Both cell types are derived from rodents and show large insulin-induced increases in glucose transport and GLUT4 translocation (Sato et al., 1993; Yang et al., 1996). A study comparing rat to human adipose tissue revealed that there were no differences in basal glucose transport between species. However, the maximal rate of insulin-stimulated glucose transport was found to be 15-fold lower in human adipose cells compared to rat adipocytes (Kozka et al., 1995). Photo-labelling GLUT4 revealed that 50 % of total GLUT4 molecules translocated to the surface in both rat and human adipocytes in response to insulin stimulation. But it was found that there is a lower overall abundance of surface GLUT4 in human adipocytes. Moreover a higher proportion of total GLUT4 of about 25 % was present in the PM of human adipocytes in the basal state compared to 2 % in rat adipocytes (Kozka et al., 1995). It was hypothesised that differences in insulin response between human and rodent tissues are related to differences in metabolic demands (Kozka et al., 1995). Human adipocytes are bigger in size and can fulfil their basic metabolic needs with a smaller available residual intracellular GLUT4 reserve pool. Modest 2 to 3-fold increases in glucose transport are sufficient in human tissues (Bryant and Gould, 2020). There is a high degree of genetic and physiologic similarities between humans and rodents but species-specific differences in pathways and networks exist and can have profound effects on overall functionality of metabolism (Blais et al., 2017). A large number of rodent animal models have been developed to study T2DM over the last thirty years and numerous studies elucidated T2DM pathogenesis and treatment options in rodents (Chandrasekera and Pippin, 2014). There are still huge gaps in our understanding of human T2DM pathogenesis and no novel treatments indicating a discrepancy in

translation of research results between rodent models and human patients. It has been pointed out that species-specific differences exist between rodents and humans at many levels of glucose regulation reaching from gene/protein expression over cellular signalling mechanisms up to the tissue and organ level (Chandrasekera and Pippin, 2014). Viewed in this context the magnitude of insulin responses in rodent tissues appears to be a species-specific adaptation that should not determine the validity of models to study glucose metabolism, GLUT4 trafficking and dispersal. HeLa cells have much smaller insulin responses and were dismissed as lacking the GLUT4 trafficking machinery in previous years (Bryant and Gould, 2020). This study has reported that HeLa cells respond appropriately to insulin as a stimulus. Insulin did not only stimulate GLUT4 translocation but also controlled GLUT4 distribution within the PM following GLUT4 fusion. We argue that HeLa cells provide a valuable model organism to study GLUT4 dynamics that further the elucidation of mechanisms that operate in human adipose tissues.

Most research of how insulin regulates GLUT4 distribution within the plasma membrane has been carried out in adipocytes to this date. In the next chapter we aim to investigate GLUT4 dispersal in cardiac tissues.

5. Plasma membrane GLUT4 dispersal in cardiomyocytes

5.1 Introduction

5.1.1 Glucose transporters in the healthy heart

The heart beats 100,000 times per day to supply the body with oxygen and nutrients and remove waste products. It needs a continuous energy supply to maintain its contractile function and has adapted to utilise a variety of metabolic substrates (Shao and Tian, 2015; Szablewski, 2017). Substrate utilization is tightly controlled and changed in response to substrate availability. Free fatty acids are the major metabolic substrate for the healthy adult heart to generate ATP (Saddik et al., 1993). Glucose generates 25-30 % of myocardial ATP at rest (Bing et al., 1953). During anoxic conditions the heart switches substrate preference from fatty acid to glucose (Shao and Tian, 2015; Szablewski, 2017). The rate-limiting step of glucose utilization in cardiac muscle is glucose uptake which is mediated by glucose transporters (GLUT) (Chanda et al., 2016). The main GLUT isoforms expressed in the healthy human heart are GLUT1 and GLUT4. Both transporters are differentially expressed during development. GLUT1 is the predominant GLUT in the embryonic and early neonatal heart and is located in the sarcolemma during basal conditions. After birth GLUT1 is downregulated rapidly and GLUT4 is upregulated and becomes the main isoform expressed in the new-born and adult heart (Santalucía et al., 1992). GLUT4 is located in intracellular membrane compartments and translocated to the plasma membrane and T-tubules of cardiomyocytes in response to insulin, catecholamines, increased workload and ischaemia (Egert et al., 1997, 1999; Wheeler et al., 1994). Overall expression of GLUT1 and GLUT4 and their relative distribution determine the rate of glucose transport in the heart. GLUT1 expression in the adult heart is regulated by chronic-hypoxia and long-term fasting (Kraegen et al., 1993; Malhotra and Brosius, 1999; Sivitz et al., 1992). Similarly GLUT4 expression in the adult heart is influenced by various stimuli such as insulin depletion, fatty acids and hormones (Fischer et al., 1996; Gosteli-Peter et al., 1996; Sivitz et al., 1992; Vettor et al., 2002). Changes of expression of these two isoforms have been observed during various pathophysiological states. While insulin (and contraction)-mediated GLUT4 translocation in cardiomyocytes is well-established, currently there is no information available regarding the role of insulin regulation of GLUT4 distribution in the plasma membrane (see Introduction section 1.5).

5.1.2 Insulin-independent stimuli of GLUT4 trafficking in the heart

In cardiac muscle insulin is not the only trigger that induces GLUT4 translocation. Ischaemia and exercise also stimulate GLUT4 translocation and increase glucose transport in the myocardium. Studies demonstrate that the underlying mechanisms are distinct from insulin-stimulated glucose transport and activation of AMPK was identified to mediate the effects (Coven et al., 2003; Egert et al., 1997; Kudo et al., 1995). Exercise was also observed to stimulate GLUT4 translocation by increasing AMPK activity (Coven et al., 2003). Transgenic mice with cardiac AMPK inactivation showed impaired GLUT4 translocation, reduced glucose uptake following ischemia and higher susceptibility to ischemic injury (Russell et al., 1999). Increased workload is associated with increased glucose transport and GLUT4 translocation and the mechanisms are incompletely understood. Recently AMPK activation was suggested to mediate this effect but additional mechanisms likely exist (Abel, 2004).

5.1.3 Challenges of investigating GLUT4 trafficking in cardiac tissue models

Glucose metabolism, insulin signalling and GLUT4 trafficking have been thoroughly investigated in adipose tissues over the past decades (Klip et al., 2019). Adipose tissue is a loose connective tissue located beneath the skin and around internal organs that is easily collected through biopsies. The development of the 3T3-L1 adipocyte cell line as an advantageous *in vitro* model has even furthered research into this particular tissue type (Green and Kehinde, 1975; Green and Meuth, 1974). More than 120 years ago it was discovered that contraction stimulates glucose uptake in skeletal muscle tissue but the mechanisms are still not fully elucidated today (Richter and Hargreaves, 2013). Skeletal muscle consists of thousands of long, large, multinucleated muscle fibres with complex membrane architecture and specialised compartments enabling voluntary movement. This tissue complexity and the existence of a variety of insulin-independent GLUT4 signalling pathways have been technically challenging to investigate. Cardiovascular research is particularly challenging because obtaining human cardiomyocytes is highly invasive and dangerous for patients and there is no appropriate *in vitro* model to study human adult cardiac cell biology (Parameswaran et al., 2013). In the heart, cells are arranged as a three-dimensional anisotropic tissue, embedded in a network of extracellular matrix and exposed to an abundance of biochemical, mechanical, electrical and other types of stimuli (Zuppinger, 2019). Cardiomyocytes repeatedly contract and undergo cyclic deformation, show rapid calcium transients and electrical signals or experience shear stress from blood flow (Zuppinger, 2019). It is impossible to completely recapitulate the physiological or pathological conditions of the

human heart in the laboratory environment (Mathur et al., 2016). However there is a vast availability of experimental models for the study of cardiovascular function and disease with inherent advantages and disadvantages and appreciation of these will help to choose the most appropriate model system for a particular question under investigation (Hearse and Sutherland, 2000).

In vitro models have the advantage that total body and systemic influences are removed and experiments are performed in comparative isolation providing the ability to manipulate a single mechanism at a time (Fearon et al., 2013). The first step in the development of a functional cardiac *in vitro* model is the identification of the optimal source of cardiomyocytes (Mathur et al., 2016). A straightforward model to study changes at the cellular level is the use fully differentiated cells directly isolated from living tissue. For more than a century animal models, explanted hearts and later isolated primary cardiomyocytes have been used to study cardiac cell physiology and electrophysiology and have increased our knowledge tremendously (Zuppinger, 2019).

Neonatal cardiomyocytes have long been used in cardiac research. These cardiomyocytes isolated from neonatal mice and rats profit from an easy and cheap isolation procedure. Furthermore the cells are not sensitive to reintroduction into a calcium-containing medium after dissociation which is associated with an increased cell yield. Neonatal cells are spontaneously beating and readily transfectable. The isolation of rat neonatal cardiomyocytes has some advantages over that of mouse cells for instance higher cell yields, better transfection efficiencies and the ability for prolonged maintenance in culture (Ehler et al., 2013; Parameswaran et al., 2013). Investigations of insulin signalling and GLUT4 trafficking have been carried out in neonatal rat ventricular myocytes previously (Czubryt et al., 2010; Heim et al., 2020; Mangmool et al., 2016; Montessuit et al., 2004, 2006; Morishima et al., 2018). Neonatal rat ventricular myocytes respond appropriately to insulin stimuli and were therefore chosen as a starting point to investigate insulin-regulated GLUT4 dispersal in cardiac tissues. Many studies investigated neonatal and adult cardiomyocytes in combination. Adult cardiomyocytes are more difficult and costly to isolate, are sensitive to calcium gradients and have low cell yields and are difficult to genetically manipulate (Louch et al., 2011). Nevertheless, they represent the most accurate model for the study of adult cardiac physiology (Parameswaran et al., 2013) and therefore they have been included as a model in this investigation.

It is known that variation exists between cardiomyocytes derived from different species (Jayasinghe et al., 2012). Insulin-regulated GLUT4 dispersal has never been investigated in cardiac tissue up to this date. T2DM patients frequently suffer from diabetic

cardiomyopathy and therefore it is of vital importance to further the knowledge of the actions of insulin on cardiac tissues and changes occurring in disease. This is the aim of this investigation. There is no adequate cardiac cell culture model and therefore it is important to approach the investigation from several angles and include a variety of cardiac *in vitro* models to slowly elucidate GLUT4 dispersal cardiac tissues. Recently, there has been a shift in cardiac research towards the use of human-derived cell culture models.

5.1.4 Disease modelling in human induced pluripotent stem cells

In 2006 the ground-breaking discovery that mature cells can be reprogrammed to be pluripotent changed the scientific world (Takahashi and Yamanaka, 2006). In the following years iPSC have been generated from a variety of tissues and a number of different strategies have been explored to reprogram cells (Feng et al., 2009; Stadtfeld and Hochedlinger, 2009; Stadtfeld et al., 2008a). Use of iPSC as a clinical tool in regenerative medicine has proven challenging due to inefficient reprogramming, lack of consistency, spontaneous mutagenesis and existence of an epigenetic memory (Brambrink et al., 2008; Stadtfeld et al., 2008b; Takahashi and Yamanaka, 2013). These challenges need to be overcome for iPSC to reach their full translational potential. Meanwhile iPSC revolutionised biological research and provide an unlimited supply of human tissues for modelling and investigating diseases and high-throughput screening for drug discovery and toxicity *in vitro* (Bragança et al., 2019). The iPSC technology is increasingly used in various areas of cardiovascular research and iPSC-derived cardiomyocytes (iPSC-CM) can be reliably generated by manipulation of developmental signalling pathways required for heart development (Burrige et al., 2012, 2014; Zwi et al., 2009). iPSC-CM are spontaneously beating, arranged as isotropic tissue, exhibit cardiac specific transcription factor/gene/protein expression, demonstrate immature striated patterns, stable pacemaker activity and synchronized action potential propagation (Zwi et al., 2009). Current studies using iPSC-CM have largely focused on investigation of and drug screening for genetic cardiovascular disorders for instance long QT syndrome (Itzhaki et al., 2011; Josowitz et al., 2011; Matsa et al., 2011; Moretti et al., 2010).

Human iPSC-CM also represent an appealing cell source for modelling of DCM (Granéli et al., 2019). In 2014 iPSC-CM were used to develop the first environmentally and genetically driven *in vitro* models of the condition (Drawnel et al., 2014). Cells were cultured in a diabetogenic environment to induce features found in DCM and exposed to high insulin in the absence of glucose to force them to utilise fatty acids as carbon source (Drawnel et al., 2014). Reintroduction of glucose and addition of hormonal

mediators of diabetes were used to mimic the condition of glucose excess despite reliance on fatty acid metabolism found in DCM. Cells presented with hypertrophy, loss of sarcomeric integrity, altered calcium transients, intracellular lipid accumulation, oxidative stress and changes in gene expression indicative of diabetic cardiomyopathic phenotype *in vitro* (Drawnel et al., 2014). Furthermore, dermal fibroblasts from different DCM patients were retrovirally reprogrammed to pluripotency and differentiated into iPSC-CM. The patient-derived iPSC-CM presented with a similar disease phenotype as the cells exposed to a diabetogenic environment (Drawnel et al., 2014) and were used in a screen to identify potentially protective drugs. Such studies emphasise the utility of iPSC-CM, and their value in the investigation of DCM. Therefore, we have chosen iPSC-CM as a model to investigate GLUT4 dispersal in cardiomyocytes of human origin.

5.1.5 Hypothesis and research aims

The aim of this chapter was to investigate and quantify surface GLUT4 spatial patterning at the single molecule level in cardiac tissues using dSTORM. One of the biggest challenges of cardiovascular science is the identification of appropriate *in vitro* models. Here, we aimed to optimise dSTORM imaging in a variety of cardiac cell culture models to research whether insulin stimulation would shift GLUT4 distribution in the PM from a clustered to a more dispersed state as observed in adipocytes. We used neonatal rat ventricular myocytes as starting point for our investigation because their isolation and culture has several advantages. We then moved on to the use of adult rabbit cardiomyocytes to investigate insulin-stimulated GLUT4 dispersal in cardiac tissues because their electrophysiology is closely related to that of the human heart. Finally, we used iPSC-CM as a relevant physiological model of human origin.

5.2 Results

5.2.1 Insulin does not regulate GLUT4 dispersal in neonatal rat ventricular myocytes

A commercial adenovirus was commissioned to express the HA-GLUT4-GFP construct in a variety of cardiac cell culture systems. The construct used for adenovirus generation was similar to that expressed in 3T3-L1 adipocytes and has been previously described (see section 4.2.1). HeLa cells were infected with the HA-GLUT4-GFP adenovirus (Ad-HA-GLUT4-GFP) at varying concentrations and GLUT4 protein expression was assessed by western immunoblotting to verify the efficacy of the virus (Figure 5.1). There was no exogenous GLUT4 protein present in control samples but protein was detected in all HeLa cell samples transduced with Ad-HA-GLUT4-GFP at varying concentrations.

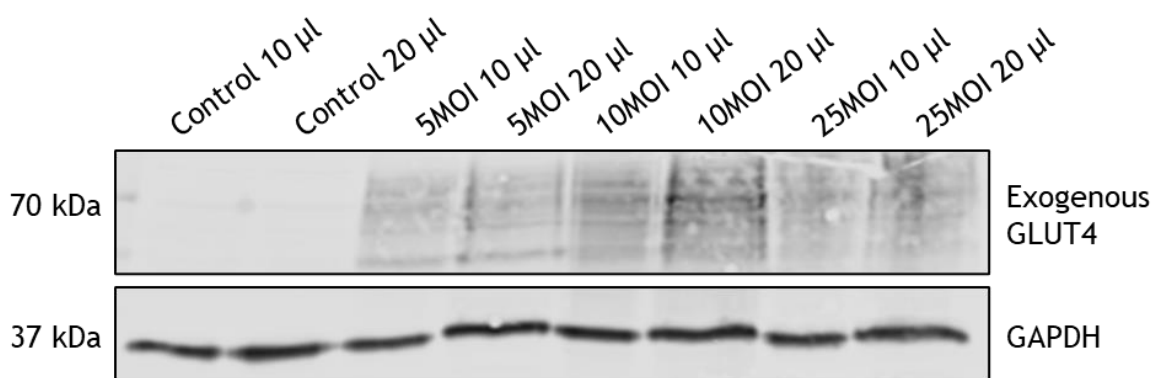


Figure 5.1 GLUT4 protein expression in HeLa cells infected with a commercial HA-GLUT4-GFP adenovirus.

HeLa cells were left untreated (control) or transduced with viral medium containing Ad-HA-GLUT4-GFP at a multiplicity of infection (MOI) of 5, 10 or 25 as labelled (see section 2.3.3. Cells were lysed as outlined (in section 2.6) and 10 μ l and 20 μ l of each sample were loaded (this equates to 30 and 60 % lysate from a 12-well plate). Blots were incubated with anti-GLUT4 or anti-GAPDH (as a loading control) as labelled. Blots were visualised with a LI-COR Odyssey-SA system; data from a typical experiment is shown. HA-GLUT4-GFP is a characteristic ‘smear’ as a consequence of heterogeneous glycosylation at around 70 kDa.

Neonatal rat ventricular myocytes (NRVM) are one of the most well-established models for *in vitro* cardiac research and permit the study of many morphological, biochemical and electrophysiological characteristics of the heart. We chose this model to investigate spatial plasma membrane GLUT4 distribution due to its numerous advantages such as availability, cost-efficiency, ease of gene transfer and ease of isolation and culture. As a starting point we assessed GLUT4 protein expression and insulin sensitivity of isolated NRVM by western immunoblotting (Figure 5.2). NRVM lacked expression of GLUT4 protein which was expected given their early developmental stage. NRVM exhibited insulin-stimulated phosphorylation of Akt, indicating a robust insulin response.

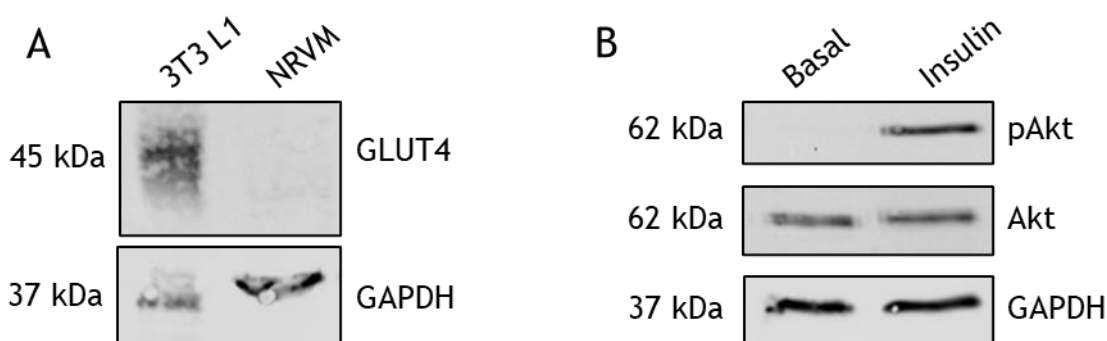


Figure 5.2 Endogenous GLUT4 protein expression and insulin sensitivity in neonatal rat ventricular myocytes.

Neonatal rat ventricular myocytes (NRVM) were isolated as previously described (see 3.3.9) and protein expression was assessed by western immunoblotting. (A) 10 μ l of NRVM sample were loaded (this equates to 25 % lysate from a 6-well plate) next to an equal amount of lysate from 3T3-L1 adipocytes as a control. Blots were incubated with anti-GLUT4 or anti-GAPDH (as a loading control) as labelled. (B) Cells were treated with or without 1 μ M insulin for 20 min as indicated and 20 μ l of NRVM sample were loaded (this equates to 50 % lysate from a 6-well plate). Blots were incubated with anti-Akt or anti-phospho Akt (pAkt). Blots were visualised with a LI-COR Odyssey-SA system; data from a typical experiment is shown.

NRVM were infected with Ad-HA-GLUT4-GFP to perform imaging experiments. The expression of GFP-tagged GLUT4 protein following adenoviral transduction was confirmed by epifluorescence microscopy 48 h post-transduction prior to each imaging experiment. A high number of NRVM expressing GFP was observed and this was indicative of a satisfactory transduction efficiency (data not shown). NRVM transduced with Ad-HA-GLUT4-GFP were beating rhythmically indicating high cell viability and maintenance of functional properties post-transduction. To observe the molecular distribution and quantify the spatial patterning of GLUT4 within the PM HA-staining was carried out and dSTORM images acquired. For the acquisition of dSTORM images NRVM were screened in TIRF mode (Figure 5.3 A and D) and only cells that were brightly fluorescent were chosen and dim cells were avoided. Representative TIRF images show selectively excited diffraction-limited GLUT4-GFP in close proximity to the plasma membrane with elimination of background fluorescence originating from out of focus GLUT4-GFP (Figure 5.3 A and D). Reconstructed dSTORM images show clearly visible single GLUT4 molecules as well as clusters within the PM (Figure 5.3 B and E). The black dots in the cell reconstructions (Figure 5.3 B and E) are density artefacts that may have originated from laminin-coating of glass coverslips to ensure adherence of NRVM. Magnifications of reconstructed images for (C) basal and (F) insulin-stimulated cells are shown in figure 5.3.

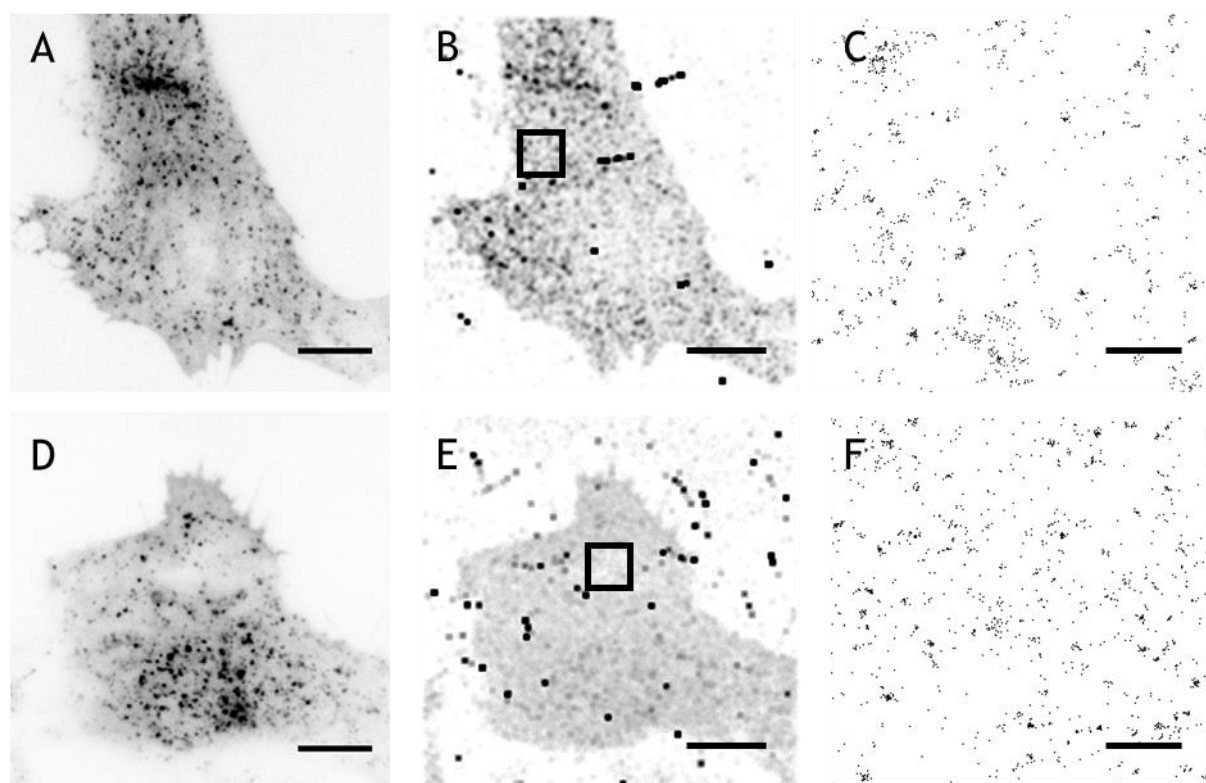


Figure 5.3 TIRF and STORM images of surface GLUT4 in basal and insulin-stimulated neonatal rat ventricular myocytes.

NRVM transduced with Ad-HA-GLUT4-GFP were incubated in serum-free medium for 2 h prior to the experiment and stimulated with 1 μM insulin for 20 min or left untreated. Cells were fixed and stained for surface HA and dSTORM images acquired on a Zeiss Elyra PS.1 (see section 2.3). Reconstructions of raw images were calculated using the ImageJ plugin ThunderSTORM. (A) Representative TIRF image of a NRVM. (B) Representative scatterplot of a basal cell showing localisations of single GLUT4 molecules. (C) Magnified section of image B. (D) Representative TIRF image of an insulin-stimulated cell. (E) Representative scatterplot of an insulin-stimulated cell showing localisations of single GLUT4 molecules. (F) Magnified section of image D. Scale bars = 10 μm (A, B, D, E) and 1 μm (C and F). This experiment was repeated 3 times with similar results.

Insulin stimulates GLUT4 translocation in several tissues (Bryant and Gould, 2020) and we investigated whether this applies to NRVM by determination of GLUT4 localisation density in the plasma membrane per μm^2 (Figure 5.4). The localisation density of GLUT4 molecules significantly increased by 35 % from 347 localisations per μm^2 in the basal state to 517 per μm^2 after insulin stimulation. This shows that more GLUT4 molecules were present in the plasma membrane of NRVM following insulin stimulation. Therefore, insulin-stimulated GLUT4 translocation occurs in NRVM but the observed effect is modest (but statistically significant).

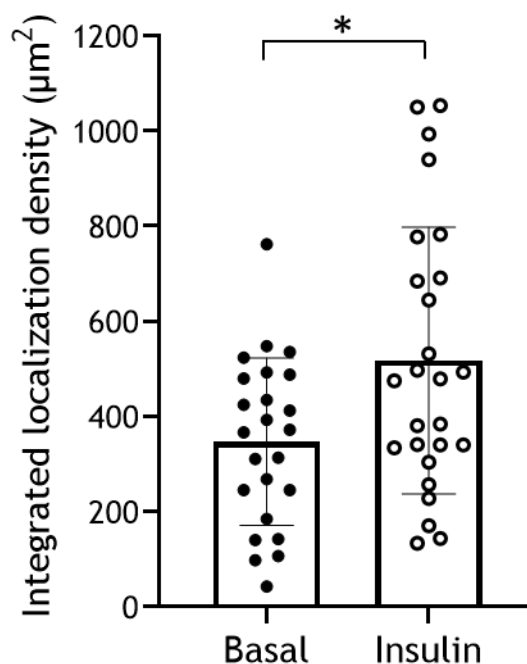


Figure 5.4 Localisation density in basal and insulin-stimulated neonatal rat ventricular myocytes determined by dSTORM imaging.

NRVM transduced with Ad-HA-GLUT4-GFP were incubated in serum-free medium for 2 h prior to the experiment and stimulated with 1 μM insulin for 20 min or left untreated. Cells were fixed and stained for surface HA and dSTORM images acquired on a Zeiss Elyra PS.1 (described in section 2.3). Reconstructions of raw images were calculated using the ImageJ plugin ThunderSTORM. Localisation density was determined using the ImageJ plugin LocFileVisualizer (see section 2.3.10). Basal: 347 ± 175 ($n = 24$), Insulin: 517 ± 280 ($n = 26$). Mean \pm SD. $p = 0.0141$; determined by unpaired two-tailed Student's t-test.

Ripley's L-function analysis was carried out to quantify changes in GLUT4 dispersal in the PM of basal and insulin-stimulated NRVM (previously described in 4.2.1). Figure 5.5 shows the averaged L(r) functions for basal and insulin-stimulated cells from three independently performed experiments. The observed L(r) peaked at similar clustering values for GLUT4 on the PM of untreated and insulin-stimulated cells. This indicates that there was no significant difference in GLUT4 clustering on the plasma membrane in response to insulin-stimulation.

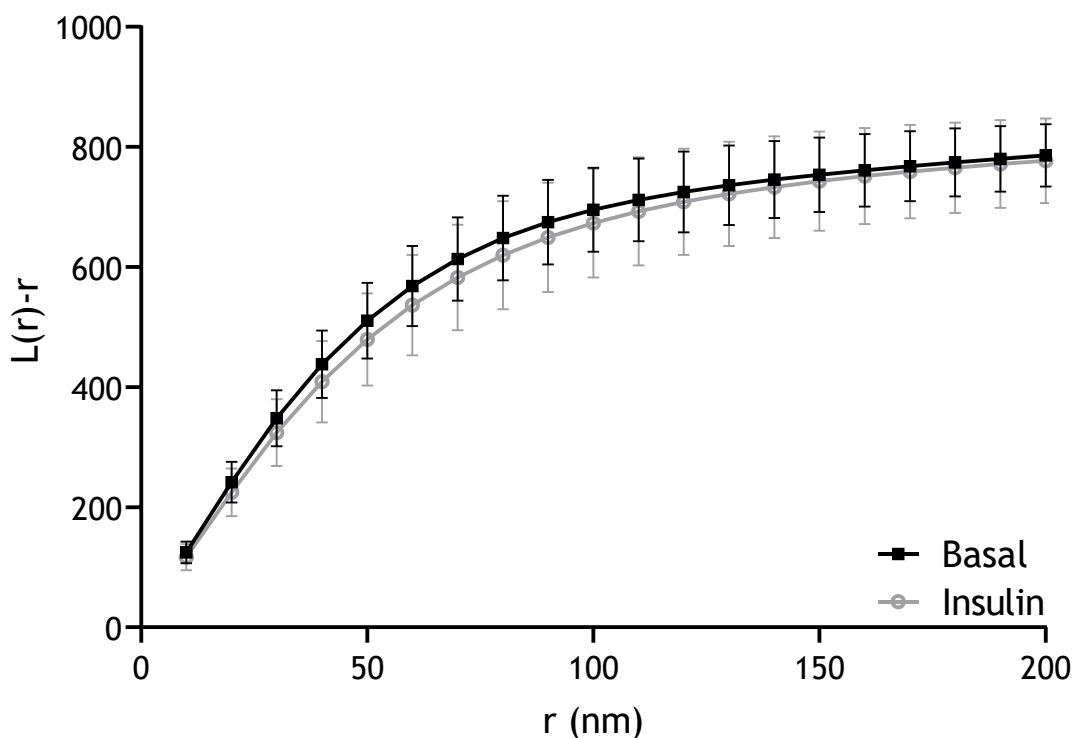


Figure 5.5 Ripley's L-function analysis of GLUT4 clustering in basal and insulin-stimulated neonatal rat ventricular myocytes.

Representative plot of Ripley's K function analysis of the clustering abilities of GLUT4 molecules in the PM of HA-GLUT4-GFP NRVM. Cells were serum-starved for 2 h prior to the experiment and stimulated with 1 μ M insulin for 20 min or left untreated. Cells were fixed and stained for surface HA and dSTORM images acquired. GLUT4 molecule coordinates were obtained using ThunderSTORM and the obtained localization data was subjected to Ripley's K-function analysis using SR Tesseler with the minimum radius 10 nm, step radius 10 nm, and maximum radius 200 nm. $L(r)-r$ (y-axis) represents the clustering ability and r (x-axis) represents the radial scales of clustering. The presented data are mean \pm SD. The experiment was performed independently 3 times for basal (N=24 cells) and insulin-stimulated (N=26 cells) conditions. $p > 0.99$; determined by one-way ANOVA.

NRVM are in the postnatal developmental stage and still have the ability to grow, divide and differentiate providing many advantages for long-term cell culture applications. However, NRVM have unique features and differ from adult fully differentiated cardiomyocytes. GLUT4 expression and trafficking change greatly throughout development and therefore NRVM may not be the most advantageous model to study insulin-stimulated GLUT4 dispersal. In the following we used cardiomyocytes isolated from rabbits to further our knowledge of GLUT4 trafficking in a physiologically relevant system of the adult myocardium.

5.2.2 Primary cardiomyocytes are a challenging model for the investigation of GLUT4 dispersal in cardiac tissues

We assessed GLUT4 protein expression of freshly isolated cardiomyocytes by western immunoblotting (Figure 5.6). Rabbit cardiomyocytes expressed GLUT4 protein after isolation but GLUT4 protein was less abundant than in adipocytes.

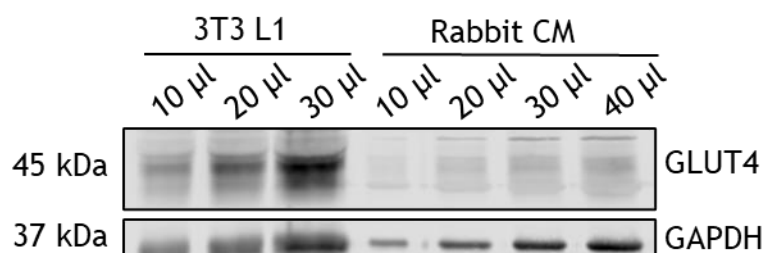


Figure 5.6 Endogenous GLUT4 protein expression of isolated rabbit cardiomyocytes. Rabbit cardiomyocytes were isolated as previously described (see 3.3.7) and protein expression was assessed by western immunoblotting. (A) Different amounts of cardiomyocyte samples were loaded as labelled (10 μ l of sample equate to 25 % from a 12-well plate). Equal amounts of lysate from 3T3-L1 adipocytes were loaded as a control. Blots were incubated with anti-GLUT4 or anti-GAPDH (as a loading control) as labelled. Blots were visualised with a LI-COR Odyssey-SA system; data from a typical experiment is shown.

Cardiomyocytes in the whole heart are strongly connected by intercalated discs and extracellular matrix and form a functional syncytium. Dissociation and maintenance in culture as single cells results in dedifferentiation associated physiological changes. Therefore, we assessed changes in GLUT4 protein expression in cultured cardiomyocytes over time by western immunoblotting (Figure 5.7). We observed that GAPDH protein expression decreased by around 40 % at 48 h in culture indicating a decline in cell survival. Furthermore, GLUT4 protein expression, normalised against GAPDH levels, decreased by about 50 % over a similar period (Figure 5.7 B). It appears that GLUT4 protein expression is relatively stable during the first 24 h post-isolation, then decreases dramatically after the second day in culture.

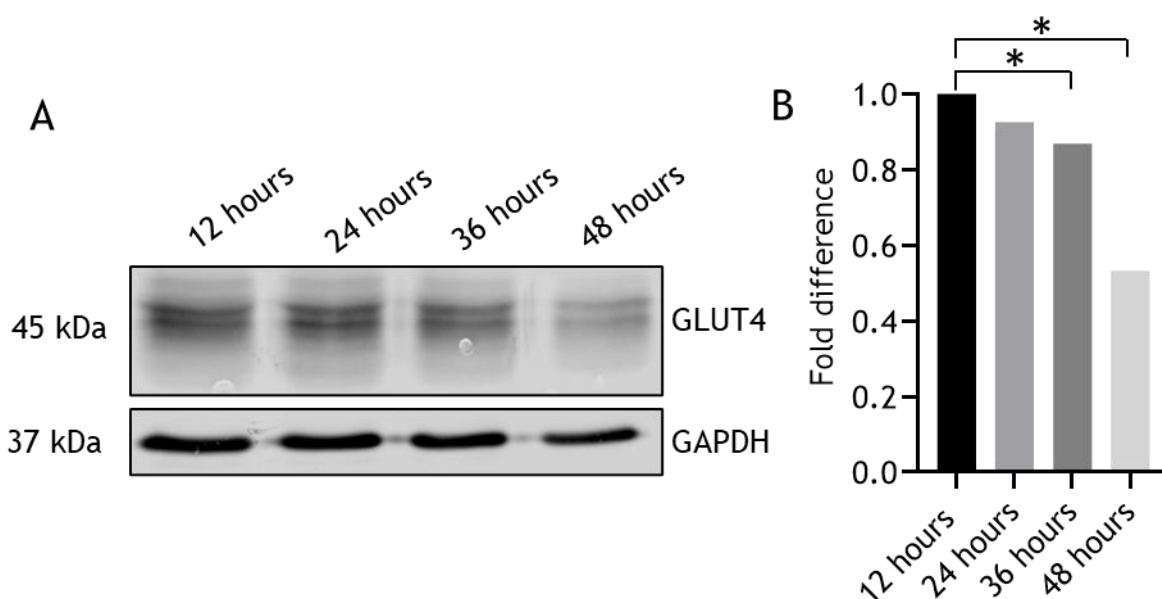


Figure 5.7 Changes in endogenous GLUT4 protein expression of isolated rabbit cardiomyocytes over time.

Rabbit cardiomyocytes were isolated as previously described (see 3.3.7) and protein expression was assessed by western immunoblotting. (A) Cardiomyocytes were plated in culture medium and protein expression assessed at 12h, 24h, 36h and 48h as labelled. 20 μ l of lysate were loaded (this equates to 50 % of sample from a 12-well plate). Blots were incubated with anti-GLUT4 or anti-GAPDH (as a loading control) as labelled. (B) Quantification of the immunoblot displayed in panel (A) performed via densitometry, expressed as fold change of basal GLUT4 signal normalized against GAPDH. $p < 0.0001$ indicated by *; determined by one-way ANOVA. Blots were visualised with a LI-COR Odyssey-SA system; data from a typical experiment is shown.

The previous experiment showed a reduction in cell viability over time. Cardiomyocytes had to be kept in culture for at least 48 h post-isolation to be able to express the GFP-tagged GLUT4 construct via adenoviral transduction. Therefore, we assessed the insulin sensitivity of adult cardiomyocytes over time to ensure the cells remained responsive for the time needed to transduce them with Ad-HA-GLUT4-GFP (Figure 5.8). The cells showed insulin-stimulated phosphorylation of Akt and this response was preserved up to 48 h post-isolation (Figure 5.8 A). However, the experiment was replicated many times and in several batches of cardiomyocytes a loss of insulin-stimulated phosphorylation of Akt was frequently detected (Figure 5.8 B) indicating batch-to-batch variations.

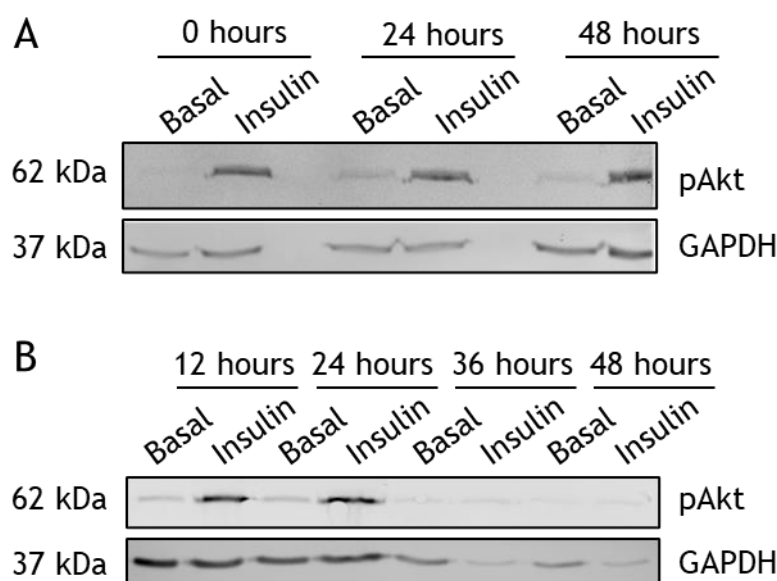


Figure 5.8 Changes of insulin sensitivity in rabbit cardiomyocytes over time. Rabbit cardiomyocytes were isolated as previously described (see 3.3.7) and protein expression was assessed by Western immunoblotting. Cells were stimulated with 1 μ M insulin for 20 min or left untreated and 20 μ l of sample were loaded (this equates to 50 % lysate from a 12-well plate). (A) Protein expression assessed at 0, 24 and 48 h post-isolation. Blots were incubated with anti-phospho Akt or anti-GAPDH (as a loading control) as labelled. (B) Similar experiment performed on a different batch of isolated cardiomyocytes at 12, 24, 36 and 48 h post-isolation. Blots were visualised with a LI-COR Odyssey-SA system; data from two typical experiments is shown.

GAPDH protein expression was observed to decline similarly which might be due to reduced cell viability (Figure 5.8 B). We also observed that cardiomyocytes did not attach well to surfaces (data not shown). Next, we investigated the use of different substrates for efficient cardiomyocyte attachment. Several substrates were used to attach cardiomyocytes to glass coverslips (Figure 5.9). Poly-D-lysine provided the best overall cell attachment and was superior to other reagents examined and consequently this method was used for further experiments.

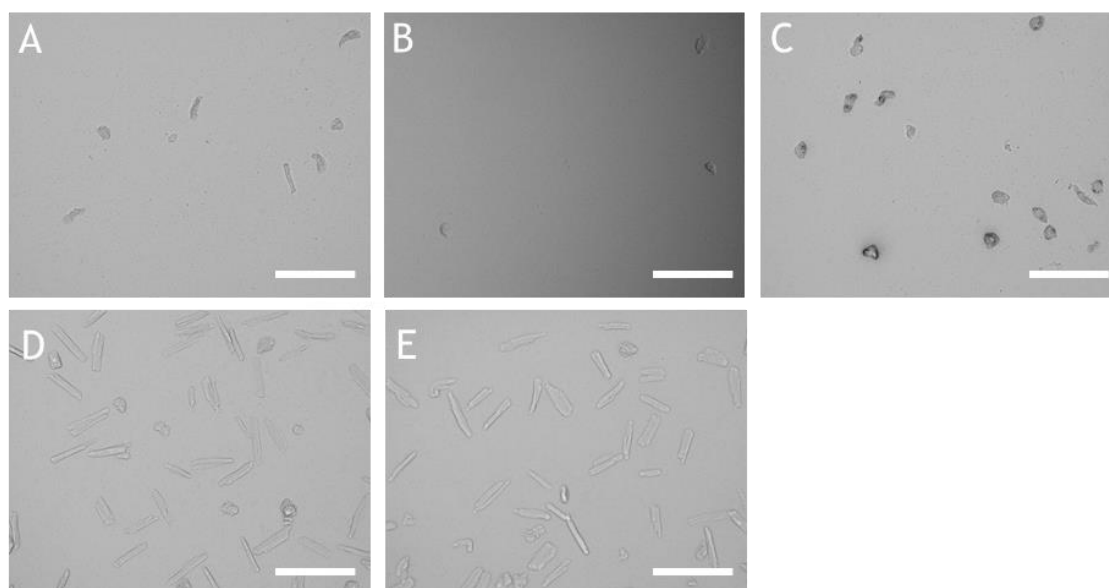


Figure 5.9 Optimisation of substrates used in primary cardiomyocyte culture to attach cells to glass coverslips.

Rabbit cardiomyocytes were isolated as previously described (see 3.3.7). Glass coverslips were cleaned and (A) left uncoated or coated with (B) 2% gelatin, (C) Collagen type I, (D) poly-D-lysine 50mg/mL, (E) poly-D-lysine 100mg/ml. Phase contrast images of fixed cells were acquired on an EVOS FL Auto imaging system 48 h after seeding the cardiomyocytes onto the substrates. Data from one typical experiment is shown. Scale bars = 250 μ m.

Having established reasonable cell adherence, we then investigated glucose uptake in isolated rabbit cardiomyocytes using ^3H labelled 2-deoxyglucose as a means to establish the validity of this model system (Figure 5.10). Rabbit cardiomyocytes were left untreated or stimulated with 1 μ M insulin for 20 min and a significant 2-fold increase in glucose uptake was observed.

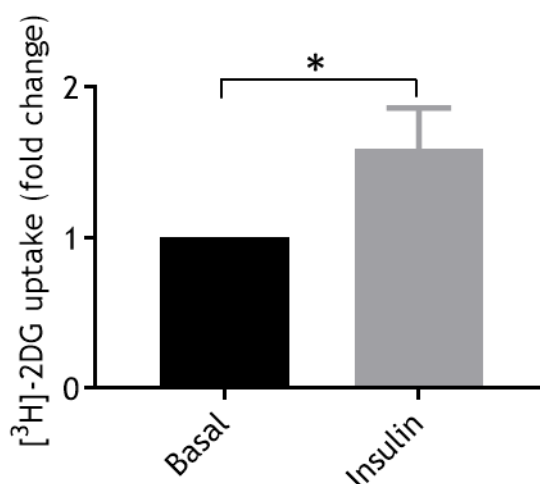


Figure 5.10 Insulin-stimulated deoxyglucose uptake in rabbit cardiomyocytes.

2-deoxyglucose uptake was measured as described (section 2.5.2). Cardiomyocytes were washed with KRP and treated with or without 1 μ M insulin for 20 min followed by a 30 min uptake of 2-deoxyglucose at 37 $^{\circ}$ C. Basal glucose uptake rates were typically of the order of 1,600 counts per min/well. The data displayed represent fold changes of insulin stimulation from one representative experiment. The experiment was performed three times. $p=0.0059$ indicated by *; determined by two-tailed Student's t-test.

After optimisation of primary cardiomyocyte culture conditions, we transduced cells with Ad-HA-GLUT4-GFP to perform imaging experiments. Epifluorescence microscopy images of HA-GLUT4-GFP cardiomyocytes showed that the rod-shaped cardiomyocytes had rounded edges and sarcomeres appeared disorganized (Figure 5.11 A). These changes are commonly observed during primary cardiomyocyte culture. Imaging the cells in TIRF-mode revealed that cardiomyocytes attached only partly to the glass coverslips and that the membrane does not sit flat on the glass (Figure 5.11 B). This made it impossible to image these cells in TIRF mode and perform successful dSTORM experiments.

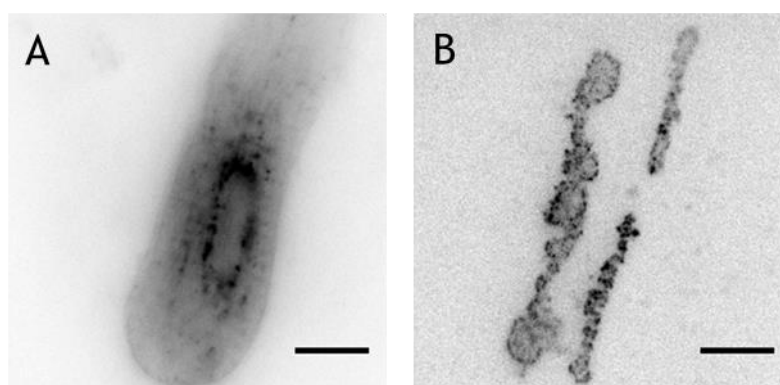


Figure 5.11 Epifluorescence and TIRF images of HA-GLUT4-GFP cardiomyocytes. Isolated cardiomyocytes were transduced with Ad-HA-GLUT4-GFP and fixed and images acquired on a Zeiss Elyra PS.1 (see section 2.3). (A) Representative epifluorescence image of cardiomyocyte showing GLUT4-GFP. (B) Representative TIRF image of the same cardiomyocyte showing only GLUT4-GFP in close proximity to the glass coverslip. Scale bars 10 μm .

A wide range of substrates was examined to attach cardiomyocytes more effectively to the glass coverslips to perform successful super resolution imaging (data not shown). But the rod-shaped cardiomyocytes were observed mostly floating above the glass coverslips which only exposed a small part of their membrane for imaging experiments (Figure 5.12 A). Another obstacle was that primary cardiomyocyte cultures contained a high number of apoptotic cells and the cellular debris interfered with HA-staining and produced imaging artefacts (Figure 5.12 B). Even those cells that attached partly to the coverslips and were successfully imaged in TIRF mode did not lead to the production of clean reconstructions of GLUT4 localisations. Numerous imaging experiments were performed with different parameters but the quality of the raw data remained questionable.

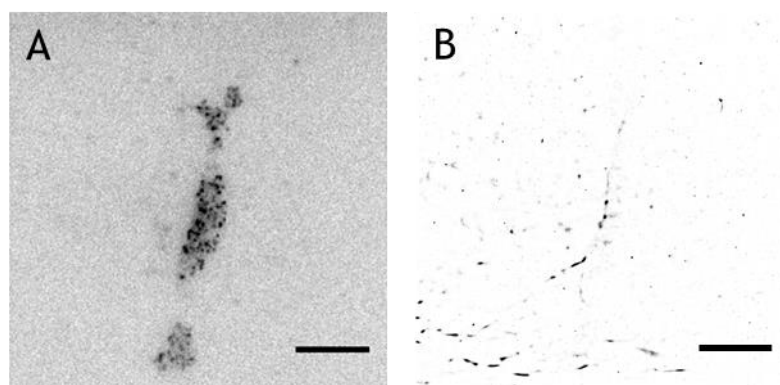


Figure 5.12 TIRF and dSTORM images of HA-GLUT4-GFP cardiomyocytes. Isolated cardiomyocytes were transduced with Ad-HA-GLUT4-GFP. Cells were fixed and stained for surface HA and images acquired on a Zeiss Elyra PS.1 (see section 2.3). (A) Representative TIRF image of a cardiomyocyte. (B) Representative scatterplot of the same cell showing localisations of single GLUT4 molecules. Scale bars 10 μ m.

5.2.3 Insulin regulates GLUT4 dispersal in human induced pluripotent stem cell-derived cardiomyocytes (NCardia)

We commercially obtained induced pluripotent stem cell-derived cardiomyocytes (iPSC-CM) from Axiogenesis (this company has recently merged with Pluriomics to form NCardia) and FUJIFILM Cellular Dynamics International (CDI) and performed western immunoblotting to assess GLUT4 protein expression and insulin sensitivity (Figure 5.13 and 5.14). These experiments were carried out and published by Peter Bowman, a member of our lab (Bowman et al., 2019), and not repeated by myself due to the high cost associated with these cells. Relative to primary rodent cardiomyocytes both iPSC-CM obtained from NCardia and CDI were found to express low levels of endogenous GLUT4 (Figure 5.13).

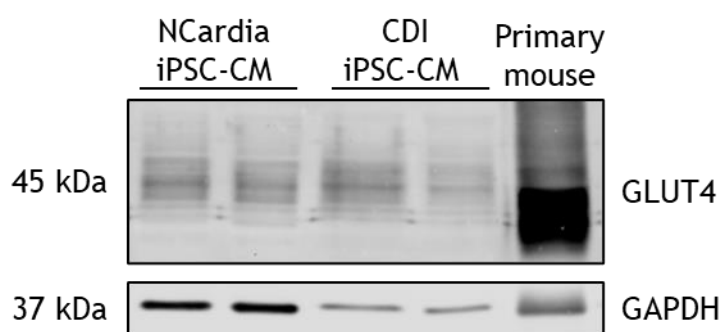


Figure 5.13 Endogenous GLUT4 protein expression of induced pluripotent stem cell-derived cardiomyocytes from two commercial sources.

Induced pluripotent stem cell-derived cardiomyocytes (iPSC-CM) were obtained from two sources and protein expression was assessed by western immunoblotting. Two times 20 μ l of sample generated from NCardia and CDI iPSC-CM was loaded next to one sample of primary mouse cardiomyocytes (5 μ g total protein). Note that 20 μ l iPSC-CM corresponds to lysate generated from approximately 20,000 cells. Blots were incubated with anti-GLUT4 or anti-GAPDH (as a loading control) as labelled. Blots were visualised with a LI-COR Odyssey-SA system; data from a typical experiment is shown that was carried out independently three times (N=3).

In iPSC-CM the insulin signalling intermediate Akt was expressed and capable of exhibiting insulin-stimulated phosphorylation (Figure 5.14). In NCardia iPSC-CM insulin-stimulated phosphorylation of Akt was hard to detect because a very strong basal phosphorylation of Akt was observed (Figure 5.14 A). CDI iPSC-CM showed a more pronounced increase in Akt phosphorylation in response to insulin stimulation with a lower basal Akt phosphorylation (Figure 5.14 B).

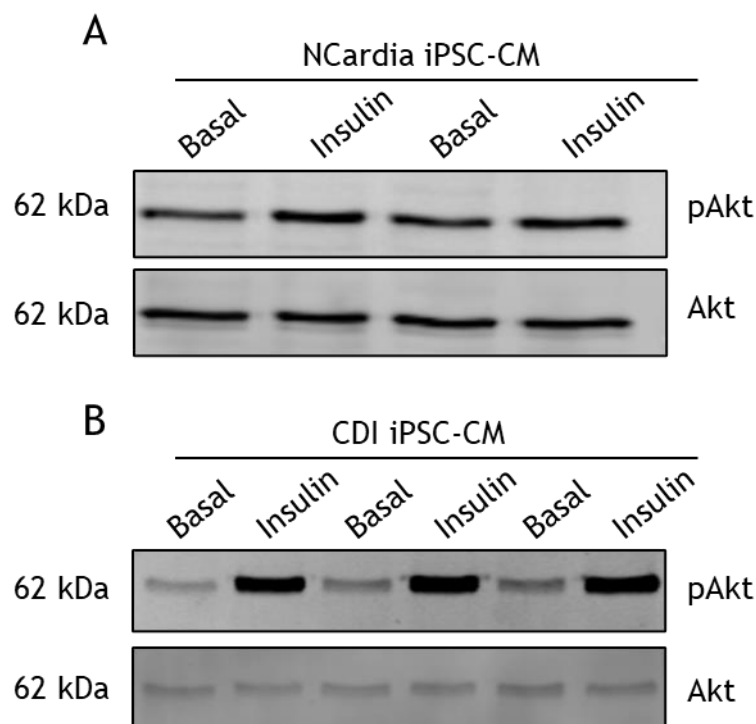


Figure 5.14 Insulin sensitivity of induced pluripotent stem cell-derived cardiomyocytes from two commercial sources.

iPSC-CM were commercially obtained and protein expression assessed by western immunoblotting. Cells were serum starved 3 h prior to the experiment and stimulated with 860 nM insulin for 30 min or left untreated and 20 μ l of sample were loaded. (A) Protein expression of NCardia iPSC-CM from 2 technical replicates of basal and insulin stimulated lysates from 1 biological sample. Blots were incubated with anti-phospho Akt or anti-Akt as labelled. (B) Similar experiment for CDI iPSC-CM including 3 replicate samples for each condition within one experimental day. Blots were visualised with a LI-COR Odyssey-SA system; data from a typical experiment is shown, carried out independently three times (N=3).

In the following we transduced NCardia iPSC-CM with Ad-HA-GLUT4-GFP to investigate the spatial patterning of GLUT4 within the PM. HA-staining was carried out and dSTORM images acquired. As previously described NCardia iPSC-CM were screened in TIRF mode to selectively excite GLUT4-GFP in close proximity to the PM (Figure 5.15 A and D). Reconstructed dSTORM images of HA-GLUT4-GFP iPSC-CM show clearly visible single GLUT4 molecules as well as clusters within the PM (Figure 5.15 B and E). Magnifications of these images seen in figure 5.15 for a (C) basal and (F) insulin-stimulated cell show clearly defined GLUT4 clusters at the cell surface of basal cells.

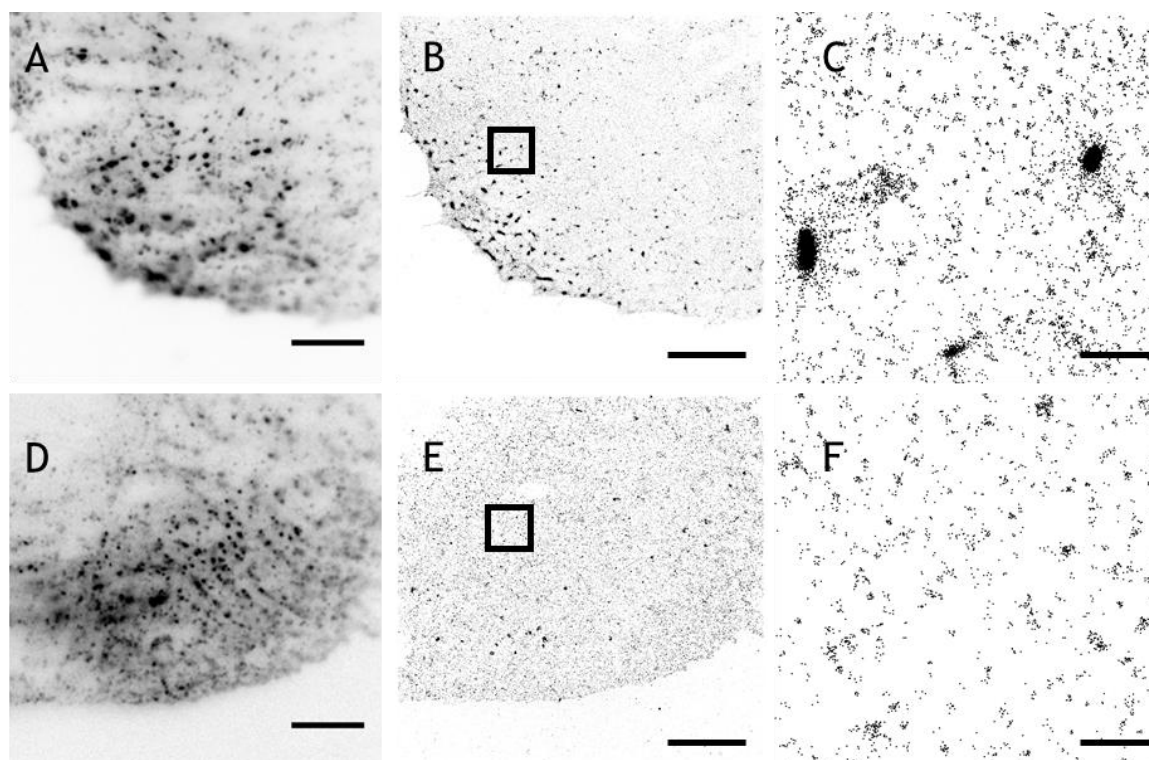


Figure 5.15 TIRF and STORM images of surface GLUT4 in basal and insulin-stimulated induced pluripotent stem cell-derived cardiomyocytes obtained from NCardia. NCardia iPSC-CM transduced with Ad-HA-GLUT4-GFP were incubated in serum-free medium for 2 h prior to the experiment and stimulated with 1 μM insulin for 20 min or left untreated. Cells were fixed and stained for surface HA and dSTORM images acquired on a Zeiss Elyra PS.1 (see section 2.3). Reconstructions of raw images were calculated using the ImageJ plugin ThunderSTORM. (A) Representative TIRF image of a cell. (B) Representative scatterplot of a basal cell showing localisations of single GLUT4 molecules. (C) Magnified section of image B. (D) Representative TIRF image of an insulin-stimulated iPSC-CM. (E) Representative scatterplot of an insulin-stimulated cell showing localisations of single GLUT4 molecules. (F) Magnified section of image D. Scale bars 10 μm (A, B, D, E) and 1 μm (C and F). This experiment was repeated 2 times with similar results.

We investigated whether insulin stimulates GLUT4 translocation in NCardia iPSC-CM by determination of GLUT4 localisation density in the plasma membrane per μm^2 (Figure 5.16). The localisation density of GLUT4 molecules significantly increased by 70 % in response to insulin stimulation indicating occurrence of GLUT4 translocation in iPSC-CM.

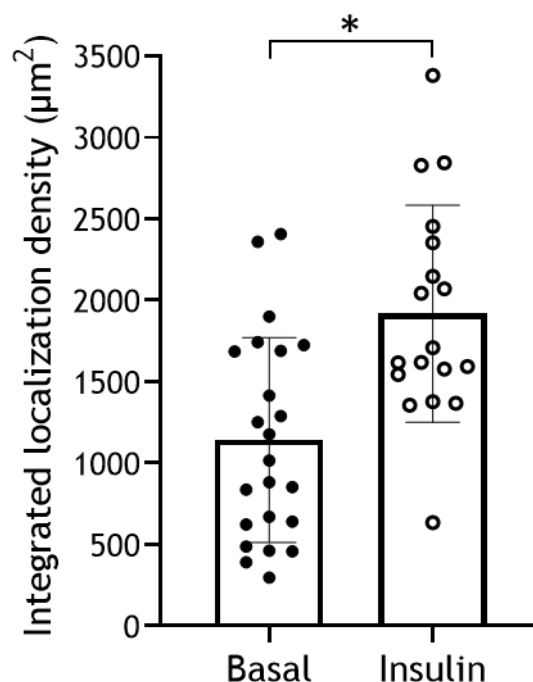


Figure 5.16 Localisation density in basal and insulin-stimulated induced pluripotent stem cell derived cardiomyocytes determined by dSTORM imaging.

IPSC-CM transduced with Ad-HA-GLUT4-GFP were incubated in serum-free medium for 2 h prior to the experiment and stimulated with 1 μM insulin for 20 min or left untreated. Cells were fixed and stained for surface HA and dSTORM images acquired on a Zeiss Elyra PS.1 (described in section 2.3). Reconstructions of raw images were calculated using the ImageJ plugin ThunderSTORM. Localisation density was determined using the ImageJ plugin LocFileVisualizer (see 2.3.10). Basal: 1142 ± 131 ($n = 23$), Insulin: 1918 ± 157 ($n = 18$). Mean \pm SD. $p = 0.0005$; determined by unpaired two-tailed Student's t-test.

Ripley's L-function analysis was carried out to quantify changes in GLUT4 dispersal in the PM of basal and insulin-stimulated NCardia iPSC-CM. Figure 5.17 shows the averaged L(r) functions for basal and insulin-stimulated cells from two independently performed experiments. The observed L(r) peaked at higher clustering values for GLUT4 on the PM of untreated iPSC-CM compared to insulin-stimulated cells with a significant difference (section 2.3.10). This indicates that GLUT4 on the plasma membrane was less clustered in response to insulin-stimulation. To our knowledge this was the first time that insulin-stimulated GLUT4 dispersal was observed in a cardiac cell culture model.

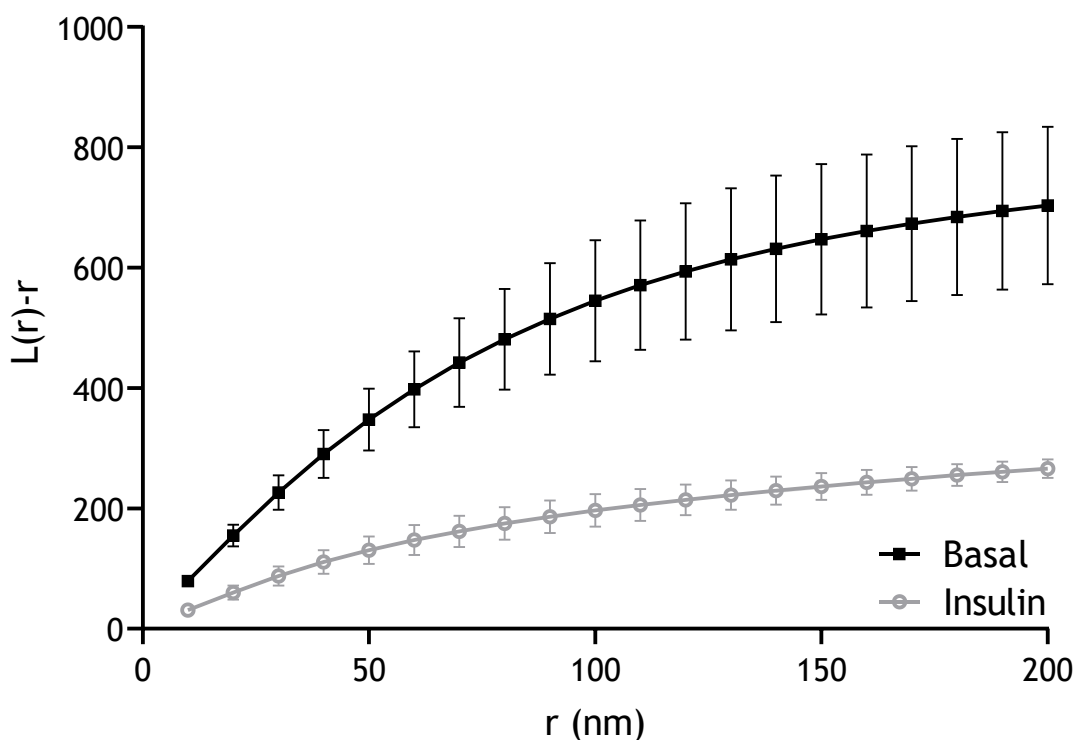


Figure 5.17 Ripley's L-function analysis of GLUT4 clustering in basal and insulin-stimulated induced pluripotent stem cell-derived cardiomyocytes from NCardia. Representative plot of Ripley's K function analysis of the clustering abilities of GLUT4 molecules in the PM of HA-GLUT4-GFP iPSC-CM. Cells were serum-starved for 2 h prior to the experiment and stimulated with 1 μ M insulin for 20 min or left untreated. Cells were fixed and stained for surface HA and dSTORM images acquired. GLUT4 molecule coordinates were obtained using ThunderSTORM and the obtained localization data was subjected to Ripley's K-function analysis using SR Tesseler with the minimum radius 10 nm, step radius 10 nm, and maximum radius 200 nm. $L(r)-r$ (y-axis) represents the clustering ability and r (x-axis) represents the radial scales of clustering. The presented data are mean \pm SD. The experiment was performed independently 2 times for basal (N=24 cells) and insulin-stimulated (N=20 cells) conditions. $p < 0.0001$; determined by one-way ANOVA of all cells combined from N=2.

After the performance of these two independent experiments NCardia announced that they detected embryonic markers in their batches of iPSC-CM making the origin of the cells questionable (personal communication). The cells were no longer commercially available for an indefinite amount of time until quality control measures of iPSC production were met again by the company. Our previous experiments showed differences in GLUT4 protein expression and insulin sensitivity between NCardia and CDI iPSC-CM. We continued our investigation of GLUT4 dispersal in cardiac tissues using CDI iPSC-CM and repeated the super resolution microscopy experiments previously carried out in NCardia iPSC-CM.

5.2.4 Differences in insulin-stimulated GLUT4 dispersal exist in human induced pluripotent stem cell-derived cardiomyocytes depending on their source

CDI iPSC-CM transduced with Ad-HA-GLUT4-GFP exhibited a less strong expression of GFP hinting at a lower transduction efficiency compared to cells obtained from NCardia (Figure 5.18). Furthermore, it was observed that CDI iPSC-CM are morphologically different from NCardia iPSC-CM. CDI cells (Figure 5.18) were generally smaller compared to NCardia cells (Figure 5.15). Screening the cells in TIRF mode it became obvious that NCardia cells are bigger and spread out more evenly on the glass coverslips so that their complete membrane comes in close contact with the coverslip (Figure 5.15). However, CDI iPSC-CM seemed smaller and more rounded and formed adhesions to the coverslips only on their outer edges (Figure 5.18). Reconstructions of dSTORM images show GLUT4 molecules in the plasma membrane (Figure 5.18 B and D) and magnifications of these images show no difference in GLUT4 clustering or molecule density in (C) basal and (F) insulin-stimulated CDI iPSC-CM.

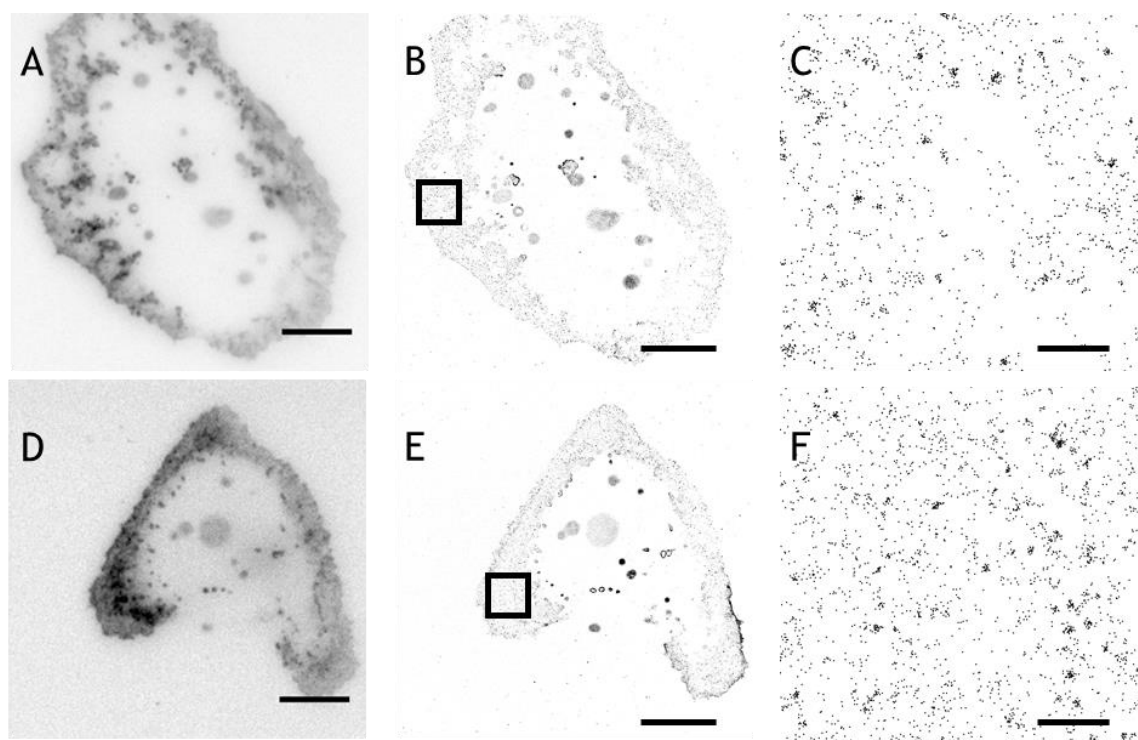


Figure 5.18 TIRF and STORM images of surface GLUT4 in basal and insulin-stimulated induced pluripotent stem cell derived cardiomyocytes.

iPSC-CM transduced with Ad-HA-GLUT4-GFP were serum starved for 2 h and stimulated with 1 μ M insulin for 20 min or left untreated. Cells were fixed and stained for surface HA and dSTORM images acquired (see section 2.3). Reconstructions were calculated using ThunderSTORM. (A) Representative TIRF image of a basal cell (B) Scatterplot of a basal cell showing localisations of single GLUT4 molecules. (C) Magnified section of image B. (D) Representative TIRF image of an insulin-stimulated iPSC-CM. (E) Scatterplot of an insulin-stimulated cell showing localisations of single GLUT4 molecules. (F) Magnified section of image D. Scale bars = 10 μ m (A, B, D, E) and 1 μ m (C and F). This experiment was repeated 2 times with similar results.

We investigated whether insulin stimulates GLUT4 translocation in CDI iPSC-CM as previously described (Figure 5.19). The localisation density of GLUT4 molecules significantly increased by 40 % in response to insulin stimulation indicating occurrence of GLUT4 translocation in iPSC-CM. GLUT4 localisation density per μm^2 in basal and insulin-stimulated CDI cells was 75 % less compared to cells obtained from NCardia (Figure 5.16).

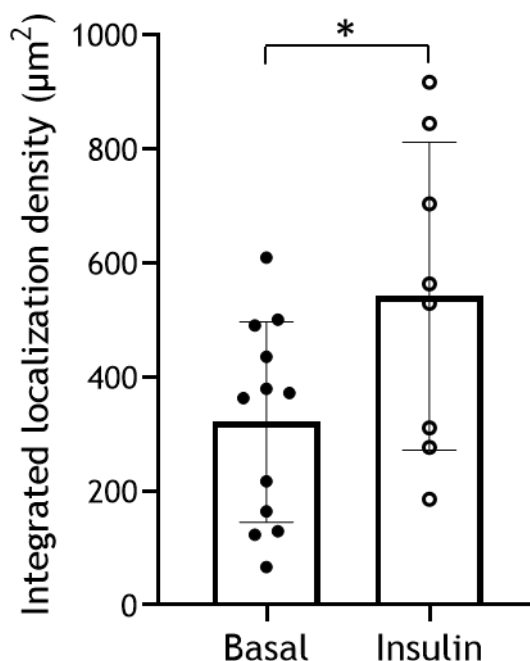


Figure 5.19 Localisation density in basal and insulin-stimulated induced pluripotent stem cell derived cardiomyocytes determined by dSTORM imaging.

IPSC-CM transduced with Ad-HA-GLUT4-GFP were incubated in serum-free medium for 2 h prior to the experiment and stimulated with $1 \mu\text{M}$ insulin for 20 min or left untreated. Cells were fixed and stained for surface HA and dSTORM images acquired on a Zeiss Elyra PS.1 (described in section 2.3). Reconstructions of raw images were calculated using the ImageJ plugin ThunderSTORM. Localisation density was determined using the ImageJ plugin LocFileVisualizer (see 3.4.10). Basal: 321 ± 176 ($n = 12$), Insulin: 541 ± 270 ($n = 8$). Mean \pm SD. $p = 0.0394$; determined by unpaired two-tailed Student's t-test.

Again we used Ripley's L-function analysis to quantify changes in GLUT4 dispersal in CDI iPSC-CM. The experiment was carried out several times but in most cases the transduction was ineffective and the fluorescence signal was too low to quantify molecular GLUT4 dynamics. Figure 5.20 shows the averaged L(r) functions for basal and insulin-stimulated cells from one successful experiment. The observed L(r) peaked at similar clustering values for GLUT4 on the PM of untreated and insulin-stimulated cells indicating no difference in GLUT4 clustering on the plasma membrane in response to insulin-stimulation.

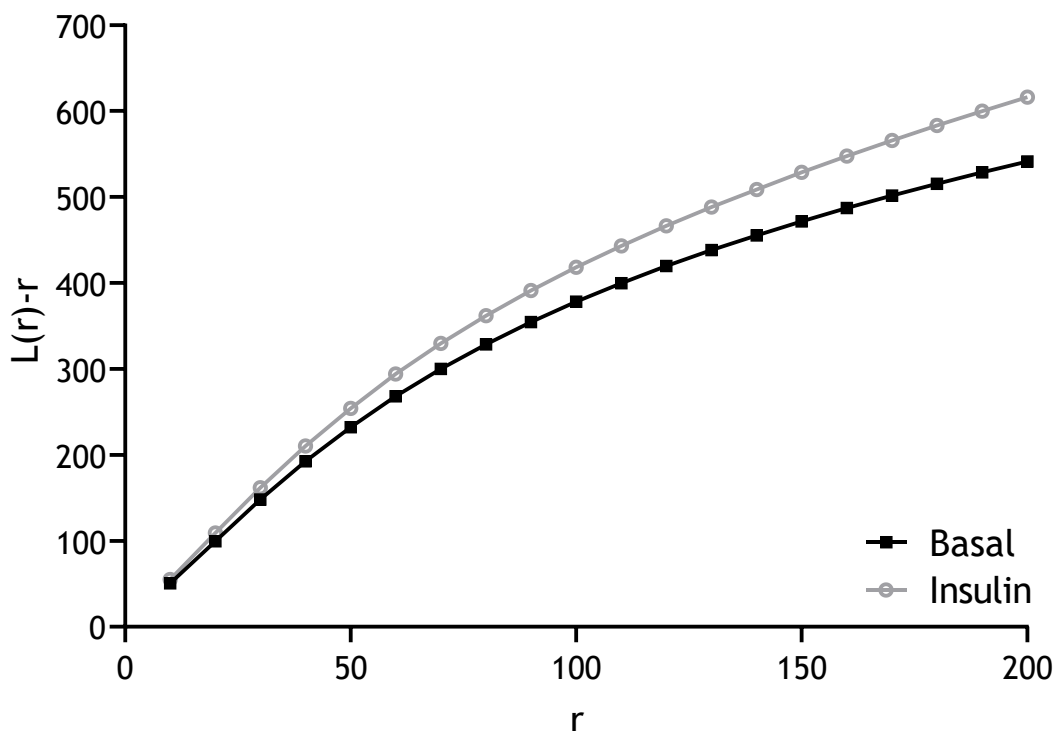


Figure 5.20 Ripley's L-function analysis of GLUT4 clustering in basal and insulin-stimulated induced pluripotent stem cell-derived cardiomyocytes from CDI. Representative plot of Ripley's K function analysis of the clustering abilities of GLUT4 molecules in the PM of HA-GLUT4-GFP iPSC-CM. Cells were serum-starved for 2 h prior to the experiment and stimulated with 1 μM insulin for 20 min or left untreated. Cells were fixed and stained for surface HA and dSTORM images acquired. GLUT4 molecule coordinates were obtained using ThunderSTORM and the obtained localization data was subjected to Ripley's K-function analysis using SR Tesseler with the minimum radius 10 nm, step radius 10 nm, and maximum radius 200 nm. $L(r)-r$ (y-axis) represents the clustering ability and r (x-axis) represents the radial scales of clustering. The presented data are mean \pm SD. The experiment was performed once for basal (N=12 cells) and insulin-stimulated (N=8 cells) conditions. $p = 0.4211$; determined by two-tailed Student's t-test.

5.3 Discussion

5.3.1 GLUT4 clustering in neonatal ventricular cardiomyocytes

Following the discovery that insulin regulates plasma membrane distribution of GLUT4 in adipocytes the aim of this study was to investigate whether a similar mechanism exists in cardiac tissues. We used neonatal rat ventricular cardiomyocytes (NRVM) as a model system because it has several advantages above the culture of primary cardiomyocytes. Several studies have investigated glucose metabolism in these cells and reported an increase in glucose transport and GLUT4 translocation in response to insulin stimulation (Austin and Langley-Evans, 2011; Contreras-Ferrat et al., 2010; Florian et al., 2010; Guan et al., 2008; Heim et al., 2020; Malhotra and Brosius, 1999; Morisco et al., 2005; Pentassuglia et al., 2016). Neuregulin-1 β is a cell adhesion molecule critically involved in cardiac development that improves cardiac performance under a range of pathological conditions. Several studies have investigated the effect of neuregulin-1 β in NRVM and reported that it enhanced glucose uptake in NRVM via Akt phosphorylation in a similar magnitude as insulin stimulation (Heim et al., 2020; Pentassuglia et al., 2016). Pharmacological interventions have shown that neuregulin-1 β and insulin-induced glucose uptake require PI3K and Akt and both increase phosphorylation of the Akt downstream target AS160. Interestingly, neuregulin-1 β and insulin treatment had an additive effect on Akt phosphorylation but not on AS160 phosphorylation in NRVM (Heim et al., 2020). Several other stimuli have been identified to stimulate glucose uptake and GLUT4 translocation in NRVM. One study reported that azide-induced hypoxia and the AMPK activator AICAR increased glucose uptake and GLUT4 translocation in NRVM and that AICAR stimulation had an additive effect on insulin action (Guan et al., 2008). Treatment with the AMPK inhibitor Ara A was reported to lead to a decrease in AICAR- and azide-stimulated glucose uptake but had no effect on basal and insulin-stimulated glucose uptake. These studies indicate that glucose uptake in NRVM is mechanistically similar to insulin action and AMPK activation (Guan et al., 2008).

In our study we found that isolated NRVM lacked expression of GLUT4 protein but exhibited a strong insulin-stimulated phosphorylation of Akt. In the literature, weak expression of GLUT4 protein has been frequently reported in NRVM (Czubryt et al., 2010; Mangmool et al., 2016; Montessuit et al., 2006). Although several interventions have been reported to increase GLUT4 content in NRVM (Czubryt et al., 2010; Mangmool et al., 2016; Montessuit et al., 2006), we virally expressed human GLUT4 in NRVM to study whether insulin affected plasma membrane GLUT4 distribution. Insulin stimulation did not result in GLUT4 dispersal previously observed in adipocytes in this model of cardiac muscle (see Figure 5.5).

Since the first isolation of NRVM in 1963 these cells have been invaluable for *in vitro* cardiac cell biology (Harary and Farley, 1963). The immature phenotype of NRVM presents the biggest disadvantage of working with these cells and is similarly the source of their many advantages (Peter et al., 2016). In rodents and humans the growing heart undergoes considerable structural and functional changes at the cardiomyocyte level (Karbassi et al., 2020). Growth of the prenatal heart predominantly occurs through hyperplasia and NRVM still exhibit this proliferative potential. In rodents cardiomyocytes undergo mitotic quiescence in the first week of postnatal life and after this further growth of the heart occurs by increasing cardiomyocyte size. Mature cardiomyocytes increase in size, become anisotropic, lose automaticity, acquire a more negative membrane potential and an increase in action potential duration and amplitude, polarized gap junctions concentrated at cell ends, improved calcium handling with increased calcium stores and development of T-tubules, increased force of contraction due to presence of more myofibrils and alignment, increased fatty acid utilisation and mitochondrial content (Karbassi et al., 2020). Expression of GLUTs especially GLUT1 and GLUT4 is highly flexible during cardiac development and therefore we chose a more mature model to overcome this limitation.

5.3.2 Investigation of GLUT4 dispersal in adult cardiomyocytes has several challenges

The biggest advantage of using isolated adult cardiomyocytes as a model for cardiac research is the similarity of morphology and behaviour they share with cardiomyocytes of intact cardiac tissue (Peter et al., 2016). Adult cardiomyocytes are large and rod shaped (~150 µm in length), binucleated and have well organized sarcomeres throughout their cell bodies (Louch et al., 2011). In our study adult cardiomyocytes were successfully isolated from New Zealand white rabbits and maintained in culture for up to 48 h. As any experimental system the culture of adult cardiomyocytes has some significant limitations (Peter et al. 2016). Reproducible isolation of high-quality cardiomyocytes is the most important factor for successful experimentation with these cells. Single cardiomyocytes have been isolated for over 40 years but up to this date no single universal method has been developed (Peter et al., 2016; Powell and Twist, 1976). In general isolation protocols include retrograde perfusion of the isolated heart with a Langendorff apparatus but details such as apparatus of choice, enzymes and dissociation methods differ widely within the scientific community (Louch et al., 2011). Isolation of cardiomyocytes remains challenging and even laboratories that perform routine isolations suddenly and unpredictably experience difficulties. This can be due to a number of factors such as cleaning of glassware, water quality, pH and temperature of

solutions, lots of chemicals (especially enzymes), air bubbles in the perfusate and detail in handling the hearts (Louch et al., 2011). In our study we repeatedly observed huge discrepancies in cell viability and insulin-stimulated Akt phosphorylation between different batches of isolated cardiomyocytes. Isolating cardiomyocytes from rabbit hearts is relatively costly compared to smaller animal models and cells from each isolation were used by multiple investigators. Protocols for isolation typically need to be optimised for the type of experiment that is planned but in reality this is not affordable from a financial or ethical point of view because cells are shared to reduce numbers of animals needed.

Long-term culture of these cells results in morphological, electrical and mechanical alterations revoking one of their key advantages (Banyasz et al., 2008). Progressive reduction in cell size, T-tubule density, systolic shortening and membrane currents was observed from the first day of maintenance in culture (Banyasz et al., 2008). Adult cardiomyocytes isolated from rats showed spontaneous upregulation of GLUT1 and downregulation of GLUT4 after two days in primary culture (Montessuit et al., 2004). In line with this result we also observed a significant reduction in GLUT4 protein expression in rabbit adult cardiomyocytes at the same time point. To circumvent the limitation of dedifferentiation investigators frequently perform their analysis within 24 h of isolation (Peter et al., 2016). Treatment with IGF-1 has also been observed to restore GLUT4 protein and mRNA levels during prolonged culture periods (Montessuit et al., 2004).

Generally imaging techniques are limited in thick tissue and the long and flat morphology of adult cardiomyocytes makes them well-suited for experiments aimed at visualizing cell structure and localization of intracellular molecules. In this study several substrates were used to attach cardiomyocytes to glass coverslips and no optimal substrate was identified. Generally adult cardiomyocytes are cultured on laminin-coated coverslips but we experienced that cells did not attach well (Louch et al., 2011). Further experiments were carried out using poly-d-lysine as a substrate because we observed that the cells stuck down well on coated coverslips. However, it remained challenging to image cardiomyocytes in TIRF mode. Unlike immortalised cell lines and NRVM, adult cardiomyocytes do not proliferate in culture and tightly attach to the substrate via focal adhesions. During our dSTORM imaging experiments we frequently observed that cardiomyocytes only formed contact with the glass coverslip in very small areas and therefore it was impossible to illuminate bigger parts of their plasma membrane in TIRF mode. This limitation could have been possibly resolved by changing the experimental method. Light sheet fluorescence microscopy is a technique that uses

a plane of light to optically section tissues and view them with subcellular resolution (Santi, 2011). It is not within the scope of this study to try this novel technique but obtaining serial sections of HA-stained adult cardiomyocytes allowing three-dimensional reconstructions might be well suited to elucidate the plasma membrane distribution of GLUT4 in this cardiac model. Highly inclined and laminated optical sheet (HILO) imaging uses an incredibly thin highly inclined beam of light that is directed through the sample (Tokunaga et al., 2008). Unlike TIRF this technique is not limited to 200 nm from the glass surface of the coverslip. HILO allows deeper sample penetration and is another method that should be explored to image the plasma membrane of cardiomyocytes hovering above the glass coverslips.

In this study we have used rabbit cardiomyocytes because they are available through a collaboration and they share physiology and electrophysiology that is most closely related to that of human cardiomyocytes. However different sources of adult cardiomyocytes should be explored. The current standard of adult cardiomyocytes are adult rat ventricular myocytes due to high cell yields, ease of isolation and cost-effectiveness (Peter et al., 2016). Furthermore, cardiomyocytes can be prepared from adult mice. Cell yields are generally lower and isolation is more difficult due to the small size of the hearts. However a big variety of transgenic mouse models are available that allow the study of different pathologies or offer models with fluorescently-tagged proteins (Peter et al., 2016). A transgenic mouse model in which HA-GLUT4-GFP is expressed in cardiac and skeletal muscle under the control of the MCK promoter is commercially available and has been characterised in the literature (Fazakerley et al., 2009; Lizunov et al., 2012). In the model HA-GLUT4-GFP was observed to translocate to the plasma membrane and T-tubules of skeletal (Lizunov et al., 2012) and cardiac muscle (Fazakerley et al., 2009) in response to insulin similarly to endogenous GLUT4. Adult cardiomyocytes need to be virally transduced to express fluorescently labelled proteins and another limitation of our study was that cells had to be cultured for several days to express the GFP-tagged GLUT4 protein which led to a significant decrease in cell viability and dedifferentiation. Establishing the transgenic HA-GLUT4-GFP mouse model in our lab would give the opportunity to isolate cells and image them. Efforts towards this goal were hampered by the Covid-19 outbreak.

5.3.3 The promise of human induced pluripotent stem cell-derived cardiomyocytes

Human induced pluripotent stem cell-derived cardiomyocytes (iPSC-CM) are the most novel and innovative technology available to model cardiac disease mechanisms *in vitro*

(Peter et al., 2016). In recent years several advances have been made to direct differentiation of iPSCs into cardiac lineages and a number of protocols exist to generate cardiomyocytes with improved cell yields (Burrige et al., 2011, 2012, 2014; Josowitz et al., 2011; Zwi et al., 2009). Cardiomyocyte differentiation of iPSC is associated with high costs, a high amount of required resources, technical challenges and time consumption and requires trained staff. An attempt was made to generate cardiomyocytes from iPSC in the lab of our collaborator Nikolaj Gadegaard (University of Glasgow) but was abandoned due to high time consumption, low cell yields and difficulty of quality control (data not shown). In recent years iPSC-CM have become commercially available from a number of companies that specialise in cardiomyocyte generation and ensure quality control (Peter et al., 2016). iPSC-CM exhibit cardiomyocyte specific gene and protein expression and general function and were commercially obtained from two sources to study insulin-stimulated GLUT4 dispersal. It was observed that iPSC-CM obtained from NCardia showed a significant increase in HA-GLUT4 localization density and dispersal in response to insulin treatment. However, experiments included a relatively small amount of cells and investigation of more samples is required to validate the observed effect. Unfortunately, NCardia experienced problems with their quality control and the cells were withdrawn from the market in the middle of this study. Similar experiments were carried out using iPSC-CM produced by CDI but these yielded conflicting results. CDI iPSC-CM showed a similar fold increase in HA-GLUT4 plasma membrane localization density but the overall GLUT4 density per μm^2 observed was much lower compared to cells obtained from NCardia. CDI iPSC-CM did not exhibit insulin-stimulated GLUT4 dispersal assessed by dSTORM. This indicates differences between the two iPSC-CM lines that were commercially obtained. One possible explanation for this is the huge variety of differentiation and purification protocols that are employed by different companies and laboratories resulting in problems with consistency. We observed morphological differences between cells obtained from NCardia and CDI. In general cells had a circular shape but it was observed that cells from CDI were smaller with typical diameters of $\sim 30 \mu\text{m}$ and that NCardia cells were much bigger and more spread out. Cells from both sources were spontaneously beating but the frequency of spontaneous beating and the size of beating clusters of cells varied. These variations in iPSC-CM cultures have been previously reported in the literature (Karbassi et al., 2020).

One widely accepted major limitation of iPSC-CM is that protocols generate immature cardiomyocytes at embryonic or early foetal stages (Karbassi et al., 2020). Previous studies carried out in our laboratory assessed the capacity of iPSC-CM to act as a novel cellular model of cardiomyocytes for metabolic disease (Bowman et al., 2019). A

general observation was that iPSC-CM obtained from both NCardia and CDI expressed insulin signalling intermediates and trafficking proteins but lacked significant expression of GLUT4 protein (Bowman et al., 2019). Furthermore it was discovered that iPSC-CM did not exhibit insulin-stimulated glucose uptake (Bowman et al., 2019). It was observed that iPSC-CM had high levels of GLUT1 protein expression. Consistent with the current literature taken together these results indicate that iPSC-CM are metabolically immature. Several interventions were explored to increase the low endogenous levels of GLUT4 protein in these cells in our laboratory. Treatment with thyroid hormone tri-iodothyronine (T_3) and maturation medium conditioning with low glucose were not successful and had no or limited impact on GLUT4 expression (Bowman et al., 2019). The observed differences in insulin-stimulated GLUT4 dispersal observed in this study might be attributed to different levels of maturation of the cells. NCardia iPSC-CM showed higher levels of GFP fluorescence intensity following transduction with Ad-HA-GLUT4-GFP compared to CDI iPSC-CM. Transduction efficiency was higher in NCardia iPSC-CM and similar to that observed in highly proliferative and immature NRVM and therefore it might be that these cells can be classed as more immature. CDI iPSC-CM appeared dim after transduction with Ad-HA-GLUT4-GFP and this resulted in lower quality dSTORM image raw data quality which made it harder to investigate GLUT4 spatial dynamics in these cells. Human iPSC-CM provide the opportunity to capture the heterogeneity of the human population that arises from gender, ethnicity and patient-specific gene modifications and have been successfully used to model genetic cardiac disorders (Itzhaki et al., 2011; Josowitz et al., 2011; Matsa et al., 2011; Moretti et al., 2010). The cells can be directly derived from patients and have been used to successfully model diabetic cardiomyopathy and study drug-gene interactions and evaluate potency of candidate drugs in reversing aberrant phenotypes (Bellin et al., 2012; Drawnel et al., 2014; Granéli et al., 2019; Takahashi and Yamanaka, 2013).

5.3.4 Conclusions and future directions

To our knowledge this was the first study that investigated insulin-stimulated GLUT4 dispersal in a variety of *in vitro* models of cardiac muscle tissue. It was observed that insulin did not stimulate GLUT4 dispersal in NRVM and CDI iPSC-CM. Insulin did have an effect on GLUT4 plasma membrane distribution in NCardia iPSC-CM. This study was unable to study GLUT4 translocation or dispersal in adult cardiomyocytes due to a number of experimental limitations. Therefore, it can be concluded that this study shed some light on the mechanisms of GLUT4 dispersal that exist in cardiac tissues but more studies are needed to explore more cell culture models and also experimental techniques. Cardiac cell culture models differ vastly in their individual stage of development and each model has advantages and disadvantages and only the use of a

combination of experimental systems can solve the nature of cardiac GLUT4 dispersal in the future. In the future it would be highly desirable to expose different *in vitro* models to drug treatments and investigate models of cardiac disease which was not within the scope of this study.

6. Plasma membrane GLUT4 dispersal in health and disease

6.1 Introduction

6.1.1 Skeletal muscle glucose uptake

In vivo, skeletal muscle is the primary tissue in which the vast majority (about 90 %) of insulin-stimulated glucose uptake occurs (Kraegen et al., 1993). Similarly to adipocytes skeletal muscle fibres express both GLUT1 and GLUT4 transporter isoforms with a higher abundance of GLUT4 (Marette et al., 1992). GLUT4 is the main isoform facilitating insulin-dependent glucose transport in skeletal muscle (Hansen et al., 1995). Although GLUT4 trafficking has been extensively studied in adipose tissue far less is known about GLUT4 trafficking in skeletal muscle (Mueckler, 2001). This may be due to the more complex tissue architecture, lack of appropriate cell culture models closely reflecting the anatomy and physiology of striated muscle fibres and difficulty of performing traditional experimental techniques on skeletal muscle tissues compared to adipocytes. Analysis of single muscle fibres from the vastus lateralis of eight male subjects has shown that GLUT4 protein content was highest in muscle fibres expressing myosin heavy chain (MHC) 1 compared to fibres expressing MHC IIA and MHC IIX (Daugaard et al., 2000). Another study found that mRNA concentrations of GLUT4 were highest in human muscle samples compared to mRNA concentrations of other GLUT isoforms (Stuart et al., 2006). Human muscle homogenates predominantly expressed GLUT4 protein and showed lower expression of GLUT5 and GLUT12 isoforms. Immunostaining experiments showed that GLUT4 and GLUT12 were predominantly expressed in type I oxidative fibres whereas GLUT5 was most abundant in type II white fibres (Stuart et al., 2006).

Contrary to adipocytes, skeletal muscle fibres contain two anatomically distinct plasma membrane domains: the sarcolemma (plasma membrane) and transverse tubules (t-tubules) which are invaginations of the plasma membrane that penetrate deep into the centre of the muscle fibre. GLUT1 is restricted to the surface of the muscle cells and does not respond to insulin stimulation in contrast to adipocytes (Marette et al., 1992). GLUT4 is localised to both the sarcolemma and the interior of the fibres. Insulin stimulation results in translocation of GLUT4 to both the sarcolemma and the t-tubules but the majority of insulin-stimulated glucose transport occurs across t-tubules (Wang et al., 1996). Electron microscopy experiments of human muscle revealed no GLUT4 immunogold labelling on the sarcolemma and specific GLUT4 labelling within the t-tubules and possibly the sarcoplasmic tubules (Friedman et al., 1991). Using immunogold labelling in transgenic mice overexpressing GLUT1 and GLUT4 it was

reported that 90 % of GLUT4 is present in the t-tubules after insulin stimulation (Wang et al., 1996).

GLUT4 trafficking in muscle tissue is more complex because contraction is a major physiological stimulus of GLUT4 translocation independent of insulin. Observations of changes in arteriovenous glucose in equine masseter muscle during chewing indicated the existence of contraction-induced skeletal muscle glucose uptake more than 120 years ago (Richter and Hargreaves, 2013). In the 1950s quantitative physiological studies using rats and dogs confirmed that contractions stimulate muscle glucose uptake (Goldstein et al., 1953; Huycke and Kruhoffer, 1955). Several studies confirmed that contraction-induced glucose uptake is primarily due to translocation of GLUT4 from intracellular stores to the sarcolemma and t-tubules. Recently, immunofluorescence microscopy was used to quantify net GLUT4 translocation to the PM in human vastus lateralis biopsies from ten human subjects following glucose ingestion for the first time (Bradley et al., 2015). Moreover, It has been reported that electrical stimulation or a 3 h swim exercise had no effect on glucose uptake in muscle in GLUT4-deficient mice highlighting the fundamental importance of GLUT4 in exercise-induced glucose uptake (Ryder et al., 1999; Zisman et al., 2000).

6.1.2 Insulin resistance

6.1.2.1 Theories of peripheral insulin resistance

Insulin resistance is the inability of the body's cells to respond appropriately to insulin as a stimulus to increase glucose transport across cell surface membranes in target tissues to reduce blood sugar levels (Samuel and Shulman, 2016). Many causes have been proposed to lead to the development of insulin resistance and the underlying molecular mechanisms are not completely elucidated. Skeletal muscle accounts for the majority of glucose disposal after a meal in healthy individuals. Therefore skeletal muscle is the major glucose sink of the body and has to play an important role in the pathogenesis of insulin resistance which has been extensively studied (Abdul-Ghani and DeFronzo, 2010). Insulin resistance has been identified as a key defect in T2DM and is heavily associated with obesity and metabolic syndrome in which insulin-stimulated glucose transport into skeletal muscle is significantly impaired (DeFronzo, 2004; DeFronzo et al., 1985; Mitrakou et al., 1990). Under normal conditions insulin secretion after a meal suppresses lipolysis resulting in a decrease in plasma free fatty acids (FFA) levels and drop in the rate of lipid oxidation. It has been proposed that chronic overfeeding leads to increased FFA availability and onset of obesity. Different studies have consistently reported that weight gain is accompanied by a sharp rise in skeletal

muscle insulin resistance in human subjects (Erdmann et al., 2008; Lemay et al., 2010; Schrauwen, 2007; Wedick et al., 2009). Muscle biopsies have revealed an accumulation of triglycerides in skeletal muscle cells and that these deposits negatively impact insulin sensitivity (Pan et al., 1997; Phillips et al., 1996).

One defect that has been proposed is that levels of GLUT4 may be reduced in insulin-resistant individuals. One study investigated the insulin resistance of aging in relationship to GLUT4 protein content in vastus lateralis muscle in men and women (Houmard et al., 1995). With increasing age insulin sensitivity was observed to decrease significantly and this was associated with a decrease in skeletal muscle GLUT4 protein concentration (Houmard et al., 1995). However, there is evidence that GLUT4 content and levels of mRNA are not changed in individuals with obesity, impaired glucose tolerance, non-insulin-dependent diabetes or gestational diabetes (Garvey et al., 1992). Another study reported no change in GLUT4 gene and protein expression in vastus lateralis muscle of subjects with insulin-dependent diabetes mellitus compared to healthy controls in the same year (Kahn et al., 1992). A study comparing gene and protein expression of muscle biopsies isolated from T2DM patients, T2DM first-degree relatives and healthy controls showed that T2DM patients and their relatives had an impairment in insulin-stimulated total-body glucose disposal indicating insulin resistance (Eriksson et al., 1992). The observed skeletal muscle insulin resistance was not associated with a defect GLUT4 gene expression (Eriksson et al., 1992). A study using a novel photoaffinity labelling agent has found that GLUT4 cell surface levels in skeletal muscle of nine T2DM patients were only 10% of those observed in nine healthy controls (Ryder et al., 2000). Glucose transport activity in T2DM skeletal muscle samples was approximately 50% of that in healthy controls. This study highlights that a reduction in GLUT4 translocation majorly contributes to the impairment of glucose transport observed in T2DM subjects (Ryder et al., 2000). As outlined in section 1.5.5 there is strong evidence for the impairment of molecular pathways of insulin signalling for instance reduced insulin receptor phosphorylation, decreased IRS-1 tyrosine phosphorylation and decreased PI3-kinase activation (Björnholm et al., 1997; Cusi et al., 2000; Dresner et al., 1999; Isakoff et al., 1995; Kim et al., 1999). Furthermore, in skeletal muscle of T2DM subjects reduced insulin-stimulated Akt kinase activity (Krook et al., 1998) and impairment of AS160 phosphorylation (Karlsson et al., 2005) have been documented.

6.1.2.2 Defects in the adipocyte glucose transport system and cellular insulin resistance

Isolated omental adipocytes obtained during caesarean sections from healthy and gestational diabetes patients were used to study defects in the adipocyte glucose transport system and insulin resistance at the cellular level (Garvey et al., 1993). It was observed that basal and insulin-stimulated glucose transport rates were markedly reduced in adipocytes isolated from gestational diabetes patients indicative of cellular insulin resistance. Cellular content of GLUT4 was found to be decreased in diabetic patients with segregation into two groups. One group suffered severe GLUT4 depletion and the other group had GLUT4 levels within the normal range. Insulin stimulated GLUT4 translocation from low-density microsomes to the PM in healthy subjects but failed to stimulate GLUT4 translocation in diabetic patients indicating abnormalities in cellular traffic and targeting of GLUT4 (Garvey et al., 1993). 3T3-L1 adipocytes are the model system of choice for investigating regulatory effects on glucose transport at the cellular level and researchers have developed experimental approaches to mimic adipocyte insulin resistance in culture. Chronic treatment with 500 nM insulin for 24 h has been used to mimic insulin resistance and study its consequences. It has been reported that chronic insulin treatment of 3T3-L1 adipocytes results in an increase in GLUT1 protein expression but had no effect on GLUT4 (Tordjman et al., 1989). Using a novel bis-mannose-photolabeling technique cell surface levels of GLUT4 were found to be 53 % reduced following chronic insulin stimulation compared to that of acute insulin stimulation (Kozka et al., 1991). Furthermore, as a result of chronic insulin treatment a 6-fold rise of total amount of GLUT1 was reported whereas total amount of GLUT4 increased by 1.4-fold. Radioactive glucose uptake experiments showed that chronic insulin treatment by itself increased glucose transport in 3T3-L1 adipocytes whereas a second challenge with insulin resulted in a blunted response (Kozka et al., 1991). It was observed that binding of insulin tracer was not altered after chronic insulin treatment of the cells. Therefore it was proposed that the downregulation of cell surface GLUT4 in 3T3-L1 cells was not due to resistance at the insulin receptor level or depleted GLUT4 pool but rather dependent on a defect existing in the signalling pathway (Kozka et al., 1991). Another study using iodixanol gradient centrifugation to separate intracellular GLUT4 compartments into recycling endosomes and GSVs reported that an acute insulin stimulus reduced GLUT4 content in the GSV but not in the endosomal compartment (Maier and Gould, 2000). Chronic insulin treatment resulted in a decreased GLUT4 content by 40 % and blunted the GLUT4 translocation response to a second acute insulin challenge. This study also reported that GLUT4 was selectively diminished from the GSV compartment indicating mis-targeting of GLUT4 within the cell as a result of insulin

resistance (Maier and Gould, 2000). There is only one study currently assessing the effect of chronic insulin treatment on PM GLUT4 dispersal and whether this affects cellular insulin resistance in adipocytes needs to be validated.

6.1.3 Transferrin receptor trafficking

6.1.3.1 The transferrin receptor and glucose metabolism

The Transferrin receptor (TfR) is a membrane protein that facilitates iron uptake in cells and is widely expressed throughout the body (Mayle et al., 2012). Iron-loaded transferrin binds to the TfR which imports iron by internalizing through clathrin-mediated endocytosis and intracellular trafficking pathways. The endocytosed transferrin-iron complexes are sorted into early, late and recycling endosomes. Acidification by proton pumps lowers the pH of the endosomes to 5 to release the iron from the transferrin and leaves apo-transferrin bound to the TfR (Bomford and Munro, 1985). Cargo can return directly from the early endosomes to the PM via a fast route or delivered to perinuclear recycling endosomes via a slow route before being returned to the cell surface (Mayle et al., 2012). Due to its continuous recycling pathway between the PM and endosomes TfR has become a widely recognised marker for endosomal compartments (Kobayashi and Fukuda, 2013). In 1986 it was discovered that insulin stimulated translocation of TfR from intracellular stores to the PM in isolated rat adipocytes (Davis et al., 1986). Analysing the rate of uptake of diferric ¹²⁵I-transferrin a 3-fold increase in the amount of cell surface TfR was found following insulin stimulation. This was associated with a concomitant decrease of TfR within intracellular membranes indicating insulin-mediated redistribution of the TfR similar to that observed in GLUT4 (Davis et al., 1986). Furthermore, it was reported that contraction stimulated translocation of TfR from intracellular compartments to the PM but not to the t-tubules in perfused hindlimb rat muscle (Lemieux et al., 2000). It was reported that the effect of insulin and contraction on TfR translocation was not additive and the same as recorded for the effect of contraction by itself (Lemieux et al., 2000). Contraction was observed to reduce TfR content in purified GLUT4 vesicles whereas insulin did not affect TfR content and only reduced GLUT4 content in these vesicles. This led to the conclusion that contraction stimulates GLUT4 translocation from two distinct intracellular GLUT4 pools in skeletal muscle defined by the presence of TfR (Lemieux et al., 2000). In 3T3-L1 adipocytes a vesicular fraction from intracellular membranes was identified that contained >90 % GLUT4 and 40 % TfR using immunoadsorption (Livingstone et al., 1996). Another vesicle fraction containing 50 % TfR and 40 % GLUT4 was identified similarly indicating that significant amounts of both TfR and GLUT4 reside in distinct internal compartments (Livingstone et al., 1996). A combination of subcellular fractionation, compartment ablation and immunoadsorption

resulted in the identification of a TfR-negative/GLUT4-positive, TfR-positive/GLUT4-negative and TfR-positive/GLUT4-positive compartment (Livingstone et al., 1996). Another study showed that GLUT4 is equally distributed between TfR-containing endosomes and a TfR-negative specialised compartments in the basal state in 3T3-L1 adipocytes using a fluorescent quenching assay (Zeigerer et al., 2002). It was proposed that the equal distribution of GLUT4 indicates that the rate of transport from endosomes and the specialised compartment must be similar. Insulin stimulation resulted in GLUT4 translocation from both pools and trafficking of GLUT4 from endosomes was regulated by Rab11 (Zeigerer et al., 2002). Taken together these studies highlight that GLUT4 trafficking overlaps with TfR trafficking and the general endocytic recycling pathway.

6.1.3.2 The role of the transferrin receptor in insulin resistance

Recently the association between insulin resistance and disturbances of iron homeostasis has become a popular research topic. Skeletal muscle is not only the major tissue for glucose disposal but also for iron utilization and storage and several studies described a growing link between insulin resistance and iron dysregulation. A study using human skeletal muscle myoblasts (HSMM) from Lonza and skeletal muscle biopsies as model systems found that palmitate treatment induced a state of insulin resistance in HSMM and increased intracellular iron levels (Cui et al., 2019). Knock-down of TfR1 resulted in protection of HSMM from excess iron-induced insulin resistance indicating that TfR is important for maintenance of insulin sensitivity in these cells. Furthermore, it was observed that palmitate treatment induced overexpression of TfR1 at the protein and mRNA level in HSMM and this result corresponded with results obtained from muscle biopsies of diabetic patients (Cui et al., 2019). In this model intracellular iron accumulation was induced by excess FFA availability and modulated by upregulation of TfR and increased TfR internalization indicating a critical role of TfR in the development of insulin resistance (Cui et al., 2019). Simple incubation of 3T3-L1 adipocytes with transferrin has been observed to result in decreased rates of insulin-stimulated glucose uptake indicating that transferrin alone induced insulin resistance of glucose uptake in adipocytes (Green et al., 2006). A study investigating serum soluble TfR in men with normal glucose tolerance, impaired glucose tolerance and T2DM reported that insulin sensitivity predicted circulating TfR in normal glucose tolerance and non-obese subjects (Fernández-Real et al., 2007). Another cross-sectional study found an independent and positive association between circulating TfR and insulin resistance in men and postmenopausal women (Suárez-Ortegón et al., 2016). In a French epidemiological study on the insulin resistance syndrome (DESIR) cohort

including 1,277 men and women transferrin was found to be predictive of the onset of hyperglycaemia within 3 years (Fumeron et al., 2006). A retrospective longitudinal study including 30,000 Koreans found that serum transferrin levels were elevated in T2DM subjects compared to controls (Kim et al., 2020). Furthermore, transferrin levels helped to predict future incident of T2DM in healthy subjects in this population (Kim et al., 2020). Assessment of gene expression, genotype, and insulin sensitivity of adipose tissue in 256 nondiabetic African Americans revealed that 30 iron homeostasis genes were correlated with insulin sensitivity (McClain et al., 2018). Findings were successfully replicated in two European cohorts independently. Knock-down of transferrin *in vitro* in SGBS cells changed gene expression related to glucose transport, mitochondrial function and chemokine activity (McClain et al., 2018). The study indicates that genetic regulation of transferrin expression in adipocytes plays an important role in regulating insulin sensitivity (McClain et al., 2018). A meta-analysis including 46 observational studies investigating the association of iron metabolism and development of T2DM concluded that results were extremely heterogeneous across studies (Orban et al., 2013). However, clinically elevated transferrin saturation was found to be highly correlated with an increased risk of T2DM with current evidence hinting at a causal effect (Orban et al., 2014). Recently a bifunctional proinsulin-transferrin fusion protein containing two functional moieties of insulin and transferrin was designed to serve as a liver-targeted prodrug for treatment of type I diabetes in mice (Liu et al., 2020). The fusion protein activated both the IR and TfR and attenuated insulin resistance in palmitate-treated HepG2 cells and non-obese diabetic mice (Liu et al., 2020). This study highlights the therapeutic potential of the investigation of the role of the TfR in the development of T2DM and insulin resistance. Taken together these studies highlight a close link between iron and glucose metabolism. Elevated TfR levels have been associated with decreased insulin sensitivity and onset of metabolic disease.

6.1.4 Hypothesis and research aims

The aim of this chapter was to investigate different aspects of GLUT4 trafficking and dispersal in several cell culture models of health and disease. Firstly, we aimed to characterise the effect of chronic insulin treatment on surface GLUT4 spatial patterning at the single molecule level in adipocytes using dSTORM. We hypothesised that chronic insulin treatment would result in a state of cellular insulin resistance and attenuation of insulin-stimulated GLUT4 dispersal could be an underlying cause in adipocytes. Subsequently we aimed to investigate whether the mechanism of insulin-stimulated dispersal is specific to GLUT4. We aimed to produce a novel plasmid vector with a pCDH backbone and CMV promoter for the production of a lentivirus to express a GFP-tagged version of TfR. We aimed to perform dSTORM experiments to investigate the spatial

patterning of TfR on the cell surface. Given the emerging role of the TfR in insulin resistance these baseline studies are a valuable contribution.

Finally, we aimed to characterise GLUT4 dispersal in a cell culture model of human skeletal muscle for the first time. We also aimed to investigate the expression of several proteins involved in the GLUT4 trafficking cascade to gain insights into underlying molecular processes. There is a gap in our understanding of the mechanisms that contribute to peripheral and cellular insulin resistance and the experiments conducted in this chapter aim to contribute to our understanding.

6.2 Results

6.2.1 Insulin resistance reorganises plasma membrane GLUT4 clustering

As a starting point we assessed whether chronic insulin treatment with 500 nM for 24 h resulted in an insulin resistant phenotype in 3T3-L1 adipocytes as previously reported in the literature. Insulin resistance is characterised by impaired glucose uptake and therefore a radioactive glucose uptake assay was conducted to confirm this. Insulin stimulation resulted in a 4.5-fold increase of glucose uptake in control cells and this was significantly reduced to a 1.2-fold increase in the chronic insulin treatment group (Figure 6.1). This data is in good agreement with other studies (Kozka et al., 1991; Maier and Gould, 2000). After establishing that we can induce insulin resistance experimentally in 3T3-L1 adipocytes we adapted the same protocol for all future experiments.

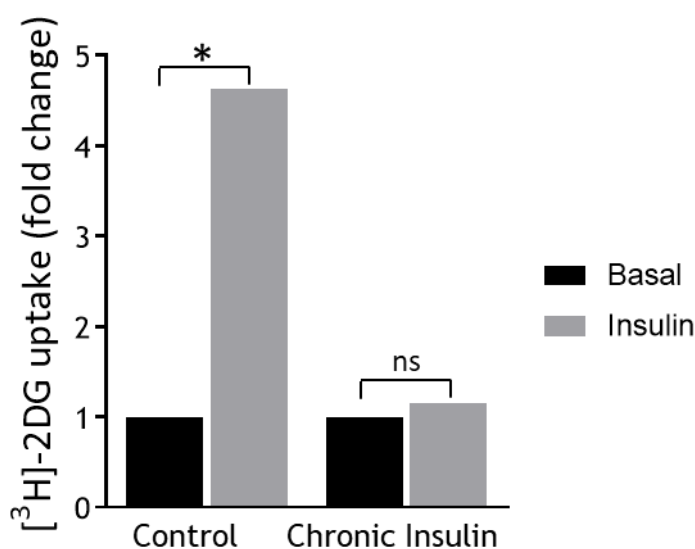


Figure 6.1 Insulin-stimulated deoxyglucose uptake in control and chronic insulin-treated 3T3-L1 adipocytes.

2-deoxyglucose uptake was measured as described (section 2.4.1). 3T3-L1 adipocytes were differentiated and either left untreated (control) or treated with 500 nM insulin on Day 10 for 24 h (chronic insulin). On Day 11 cells were incubated in serum-free medium for 2 h prior to experiments. Cells were washed with KRP and either left untreated or treated with 100 nM insulin for 20 min followed by a 5 min uptake of 2-deoxyglucose at 37°C. Basal glucose uptake rates were typically of the order of 600 counts per min/well. The data displayed represent fold changes of insulin stimulation from one experiment conducted in triplicate. $p < 0.0001$ indicated by *, ns=not significant; determined by one-way ANOVA.

Subsequently we carried out STORM imaging experiments for 3T3-L1 adipocytes under control and chronic insulin treated basal and insulin-stimulated conditions. Ripley's L-function analysis was carried out to quantify changes in GLUT4 dispersal in the PM. Figure 6.2 shows the averaged L(r) functions for control and chronic insulin-treated

basal and insulin-stimulated cells from three independently performed experiments. The observed $L(r)$ peaked at similar clustering values for GLUT4 on the PM of untreated control and chronic insulin treated cells. This indicates that there was no significant difference in GLUT4 clustering on the plasma membrane in the absence of insulin stimulation. Insulin stimulation shifted $L(r)$ to lower values indicating GLUT4 dispersal. Furthermore, chronic insulin treatment was observed to attenuate the observed insulin-stimulated GLUT4 dispersal in 3T3-L1 adipocytes significantly (Figure 6.2).

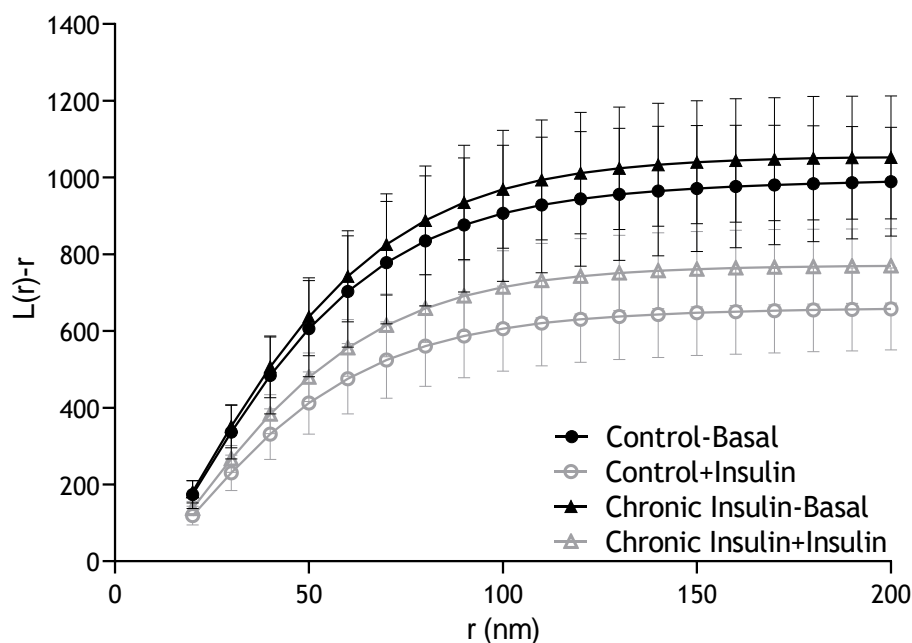


Figure 6.2 Ripley's K-function analysis of the effect of chronic insulin treatment on GLUT4 clustering in basal and insulin-stimulated 3T3-L1 adipocytes.

Representative plot of Ripley's K function analysis of the clustering abilities of GLUT4 molecules in the PM of HA-GLUT4-GFP 3T3-L1 adipocytes. 3T3-L1 adipocytes were differentiated and either left untreated (control) or treated with 500 nM insulin on Day 10 for 24 h (chronic insulin). On Day 11 cells were serum-starved for 2 h prior to the experiment and stimulated with 100 nM insulin for 20 min or left untreated. Cells were fixed and stained for surface HA and dSTORM images acquired. GLUT4 molecule coordinates were obtained using ThunderSTORM and the obtained localization data was subjected to Ripley's K-function analysis using SR Tesseler with the minimum radius 10 nm, step radius 10 nm, and maximum radius 200 nm. $L(r)-r$ (y-axis) represents the clustering ability and r (x-axis) represents the radial scales of clustering. The presented data are mean \pm SD (N=3). The experiment was performed independently 3 times for control basal (N=31 cells) and insulin-stimulated (N=30 cells), and chronic insulin basal (N=17 cells) and insulin-treated (N=29 cells) conditions. $p < 0.0001$; determined by one-way ANOVA.

We also assessed localization density of GLUT4 molecules in control and chronic insulin treated experimental groups (Figure 6.3). The localisation density of GLUT4 molecules significantly increased by 2.6-fold from 152 localisations per μm^2 in the basal state to 402 per μm^2 after insulin stimulation. Furthermore, chronic insulin treatment slightly elevated the localisation density of GLUT4 molecules by 48 % to 220 per μm^2 . Insulin

stimulation of chronically insulin-treated cells resulted in a measured GLUT4 localization density of 268 molecules per μm^2 which is 34 % less than the density observed for control insulin-stimulated cells. This shows that more GLUT4 molecules were present in the plasma membrane of 3T3-L1 adipocytes following insulin stimulation and that this effect was blunted following chronic insulin treatment. Therefore, insulin-stimulated GLUT4 translocation occurs in chronic insulin-treated 3T3-L1 adipocytes but the observed effect is attenuated compared to that observed in the control group.

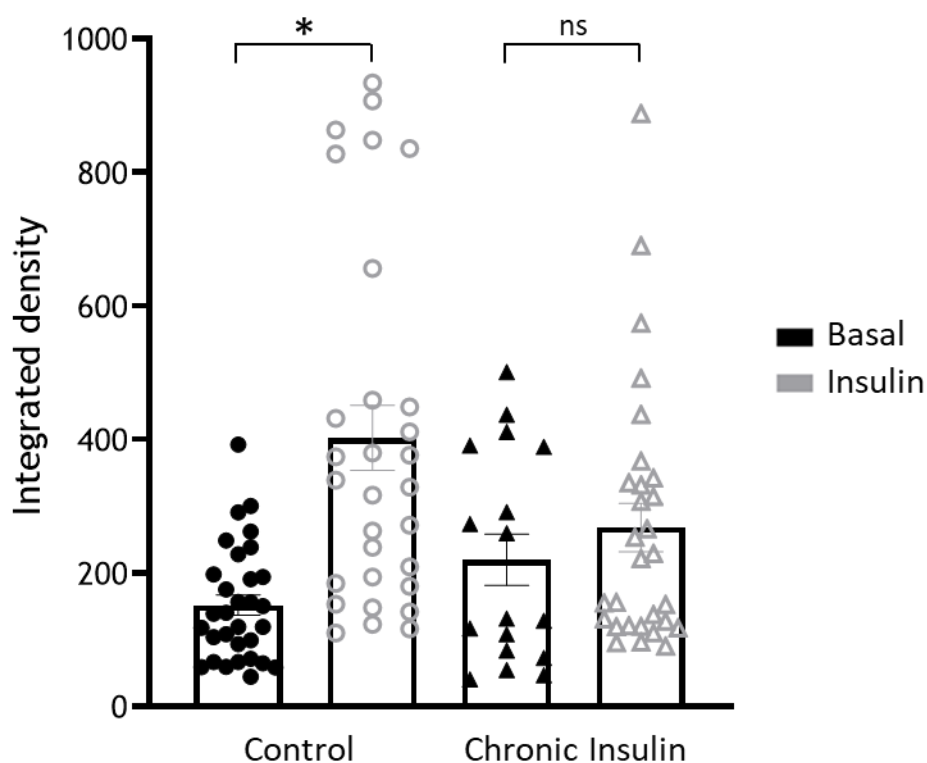


Figure 6.3 Localisation density in control and chronic insulin treated basal and insulin-stimulated 3T3-L1 adipocytes determined by dSTORM imaging.

3T3-L1 adipocytes were incubated in serum-free medium for 2 h prior to the experiment and stimulated with 100 nM insulin for 20 min or left untreated. Cells were fixed and stained for surface HA and dSTORM images acquired on a Zeiss Elyra PS.1 (described in section 2.3). Reconstructions of raw images were calculated using the ImageJ plugin ThunderSTORM. Localisation density was determined using the ImageJ plugin LocFileVisualizer (see 2.4.10). Control basal: 152 ± 86 ($n = 31$), control insulin: 402 ± 268 ($n = 30$), chronic insulin basal 220 ± 158 ($n = 17$) and chronic insulin +insulin 268 ± 195 ($n = 29$). Mean \pm SD. $p < 0.0001$; determined by one-way ANOVA.

High-throughput flowcytometry experiments have shown that 3T3-L1 adipocytes present as a very heterogenous cell population in culture (Figure 4.10). Our imaging experiments support the existence of significant morphological heterogeneity regarding cell shapes and sizes. Here we investigated how morphological heterogeneity affects metabolic heterogeneity in adipocytes and whether there is a relationship between cell size and insulin sensitivity (Figure 6.4). Figure 6.4 shows populations of basal and

insulin-stimulated 3T3-L1 adipocytes and GLUT4 molecule localization density per μm^2 over a range of cell sizes. In both basal and insulin-stimulated cells cell area was significantly negatively correlated with GLUT4 molecule density indicating that bigger cells have a lower GLUT4 molecule density and are less insulin sensitive.

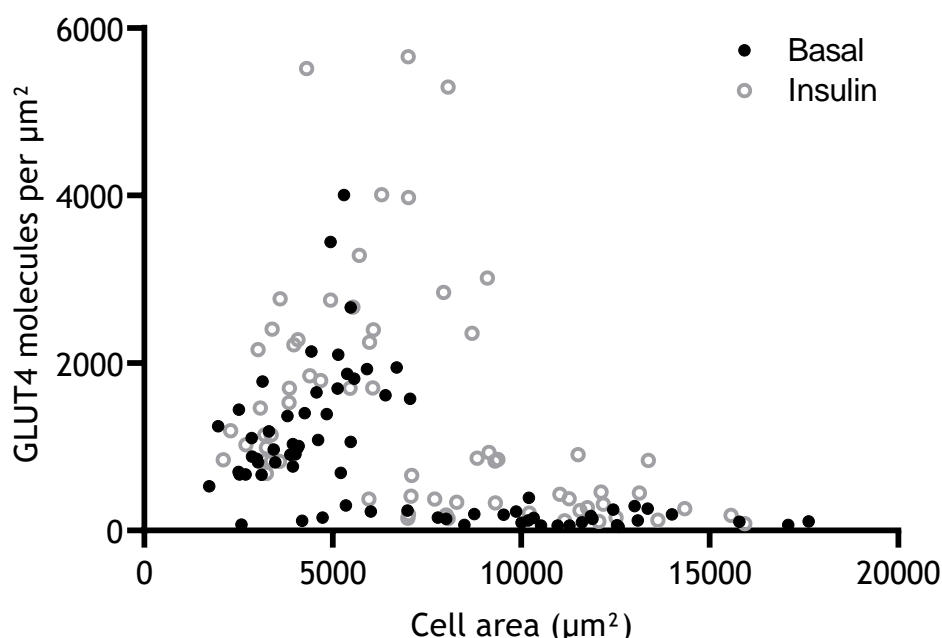


Figure 6.4 GLUT4 localisation density as a function of cell area for basal and insulin-treated 3T3-L1 adipocytes determined by dSTORM imaging.

3T3-L1 adipocytes were serum-starved and stimulated with 100 nM insulin for 20 min or left untreated. Cells were fixed, stained for anti-HA and dSTORM images acquired (described in section 2.3). Reconstructions were calculated using ThunderSTORM. Localisation density was determined using LocFileVisualizer (see 2.4.10). ROIs were drawn around each cell to determine cell area and GLUT4 molecule localization density. Basal cells (N=72) Pearson $r=-0.5$ with $p<0.0001$; Insulin-stimulated cells (N=66) Pearson $r=-0.4$ with $p=0.0011$, correlation analysis with Graphpad Prism.

Segmentation of data according to mean cell area allowed further comparison of the effect of insulin stimulation on small and big cells (Figure 6.5). It was observed that insulin stimulation resulted in a significant increase in GLUT4 molecule density in cells with areas above and below $7,500 \mu\text{m}^2$. However, figure 6.5 shows that the increase in GLUT4 molecule density was higher in small cells with areas below $7,500 \mu\text{m}^2$ following insulin stimulation.

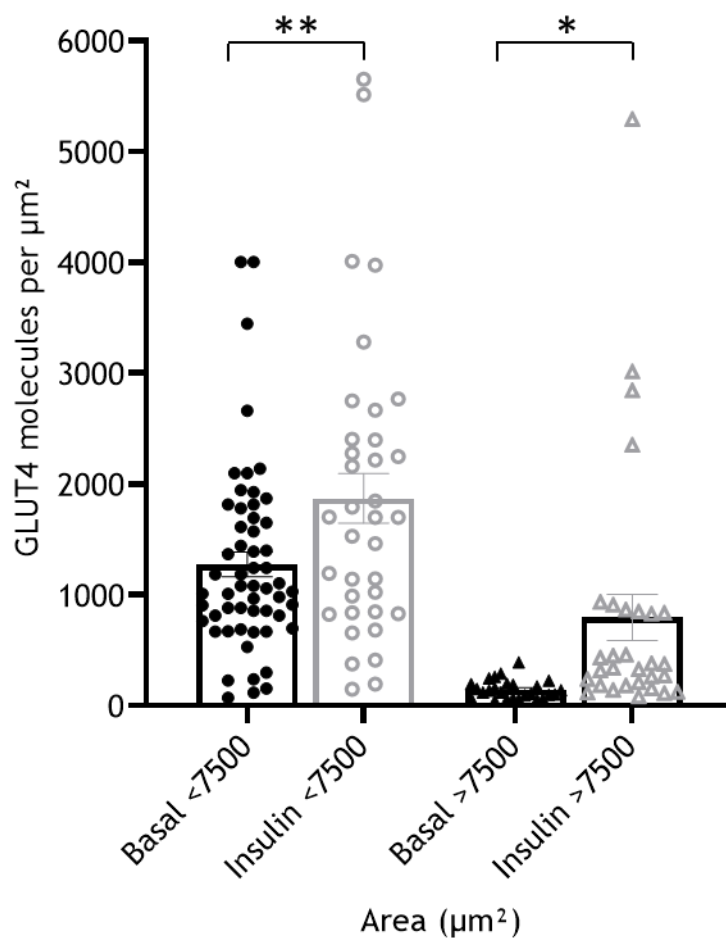


Figure 6.5 Comparison of GLUT4 localisation density in small and bigger basal and insulin-stimulated 3T3-L1 adipocytes determined by dSTORM imaging. 3T3-L1 adipocytes were serum-starved and stimulated with 100 nM insulin for 20 min or left untreated. Cells were fixed, stained for anti-HA and dSTORM images acquired (described in section 2.3). Reconstructions were calculated using ThunderSTORM. Localisation density was determined using LocFileVisualizer (see 2.4.10). ROIs were drawn around each cell to determine cell area and GLUT4 molecule localization density. The mean GLUT4 localization density comparing basal and insulin-stimulated adipocytes with areas below or above the mean cell area of $\sim 7,500 \mu\text{m}^2$. Mean \pm SEM. Basal vs insulin <7500 ** $p > 0.0001$; Basal vs insulin >7500. * $p = 0.009$; determined by Student's t-test.

6.2.2 Generation of a novel pCDH-TfR-GFP lentiviral vector to investigate the specificity of GLUT4 dispersal

To assess whether insulin-stimulated plasma membrane dispersal is specific to GLUT4 we decided to investigate dispersal of TfR in a similar manner. The performance of imaging experiments requires a fluorescent tag to visualise the protein of interest. Therefore we decided to develop a lentivirus capable of expressing a GFP-tagged version of the TfR in a variety of cell culture models. To achieve this goal the TfR-GFP sequence from a plasmid that was gifted to our lab was subcloned into a pCDH vector for lentivirus production. Steps in this process are shown in Figure 6.6.

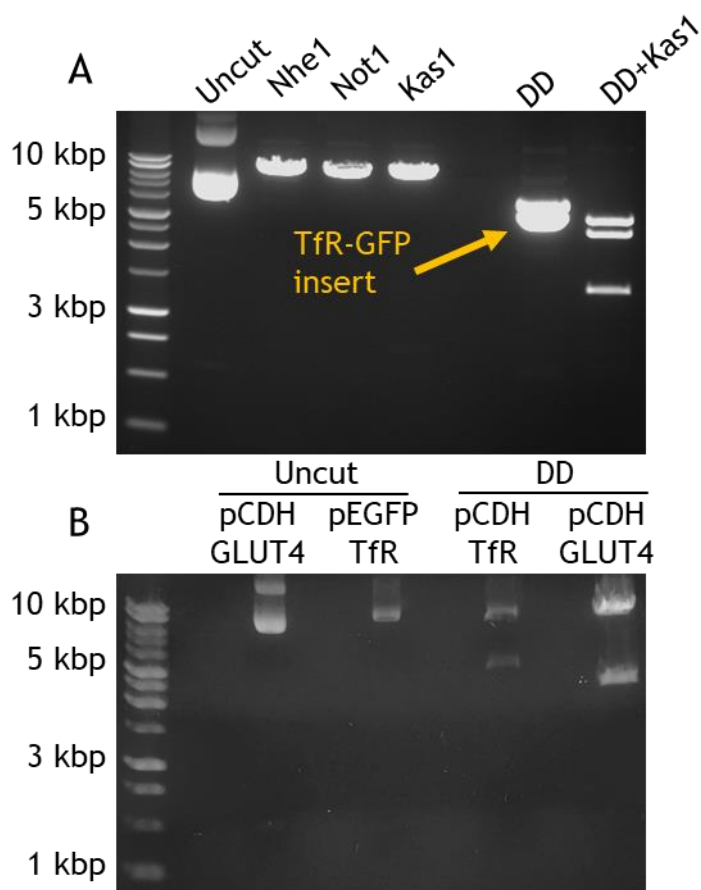


Figure 6.6 Generation of a novel pCDH-CMV-MCS-EF1-TfR-GFP DNA plasmid. Representative restriction enzyme digests of plasmid vectors. (A) Cutting the pEGFP-N1-Flag-TfR-GFP with both Nhe1 and Not1 restriction enzymes resulted in excision of the TfR-GFP gene fragment with the size 4000 bp. Kas1 was used to break the vector apart further to distinguish the vector backbone clearly from the TfR-GFP fragment. (B) Cutting the original pCDH-CMV-MCS-EF1-HA-GLUT4-GFP with both Nhe1 and Not1 restriction enzymes resulted in excision of the GLUT4-GFP gene fragment with the size 5000 bp. The TfR-GFP gene sequence was ligated into the open pCDH backbone to generate a novel pCDH-CMV-MCS-EF1-TfR-GFP plasmid and successful ligation was assessed by comparing the sizes of fragments after digestion. The pCDH backbone of the novel pCDH-CMV-MCS-EF1-TfR-GFP plasmid was similar to that found in the original pCDH-CMV-MCS-EF1-HA-GLUT4-GFP plasmid but the newly inserted TfR-GFP gene fragment was smaller compared to the HA-GLUT4-GFP sequence found in the original plasmid. pCDH GLUT4 = pCDH-CMV-MCS-EF1-HA-GLUT4-GFP; pEGFP TfR = pEGFP-N1-Flag-TfR-GFP; pCDH TfR = pEGFP-N1-Flag-TfR-GFP; DD = double digest with Nhe1 and Not1 restriction enzymes.

Next, we confirmed whether the newly developed plasmid was capable of inducing cells to produce GFP-tagged TfR protein. The novel pCDH-CMV-MCS-EF1-TfR-GFP plasmid was amplified in Stbl 3 competent *E. coli* and used to transfect HeLa cells. Figure 6.7 shows that transfected HeLa cells contained clearly detectable levels of TfR-GFP protein at 120 kDa. Our intention was to generate recombinant lentivirus to allow expression of TfR-GFP in 3T3-L1 adipocytes. However, as a result of the lockdown, insufficient time remained to allow us to optimise this, as initial attempts failed to generate infectious

virus. We have previously shown that GLUT4 translocates and disperses in response to insulin stimulation in HeLa cells which are easily transfected with DNA (Morris et al., 2020; Figure 4.18). Therefore, we transfected HeLa cells again with pCDH-CMV-MCS-EF1-TfR-GFP plasmid DNA and carried out dSTORM experiments to investigate the molecular distribution of TfR-GFP in the PM of this model organism.

Lipofectamine/well (μ l):	8	4	6	8	0	8
DNA/well (μ g):	2.4	2.4	2.4	3.2	3.2	0
Loading volume (μ l):	20	20	20	20	20	20

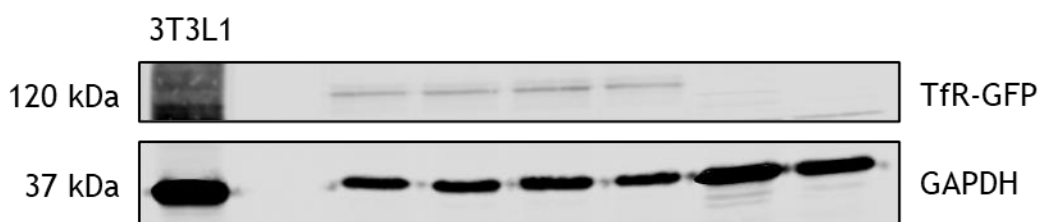


Figure 6.7 Transfection of HeLa cells with pCDH-CMV-MCS-EF1-TfR-GFP plasmid. HeLa cells were plated into wells of a 12-well plate and maintained until 70% confluence. Cells were transfected according to the manufacturer's protocol, as described in methods section 2.6.2. Final volumes of Lipofectamine 2000 and DNA added per well are indicated. 48 h later lysates were generated and 35 μ L of each sample was subjected to SDS-PAGE and immunoblotting in order to assess the expression of GFP and GAPDH protein.

We performed Ripley's K-function analysis of dSTORM images of untreated and insulin-stimulated HeLa cells expressing TfR-GFP. Data from three independent experiments are shown in figure 6.8. Insulin stimulation for 20 min did not affect the L(r) function indicating that there was no difference in clustering of TfR-GFP molecules in the PM ($p=0.0683$; determined by two-tailed Student's t-test). TfR expression has been linked to insulin sensitivity and the development of T2DM. Here we report that insulin did not stimulate TfR dispersal in HeLa cells as observed in GLUT4. Therefore, in HeLa cells TfR dispersal is not an aspect of insulin action.

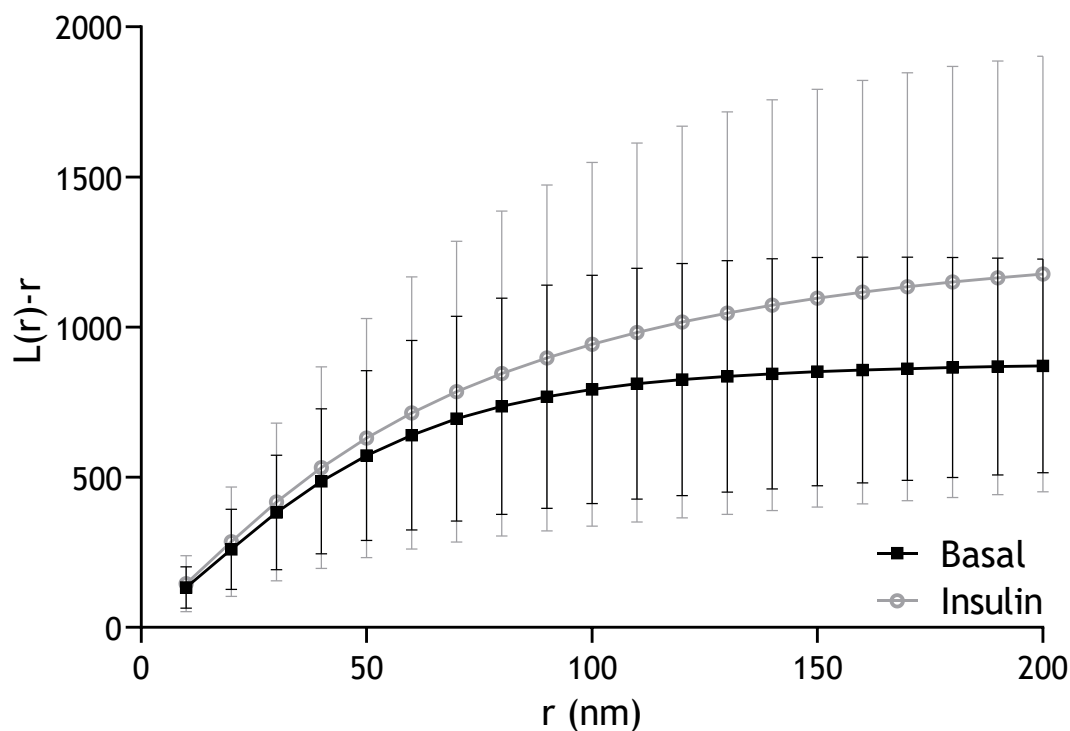


Figure 6.8 Ripley's K-function analysis of TfR-GFP clustering in basal and insulin-stimulated HeLa cells.

Representative plot of Ripley's K function analysis of the clustering abilities of TfR-GFP molecules in the PM of HA-GLUT4-GFP HeLa cells. Cells were transfected with TfR-GFP as previously described. Cells were serum-starved for 2 h prior to the experiment and stimulated with 1 μ M insulin for 20 min or left untreated. Cells were fixed, permeabilised and stained for GFP and dSTORM images acquired. GLUT4 molecule coordinates were obtained using ThunderSTORM and the obtained localization data was subjected to Ripley's K-function analysis using SR Tesselator with the minimum radius 10 nm, step radius 10 nm, and maximum radius 200 nm. $L(r)-r$ (y-axis) represents the clustering ability and r (x-axis) represents the radial scales of clustering. The presented data are mean \pm SD (N=3). The experiment was performed independently 3 times for basal (N=16 cells) and insulin-stimulated (N=16 cells) conditions. $p = 0.0683$; determined by two-tailed Student's t-test.

6.2.3 GLUT4 dispersal in primary human skeletal muscle cells from healthy and diabetic donors

Cryopreserved Clonetics™ Human Skeletal Muscle Myoblasts (HSMM) were commercially obtained from Lonza. The cells were isolated from the upper arm or leg muscle tissue from normal donors and donors diagnosed with T2DM allowing for comparisons between healthy and diseased tissue. Firstly, we confirmed the ability of healthy and T2DM HSMM to differentiate into multinucleated myotubes in cell culture. Bright field images show that HSMM from both sources demonstrated robust morphological differentiation into myotubes 5 days after initiation of differentiation according to the supplier's recommendations (Figure 6.9).

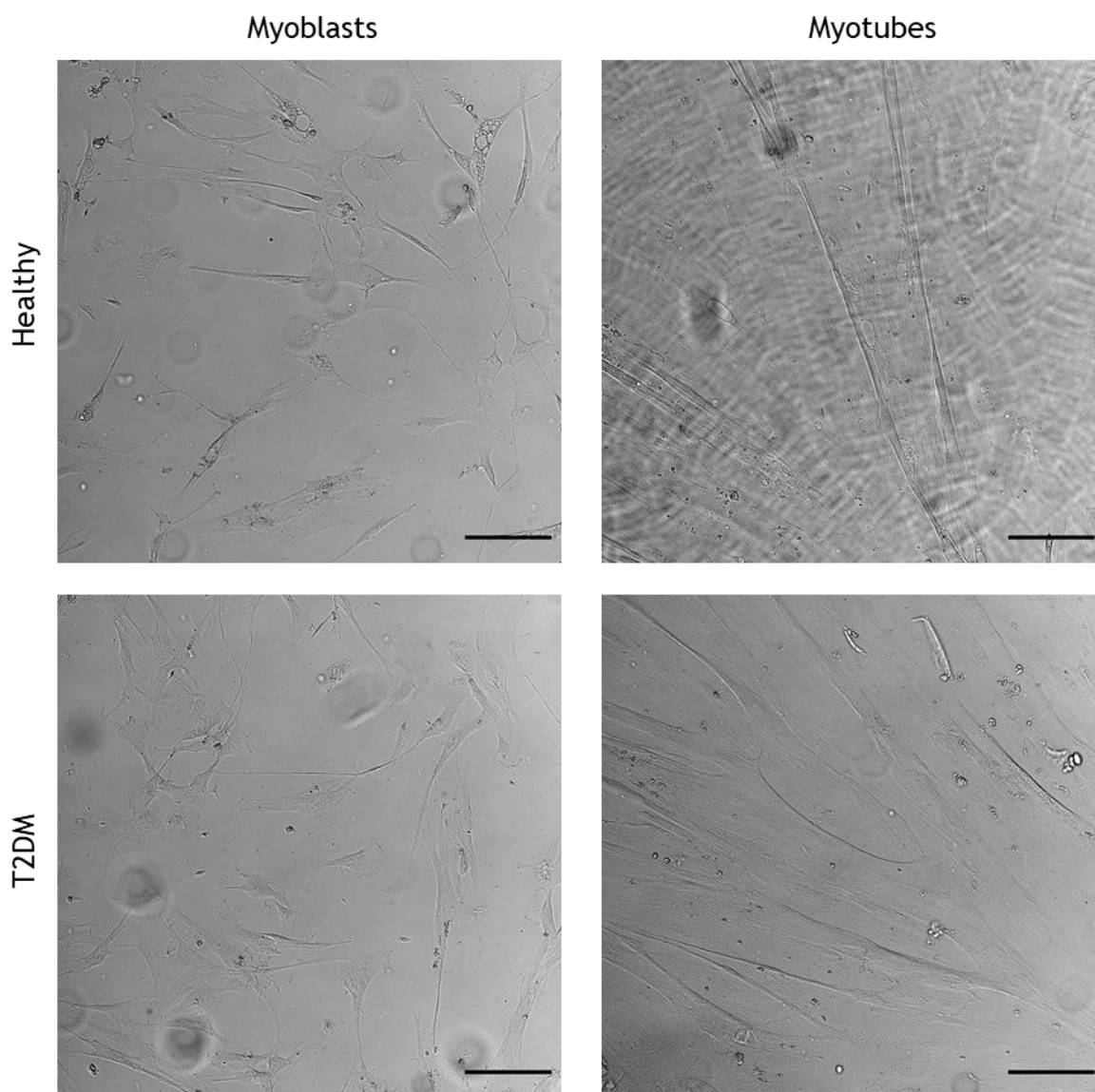


Figure 6.9 Bright field images of undifferentiated and differentiated HSMM derived from healthy and T2DM donors.

Representative confocal images of HSMM. The upper panel shows cells derived from a healthy donor whereas the lower panel shows cells derived from a T2DM donor. Images on the right show myoblasts and images on the left show myotubes 5 days after initiation of differentiation. Scale bars=100 μm .

Desmin is an abundant class-III intermediate filament protein known to regulate sarcomere architecture in human muscle. Staining for desmin is frequently used to confirm skeletal muscle differentiation and therefore was used to characterise the differentiation process of HSMM further in this study. Confocal images show that undifferentiated healthy and T2DM myoblasts did not express desmin but differentiated into desmin-positive multinucleated myotubes after 5 days (Figure 6.10).

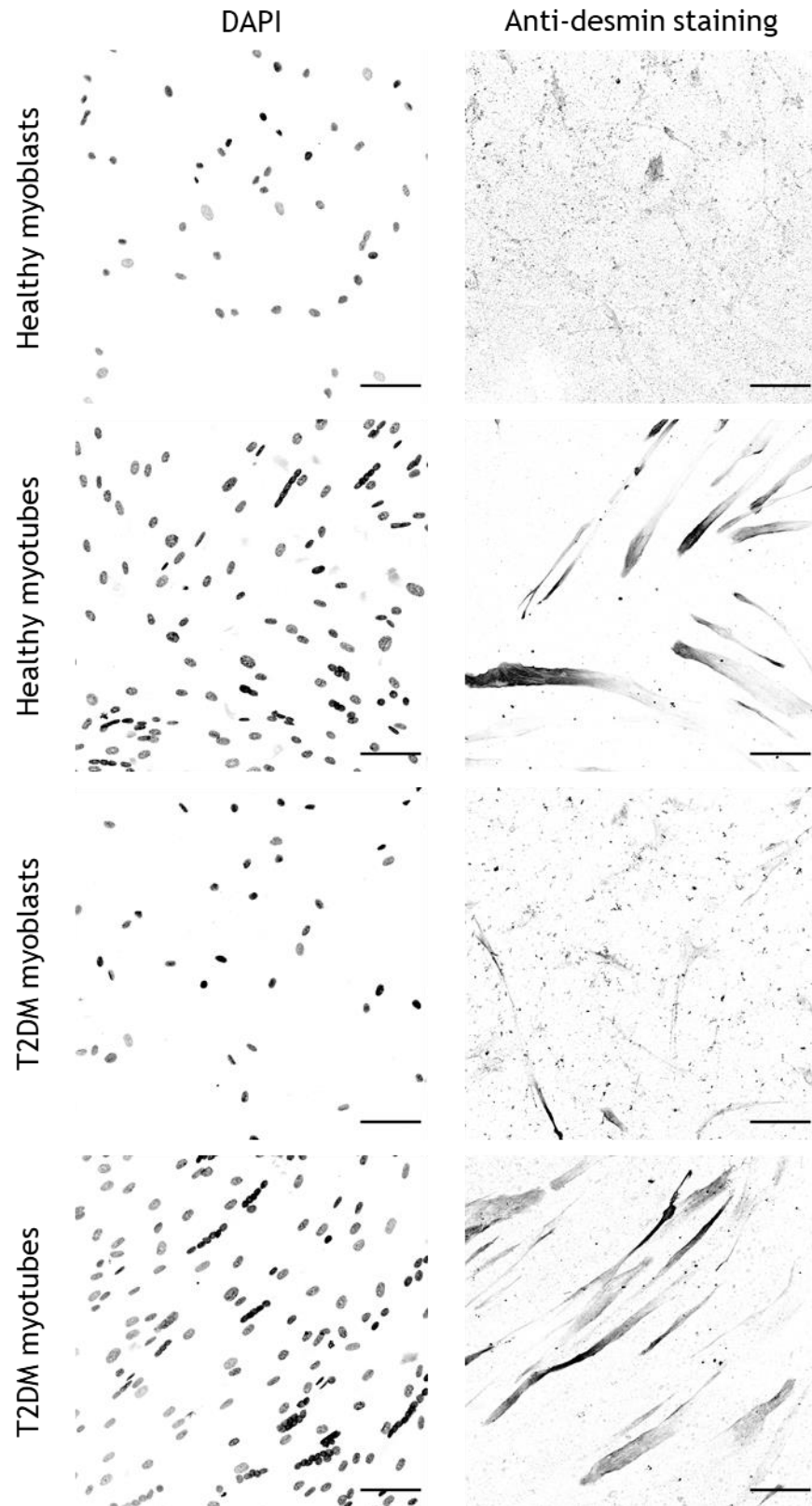


Figure 6.10 Confocal images HSMM stained for DAPI and desmin.

Representative confocal images of undifferentiated and differentiated HSMM derived from healthy and T2DM donors. Images on the right show DAPI-stained cell nuclei and images on the left show anti-desmin staining. Displayed are grayscale images with inverted LUTs. Scale bars=100 μm .

In the following immunofluorescence staining of GLUT4 was used to assess basal state GLUT4 localization in HSMM. Confocal images show that both undifferentiated and differentiated cells showed weak GLUT4-positive staining (Figure 6.11). However, the staining intensity was too low to gain reliable insights into intracellular GLUT4 localization.

HSMM were differentiated into myotubes and infected with Ad-HA-GLUT4-GFP to perform imaging experiments. The expression of GFP-tagged GLUT4 protein following adenoviral transduction was confirmed by epifluorescence microscopy 48 h post-transduction prior to each imaging experiment. Numerous differentiated HSMM expressed GFP indicating a high transduction efficiency (data not shown). Morphologically there were no differences between HSMM from a healthy or T2DM donor. To observe the molecular distribution and quantify the spatial patterning of GLUT4 within the PM HA-staining was carried out and dSTORM images acquired. As previously described myotubes were screened in TIRF mode (Figure 6.12 A and D). Representative TIRF images show selectively excited diffraction-limited GLUT4-GFP in the PM (Figure 6.12 A and D). Reconstructed dSTORM images show clearly visible single GLUT4 molecules as well as clusters within the PM (Figure 6.12 B and E). The magnifications of the reconstructed images as seen in figure 6.12 for a (C) basal and (F) insulin-stimulated cell show no difference in the density of GLUT4 molecules at the cell surface.

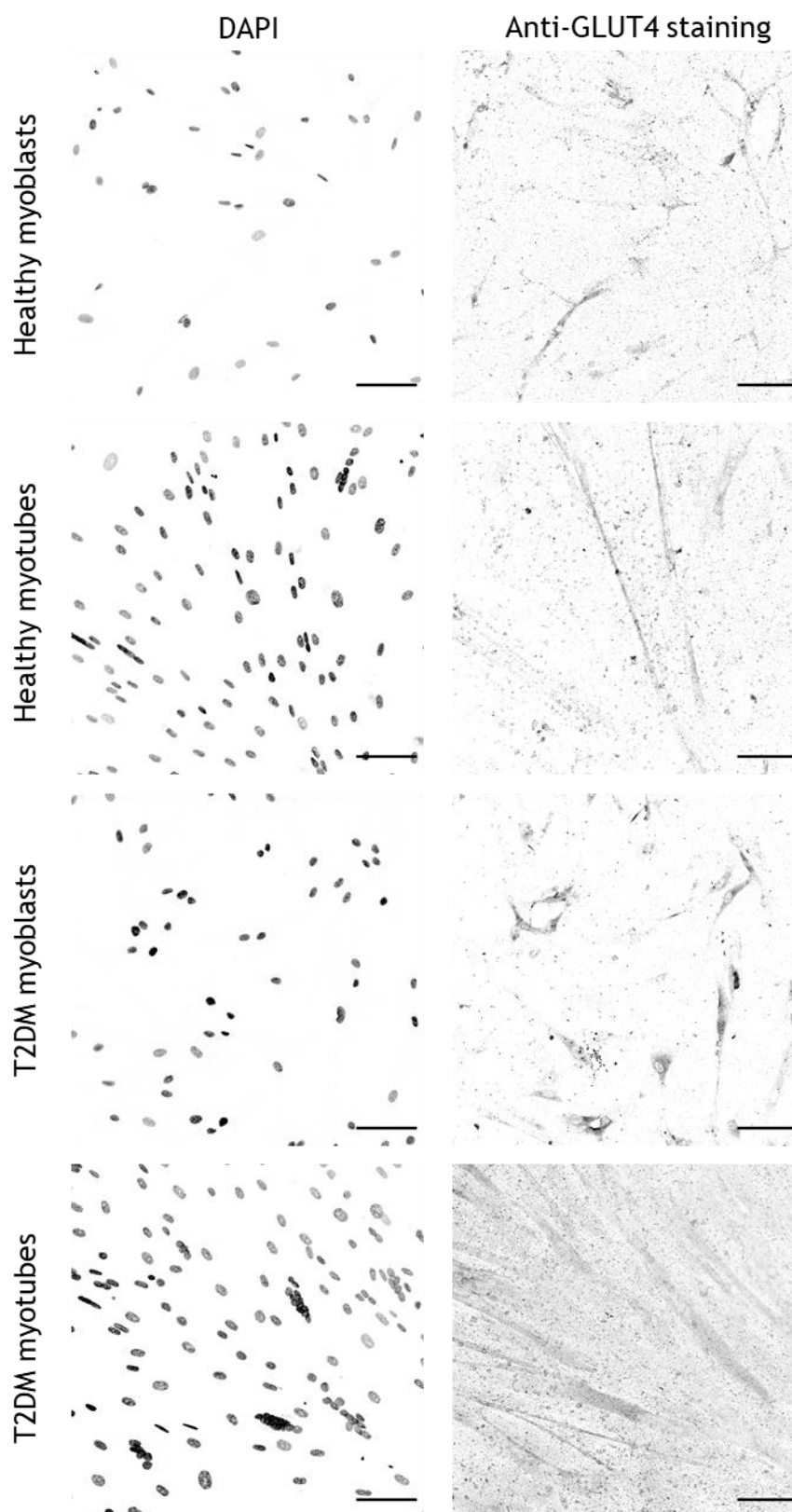


Figure 6.11 Confocal images HSMM stained for DAPI and endogenous GLUT4. Representative confocal images of undifferentiated and differentiated HSMM derived from healthy and T2DM donors. Images on the right show DAPI-stained cell nuclei and images on the left show anti-GLUT4 staining. Displayed are grayscale images with inverted LUTs. Scale bars=100 μm .

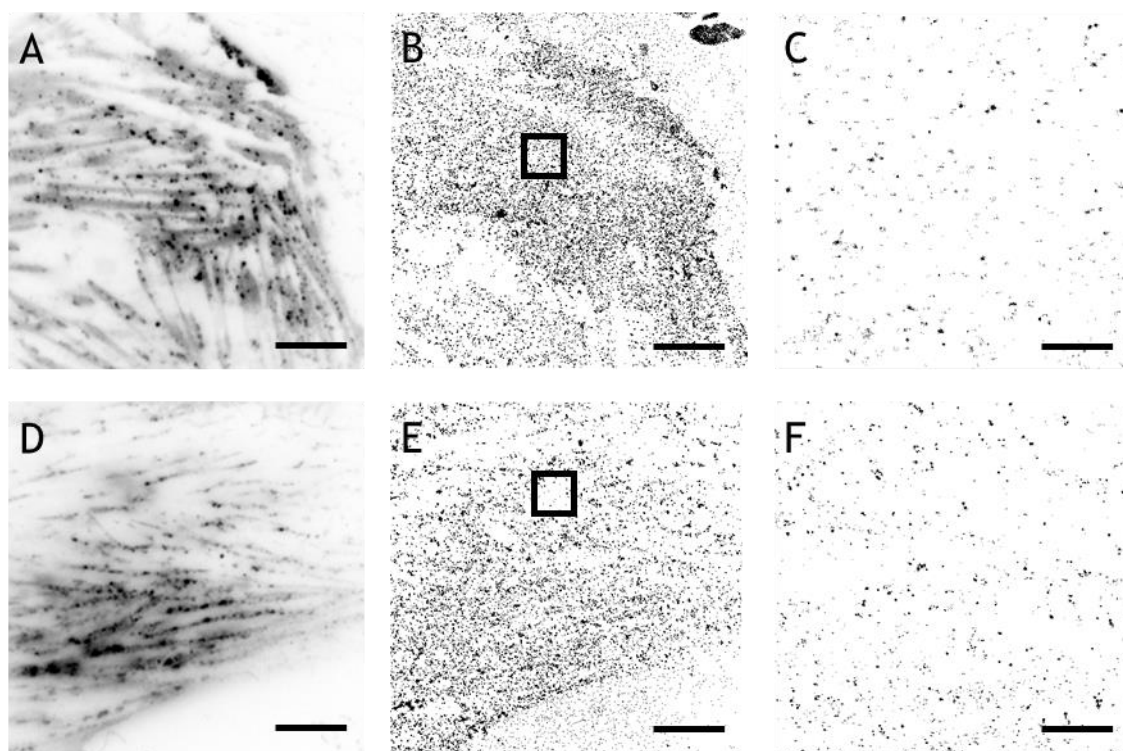


Figure 6.12 TIRF and STORM images of surface GLUT4 in basal and insulin-stimulated HSMM from a healthy donor.

HSMM transduced with Ad-HA-GLUT4-GFP were incubated in serum-free medium for 4 h and stimulated with 1 μ M insulin for 20 min or left untreated. Cells were fixed and stained for surface HA and dSTORM images acquired. Reconstructions were created using the ImageJ plugin ThunderSTORM. (A) Representative fluorescence TIRF image of a HSMM. (B) Representative scatterplot of a basal cell showing localisations of single GLUT4 molecules. (C) Magnified section of image B. (D) Representative TIRF image of an insulin-stimulated cell. (E) Representative scatterplot of an insulin-stimulated cell showing localisations of single GLUT4 molecules. (F) Magnified section of image D. Scale bars = 10 μ m (A, B, D, E) and 1 μ m (C and F). This experiment was repeated 3 times with similar results.

Ripley's L-function analysis was carried out to quantify changes in GLUT4 dispersal in the PM of basal and insulin-stimulated HSMM from healthy and T2DM donors. Figure 6.13 shows the averaged L(r) functions for basal and insulin-stimulated cells from three independently performed experiments. The observed L(r) peaked at similar clustering values for GLUT4 on the PM of untreated and insulin-stimulated cells derived from healthy (A) and T2DM (B) donors. This indicates that there was no significant difference in GLUT4 clustering on the plasma membrane in response to insulin-stimulation in HSMM.

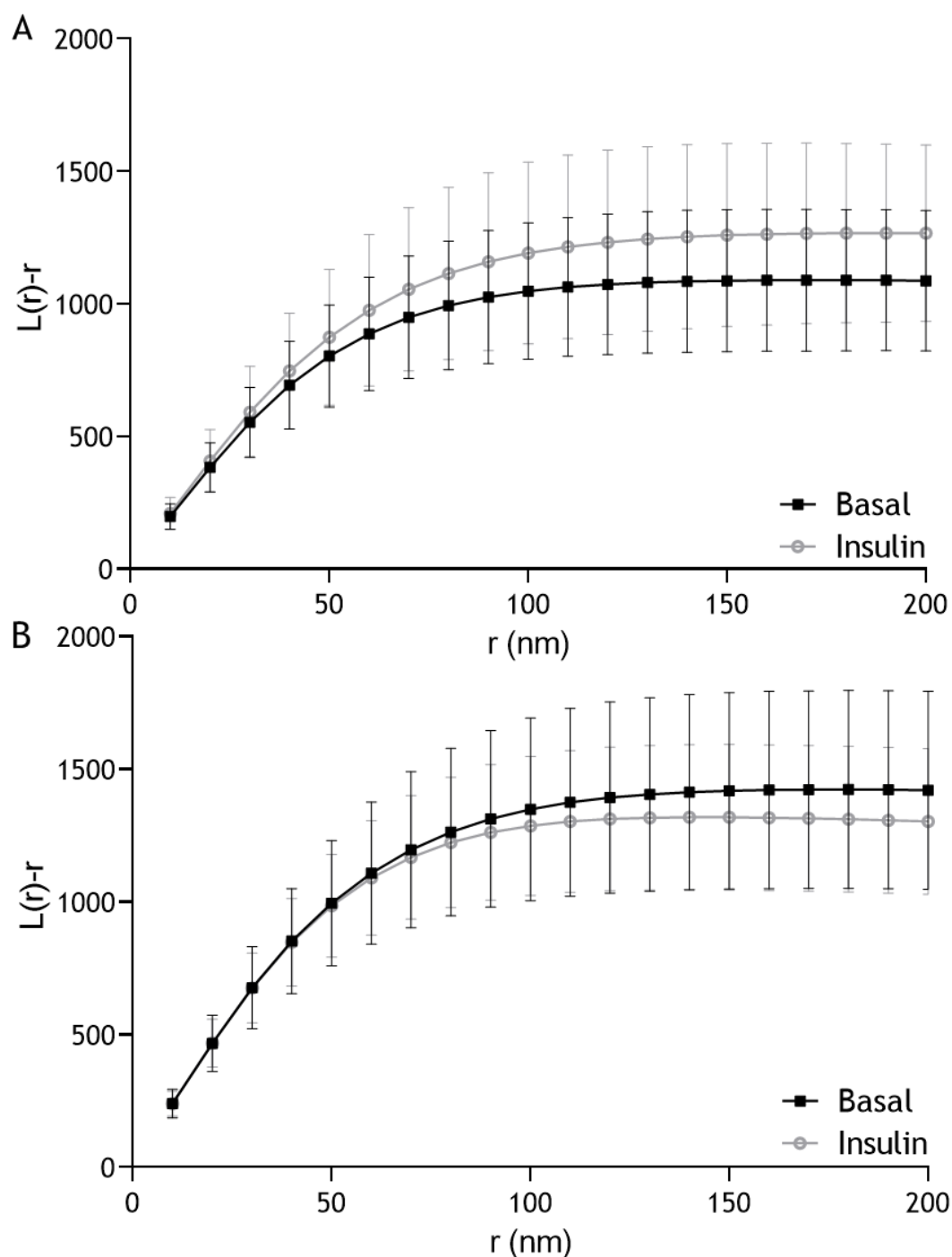


Figure 6.13 Ripley's K-function analysis of GLUT4 clustering in basal and insulin-stimulated HSMM.

Ripley's K function analysis of the clustering abilities of GLUT4 molecules in the PM of differentiated HSMM from (A) healthy and (B) T2DM donors. Cells were serum-starved and stimulated with 1 μ M insulin for 20 min or left untreated. Cells were fixed, stained for surface HA and dSTORM images acquired. Molecules were localized using ThunderSTORM and the obtained data was subjected to Ripley's K-function analysis using SR Tesseler with the minimum radius 10 nm, step radius 10 nm, and maximum radius 200 nm. The presented data are mean \pm SD and experiments were performed independently 3 times for healthy basal (N=36 cells) and insulin-stimulated (N=31 cells), and T2DM basal (32 cells) and insulin-treated (31 cells) conditions. (A) $p=0.18$; (B) $p=0.57$; determined by unpaired Student's t-test.

Subsequently, several proteins involved in GLUT4 trafficking were investigated and compared in healthy and diseased HSMM. As a starting point we assessed GLUT protein expression and insulin sensitivity of differentiated myotubes by western immunoblotting. Differentiated myotubes from each source showed a high insulin-stimulated phosphorylation of Akt, indicating a robust insulin response (Figure 6.14).

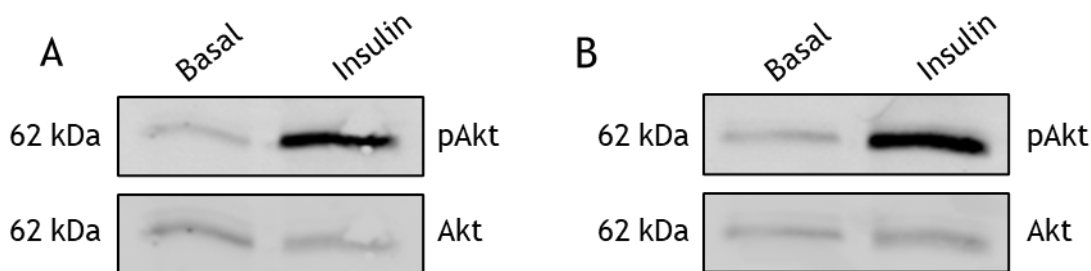


Figure 6.14 Insulin sensitivity in differentiated healthy and T2DM HSMM.

HSMM were differentiated as previously described and protein expression was assessed by western immunoblotting. Differentiated myotubes from (A) healthy and (B) T2DM donors were treated with or without 1 μ M insulin for 20 min as indicated. Blots were incubated with anti-Akt or anti-phospho Akt (p-Akt). Blots were visualised with a LI-COR Odyssey-SA system; data from a typical experiment is shown.

Furthermore, it was observed that differentiated (myotubes) and undifferentiated (myoblasts) HSMM from both healthy and T2DM donors had a relatively low endogenous expression of GLUT4 protein compared to 3T3-L1 adipocytes (Figure 6.15 A). GLUT1 protein expression was higher in both myoblasts and myotubes from healthy and T2DM donors with no striking differences between groups (Figure 6.15 B). We also assessed endogenous expression of GLUT8 and GLUT12 protein in HSMM but did not detect any signal after performance of several optimisation experiments (data not shown).

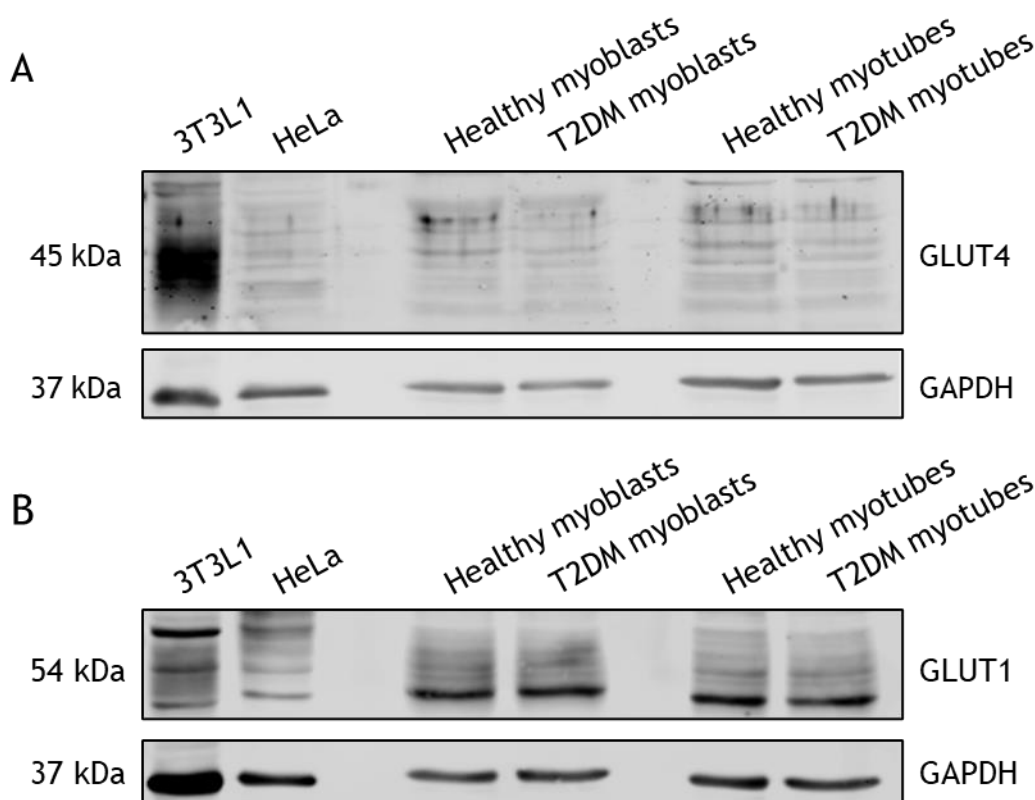


Figure 6.15 Endogenous GLUT protein expression in differentiated and undifferentiated HSMM.

3T3-L1 adipocytes and HSMM were differentiated as previously described and protein expression was assessed by western immunoblotting. (A) 20 μ L of sample were loaded. Blots were incubated with anti-GLUT4 and anti-GAPDH (as a loading control) as labelled. (B) 20 μ g of sample were loaded. Blots were incubated with anti-GLUT1 and anti-GAPDH as labelled. Blots were visualised with a LI-COR Odyssey-SA system; data from a typical experiment is shown.

Clathrins are cytoplasmic proteins that play important roles in endocytosis. The two clathrin heavy chains CHC17 and CHC22 are found in humans with CHC17 being known to be ubiquitously expressed and CHC22 being enriched in skeletal muscle. In this study we assessed CHC17 protein expression in HSMM (Figure 6.16 A/B). It can be observed that CHC17 protein expression was higher in myotubes compared to myoblasts of healthy and T2DM HSMM (Figure 6.16 B). Moreover, CHC17 protein expression was reduced in both myoblasts and myotubes derived from T2DM donors compared to those from healthy donors. Investigation of CHC22 in HSMM was hampered by the non-specificity of commercially available antibodies (data not shown). Furthermore, we investigated expression of Rab proteins 8, 10 and 14 with limited success. The antibodies used showed considerable non-specific staining that made their use unreliable (data not shown).

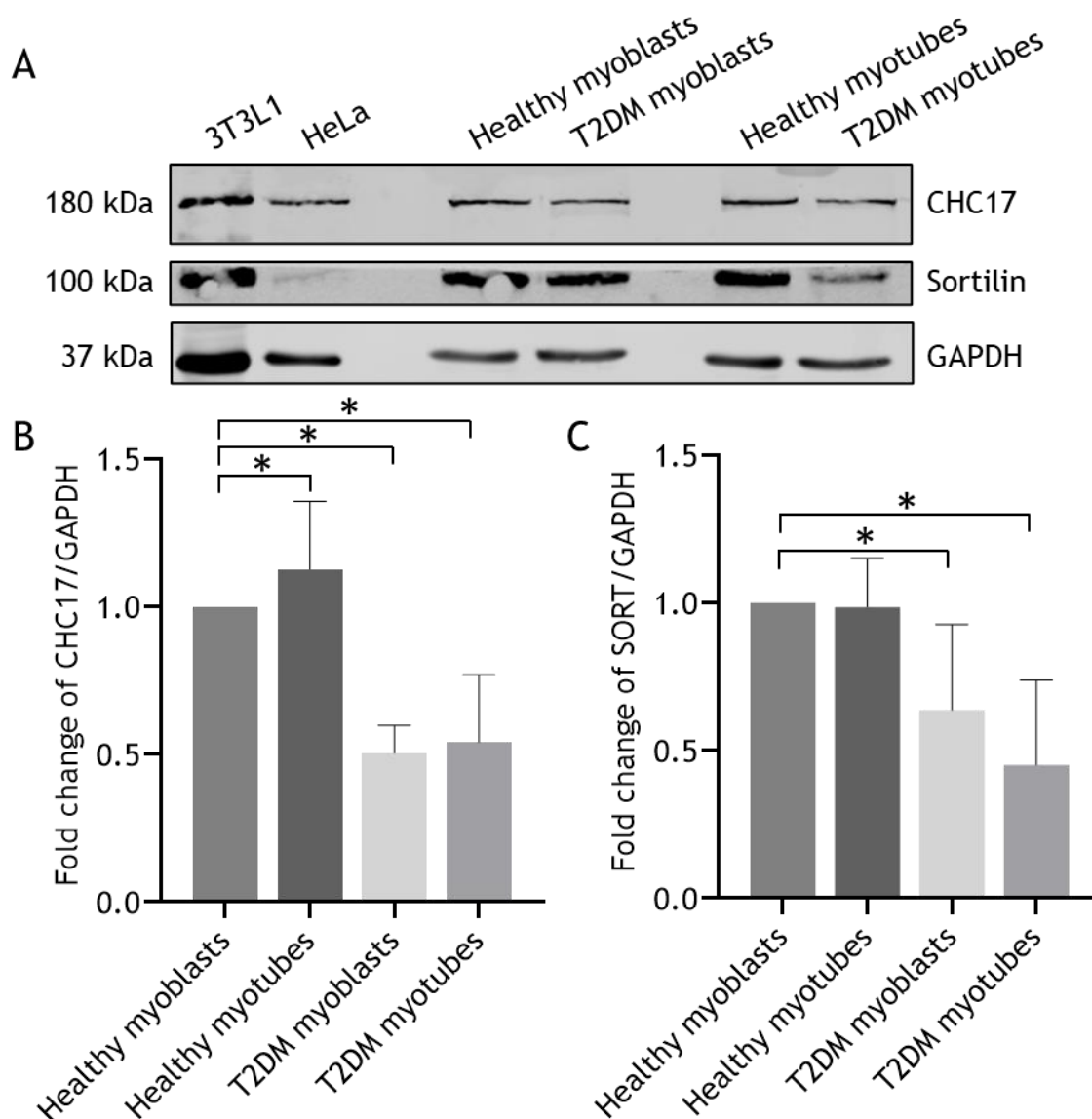


Figure 6.16 Endogenous CHC17 and sortilin protein expression in differentiated and undifferentiated HSMM.

3T3-L1 adipocytes and HSMM were differentiated as previously described and protein expression was assessed by western immunoblotting. (A) 20 μ L of sample were loaded and blots were incubated with anti-CHC17, anti-sortilin and anti-GAPDH as labelled. Blots were visualised with a LI-COR Odyssey-SA system. Quantification of (B) CHC17 and (C) sortilin immunoblots performed via densitometry, expressed as fold change of protein ratio from healthy myoblasts. Data from 3 independently conducted experiments are shown. * indicating $p < 0.05$. (B) $p = 0.0037$ (C) $p = 0.0393$; determined by one-way ANOVA.

Sortilin is widely abundant on cell surfaces and the endoplasmic reticulum-Golgi apparatus where it acts as a sorting receptor for a variety of intracellular proteins between endosomes, lysosomes, the trans-Golgi network, secretory granules and the PM. Its molecular function enables sortilin to participate in GLUT4 translocation from intracellular stores to the PM in response to insulin. Here we investigated endogenous levels of sortilin protein expression in HSMM (Figure 6.16 A/C). Figure 6.16 A shows

expression of sortilin at an expected size of 100 kDa in both myoblasts and myotubes derived from healthy and T2DM donors. Again it can be observed that sortilin expression was reduced in both myoblasts and myotubes derived from T2DM donors (Figure 6.16 C).

6.3 Discussion

6.3.1 Insulin resistance reorganises GLUT4 clustering

Cellular insulin resistance is strongly associated with defects in the adipocyte glucose transport system and in this study we investigated the effect of insulin resistance on GLUT4 dispersal. It was observed that chronic insulin treatment induced a state of insulin resistance in 3T3-L1 adipocytes (Figure 6.1) and this treatment resulted in attenuated insulin-stimulated GLUT4 dispersal in the PM (Figure 6.2). Up to date there is only one report of induced cellular insulin resistance resulting in the reorganization of GLUT4 clustering in adipocytes (Gao et al., 2017). In this study 3T3-L1 adipocytes were treated with 100 nM insulin overnight and this treatment resulted in inhibition of the phosphorylation of Akt assessed by western immunoblotting indicating the inability of the adipocytes to appropriately respond to insulin stimuli. STORM was used to investigate GLUT4 clustering dynamics and it was reported that insulin resistance resulted in enhanced GLUT4 clustering under both basal and insulin stimulated conditions (Gao et al., 2017). Ripley's K function analysis revealed that insulin stimulated GLUT4 dispersal moderately in insulin-resistant cells and that the effect was not as large as observed in control 3T3-L1 cells (Gao et al., 2017). Insulin resistance did not change cluster properties for instance number of molecules per cluster, clusters/ μm^2 and molecules/ μm^2 (in this study Ripley's K function analysis was chosen to quantify GLUT4 clustering as lined out in Chapter 1). However, there was an increase in the total amount of molecules found in large GLUT4 clusters in insulin-resistant cells. In line with this study we report that insulin resistance affected the spatial distribution of GLUT4 in the PM of 3T3-L1 adipocytes. Ripley's K function analysis of three independently conducted experiments revealed that chronic insulin treatment with 500 nM for 24 h resulted in a shift of $L(r)$ towards peaking at higher clustering values for both basal and insulin-stimulated cells (Figure 6.2). This result is similar to the accounts of the previous study (Gao et al., 2017). In addition, we analysed localization density of GLUT4 molecules and found that chronic insulin treatment affected translocation of GLUT4 from intracellular stores to the PM. In control cells insulin stimulation resulted in a higher density of GLUT4 molecules in the PM and this effect was reduced by 34 % following chronic insulin treatment indicating a reduction in GLUT4 translocation (Figure 6.3). Our results suggest that insulin resistance affects intracellular GLUT4 trafficking pathways as well as the organization of the transporter within the PM.

A negative correlation between adipocyte cell area and GLUT4 molecule density was observed in both basal and insulin-stimulated cells indicating that more GLUT4 translocated to the PM following insulin stimulation in small cells compared to large cells (Figure 6.4). Therefore, small 3T3-L1 adipocytes were identified to be more insulin sensitive (Figure 6.5). Adipose tissue expands by increasing cell size (hypertrophy) and cell number (hyperplasia) and consequently contains cells of various sizes *in vivo* and *in vitro*. Over the years numerous studies have investigated the relationship between cell size and pathological states such as insulin resistance and T2DM (Acosta et al., 2016; Bernstein et al., 1975; Haller et al., 1979; Laforest et al., 2015; McLaughlin et al., 2007; Stenkula and Erlanson-Albertsson, 2018; Verboven et al., 2018; Weyer et al., 2000). In isolated human adipose tissues metabolism of glucose to carbon dioxide and triglycerides was observed to be closely related to cell numbers but not cell size (Salans et al., 1968). In contrast, insulin sensitivity was discovered to be dependent on adipose cell size. The larger the cells composing the adipose tissue the less insulin responsive it was (Salans et al., 1968). Weight loss accompanied by a reduction in adipocyte cell size was found to restore insulin responsiveness (Salans et al., 1968). Several studies have indicated that adipocyte size serves as a predictor of metabolic disease and diabetes independent of body mass index (Haller et al., 1979; Laforest et al., 2015; Weyer et al., 2000). A study including 280 Pima Indians with normal, impaired or diabetic glucose tolerance found that subcutaneous abdominal adipocyte size was higher in subjects with impaired or diabetic glucose tolerance (Weyer et al., 2000). Of 108 control subjects that were followed up for a decade 33 subjects developed diabetes with subcutaneous abdominal adipocyte size being an independent predictor of disease onset (Weyer et al., 2000). Interestingly it has been reported that even non-obese individuals with T2DM have adipocytes of increased size compared to healthy controls (Acosta et al., 2016). Furthermore, 166 healthy individuals with genetic predisposition for T2DM, but not for obesity, have been reported to display adipose tissue hypertrophy and reduced insulin sensitivity (Arner et al., 2011). One study investigated insulin responsiveness in small and large populations of adipocytes obtained from the same individual to eliminate biological variation as a confounding variable (Franck et al., 2007). Small and large primary human fat cells from the same volunteer were found to have similar amounts of IR, IRS-1 and GLUT4 protein and similar activation of proteins involved in the insulin signalling cascade (Franck et al., 2007). However, confocal images showed that insulin stimulation resulted in reduced GLUT4 translocation to the PM in large cells compared to small cells (Franck et al., 2007). This result is in line with the reduced GLUT4 localization density in large 3T3-L1 cells reported in this study. Recently a study reported that C57BL6/J mice that were fed a high-fat diet for 2 weeks leading to expansion in adipocyte cell size resulted in drastic cytoskeletal actin remodelling

(Hansson et al., 2019). In hypertrophic adipocytes the insulin response was impaired and filamentous actin was significantly increased. This mechanism could significantly contribute to the deteriorating adipocyte function observed in T2DM (Hansson et al., 2019). Taken together these results suggest that adipocyte size is an important feature and even predictor of T2DM. Impaired cellular function of hypertrophic adipocytes is an understudied aspect of adipose tissue biology and further studies are warranted to establish a knowledge basis that could fuel the development of novel therapeutic strategies.

6.3.2 Is plasma membrane dispersal specific to GLUT4?

Super resolution microscopy has not only revealed the existence of GLUT4 dispersal but also advanced our understanding of GLUT1 spatial organization and function (Yan et al., 2018). GLUT1 is responsible for constitutive basal glucose uptake that sustains respiration in all mammalian cells. STORM showed that GLUT1 was organised within clusters in the PM of cultured HeLa cells (Yan et al., 2018). GLUT1 formed clusters of up to 25 molecules but the majority of GLUT1 clusters contained 2-4 molecules and were small in size. Dual-colour STORM experiments using anti-cholera toxin subunit B staining to visualise lipid rafts were performed to investigate the interactions between GLUT1 clusters and these membrane microdomains. It was observed that 35 % of GLUT1 clusters were colocalised with lipid rafts and disruptions of lipid rafts with MBCD attenuated GLUT1 clustering (Yan et al., 2018). Glucose uptake experiments showed that MBCD treatment of HeLa cells resulted in increased rates of uptake and activation of GLUT1. This study supports that GLUT1 similar to many membrane proteins forms aggregates and clustering dynamics are associated with its activation and function.

GLUT1 is constitutively expressed and does not translocate in response to insulin. However, apart from GLUT4 insulin recruits transmembrane proteins such as TfR and the insulin-responsive amino peptidase (IRAP) to the PM of fat and muscle cells. GLUT4 and IRAP have been identified to colocalise and cycle through similar endocytic pathways (Bryant et al., 2002). Several studies have observed colocalization of GLUT4, IRAP and the endosomal marker TfR (Chen et al., 2012; Lim et al., 2001; Livingstone et al., 1996; Watson et al., 2008). TIRF microscopy revealed that in fibroblasts the majority of GLUT4 and IRAP colocalises with TfR in the endosomal system (Lampson et al., 2001). In contrast in the highly insulin-responsive 3T3-L1 adipocytes it was found that only 30-40 % of GLUT4 is located in endosomal compartments with TfR under basal conditions (Martin et al., 1996). In this study we aimed to produce a lentivirus to express TfR-GFP to perform imaging experiments in 3T3-L1 adipocytes. Our aim was to investigate whether insulin-stimulated dispersal is specific to GLUT4 or can be observed

in related transmembrane proteins such as TfR. HeLa cells have comparable GLUT4 trafficking and dispersal mechanisms to those observed in adipocytes (Morris et al., 2020). Taken together with the evidence that GLUT4 and TfR colocalise in several cell types that show small insulin responses we decided to overexpress TfR-GFP in HeLa cells and use dSTORM to investigate clustering dynamics of TfR similarly to GLUT4. Here we report for the first time that insulin did not stimulate the reorganisation of TfR in the PM of HeLa cells (Figure 6.6). Chemical ablation of endosomes did not block insulin-stimulated GLUT4 translocation in adipocytes (Martin et al., 1998) indicating that even though insulin has a small effect on general endosomal recycling by stimulating translocation of TfR endosomes are not the main insulin-responsive vesicles (IRV) (Bryant et al., 2002). Recently, using TIRFM it was reported that GLUT4 and the TfR are packaged into distinct intracellular vesicles budding from the endosomal recycling compartment in CHO cells (Lampson et al., 2001; Lim et al., 2001). It was proposed that in fibroblasts GLUT4 is located in slowly recycling vesicles and TfR in rapidly recycling vesicles that directly fuse with the PM even in the absence of insulin (Lampson et al., 2001). In insulin responsive tissues this is not the case and taken together these findings indicate the segregation of GLUT4 from recycling endosomes during insulin-stimulated trafficking (Bryant et al., 2002). The finding that insulin stimulation did not result in dispersal of TfR in HeLa cells might be an indication that the insulin-stimulated GLUT4 dispersal we previously observed in these cells (see figure 4.18) originated from separate IRV and not endosomal compartments. Our finding also supports that HeLa cells have similar GLUT4 trafficking and dispersal mechanisms as observed in adipocytes. Further studies are needed to confirm whether insulin stimulation affects TfR distribution in highly insulin-responsive cells and to confirm that insulin-stimulated dispersal is specific to GLUT4 from IRV.

6.3.3 GLUT4 dispersal in primary human skeletal muscle cells from healthy and diabetic donors

In recent years human skeletal muscle myoblasts have become commercially available (Owens et al., 2013). Myoblasts are mononucleate precursors of skeletal muscle that fuse during development to form multinucleated myotubes that mature into muscle fibres (Zammit et al., 2006). This process can be partly mimicked in vitro by propagating skeletal muscle myoblasts in culture and chemically inducing them to fuse and differentiate into myotubes (Wasserman and Halseth, 1998). One study aimed to characterise myotube formation and differentiation of a variety of cells from different commercial vendors (Owens et al., 2013). HSMM purchased from Lonza Bioscience were found to be easily cultured as undifferentiated cells in growth media and demonstrated

robust myotube formation in cell culture (Owens et al., 2013), therefore we adopted this model for use. HSMM from both healthy and T2DM donors developed into myotubes 5 days after initiation of differentiation (Figure 6.7). Myotubes stained desmin-positive and myoblasts desmin-negative (Figure 6.8) but levels of GLUT1 and GLUT4 were found to be too low to accurately quantitate (Figure 6.9). In foetuses GLUT1 is majorly expressed in the PM of myoblasts and myotubes but the total amount is higher in myoblasts compared to myotubes and decreases markedly during postnatal life. GLUT4 expression follows an opposing trend with levels being low during early development and levels peaking progressively during postnatal life (Castelló et al., 1993). In our hands, HSMM were highly insulin sensitive but expressed low levels of GLUT4 (Figure 6.12/13). This result could be explained by the state of differentiation of skeletal muscle myotubes that lies between undifferentiated myoblasts and fully mature muscle fibres.

In this study we observed that sortilin protein expression was lower in differentiated HSMM derived from diabetic donors. It has been largely documented that sortilin colocalises with GLUT4 in differentiated myotubes and adipocytes and several studies reported that sortilin is crucial for insulin-mediated glucose metabolism (Ariga et al., 2008, 2017; Morris et al., 1998; Shi and Kandror, 2005). Induction of sortilin on day 2 of 3T3-L1 adipocyte differentiation was reported to result in the formation of IRV (Shi and Kandror, 2005). Furthermore, overexpression of sortilin was observed to increase the formation of IRV and insulin-stimulated glucose transport whereas GLUT4 expression before induction of sortilin resulted in GLUT4 degradation. This indicates that sortilin is vital for the biogenesis of IRV in adipocytes (Shi and Kandror, 2005). Later the same group reported that sortilin interacts with GLUT4 and IRAP in the vesicular lumen of adipocytes resulting in IRV biogenesis (Shi and Kandror, 2007). Similarly it was found that sortilin expression was upregulated during differentiation of C2C12 skeletal muscle myotubes and contributed to the development of the insulin-responsive glucose transport system (Ariga et al., 2008, 2017). Co-expression of myc7-tagged GLUT4 and sortilin in 3T3-L1 adipocytes has resulted in increased GLUT4 targeting to insulin-responsive vesicles and maximal levels of insulin responsiveness (Huang et al., 2013). These studies indicate that the presence of sortilin is vital for insulin responsiveness in adipocytes and skeletal muscle and decreased levels of sortilin might result in insulin resistance. Specifically sortilin was found to enable two critical steps in the GLUT4 sorting pathway namely retrieval of GLUT4 from early endosomes to the *trans*-Golgi network followed by the formation of IRV from *trans*-Golgi network donor membranes (Blondeau et al., 2018). In endosomes the luminal Vps10p domain of sortilin was found to bind to the first extracellular loop of GLUT4 whilst its c-terminus binds to retromer

(Pan et al., 2017). This results in the retrieval of GLUT4 from endosomes. For the biogenesis of IRV the sortilin C-terminus interacts with specific clathrin adaptor proteins (Li and Kandrór, 2005). Defects in the described GLUT4 sorting mechanisms play a role in the development of T2DM. In C2C12 myotubes it was observed that palmitate treatment decreased sortilin expression which resulted in impairment of GLUT4 trafficking (Tsuchiya et al., 2010). Sortilin mRNA and protein levels were reported to be decreased in adipose and muscle tissues from obese *db/db* and *ob/ob* mice (Kaddai et al., 2009). Moreover, sortilin mRNA and protein levels were downregulated in tissues of morbidly obese T2DM patients (Kaddai et al., 2009). Here, we report a decrease in sortilin protein expression in HSMM from a normal weight subject which is in line with the current evidence that sortilin is key to regulation of intracellular GLUT4 location and defects in GLUT4 sorting contribute to the development of the T2DM phenotype.

Clathrin heavy chains interact at their C-termini to form the clathrin triskelion in the cytoplasm that binds adaptor proteins linking it to the PM (Pearse, 1976). The triskelion will bind other membrane-bound triskelia to form a clathrin lattice that facilitates vesicle formation and is able to capture cargo molecules for transport. The CHC17 and CHC22 heavy chains build two clathrin lattices with distinct cellular functions. CHC17 is important for receptor-mediated endocytoses at the PM and organelle biogenesis in the trans-Golgi network whereas CHC22 plays a key role in intracellular targeting of GLUT4 and has been observed to accumulate during insulin resistance (Dannhauser et al., 2017). In this study we have observed CHC17 protein expression in all HSMM but unfortunately were not able to detect CHC22 protein in our samples.

6.3.4 Conclusions and future directions

Here we confirmed that insulin resistance induced by chronic insulin treatment attenuated insulin-stimulated GLUT4 dispersal in 3T3-L1 adipocytes. Furthermore, we produced a novel plasmid vector to study the spatial patterning of TfR-GFP in the PM of HeLa cells. We found that TfR does not disperse in response to insulin stimulation. Further studies are needed to investigate whether this effect can also be observed in adipocytes and muscle cells. It would be desirable to further investigate the link between TfR and insulin resistance.

To our knowledge this was the first study that investigated insulin-stimulated GLUT4 dispersal in a commercially available model of skeletal muscle. It was observed that insulin did not stimulate GLUT4 dispersal in HSMM from healthy and T2DM donors. We report that HSMM were highly insulin-sensitive but did not have similar GLUT1 or GLUT4 protein expression levels compared to those observed in mature muscle fibres. We did

not find any significant difference in expression of GLUT or clathrin heavy chain proteins between myoblasts and myotubes from healthy and T2DM donors. We did find that sortilin protein levels were reduced in T2DM myotubes. It can be concluded that this study shed some light on the mechanisms of GLUT4 dispersal in health and disease but more studies are needed employing a range of cell culture models and experimental techniques. A future aim is to study how HSMM from healthy and T2DM donors compare in their levels of insulin resistance and what mechanisms govern this.

7. Discussion

7.1 Summary of key findings

Firstly, we successfully developed a microscopy-based assay to quantify GLUT4 clustering within the PM of adipocytes at the single molecule level. To achieve this aim we explored a range of sample preparation and image processing methods to perform GLUT4 cluster analysis. Automated Ripley's K function analysis was recognised as a valuable tool to summarize spatial dependence of GLUT4 molecules over a range of distances and indicate changes in GLUT4 clustering dynamics. It was the fastest and most user-friendly cluster analysis approach and thus was used for analysis throughout this study.

We measured GLUT4 clustering and insulin-stimulated dispersal with the use of dSTORM in a variety of cell culture model systems. This provided us with a tool to assess how clustering might underpin key aspects of glucose transport regulation. For the first time it was observed that AMPK activation attenuated insulin-stimulated GLUT4 dispersal and shifted the molecular distribution of GLUT4 towards a more clustered state in 3T3-L1 adipocytes. AMPK is activated in response to cellular stress in adipocytes and inhibits the effects of insulin. Here we propose that AMPK activation prevents insulin-stimulated GLUT4 dispersal in the PM, identifying a new facet of AMPK biology. Furthermore, we observed that cholesterol depletion resulted in increased basal glucose transport and enhanced GLUT4 clustering. This finding seems contradictory but could be due to the functional role of GLUT4 clustering being linked to insulin action specifically or the possibility that GLUT4 clusters are readily endocytosed in the presence of cholesterol. In the absence of cholesterol endocytosis is diminished resulting in increased glucose transport. Previous work in our laboratory indicated that the membrane protein EFR3 plays a role in the regulation of PM GLUT4 (Laidlaw, 2018; Morris, 2020). In this study we used spatial point pattern analysis with spatstat to reanalyse existing imaging data of control and EFR3 knock down conditions in basal and insulin-stimulated 3T3-L1 adipocytes and found that EFR3 knock down diminished insulin-stimulated GLUT4 dispersal. We observed insulin-stimulated GLUT4 dispersal in HeLa cells for the first time and argue that experimentally tractable HeLa cells provide a valuable model organism to study GLUT4 dynamics and the elucidation of mechanisms that operate in human adipose tissues.

To our knowledge this was the first study that investigated GLUT4 dispersal in a variety of *in vitro* models of cardiac muscle tissue. It was observed that insulin did not stimulate GLUT4 dispersal in NRVM and CDI iPSC-CM. Insulin did have an effect on

GLUT4 plasma membrane distribution in NCardia iPSC-CM. Cardiac cell culture models differ vastly in their individual stage of development and each model has advantages and disadvantages. This study employed a combination of experimental model systems and insulin-stimulated GLUT4 dispersal was found to be present in some models, but not others.

Finally, we investigated insulin-stimulated GLUT4 dispersal in models of health and disease. Chronic insulin treatment was observed to induce a state of cellular insulin resistance in 3T3-L1 adipocytes and resulted in a more clustered GLUT4 configuration for both basal and insulin-stimulated cells. Analysis of GLUT4 molecule localization density revealed that chronic insulin treatment also affected translocation of GLUT4 from intracellular stores to the PM. This indicates that insulin resistance affects intracellular GLUT4 trafficking pathways as well as the organization of the transporter within the PM in adipocytes. Moreover, we found a negative correlation between adipocyte cell area and GLUT4 molecule density in both basal and insulin-stimulated cells.

We also report that insulin did not stimulate the reorganisation of TfR in the PM of HeLa cells suggesting that insulin-stimulated GLUT4 dispersal originated from separate IRV and not endosomal compartments in HeLa cells and that this observed effect may be specific for GLUT4.

Finally, we investigated insulin-stimulated GLUT4 dispersal in a commercially available model of skeletal muscle from healthy and T2DM donors. HSMM were highly insulin-sensitive but insulin stimulation did not result in GLUT4 dispersal. Sortilin protein levels were found to be reduced in HSMM myotubes derived from a T2DM donor.

7.2 Current limitations and future directions

7.2.1 Super resolution microscopy as a tool to quantify membrane protein clustering dynamics

Super resolution microscopy has become a valuable research tool for cell biologists to investigate the nanoscale organization of biological structures and processes (Gormal et al., 2020). SMLM techniques produce super-resolved images from precise localization of single fluorophores across thousands of data-acquisition frames (Godin et al., 2014). The prolonged image acquisition times result in considerable photo-bleaching of fluorophores and toxicity for live cells making SMLM particularly powerful for fixed cell applications. However, to fully understand cell signalling mechanisms that govern the

dynamic molecular reorganisation of membrane proteins in response to several stimuli live cell imaging is advantageous. But imaging live cells is a challenge for all current super resolution microscopy techniques. One limitation of the current study using dSTORM to investigate GLUT4 clustering in the PM is that information was obtained exclusively on spatial dynamics and temporal dynamics were disregarded. Current SMLM techniques achieve high resolution at the expense of acquisition time but fast imaging acquisition rates with large fields of view are required to image membrane receptors that can move up to $1 \mu\text{m}^2/\text{s}$ (Godin et al., 2014). Moreover dSTORM experiments require the use of reducing/oxidizing buffers which are toxic for cells making this technique not suitable for live cell imaging (Jones et al., 2011). PALM is better suited for super resolution live cell imaging and has been used to monitor mobility states of single proteins by single-particle tracking (sptPALM) (Manley et al., 2008). This method can create spatially resolved maps of single molecule trajectories in the PM and provide insight into spatial and temporal dynamics simultaneously. It has been successfully employed to observe that lateral diffusion of syntaxin1A and its organisation in nanoclusters regulate neurotransmitter release in nerve terminals (Bademosi et al., 2017) and that Munc18 controls syntaxin-1A engagement into SNARE complex assembly (Kasula et al., 2016). Single molecule imaging of GLUT4 diffusion in the PM was achieved using TIRF/FPALM imaging of GLUT4-EOS (Lizunov et al., 2013). However it will be of considerable interest to investigate GLUT4 dynamics in the PM using sptPALM.

It has been suggested that subtle changes in conformational states of proteins promote transient confinement in functionally essential clusters within the PM (Gormal et al., 2020). Even the sptPALM technique is not suited to investigate changes in mobility and clustering associated with possible activity-dependent conformational changes due to the requirement for genetic overexpression of fluorescently labelled proteins. Recently one group coupled anti-GFP nanobodies to single-molecule imaging-amenable tags to study endogenous proteins in discrete conformational states at high resolution in various living cells (Gormal et al., 2020). Single-particle tracking of conformation-specific nanobodies revealed that the activated β_2 -adrenoreceptor is organised into stationary nanoclusters in live neurosecretory cells and selectively targeted for endocytosis (Gormal et al., 2020). This study highlights the importance to investigate highly transient changes in the dynamic nanoscale organization of endogenous proteins which has recently become possible. Quantum dot technology was used for the analysis of intracellular GLUT4 dynamics at the single molecule level in 3T3-L1 adipocytes (Fujita et al., 2010; Hatakeyama and Kanzaki, 2011) and L6 cells in the past (Qu et al., 2010) but in recent years newly developed technologies have become available.

Universal point accumulation imaging in the nanoscale topography (uPAINT) is a novel super resolution microscopy method that relies on the stochastic binding of specific ligands coupled to fluorescent dyes to a target molecule instead of stochastic photo switching of fluorophores (Giannone et al., 2010; Sharonov and Hochstrasser, 2006). Low concentrations of fluorescently labelled ligands that start to fluoresce upon binding to an object of interest are diffused in a solution surrounding the specimen. Fast molecule diffusion by Brownian motion results in constant flux of ligands at the proximity of the specimen and stochastic binding of ligands to their targets on the cell surface (Giannone et al., 2010). Fluorophores are excited selectively with a HILO beam and imaged. By combining single-molecule detection with ligand-induced receptor activation, uPAINT currently is the technique that allows investigation of activated functional receptors and their interactions at the membrane of living cells in real-time at high resolution (Godin et al., 2014). Future investigations of GLUT4 membrane dynamics should take advantage of this recently developed technology. Real time imaging and tracking of diffusing fluorescent ligands has the big advantage that single emitters are imaged at low density upon labelling their biomolecular targets (Giannone et al., 2010). dSTORM relies on the stochastic switching of fluorophores that can result in bias of quantitative analysis because fluorescently labelled molecules can be observed more than once. Antibody linkage error is also avoided using uPAINT making it the most superior super resolution technique for quantitative imaging (Giannone et al., 2010). The Gould lab is presently developing modified versions of GLUT4 suitable to analysis using PAINT and SPT.

The biggest limitation of this study is that specific quantification of cluster descriptors was not possible with the current experimental setup (discussed in detail in chapter 1). The use of a commercial HA-tag antibody increased the apparent size of visualised structures and photo switching itself introduced a bias and therefore it is not scientifically accurate to quantify GLUT4 cluster sizes. However it is generally desirable to make estimates regarding GLUT4 cluster size, cluster radius and percentage and number of molecules in clusters. Bayesian cluster analysis provided some information of GLUT4 cluster parameters in 3T3-L1 adipocytes and iPSC-CM. But as previously mentioned for the correct interpretation of SMLM data several sample preparation limitations need to be considered. Nevertheless, Ripley's L function analysis provides accurate information on the radial scales of clustering across a variety of distances and can serve to compare GLUT4 clustering between several cell types. We have established that spatial analysis of point pattern data using spatstat with appropriate controls and corrections is comparable to the automated fast Ripley's L function that was carried out in this study. Ripley's K function analysis is frequently used in SMLM to analyse clusters

of proteins in the PM and it was shown that cluster size can be estimated reliably using this method (Ruan et al., 2019). Figure 7.1 provides a summary of Ripley's L function analysis of all cell types included in this study that were presented in the previous chapters.

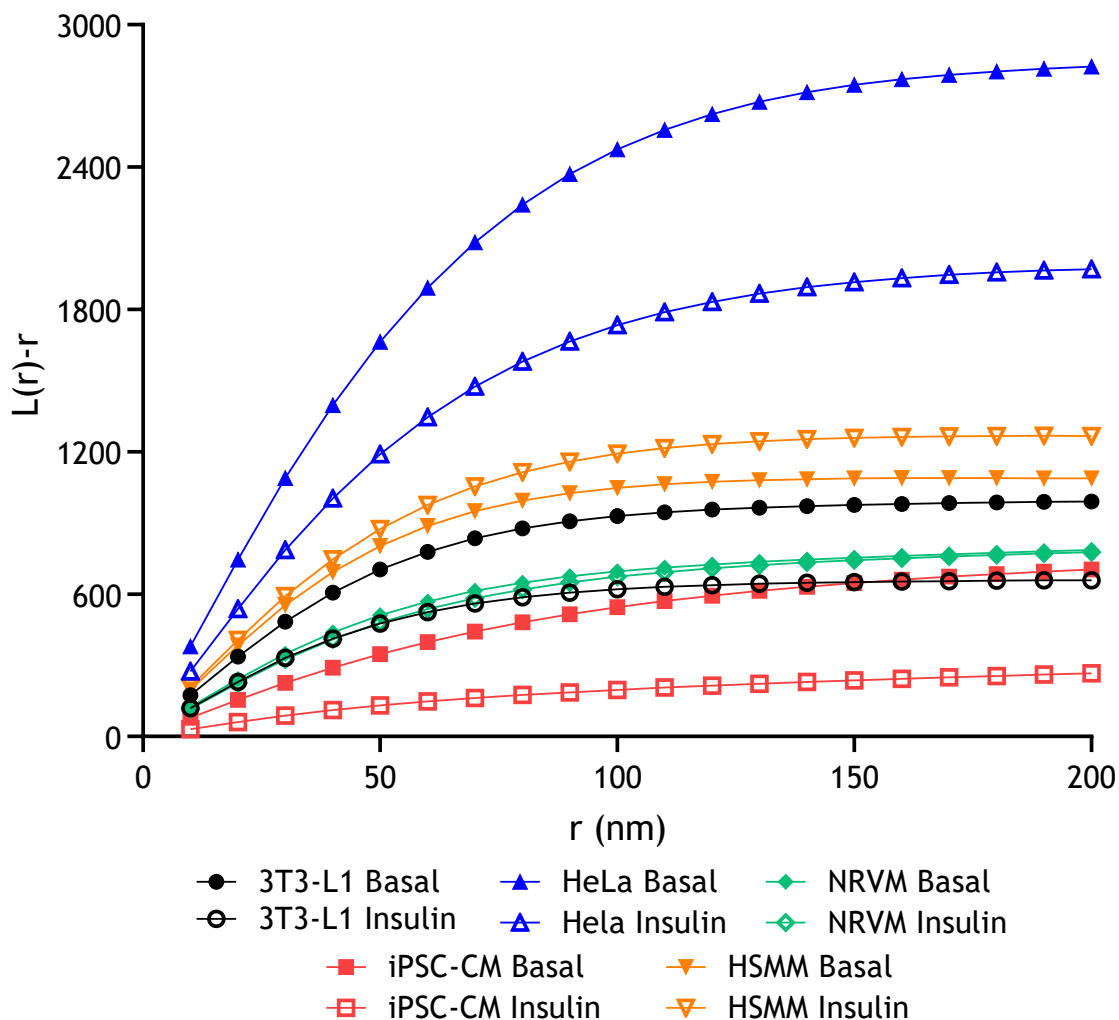


Figure 7.1 Summary of Ripley's K-function analysis of GLUT4 clustering in a range basal and insulin-stimulated cell types.

Representative plot of Ripley's K function analysis of the clustering abilities of GLUT4 molecules in the PM of HA-GLUT4-GFP expressing cells. Cells were serum-starved for 2 h prior to experiments and stimulated with insulin or left untreated. Cells were fixed and stained for surface HA and dSTORM images acquired. GLUT4 molecule coordinates were obtained using ThunderSTORM and the obtained localization data was subjected to Ripley's K-function analysis using SR Tesseler with the minimum radius 10 nm, step radius 10 nm, and maximum radius 400 nm. $L(r)-r$ (y-axis) represents the clustering ability and r (x-axis) represents the radial scales of clustering. The presented data are means.

The amplitude of $L(r)-r$ can be influenced by varying particle density and needs to be normalised for the comparison of data from several imaging experiments. However the peak of $L(r)-r$ has been shown to correspond to the diameter of the cluster and the maximum radius of aggregation was at 200nm for a majority of cell types that were

investigated in this study. This result is an estimate of GLUT4 cluster size and in line with previously published accounts for adipocytes (Gao et al., 2017). To obtain a full understanding of the spectrum of mobility behaviours of GLUT4 in the PM over time several imaging approaches should be combined as each approach has its own inherent advantages and drawbacks.

7.2.2 Insulin-stimulated plasma membrane GLUT4 dispersal in adipocytes

The phenomenon of insulin-stimulated GLUT4 dispersal was firstly recognised in adipocytes and all current studies have employed this cell type as model organism (Gao et al., 2017; Lizunov et al., 2013a; Stenkula et al., 2010). Therefore GLUT4 clustering dynamics are best elucidated in adipocytes even though studies are scarce. Currently the most significant caveat seems to be to directly link the structural information of imaging studies regarding GLUT4 clustering dynamics with functional assays such as glucose uptake. It is of foremost interest to establish how structural changes in GLUT4 clustering directly affect the functional status of the transporter. Studies investigating GLUT4 dispersal in response to insulin stimulation have employed diffraction-limited live cell TIRF imaging (Stenkula et al., 2010), single molecule tracking of GLUT4-EOS in live cells using PALM (Lizunov et al., 2013a) and dSTORM in fixed cells (Gao et al., 2017). Recently highly responsive, single fluorescent protein-based glucose sensors of wide dynamic range have been developed for real-time glucose detection *in vitro* and *in vivo* (Hu et al., 2018a). Furthermore, glucose transporter activity was successfully imaged in HEK293 cells (Keller et al., 2019). HEK293 cells were co-transfected with the cytoplasmic single wavelength iGlucoSnFR glucose sensor and GLUT1 and exposed to buffers alternating between 0 and 20 mM glucose. Cytochalasin B was added to the buffers to decrease GLUT1 transport activity in a dose dependent manner and fluorescence changes were recorded to quantify magnitudes of glucose transport relative to baseline (Keller et al., 2019). Future studies of insulin-stimulated GLUT4 dispersal should optimise experimental protocols to use a glucose sensor to measure functional glucose transport activity at the same time as structural changes in PM GLUT4 clusters in response to various stimuli.

Currently overexpression and knock down of signalling molecules and treatments with pharmacological mimetics and inhibitors are the most appropriate way to elucidate underlying mechanisms of GLUT4 dispersal. In this study we have for instance manipulated the activation of AMPK and presence of cholesterol in 3T3-L1 adipocytes. It was observed that AMPK activation affected insulin signalling within the PM through

shifting GLUT4 towards a more clustered distribution. Simultaneously AMPK activation decreased insulin-stimulated glucose transport in adipocytes as previously reported (Salt et al., 2000). AMPK plays an important role in whole body energy homeostasis and is activated when energy is low. In response to AMPK activation metabolic pathways are activated that produce ATP and diminish its consumption. It was hypothesised that AMPK activation reduced insulin-stimulated glucose transport in adipocytes to inhibit triacylglycerol synthesis to diminish ATP consumption. However, the underlying molecular processes have not been determined. Here we present attenuation of insulin-stimulated GLUT4 dispersal as a possible molecular mechanism. If GLUT4 clusters are the main site for endocytosis and recycling of GLUT4 AMPK activation might attenuate insulin-stimulated dispersal so GLUT4 is readily recycled which inhibits increased glucose transport and triacylglycerol synthesis. AMPK and insulin regulate a variety of metabolic processes with numerous complex pathways and further studies are needed to confirm how AMPK activation influences insulin signalling. This conclusion is, of course, tempered by an unknown effect of AMPK on (for example) insulin receptor clustering and signalling. Nevertheless, the observed changes in GLUT4 clustering are consistent with published work on transport rates and make a novel contribution to this field.

The current kinetic model of GLUT4 recycling suggests that GLUT4 endocytosis occurs at GLUT4 clusters in the PM (Stenkula et al., 2010). GLUT4 clusters in adipocytes were observed to be elongated with a diameter of 90-170 nm in the basal state and this was not affected by insulin stimulation (Lizunov et al., 2013a). The shape of GLUT4 clusters indicates that they are not maintained by cross-linking. Destruction of lipid raft domains with cholesterol was observed to not alter GLUT4 cluster shape or size (Lizunov et al., 2013a). Contrary to this finding another study reported that cholesterol depletion had a significant effect on GLUT4 clustering dynamics (Gao et al., 2017). In line with this result in this study it was also observed that cholesterol depletion affected the extent of GLUT4 clustering. Further studies need to address the role of lipid rafts in PM protein clusters which are generally debated in the scientific community (Pike, 2009). In recent years novel imaging techniques have revealed that mechanisms responsible for PM organization and compartmentalisation are much more complex than originally expected (Krapf, 2018). In fibroblasts single particle tracking was used to study the characteristics of transient confinement zones detected within the lateral long-term trajectories of different membrane molecules (Dietrich et al., 2002). Lipid analogues were found to spend less time in transient confinement zones compared to a glycosylphosphatidylinositol-anchored protein (Thy-1) and a glycosphingolipid (GM1). Cholesterol extraction resulted in reduced transient confinement zone abundance of

Thy-1 indicating that the observed temporary confinement was related to the presence of lipid rafts (Dietrich et al., 2002). Particle mobility within the observed transient confinement zones was markedly reduced. This study provides experimental evidence for presence of putative lipid microdomains within particle trajectories that depend strongly on the presence of cholesterol (Dietrich et al., 2002). Single particle tracking has further revolutionized our understanding of PM organization and resulted in the creation of the 'picket fence' model of membrane compartmentalisation (Kusumi et al., 2014). According to the 'picket fence' model membranes are partitioned into domains and regions are separated from each other by molecular fences and pickets. Several studies have confirmed that the actin cytoskeleton introduces barriers (fences) to the diffusion of membrane proteins creating compartments approximately ~40-300 nm in diameter (Andrade et al., 2015; Andrews et al., 2008; Fujiwara et al., 2002, 2016). Within these compartments dynamic transmembrane protein complexes bound to the actin membrane-skeleton fence exist that have been termed 'pickets' (Kusumi et al., 2014). GLUT4 clusters in the adipocyte PM could be confined within the described molecular picket fence. However it was found that disruption of actin structures did not result in a change in GLUT4 cluster features (Lizunov et al., 2013a). This indicates that GLUT4 clusters are confined in PM regions independently of the presence of the actin skeleton. Nevertheless in the basal state it is still plausible that GLUT4 clusters are confined by specific protein structures. Recently it has been discussed that current studies into factors influencing the dynamic exchange between protein monomers, nanoscale protein clusters, and microscale higher-order structures in the PM have been too fragmented (van Deventer et al., 2020). Intrinsic and extrinsic factors that regulate the dynamic PM organization probably act together and therefore it is hard to determine specific key organisers (van Deventer et al., 2020). GLUT4 clustering within the PM of adipocytes and other cell types is probably dependent on a variety of extrinsic and intrinsic factors acting jointly which should be considered in future research.

7.2.3 Plasma membrane GLUT4 dispersal in cardiac muscle

In this study the investigation of insulin-stimulated GLUT4 dispersal in the myocardium was hampered by the availability of suitable cell culture models. We obtained a HA-GLUT4-GFP transgenic mouse that overexpresses an HA-tagged human GLUT4-EGFP fusion protein under the control of a muscle creatinine kinase promoter. In homozygous animals HA-GLUT4-GFP is expressed in cardiac and skeletal muscle and this strain has been used to visualise GLUT4 translocation in response to insulin previously (Fazakerley et al., 2009; Lizunov et al., 2012). In cardiomyocytes of this animal model it was observed that insulin, contraction and hypoxia resulted in translocation of GLUT4 from intracellular compartments to the sarcolemma and T-tubules (Fazakerley et al., 2009).

Furthermore, HA-tagged GLUT4 was observed to colocalise with clathrin during early stages of internalization indicating GLUT4 endocytosis via a clathrin-mediated route (Fazakerley et al., 2009). The HA-GLUT4-GFP transgenic mouse was also used to study GLUT4 trafficking in skeletal muscle. Insulin stimulation was found to result in translocation of HA-GLUT4-GFP to the sarcolemma and T-tubules comparable to endogenous GLUT4 (Lizunov et al., 2012). Using TIRFM it was observed that 10% of intracellular GLUT4-containing vesicles were mobile and a majority of vesicles remained tethered at the PM or T-tubules and insulin stimulation resulted in exocytosis from these pre-tethered vesicles specifically (Lizunov et al., 2012). These studies show the utility of the HA-GLUT4-GFP transgenic mouse model in the study of GLUT4 trafficking in muscle tissues but currently studies are limited. In this study we aimed to isolate cardiomyocytes and muscle tissues from the transgenic animals to study GLUT4 dispersal in response to insulin using dSTORM. Unfortunately the shipment of HA-GLUT4-GFP transgenic animals was postponed due to the Covid-19 pandemic. It was not within the timeline of this study to establish a breeding transgenic mouse colony and optimise procedures effectively to image HA-GLUT4-GFP cardiomyocytes. However, the work has been started and is currently ongoing in our laboratory. Establishing a colony of the transgenic animal model opens many opportunities for the study of GLUT4 dispersal in muscle tissues. GLUT4 translocation has been observed in response to insulin, contraction and hypoxia and it would be desirable to investigate GLUT4 dispersal in these contexts as well. Furthermore, cardiomyocytes rely on fatty acids as well as glucose as an energy source. It has been observed that the fatty acid receptor CD36 translocates to the PM from intracellular stores in response to insulin stimulation and contraction similarly to GLUT4 in cardiomyocytes (Steinbusch et al., 2011). It would be interesting to investigate the clustering dynamics of CD36 alongside GLUT4 in the PM of these cells.

7.2.4 Plasma membrane GLUT4 dispersal in skeletal muscle

GLUT4 trafficking is less well studied in skeletal muscle tissues due to the more complex tissue architecture and a variety of stimuli that influence this process. In this study the commercially available HSMM from healthy and T2DM donors were used to study PM GLUT4 dynamics and it was observed that PM GLUT4 clustering was not affected by insulin stimulation. This could be due to a variety of reasons. Insulin-stimulated GLUT4 dispersal has previously only been described in the literature in adipose tissues of murine origin (Gao et al., 2017; Stenkula et al., 2010). Recent studies have identified more species-specific distinctions in GLUT4 trafficking for instance the importance of CHC22 in humans but not rodents (Gould et al., 2020). We observed GLUT4 translocation and dispersal in HeLa cells of human origin. However HeLa cells are

derived from cervical cancer and do not behave like normal human cells. Future studies need to address whether species-specific differences affect insulin-stimulated GLUT4 dispersal. Furthermore, it is known that the magnitude of GLUT4 translocation is significantly smaller in muscle tissues compared to adipocytes. Insulin-stimulated GLUT4 dispersal might also be less pronounced in muscle tissues and the chosen analysis method not sufficient to study the differences. Another complexity in skeletal muscle GLUT4 translocation from intracellular stores is that GLUT4 localises to two distinct regions the sarcolemma and T-tubules. Future studies should address whether GLUT4 dispersal is a mechanism present in the sarcolemma or also the T-tubules. GLUT4 translocation has been observed to be stimulated by treatment with exercise mimetics in skeletal muscle. A straightforward next experiment is to administer exercise mimetics to HSMM and observe GLUT4 translocation and GLUT4 trafficking machinery protein expression. HSMM myotubes are less developed than mature muscle fibres. Studying GLUT4 trafficking and dispersal in skeletal muscle from HA-GLUT4-GFP transgenic animals has the advantage to be able to investigate more mature muscle fibres.

The light-sensitive ion channel channelrhodopsin-2 can be genetically expressed in excitable cells such as cardiomyocytes and skeletal muscle cells to control contractile function using light with high spatial and temporal precision (Bruegmann et al., 2015). Optogenetic stimulation is non-invasive and a valuable experimental tool to mimic muscle contractions in the laboratory (Ganji et al., 2021). This technology could also prove useful in the investigation of GLUT4 trafficking and dispersal in response to contraction.

7.3 Conclusion

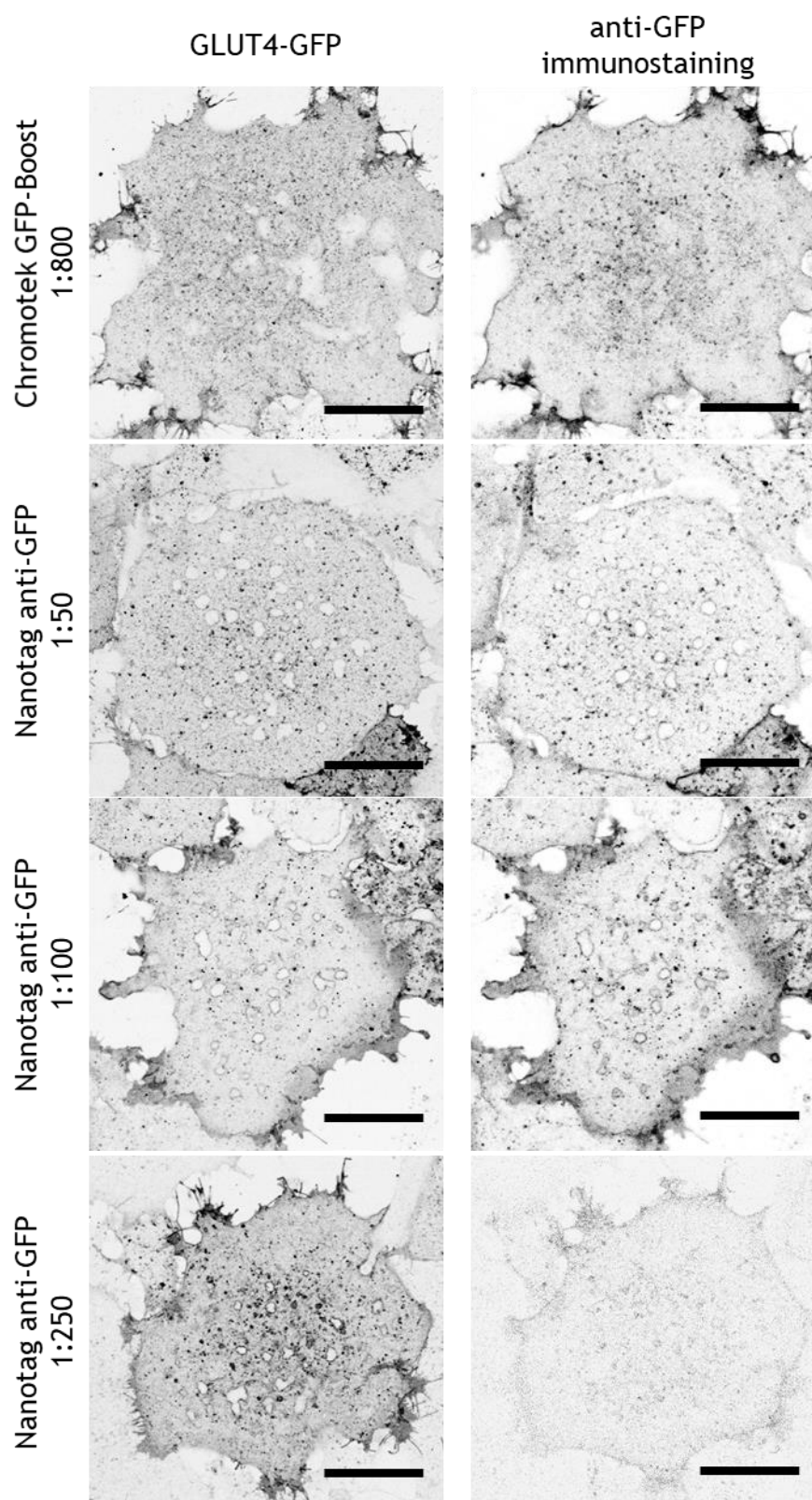
Overall, this thesis has detailed several novel findings regarding the regulation of GLUT4 clustering in adipose and muscle tissues. With dSTORM we established an experimental setup to quantify GLUT4 clustering and dispersal in the PM in response to insulin stimulation. We managed to describe several molecular mechanisms behind the observed GLUT4 clustering dynamics for instance the influence of AMPK, cholesterol and EFR3 in adipocytes. Furthermore we have characterised GLUT4 clustering in several cell culture models of skeletal and cardiac muscle for the first time. Axiogenesis iPSC-CM showed significant GLUT4 dispersal in response to insulin stimulation. Apart from that we successfully investigated how T2DM affects GLUT4 dynamics in the plasma membrane in several model organisms. Cellular states of insulin resistance resulted in attenuated GLUT4 dispersal in adipocytes which identifies another defect in GLUT4

trafficking associated with T2DM. Furthermore, we observed that TfR did not disperse in the PM following insulin stimulation indicating that GLUT4 clusters may not be derived from the endosomal system.

8. Appendices

8.1 Nanobody optimisation staining

Firstly we optimised sample preparation steps for the performance of super resolution microscopy experiments. As lined out in section 3.2.1 two commercially available anti-GFP VHH / nanobodies were used for immunostaining from Chromotek and Nanotag. It was observed that the Chromotek GFP-boost nanobody co-localized well with the GFP signal in the HA-GLUT4-GFP 3T3-L1 adipocytes at a concentration of 1:800 (Figure 8.1). Because the Atto-647N dye was not bright enough for dSTORM experiments we used another nanobody obtained from Nanotag. According to manufacturer's instructions the recommended dilution for their product was 1:500 but our experiments showed that the anti-GFP nanobody at a concentration of 1:250 co-localized poorly with GLUT4-GFP in 3T3-L1 cells (Figure 8.1). At a concentration of 1:50 the nanobody co-localized well with the GFP signal but dSTORM imaging experiments required a dilution of 1:10 to yield satisfactory results (see section 3.2.1).

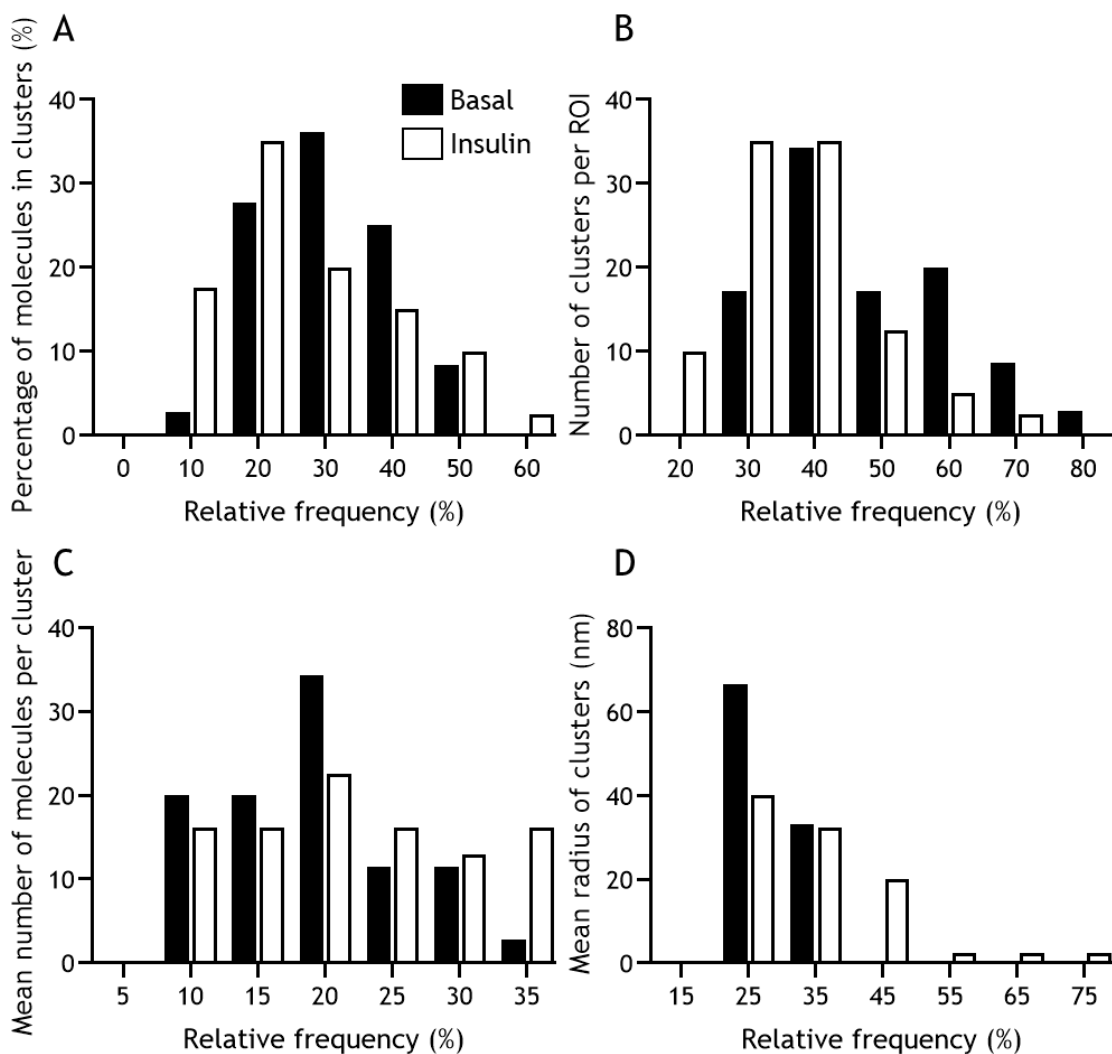


Supplemental Figure 8.1 Colocalization of HA-GLUT4-GFP with anti-GFP nanobody immunostaining in 3T3-L1 adipocytes.

Representative confocal images of 3T3-L1 adipocytes expressing HA-GLUT4-GFP. Images on the right show GLUT4-GFP and images on the left show anti-GFP staining with two different commercially available nanobodies. Cells were serum-starved and stimulated with 100 nM insulin for 20 min. Scale bars=20 μ m.

8.2 Bayesian cluster analysis of GLUT4 distribution in the plasma membrane of induced pluripotent stem cell-derived cardiomyocytes

Similarly to adipocytes we applied Bayesian cluster analysis to quantify GLUT4 clusters in basal iPSC-CM (NCardia) and dispersal of the transporter in response to insulin (see section 3.2.3). Four 3 x 3 μm sized ROIs were chosen as previously described and the percentage of molecules in clusters, the number of clusters per ROI, the mean number of molecules per cluster, and the mean radius of clusters was determined for basal and insulin-stimulated cells. The majority of the ROIs chosen for basal cells showed that 30-40 % of molecules were found in clusters whereas after insulin-stimulation the majority of the ROIs showed that 20 % of molecules were found in clusters indicating that GLUT4 molecules were less clustered and more dispersed after insulin-stimulation (Figure 8.2). In basal and insulin-stimulated iPSC-CM the frequency distribution for the number of clusters per ROI was observed to be relatively similar with a minimal shift of insulin-stimulated cells towards the left indicating that more ROIs contained fewer clusters compared to basal cells (Figure 8.2 B). The average number of molecules per cluster was slightly reduced after insulin stimulation suggesting that GLUT4 clusters decreased in size (Figure 8.2 C). This result was supported by the analysis of the mean cluster radius which was also reduced after insulin stimulation (Figure 8.2 D).

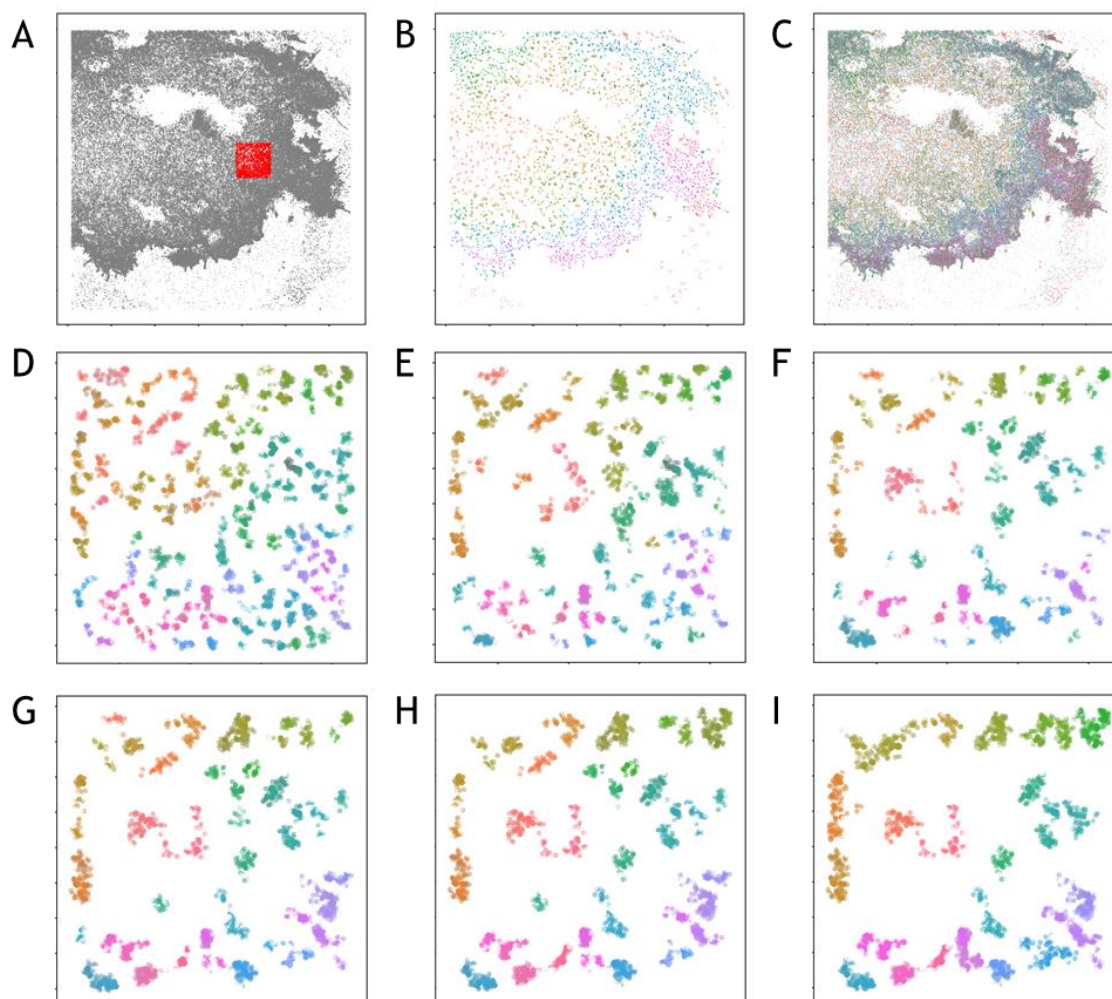


Supplemental Figure 8.2 Bayesian Cluster Analysis of GLUT4 molecules in the PM of basal and insulin stimulated iPSC-CM.

HA-GLUT4-GFP iPSC-CM (NCardia) were serum-starved for 2 h prior to the experiment and stimulated with 1 μ M insulin for 20 min or left untreated. Cells were fixed and stained for surface HA and dSTORM images acquired on a Zeiss Elyra PS.1 (see section 2.3). Reconstructions were calculated using the ImageJ plugin ThunderSTORM and molecule coordinates were subjected to Bayesian cluster analysis. Basal cells: black, $n = 8$; Insulin stimulated: white, $n = 9$. 4 ROIs of $3 \times 3 \mu$ m size per cell were analysed. (A) Percentage of molecules in clusters. (B) Number of clusters per ROI. (C) Mean number of molecules per cluster. (D) Mean radius of clusters. The bar graphs shown here are frequency distributions. This experiment was repeated twice with similar results.

8.3 Optimisation of parameters for hierarchical density-based spatial clustering of applications with noise

In section 3.2.6 HDBSCAN was used to identify clusters of GLUT4 in dSTORM images of 3T3-L1 adipocytes. As a starting point the two parameters minimum clusters and minimum samples were manipulated to observe how clustering changed in response (Figure 8.3). A minimum cluster size of 5 and minimum samples of 30 were chosen arbitrarily to get a good visualization of GLUT4 clustering in 3T3-L1 adipocytes.



Supplemental Figure 8.3 Optimisation of hierarchical density-based spatial clustering of applications with noise analysis for 3T3-L1 adipocytes.

Cells were fixed and stained for surface HA. DSTORM images were acquired (see section 2.3) and reconstructions calculated using ThunderSTORM. ROI of $8\mu\text{m} \times 8\mu\text{m}$ were selected and GLUT4 molecule coordinates processed using an HDBSCAN script written in house with Marie Cutiongco in Python. (A) GLUT4 molecule coordinates of a 3T3-L1 adipocyte. Image scale $51.2\mu\text{m}$. The red square highlights a representative ROI. (B) Coloured clusters identified in the cell. (C) Coloured clusters and grey non-clustered GLUT4 molecules in the cell. Colourful clusters identified in the chosen ROI by HDBSCAN $\text{min_cluster_size}=5$ and (D) $\text{min_samples}=10$, (E) $\text{min_samples}=20$, (F) $\text{min_samples}=30$. Colourful clusters identified in the chosen ROI by HDBSCAN $\text{min_samples}=30$ and (G) $\text{min_cluster_size}=10$, (H) $\text{min_cluster_size}=20$, (I) $\text{min_cluster_size}=50$. Image scales (C)-(I) = $8\mu\text{m}$.

8.4 Spatial analysis using spatstat

In section 3.2.7 we explored spatial summary function to quantify GLUT4 molecule distribution in the PM using spatstat. Up to this point we only considered measuring dependence between points using the concept of correlation. Ripley's K and L functions define and measure covariance in a point process with clustered patterns showing positive covariance, independently placed points showing zero variance and dispersed points showing negative covariance (Baddeley et al., 2016). Summary functions measuring spatial correlations are the most popular tools for assessing dependence but not the only ones that are available. Additional information about spatial point patterns can be obtained by the investigation of spacings between points. A duality exists between counting points in a given area and measuring shortest distances between points and each method provides information that is complementary to the other. Generally, an unmitigated analysis of spatial point pattern data should include the study of both correlation and spacings. Valuable information about the spatial arrangement of points is disclosed in the nearest-neighbour distances but simply taking the average of these distances leads to information loss. The G-function provides information about the cumulative distribution of the nearest-neighbour distances and is therefore called the 'nearest-neighbour distance distribution function'. $G(r)$ is the probability of reaching another cluster of points from any point with distance r . The nearest neighbour distance (d_i) is written as

$$d_i = d(x_i, \mathbf{x} \setminus x_i)$$

which is the shortest distance (d) from x_i to the points $\mathbf{x} \setminus x_i$ consisting of all points of \mathbf{x} except x_i . The nearest-neighbour distance distribution function is

$$G(r) = P \{d(u, \mathbf{X} \setminus u) \leq r \mid \mathbf{X} \text{ has a point at } u\}$$

defined for all distances $r \geq 0$, where u is an arbitrary reference location. P is the probability and \mathbf{X} the point process. Values obtained for $G(r)$ are probabilities between 0 and 1. The empty space function $F(r)$ provides a summary of the cumulative distribution of the empty-space distances between points in a sample. The empty space function is

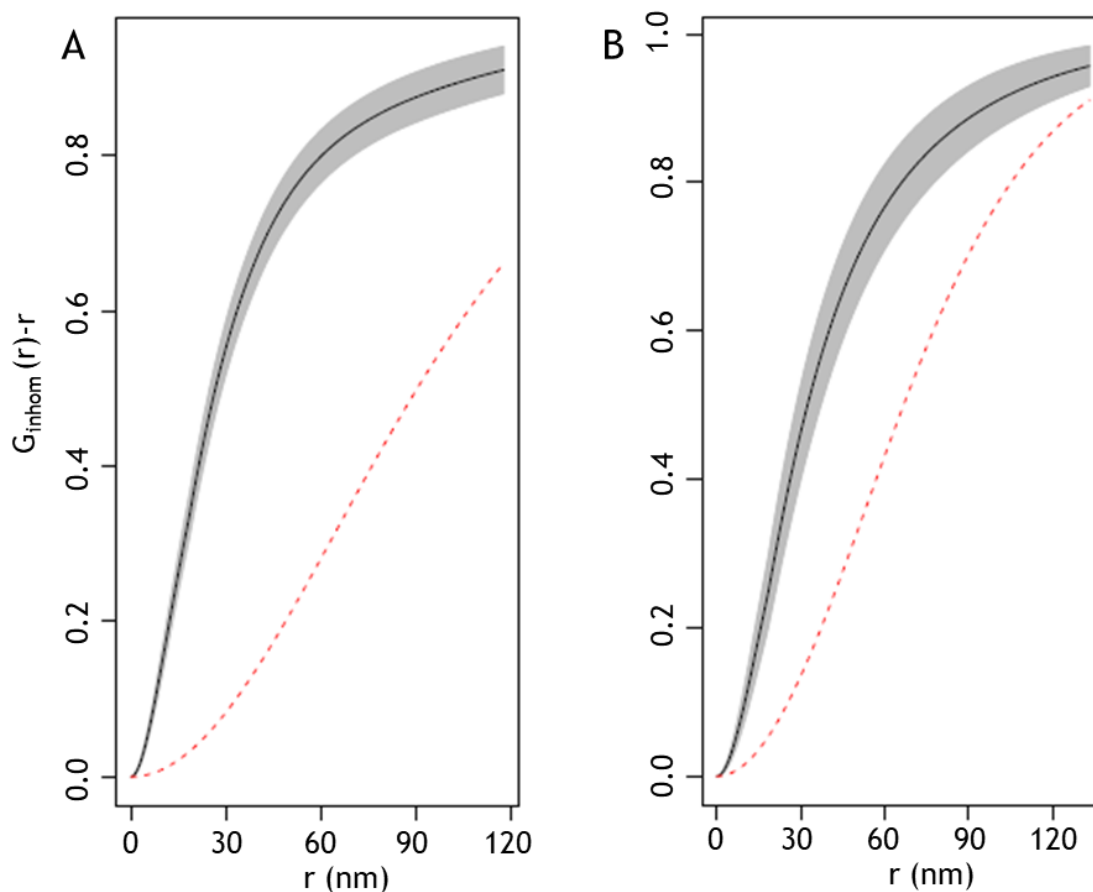
$$F(r) = P \{d(u, \mathbf{X}) \leq r\}$$

defined for all distances $r \geq 0$. Similarly to $G(r)$ the values of $F(r)$ are probabilities between 0 and 1 indicating the chance that there will be a point of \mathbf{X} lying within distance r of this location for any fixed reference location (u). The interpretation of deviations in F is opposite to each of the previously described summary functions. If a pattern is random $G(r)$ and $F(r)$ have a similar probability distribution. However, for clustered or dispersed spatial patterns $G(r)$ and $F(r)$ tend to respond in opposite directions. This relationship between the nearest-neighbour and empty-space distance

can be useful in assessing departures from complete spatial randomness further. The J-function compares $G(r)$ and $F(r)$ and is

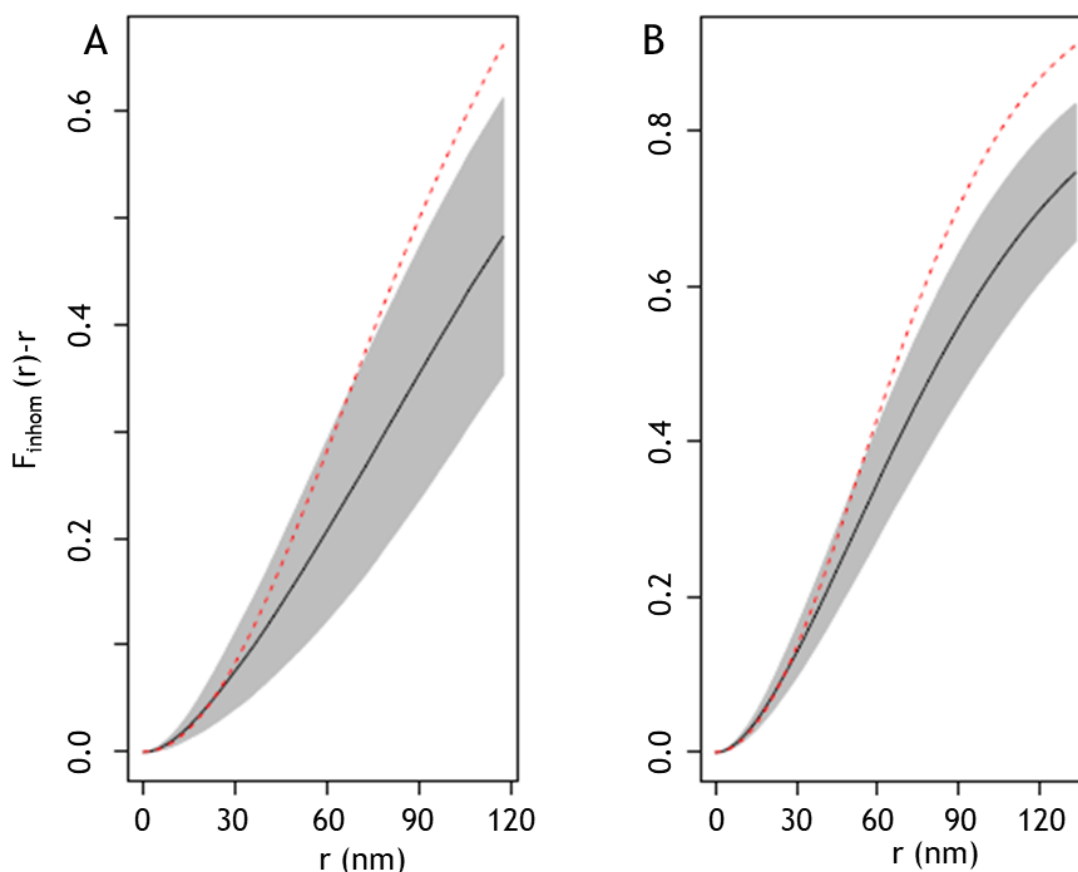
$$J(r) = \frac{1-G(r)}{1-F(r)}$$

defined for all $r \geq 0$ such that $F(r) < 1$ (Baddeley et al., 2016). If the empirical $J(r)$ is bigger than 1 a pattern is dispersed and if $J(r)$ is smaller than 1 a pattern is clustered. $G(r)$ was calculated as described for the example 3T3-L1 adipocyte data set and it was observed that the empirical curve lies above the theoretical curve for a completely random pattern for both basal and insulin-stimulated cells (Figure 8.4). This indicates that the nearest neighbour distances are shorter than expected for a random pattern which is consistent with clustering. $G(r)$ lies closer to the theoretical curve for insulin-treated cells indicating that nearest neighbour distances are bigger compared to basal cells indicating that GLUT4 is less clustered after insulin stimulation. For both basal and insulin-stimulated 3T3-L1 adipocytes the empty-space function $F(r)$ lies below the theoretical curve suggesting the empty-space distances are larger than expected from a completely random pattern and this is indicative of clustered patterns (Figure 8.5). Again $F(r)$ lies closer to the theoretical curve for insulin-stimulated 3T3-L1 adipocytes indicating smaller empty-space distances compared to basal cells indicating that GLUT4 molecules are less clustered after insulin treatment (Figure 8.5 B).



Supplemental Figure 8.4 G function of GLUT4 molecule dispersal in 3T3-L1 adipocytes using spatstat in R.

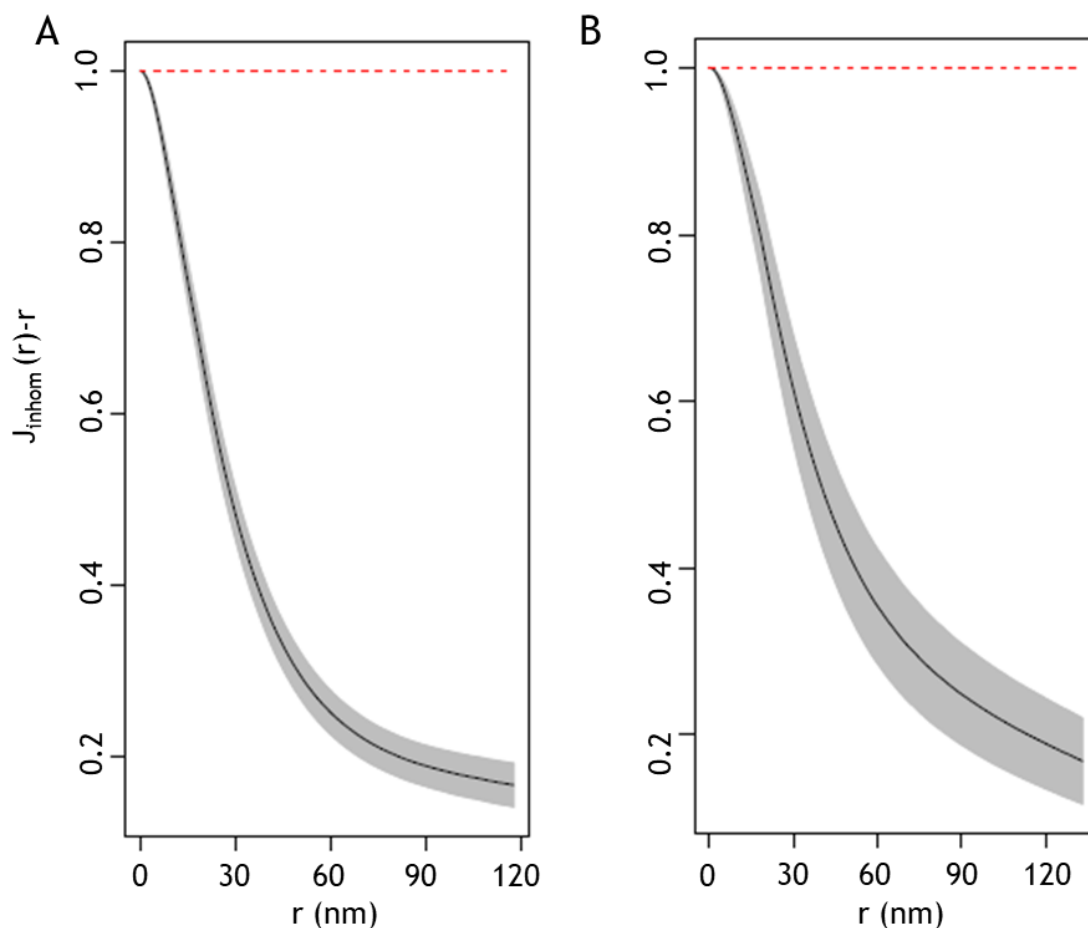
Representative plot of nearest neighbour distance function analysis of the clustering abilities of GLUT4 molecules in the PM of HA-GLUT4-GFP 3T3-L1 adipocytes. Cells were stimulated with 100 nM insulin (panel B) for 20 min or left untreated (panel A) before fixation and staining for surface HA. DSTORM images were acquired (see section 3.4) and reconstructions calculated using ThunderSTORM. GLUT4 coordinates were subjected to G function analysis using spatstat. The presented data are means (solid black lines). The grey shading indicates the global upper and lower envelopes which stand for the most extreme deviation from the theoretical L function at any distance r . The reference function is displayed as red line. The experiment was performed under basal ($N=8$ cells) and insulin-stimulated ($N=9$ cells) conditions.



Supplemental Figure 8.5 F function of GLUT4 molecule dispersal in 3T3-L1 adipocytes using spatstat in R.

Representative plot of empty-space function analysis of the clustering abilities of GLUT4 molecules in the PM of HA-GLUT4-GFP 3T3-L1 adipocytes. Cells were stimulated with 100 nM insulin (panel B) for 20 min or left untreated (panel A) before fixation and staining for surface HA. DSTORM images were acquired (see section 3.4) and reconstructions calculated using ThunderSTORM. GLUT4 coordinates were subjected to F function analysis using spatstat. The presented data are means (solid black lines). The grey shading indicates the global upper and lower envelopes. The reference function is displayed as red line. The experiment was performed under basal (N=8 cells) and insulin-stimulated (N=9 cells) conditions.

Furthermore, we investigated $J(r)$ for basal and insulin-stimulated cells (Figure 8.6). Again, the function indicates that both basal and insulin-stimulated cells show a clustered pattern of GLUT4 molecules. $J(r)$ comes down from the value 1 quicker than the empirical curve for insulin-stimulated cells indicating a lower degree of clustering of GLUT4 molecules. One advantage of $J(r)$ is that the function is completely insensitive to edge effects and time can be saved for calculation of the uncorrected version. Each function does not completely characterise a point process and therefore it is important to study each function independently to get the best idea of underlying spatial arrangement.

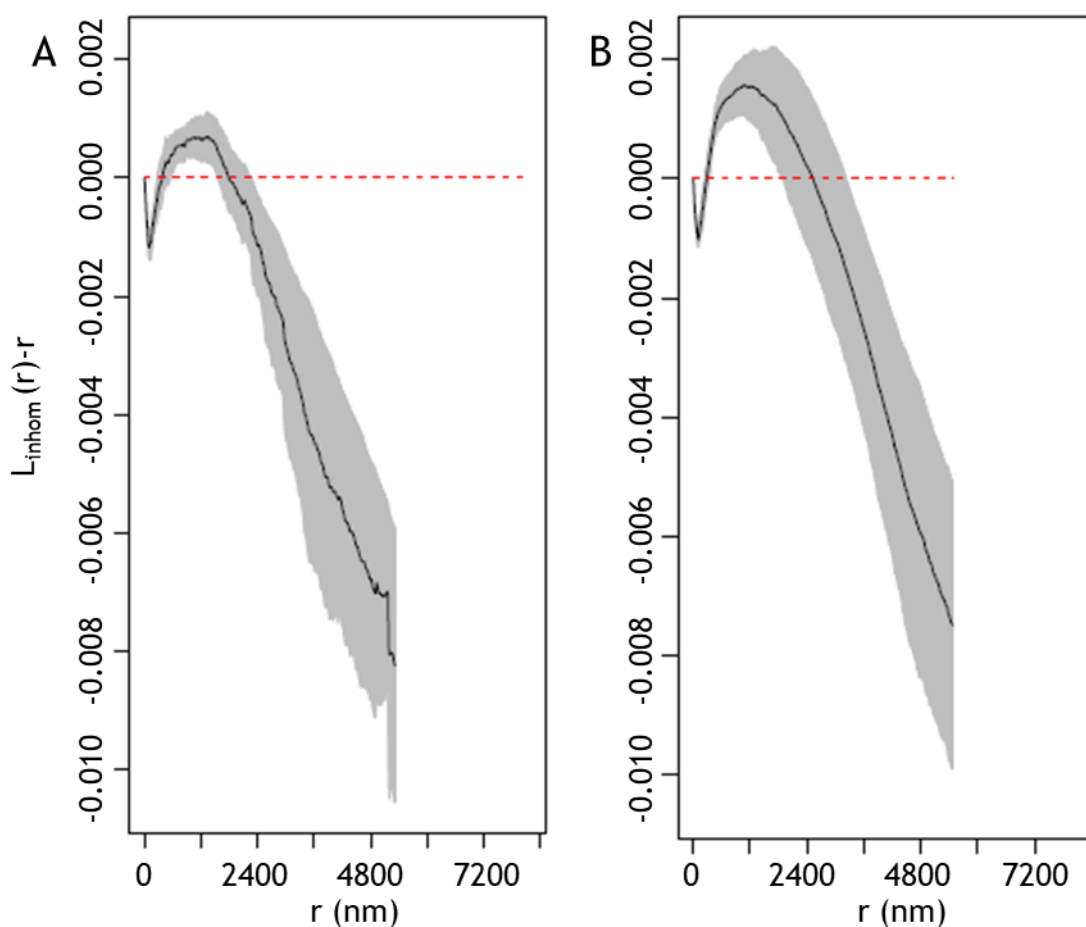


Supplemental Figure 8.6 J function of GLUT4 molecule dispersal in 3T3-L1 adipocytes using spatstat in R.

Representative plot of inhomogeneous J function analysis of the clustering abilities of GLUT4 molecules in HA-GLUT4-GFP 3T3-L1 adipocytes. Cells were stimulated with 100 nM insulin (panel B) for 20 min or left untreated (panel A) before fixation and staining for surface HA. DSTORM images were acquired (see section 2.3) and reconstructions calculated using ThunderSTORM. GLUT4 coordinates were subjected to inhomogeneous J function analysis using spatstat. The presented data are means (solid black lines). The grey shading indicates the global upper and lower envelopes. The function is displayed as centred (red line). The experiment was performed once for basal (N=8 cells) and insulin-stimulated (N=9 cells) conditions.

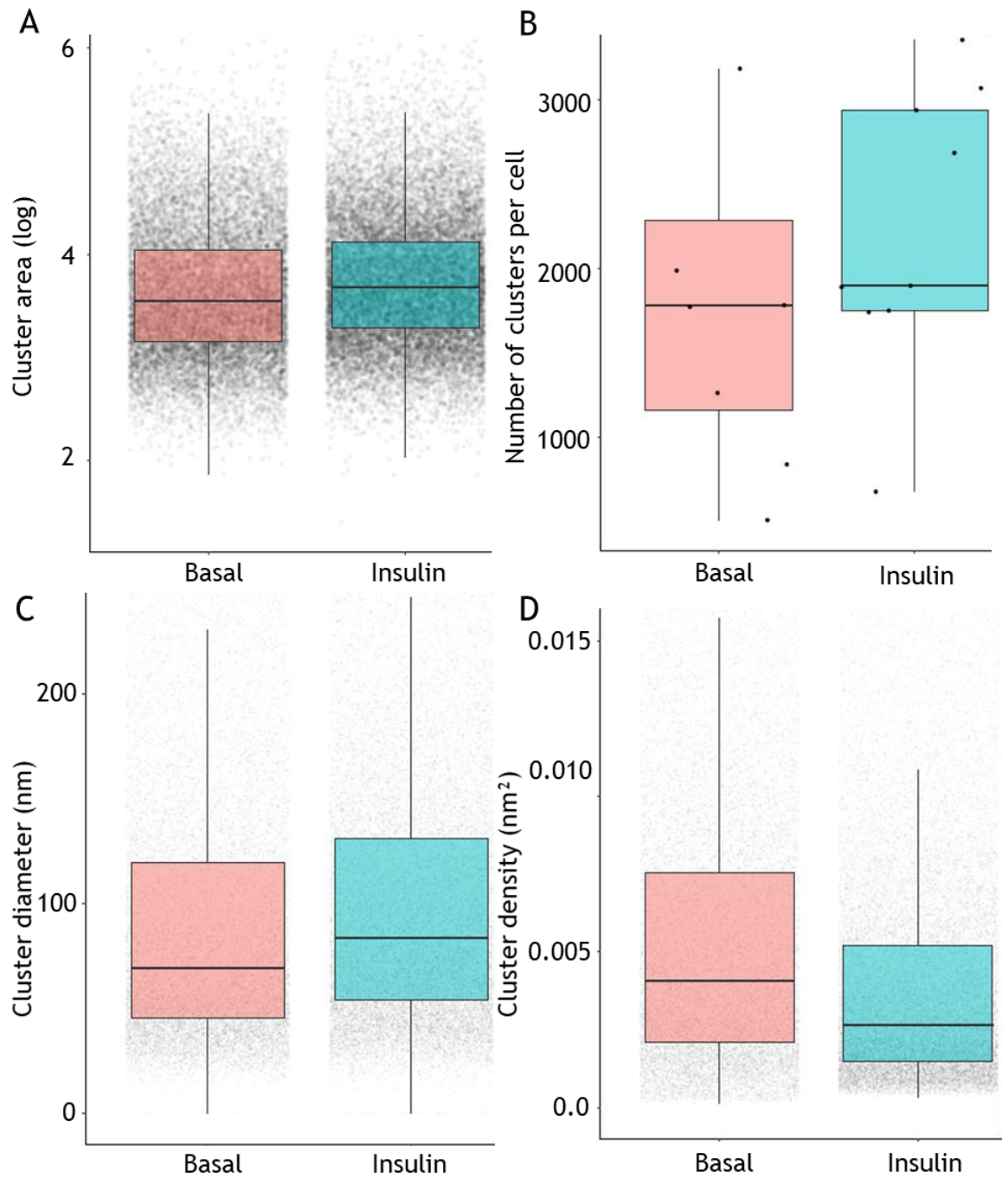
In section 3.2.5 tessellation was described as a method to segment data. We have used SR Tesseler to segment GLUT4 clustering data and performed spatial statistics on the identified clusters. Figure 8.7 shows the centred inhomogeneous L function analysis for clusters found in basal and insulin-stimulated 3T3-L1 adipocytes. It can be observed that the function shows inhibition at small distances for basal and insulin-stimulated cells. The curve then sweeps up for both conditions reaches greater values for insulin-stimulated cells indicating a higher degree of clustering. At distances above 3000 nm $L(r)$ is inhibited. This result is not in line with what is expected and difficult to interpret.

We also looked at summary statistics of the characteristics of the clusters that were previously identified through tessellation and object segmentation with SR Tessler (Figure 8.8). The results show that insulin-stimulation led to an increase in cluster area, numbers of clusters per cell and cluster diameter (Figure 8.8 A-C). The density of clusters per nm^2 was observed to be reduced after insulin stimulation in 3T3-L1 adipocytes (Figure 8.8 D). Due to GLUT4 translocation from intracellular stores to the PM we expected to find an increase in overall GLUT4 density and clusters. Identification of clusters through tessellation indicates that insulin stimulation resulted in increase of cluster diameter and area and overall clusters present in the PM. However, the cluster density was higher in basal cells indicative of GLUT4 dispersal after insulin stimulation. We also investigate cluster diameter in relation to local density (Figure 8.9). The density distribution plot shows a summary of all identified clusters within the sample and a shift in the cluster characteristics between basal and insulin-stimulated cells indicative of a change in GLUT4 clustering dynamics. Clusters identified after insulin stimulation were larger and less dense (Figure 8.9).



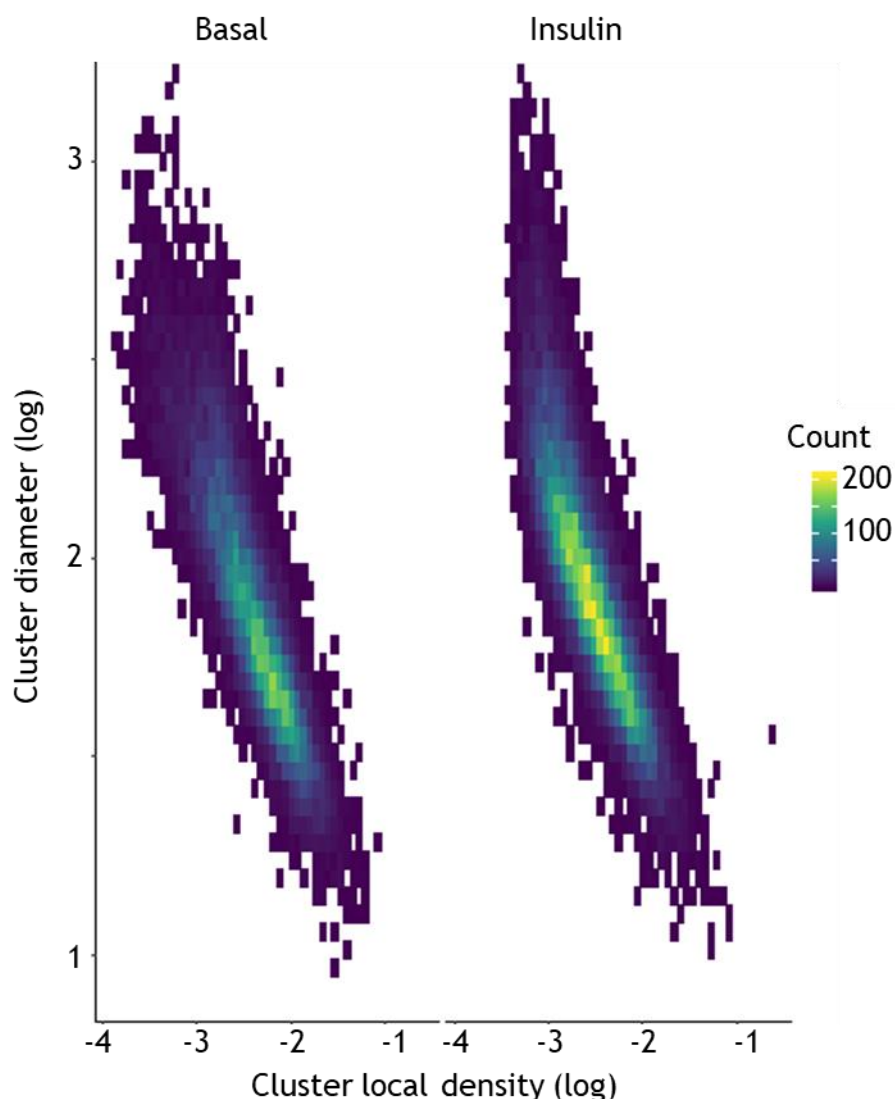
Supplemental Figure 8.7 Ripley's L function of GLUT4 clusters previously identified by tessellation in 3T3-L1 adipocytes.

Representative plot of Ripley's inhomogeneous L function analysis of the clustering abilities of GLUT4 molecules in the PM of HA-GLUT4-GFP 3T3-L1 adipocytes. Cells were stimulated with 100 nM insulin (panel B) for 20 min or left untreated (panel A) before fixation and staining for surface HA. DSTORM images were acquired (see section 2.3) and reconstructions calculated using ThunderSTORM. GLUT4 coordinates were subjected to tessellation with SR Tesseler to identify clusters. Spatial analysis of clusters for (A) basal and (B) insulin-stimulated cells was performed using Ripley's inhomogeneous L function analysis. The presented data are means (solid black lines). The grey shading indicates the global upper and lower envelopes. The function is displayed as centred (red line). The experiment was performed for basal (N=8 cells) and insulin-stimulated (N=9 cells) conditions.



Supplemental Figure 8.8 GLUT4 clusters identified by tessellation in 3T3-L1 adipocytes summary statistics.

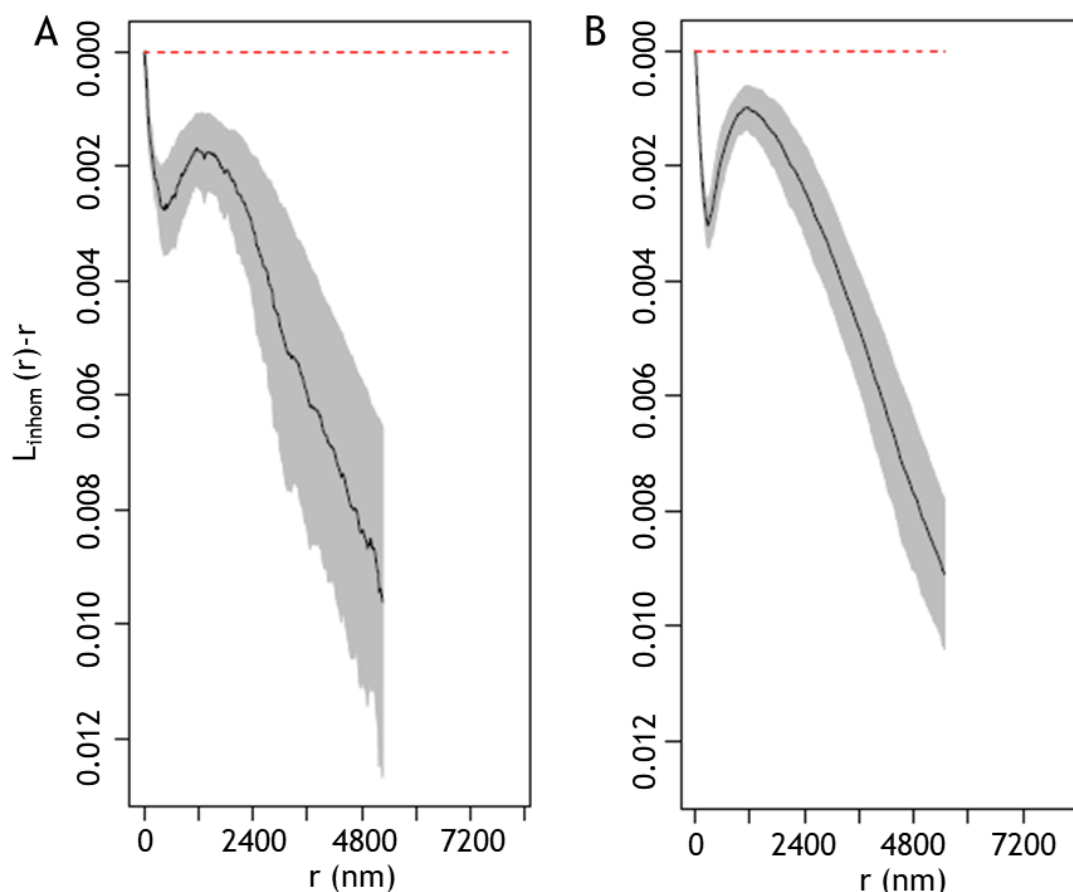
Representative plot of different cluster characteristics after cluster identification through tessellation. 3T3-L1 adipocytes were stimulated with 100 nM insulin for 20 min or left untreated before fixation and staining for surface HA. Reconstructions of dSTORM images were calculated using ThunderSTORM. GLUT4 coordinates were subjected to Tessellation with SR Tessler to identify clusters with density factor 1.8. Analysis of identified clusters through tessellation was performed using spatstat in R. (A) Cluster areas, (B) number of clusters per cell, (C) cluster diameter and (D) cluster density from basal and insulin-stimulated cells.



Supplemental Figure 8.9 GLUT4 clusters identified with Tesselation in 3T3-L1 adipocytes.

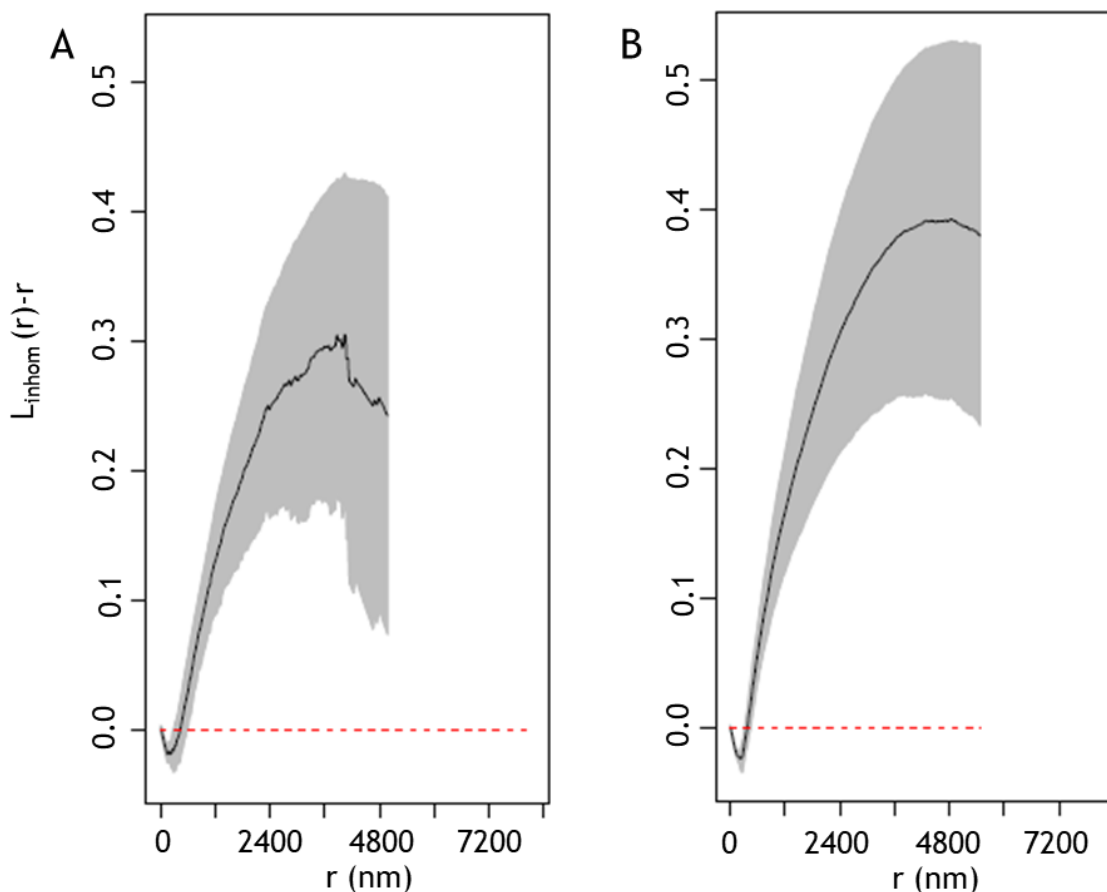
Representative plot of cluster diameter against local density (log values) for 3T3-L1 adipocytes. Cells were stimulated with 100 nM insulin for 20 min or left untreated before fixation and staining for surface HA. DSTORM images were acquired (see section 3.4) and reconstructions calculated using ThunderSTORM. GLUT4 coordinates were subjected to Tesselation with SR Tesseler to identify clusters. Spatial analysis of clusters was performed using spatstat in R.

Next, we investigated the spatial relationships of GLUT4 clusters previously identified through HDBSCAN (Figure 8.10). The L function shows inhibition at all distances for basal and insulin-stimulated cells with a different curve progression as previously observed. We observed that identification of clusters with HDBSCAN changes the summary functions generated with spatstat significantly and the results are difficult to interpret. The same analysis was performed on clusters found in ROI with HDBSCAN (Figure 8.11).



Supplemental Figure 8.10 Ripley's L function of GLUT4 clusters previously identified with HDBSCAN in 3T3-L1 adipocytes using spatstat in R.

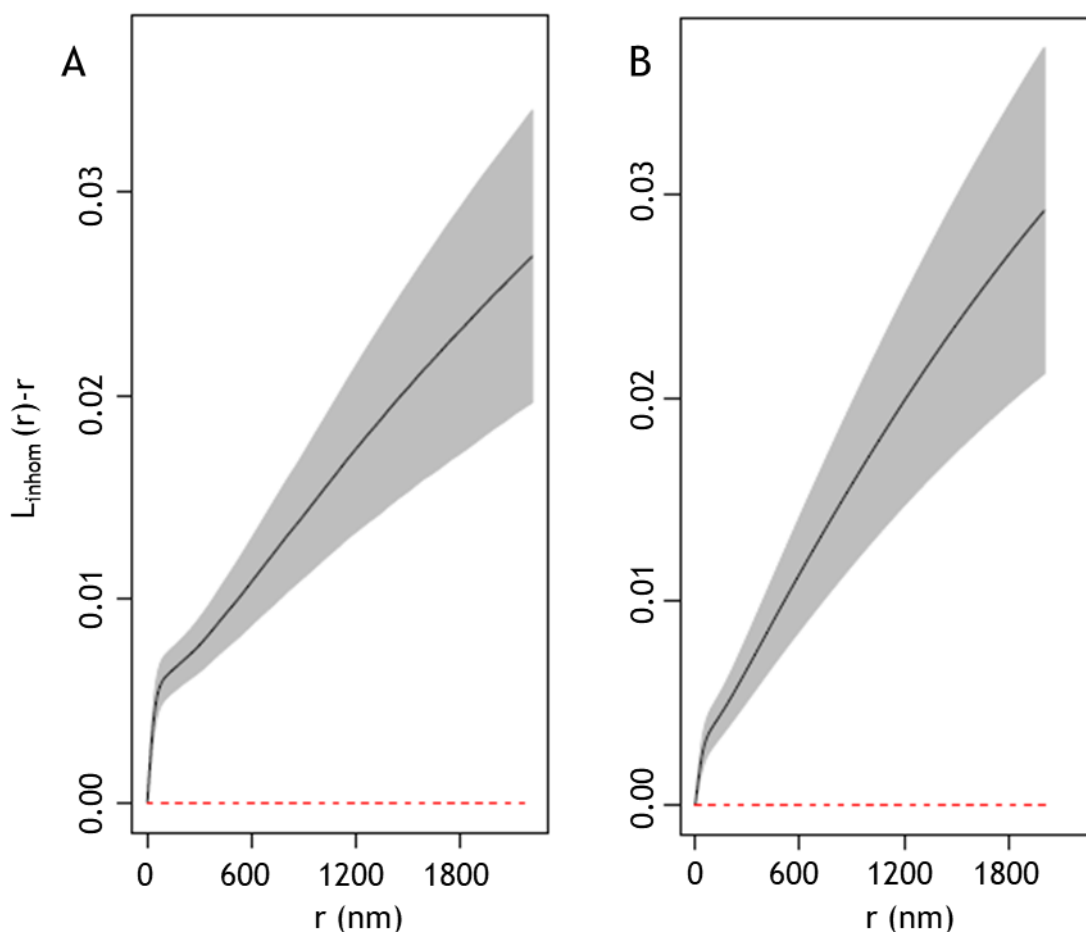
Representative plot of Ripley's inhomogeneous L function analysis of the clustering abilities of GLUT4 molecules in the PM of HA-GLUT4-GFP 3T3-L1 adipocytes. Cells were stimulated with 100 nM insulin (panel B) for 20 min or left untreated (panel A) before fixation and staining for surface HA. DSTORM images were acquired (see section 3.4) and reconstructions calculated using ThunderSTORM. GLUT4 coordinates were subjected to HDBSCAN analysis to identify clusters. Spatial analysis of clusters was performed for (A) basal and (B) insulin-stimulated cells using Ripley's inhomogeneous L function analysis. The presented data are means (solid black lines). The grey shading indicates the global upper and lower envelopes which stand for the most extreme deviation from the theoretical L function at any distance r . The function is displayed as centred (red line). The experiment was performed for basal ($N=8$ cells) and insulin-stimulated ($N=9$ cells) conditions.



Supplemental Figure 8.11 HDBSCAN ROI Ripley's L-function of GLUT4 molecule dispersal in 3T3-L1 adipocytes using spatstat in R.

Representative plot of Ripley's L function analysis of the clustering abilities of GLUT4 molecules in the PM of HA-GLUT4-GFP 3T3-L1 adipocytes, stained for surface HA and dSTORM images acquired as described. GLUT4 molecule coordinates were obtained using ThunderSTORM and subjected to Ripley's L-function analysis using SR Tessler with the minimum radius 10 nm, step radius 10 nm, and maximum radius 400 nm. $L(r)-r$ (y-axis) represents the clustering ability and r (x-axis) represents the radial scales of clustering. The presented data are means. The experiment was performed once basal (panel A; N=8 cells) and insulin-stimulated (panel B; N=9 cells) conditions.

Lastly, we calculated $L(r)-r$ for ROI chosen from raw localization data sets (Figure 8.12). The L function is higher after insulin stimulation in contrast to $L(r)-r$ calculated for the localizations without choosing ROI (Figure 3.16). The results are discussed alongside the other analysis methods in section 3.3.5.



Supplemental Figure 8.12 ROI localizations Ripley's L-function of GLUT4 molecule dispersal in 3T3-L1 adipocytes using spatstat in R.

Representative plot of Ripley's L function analysis of the clustering abilities of GLUT4 molecules in the PM of HA-GLUT4-GFP 3T3-L1 adipocytes stained for surface HA and dSTORM images acquired. GLUT4 molecule coordinates were obtained using ThunderSTORM and subjected to Ripley's L-function analysis using SR Tessler with the minimum radius 10 nm, step radius 10 nm, and maximum radius 400 nm. $L(r)-r$ (y-axis) represents the clustering ability and r (x-axis) represents the radial scales of clustering. The presented data are means. The experiment was performed once basal (panel A; N=8 cells) and insulin-stimulated (panel B; N=9 cells) conditions.

References

- Abbe, E. (1873). Beiträge zur Theorie des Mikroskops und der mikroskopischen Wahrnehmung. *Archiv f. mikrosk. Anatomie* 9, 413-418.
- Abdul-Ghani, M.A., and DeFronzo, R.A. (2010). Pathogenesis of insulin resistance in skeletal muscle. *J. Biomed. Biotechnol.* 2010, 476279.
- Abel, E.D. (2004). Glucose transport in the heart. *Front. Biosci.* 9, 201-215.
- Abel, E.D., Peroni, O., Kim, J.K., Kim, Y.B., Boss, O., Hadro, E., Minnemann, T., Shulman, G.I., and Kahn, B.B. (2001). Adipose-selective targeting of the GLUT4 gene impairs insulin action in muscle and liver. *Nature* 409, 729-733.
- Acosta, J.R., Douagi, I., Andersson, D.P., Bäckdahl, J., Rydén, M., Arner, P., and Laurencikiene, J. (2016). Increased fat cell size: a major phenotype of subcutaneous white adipose tissue in non-obese individuals with type 2 diabetes. *Diabetologia* 59, 560-570.
- Ahmed, Z., and Pillay, T.S. (2003). Adapter protein with a pleckstrin homology (PH) and an Src homology 2 (SH2) domain (APS) and SH2-B enhance insulin-receptor autophosphorylation, extracellular-signal-regulated kinase and phosphoinositide 3-kinase-dependent signalling. *Biochem. J.* 371, 405-412.
- Ahmed, Z., Smith, B.J., and Pillay, T.S. (2000). The APS adapter protein couples the insulin receptor to the phosphorylation of c-Cbl and facilitates ligand-stimulated ubiquitination of the insulin receptor. *FEBS Lett.* 475, 31-34.
- Ambrose, E.J. (1956). A surface contact microscope for the study of cell movements. *Nature* 178, 1194.
- Andrade, D.M., Clausen, M.P., Keller, J., Mueller, V., Wu, C., Bear, J.E., Hell, S.W., Lagerholm, B.C., and Eggeling, C. (2015). Cortical actin networks induce spatio-temporal confinement of phospholipids in the plasma membrane--a minimally invasive investigation by STED-FCS. *Sci. Rep.* 5, 11454.
- Andrews, N.L., Lidke, K.A., Pfeiffer, J.R., Burns, A.R., Wilson, B.S., Oliver, J.M., and Lidke, D.S. (2008). Actin restricts FcepsilonRI diffusion and facilitates antigen-induced receptor immobilization. *Nat. Cell Biol.* 10, 955-963.
- Ankerst, M., Breunig, M.M., Kriegel, H.-P., and Sander, J. (1999). OPTICS: Ordering points to identify the clustering structure. In *Proceedings of the 1999 ACM SIGMOD international conference on Management of data' - SIGMOD '99*, (New York, New York, USA: ACM Press), pp. 49-60.
- Antonescu, C.N., Díaz, M., Femia, G., Planas, J.V., and Klip, A. (2008). Clathrin-dependent and independent endocytosis of glucose transporter 4 (GLUT4) in myoblasts: regulation by mitochondrial uncoupling. *Traffic* 9, 1173-1190.

- Antonescu, C.N., Foti, M., Sauvonnet, N., and Klip, A. (2009). Ready, set, internalize: mechanisms and regulation of GLUT4 endocytosis. *Biosci. Rep.* 29, 1-11.
- Ariga, M., Nedachi, T., Katagiri, H., and Kanzaki, M. (2008). Functional role of sortilin in myogenesis and development of insulin-responsive glucose transport system in C2C12 myocytes. *J. Biol. Chem.* 283, 10208-10220.
- Ariga, M., Yoneyama, Y., Fukushima, T., Ishiuchi, Y., Ishii, T., Sato, H., Hakuno, F., Nedachi, T., and Takahashi, S.-I. (2017). Glucose deprivation attenuates sortilin levels in skeletal muscle cells. *Endocr. J.* 64, 255-268.
- Arner, P., Arner, E., Hammarstedt, A., and Smith, U. (2011). Genetic predisposition for Type 2 diabetes, but not for overweight/obesity, is associated with a restricted adipogenesis. *PLoS One* 6, e18284.
- Ashby, M.C., Ibaraki, K., and Henley, J.M. (2004). It's green outside: tracking cell surface proteins with pH-sensitive GFP. *Trends Neurosci.* 27, 257-261.
- Austin, R.M., and Langley-Evans, S.C. (2011). Cultured neonatal rat cardiomyocytes display differences in glucose uptake and sensitivity to dexamethasone related to maternal diet. *J. Dev. Orig. Health Dis.* 2, 190-194.
- Axelrod, D. (1981). Cell-substrate contacts illuminated by total internal reflection fluorescence. *J. Cell Biol.* 89, 141-145.
- Backer, J.M., Myers, M.G., Shoelson, S.E., Chin, D.J., Sun, X.J., Miralpeix, M., Hu, P., Margolis, B., Skolnik, E.Y., and Schlessinger, J. (1992). Phosphatidylinositol 3'-kinase is activated by association with IRS-1 during insulin stimulation. *EMBO J.* 11, 3469-3479.
- Baddeley, A., and Turner, R. (2005). spatstat : anr package for analyzing spatial point patterns. *J Stat Softw* 12.
- Baddeley, A., Rubak, E., and Turner, R. (2016). *Spatial Point Patterns: Methodology And Applications With R* (Chapman & Hall/crc Interdisciplinary Statistics) (Boca Raton: Chapman And Hall/crc).
- Bademosi, A.T., Lauwers, E., Padmanabhan, P., Odierna, L., Chai, Y.J., Papadopulos, A., Goodhill, G.J., Verstreken, P., van Swinderen, B., and Meunier, F.A. (2017). In vivo single-molecule imaging of syntaxin1A reveals polyphosphoinositide- and activity-dependent trapping in presynaptic nanoclusters. *Nat. Commun.* 8, 13660.
- Bae, S.S., Cho, H., Mu, J., and Birnbaum, M.J. (2003). Isoform-specific regulation of insulin-dependent glucose uptake by Akt/protein kinase B. *J. Biol. Chem.* 278, 49530-49536.
- Bai, L., Wang, Y., Fan, J., Chen, Y., Ji, W., Qu, A., Xu, P., James, D.E., and Xu, T. (2007). Dissecting multiple steps of GLUT4 trafficking and identifying the sites of insulin action. *Cell Metab.* 5, 47-57.

- Baird, D., Stefan, C., Audhya, A., Weys, S., and Emr, S.D. (2008). Assembly of the PtdIns 4-kinase Stt4 complex at the plasma membrane requires Ypp1 and Efr3. *J. Cell Biol.* *183*, 1061-1074.
- Banyasz, T., Lozinskiy, I., Payne, C.E., Edelmann, S., Norton, B., Chen, B., Chen-Izu, Y., Izu, L.T., and Balke, C.W. (2008). Transformation of adult rat cardiac myocytes in primary culture. *Exp. Physiol.* *93*, 370-382.
- Barnard, R.J., and Youngren, J.F. (1992). Regulation of glucose transport in skeletal muscle. *FASEB J.* *6*, 3238-3244.
- Bates, M., Huang, B., Dempsey, G.T., and Zhuang, X. (2007). Multicolor super-resolution imaging with photo-switchable fluorescent probes. *Science* *317*, 1749-1753.
- Beeson, M., Sajan, M.P., Dizon, M., Grebenev, D., Gomez-Daspet, J., Miura, A., Kanoh, Y., Powe, J., Bandyopadhyay, G., Standaert, M.L., et al. (2003). Activation of protein kinase C-zeta by insulin and phosphatidylinositol-3,4,5-(PO₄)₃ is defective in muscle in type 2 diabetes and impaired glucose tolerance: amelioration by rosiglitazone and exercise. *Diabetes* *52*, 1926-1934.
- Beghein, E., and Gettemans, J. (2017). Nanobody Technology: A Versatile Toolkit for Microscopic Imaging, Protein-Protein Interaction Analysis, and Protein Function Exploration. *Front. Immunol.* *8*, 771.
- Bell, G.I., Murray, J.C., Nakamura, Y., Kayano, T., Eddy, R.L., Fan, Y.S., Byers, M.G., and Shows, T.B. (1989). Polymorphic human insulin-responsive glucose-transporter gene on chromosome 17p13. *Diabetes* *38*, 1072-1075.
- Bellin, M., Marchetto, M.C., Gage, F.H., and Mummery, C.L. (2012). Induced pluripotent stem cells: the new patient? *Nat. Rev. Mol. Cell Biol.* *13*, 713-726.
- Bellve, K.D., Leonard, D., Standley, C., Lifshitz, L.M., Tuft, R.A., Hayakawa, A., Corvera, S., and Fogarty, K.E. (2006). Plasma membrane domains specialized for clathrin-mediated endocytosis in primary cells. *J. Biol. Chem.* *281*, 16139-16146.
- Bernardo, B.C., Weeks, K.L., Pretorius, L., and McMullen, J.R. (2010). Molecular distinction between physiological and pathological cardiac hypertrophy: experimental findings and therapeutic strategies. *Pharmacol. Ther.* *128*, 191-227.
- Bernstein, R.S., Grant, N., and Kipnis, D.M. (1975). Hyperinsulinemia and enlarged adipocytes in patients with endogenous hyperlipoproteinemia without obesity or diabetes mellitus. *Diabetes* *24*, 207-213.
- Betzig, E., Trautman, J.K., Harris, T.D., Weiner, J.S., and Kostelak, R.L. (1991). Breaking the diffraction barrier: optical microscopy on a nanometric scale. *Science* *251*, 1468-1470.
- Betzig, E., Patterson, G.H., Sougrat, R., Lindwasser, O.W., Olenych, S., Bonifacino, J.S., Davidson, M.W., Lippincott-Schwartz, J., and Hess, H.F. (2006). Imaging intracellular fluorescent proteins at nanometer resolution. *Science* *313*, 1642-1645.

- Bing, R.J., Siegel, A., Vitale, A., Balboni, F., Sparks, E., Taeschler, M., Klapper, M., and Edwards, S. (1953). Metabolic studies on the human heart in vivo. *Am. J. Med.* 15, 284-296.
- Birnbaum, M.J. (1989). Identification of a novel gene encoding an insulin-responsive glucose transporter protein. *Cell* 57, 305-315.
- Björnholm, M., Kawano, Y., Lehtihet, M., and Zierath, J.R. (1997). Insulin receptor substrate-1 phosphorylation and phosphatidylinositol 3-kinase activity in skeletal muscle from NIDDM subjects after in vivo insulin stimulation. *Diabetes* 46, 524-527.
- Blais, E.M., Rawls, K.D., Dougherty, B.V., Li, Z.I., Kolling, G.L., Ye, P., Wallqvist, A., and Papin, J.A. (2017). Reconciled rat and human metabolic networks for comparative toxicogenomics and biomarker predictions. *Nat. Commun.* 8, 14250.
- Blondeau, N., Béraud-Dufour, S., Lebrun, P., Hivelin, C., and Coppola, T. (2018). Sortilin in glucose homeostasis: from accessory protein to key player? *Front. Pharmacol.* 9, 1561.
- Blot, V., and McGraw, T.E. (2006). GLUT4 is internalized by a cholesterol-dependent nystatin-sensitive mechanism inhibited by insulin. *EMBO J.* 25, 5648-5658.
- Blot, V., and McGraw, T.E. (2008). Molecular mechanisms controlling GLUT4 intracellular retention. *Mol. Biol. Cell* 19, 3477-3487.
- Bogan, J.S., Hendon, N., McKee, A.E., Tsao, T.-S., and Lodish, H.F. (2003). Functional cloning of TUG as a regulator of GLUT4 glucose transporter trafficking. *Nature* 425, 727-733.
- Bojjireddy, N., Guzman-Hernandez, M.L., Reinhard, N.R., Jovic, M., and Balla, T. (2015). EFR3s are palmitoylated plasma membrane proteins that control responsiveness to G-protein-coupled receptors. *J. Cell Sci.* 128, 118-128.
- Bomford, A.B., and Munro, H.N. (1985). Transferrin and its receptor: their roles in cell function. *Hepatology* 5, 870-875.
- Bommer, C., Sagalova, V., Heesemann, E., Manne-Goehler, J., Atun, R., Bärnighausen, T., Davies, J., and Vollmer, S. (2018). Global economic burden of diabetes in adults: projections from 2015 to 2030. *Diabetes Care* 41, 963-970.
- Boucher, J., Kleinridders, A., and Kahn, C.R. (2014). Insulin receptor signaling in normal and insulin-resistant states. *Cold Spring Harb. Perspect. Biol.* 6.
- Boudina, S., Bugger, H., Sena, S., O'Neill, B.T., Zaha, V.G., Ilkun, O., Wright, J.J., Mazumder, P.K., Palfreyman, E., Tidwell, T.J., et al. (2009). Contribution of impaired myocardial insulin signaling to mitochondrial dysfunction and oxidative stress in the heart. *Circulation* 119, 1272-1283.
- Bouzakri, K., Roques, M., Gual, P., Espinosa, S., Guebre-Egziabher, F., Riou, J.-P., Laville, M., Le Marchand-Brustel, Y., Tanti, J.-F., and Vidal, H. (2003). Reduced activation of phosphatidylinositol-3 kinase and increased serine 636 phosphorylation of

- insulin receptor substrate-1 in primary culture of skeletal muscle cells from patients with type 2 diabetes. *Diabetes* 52, 1319-1325.
- Bowman, P.R.T., Smith, G.L., and Gould, G.W. (2019). GLUT4 expression and glucose transport in human induced pluripotent stem cell-derived cardiomyocytes. *PLoS One* 14, e0217885.
- Boyer, J.K., Thanigaraj, S., Schechtman, K.B., and Pérez, J.E. (2004). Prevalence of ventricular diastolic dysfunction in asymptomatic, normotensive patients with diabetes mellitus. *Am. J. Cardiol.* 93, 870-875.
- Bradley, H., Shaw, C.S., Bendtsen, C., Worthington, P.L., Wilson, O.J., Strauss, J.A., Wallis, G.A., Turner, A.M., and Wagenmakers, A.J.M. (2015). Visualization and quantitation of GLUT4 translocation in human skeletal muscle following glucose ingestion and exercise. *Physiol. Rep.* 3, 1-11.
- Bragança, J., Lopes, J.A., Mendes-Silva, L., and Almeida Santos, J.M. (2019). Induced pluripotent stem cells, a giant leap for mankind therapeutic applications. *World J. Stem Cells* 11, 421-430.
- Brambrink, T., Foreman, R., Welstead, G.G., Lengner, C.J., Wernig, M., Suh, H., and Jaenisch, R. (2008). Sequential expression of pluripotency markers during direct reprogramming of mouse somatic cells. *Cell Stem Cell* 2, 151-159.
- Brelje, T.C., Scharp, D.W., and Sorenson, R.L. (1989). Three-dimensional imaging of intact isolated islets of Langerhans with confocal microscopy. *Diabetes* 38, 808-814.
- Brissova, M., Fowler, M.J., Nicholson, W.E., Chu, A., Hirshberg, B., Harlan, D.M., and Powers, A.C. (2005). Assessment of human pancreatic islet architecture and composition by laser scanning confocal microscopy. *J. Histochem. Cytochem.* 53, 1087-1097.
- Bruegmann, T., van Bremen, T., Vogt, C.C., Send, T., Fleischmann, B.K., and Sasse, P. (2015). Optogenetic control of contractile function in skeletal muscle. *Nat. Commun.* 6, 7153.
- Bryant, N.J., and Gould, G.W. (2020). Insulin stimulated GLUT4 translocation - Size is not everything! *Curr. Opin. Cell Biol.* 65, 28-34.
- Bryant, N.J., Govers, R., and James, D.E. (2002). Regulated transport of the glucose transporter GLUT4. *Nat. Rev. Mol. Cell Biol.* 3, 267-277.
- Bugger, H., Riehle, C., Jaishy, B., Wende, A.R., Tuinei, J., Chen, D., Soto, J., Pires, K.M., Boudina, S., Theobald, H.A., et al. (2012). Genetic loss of insulin receptors worsens cardiac efficiency in diabetes. *J. Mol. Cell Cardiol.* 52, 1019-1026.
- BurrIDGE, P.W., Thompson, S., Millrod, M.A., Weinberg, S., Yuan, X., Peters, A., Mahairaki, V., Koliatsos, V.E., Tung, L., and Zambidis, E.T. (2011). A universal system for highly efficient cardiac differentiation of human induced pluripotent stem cells that eliminates interline variability. *PLoS One* 6, e18293.

- Burridge, P.W., Keller, G., Gold, J.D., and Wu, J.C. (2012). Production of de novo cardiomyocytes: human pluripotent stem cell differentiation and direct reprogramming. *Cell Stem Cell* 10, 16-28.
- Burridge, P.W., Matsa, E., Shukla, P., Lin, Z.C., Churko, J.M., Ebert, A.D., Lan, F., Diecke, S., Huber, B., Mordwinkin, N.M., et al. (2014). Chemically defined generation of human cardiomyocytes. *Nat. Methods* 11, 855-860.
- Calderhead, D.M., Kitagawa, K., Tanner, L.I., Holman, G.D., and Lienhard, G.E. (1990). Insulin regulation of the two glucose transporters in 3T3-L1 adipocytes. *J. Biol. Chem.* 265, 13801-13808.
- Campello, R.J.G.B., Moulavi, D., and Sander, J. (2013). Density-Based Clustering Based on Hierarchical Density Estimates. In *Advances in Knowledge Discovery and Data Mining*, J. Pei, V.S. Tseng, L. Cao, H. Motoda, and G. Xu, eds. (Berlin, Heidelberg: Springer Berlin Heidelberg), pp. 160-172.
- Campello, R.J.G.B., Moulavi, D., Zimek, A., and Sander, J. (2015). Hierarchical density estimates for data clustering, visualization, and outlier detection. *ACM Trans. Knowl. Discov. Data* 10, 1-51.
- Carvalho, E., Eliasson, B., Wesslau, C., and Smith, U. (2000). Impaired phosphorylation and insulin-stimulated translocation to the plasma membrane of protein kinase B/Akt in adipocytes from Type II diabetic subjects. *Diabetologia* 43, 1107-1115.
- Castelló, A., Cadefau, J., Cussó, R., Testar, X., Hesketh, J.E., Palacín, M., and Zorzano, A. (1993). GLUT-4 and GLUT-1 glucose transporter expression is differentially regulated by contractile activity in skeletal muscle. *J. Biol. Chem.* 268, 14998-15003.
- Chakrabarti, R., Buxton, J., Joly, M., and Corvera, S. (1994). Insulin-sensitive association of GLUT-4 with endocytic clathrin-coated vesicles revealed with the use of brefeldin A. *J. Biol. Chem.* 269, 7926-7933.
- Chamma, I., Letellier, M., Butler, C., Tessier, B., Lim, K.-H., Gauthereau, I., Choquet, D., Sibarita, J.-B., Park, S., Sainlos, M., et al. (2016). Mapping the dynamics and nanoscale organization of synaptic adhesion proteins using monomeric streptavidin. *Nat. Commun.* 7, 10773.
- Chanda, D., Luiken, J.J.F.P., and Glatz, J.F.C. (2016). Signaling pathways involved in cardiac energy metabolism. *FEBS Lett.* 590, 2364-2374.
- Chandrasekera, P.C., and Pippin, J.J. (2014). Of rodents and men: species-specific glucose regulation and type 2 diabetes research. *ALTEX* 31, 157-176.
- Chen, Y., and Lippincott-Schwartz, J. (2015). Selective visualization of GLUT4 storage vesicles and associated Rab proteins using IRAP-pHluorin. *Methods Mol. Biol.* 1298, 173-179.
- Chen, G., Liu, P., Pattar, G.R., Tackett, L., Bhonagiri, P., Strawbridge, A.B., and Elmendorf, J.S. (2006). Chromium activates glucose transporter 4 trafficking and

- enhances insulin-stimulated glucose transport in 3T3-L1 adipocytes via a cholesterol-dependent mechanism. *Mol. Endocrinol.* *20*, 857-870.
- Chen, Y., Wang, Y., Zhang, J., Deng, Y., Jiang, L., Song, E., Wu, X.S., Hammer, J.A., Xu, T., and Lippincott-Schwartz, J. (2012). Rab10 and myosin-Va mediate insulin-stimulated GLUT4 storage vesicle translocation in adipocytes. *J. Cell Biol.* *198*, 545-560.
- Chiu, T.T., Jensen, T.E., Sylow, L., Richter, E.A., and Klip, A. (2011). Rac1 signalling towards GLUT4/glucose uptake in skeletal muscle. *Cell Signal.* *23*, 1546-1554.
- Clarke, J.F., Young, P.W., Yonezawa, K., Kasuga, M., and Holman, G.D. (1994). Inhibition of the translocation of GLUT1 and GLUT4 in 3T3-L1 cells by the phosphatidylinositol 3-kinase inhibitor, wortmannin. *Biochem. J.* *300 (Pt 3)*, 631-635.
- Contreras-Ferrat, A.E., Toro, B., Bravo, R., Parra, V., Vásquez, C., Ibarra, C., Mears, D., Chiong, M., Jaimovich, E., Klip, A., et al. (2010). An inositol 1,4,5-triphosphate (IP3)-IP3 receptor pathway is required for insulin-stimulated glucose transporter 4 translocation and glucose uptake in cardiomyocytes. *Endocrinology* *151*, 4665-4677.
- Cook, S.A., Varela-Carver, A., Mongillo, M., Kleinert, C., Khan, M.T., Leccisotti, L., Strickland, N., Matsui, T., Das, S., Rosenzweig, A., et al. (2010). Abnormal myocardial insulin signalling in type 2 diabetes and left-ventricular dysfunction. *Eur. Heart J.* *31*, 100-111.
- Corton, J.M., Gillespie, J.G., Hawley, S.A., and Hardie, D.G. (1995). 5-aminoimidazole-4-carboxamide ribonucleoside. A specific method for activating AMP-activated protein kinase in intact cells? *Eur. J. Biochem.* *229*, 558-565.
- Coven, D.L., Hu, X., Cong, L., Bergeron, R., Shulman, G.I., Hardie, D.G., and Young, L.H. (2003). Physiological role of AMP-activated protein kinase in the heart: graded activation during exercise. *Am. J. Physiol. Endocrinol. Metab.* *285*, E629-36.
- Cozzone, D., Fröjdö, S., Disse, E., Debard, C., Laville, M., Pirola, L., and Vidal, H. (2008). Isoform-specific defects of insulin stimulation of Akt/protein kinase B (PKB) in skeletal muscle cells from type 2 diabetic patients. *Diabetologia* *51*, 512-521.
- Cui, R., Choi, S.-E., Kim, T.H., Lee, H.J., Lee, S.J., Kang, Y., Jeon, J.Y., Kim, H.J., and Lee, K.-W. (2019). Iron overload by transferrin receptor protein 1 regulation plays an important role in palmitate-induced insulin resistance in human skeletal muscle cells. *FASEB J.* *33*, 1771-1786.
- Culley, S., Albrecht, D., Jacobs, C., Pereira, P.M., Leterrier, C., Mercer, J., and Henriques, R. (2018). Quantitative mapping and minimization of super-resolution optical imaging artifacts. *Nat. Methods* *15*, 263-266.
- Cushman, S.W., and Wardzala, L.J. (1980). Potential mechanism of insulin action on glucose transport in the isolated rat adipose cell. Apparent translocation of intracellular transport systems to the plasma membrane. *J. Biol. Chem.* *255*, 4758-4762.

- Cusi, K., Maezono, K., Osman, A., Pendergrass, M., Patti, M.E., Pratipanawatr, T., DeFronzo, R.A., Kahn, C.R., and Mandarino, L.J. (2000). Insulin resistance differentially affects the PI 3-kinase- and MAP kinase-mediated signaling in human muscle. *J. Clin. Invest.* *105*, 311-320.
- Czubryt, M.P., Lamoureux, L., Ramjiawan, A., Abrenica, B., Jangamreddy, J., and Swan, K. (2010). Regulation of cardiomyocyte Glut4 expression by ZAC1. *J. Biol. Chem.* *285*, 16942-16950.
- Danaei, G., Finucane, M.M., Lu, Y., Singh, G.M., Cowan, M.J., Paciorek, C.J., Lin, J.K., Farzadfar, F., Khang, Y.-H., Stevens, G.A., et al. (2011). National, regional, and global trends in fasting plasma glucose and diabetes prevalence since 1980: systematic analysis of health examination surveys and epidemiological studies with 370 country-years and 2.7 million participants. *Lancet* *378*, 31-40.
- Danielsson, A., Ost, A., Nystrom, F.H., and Strålfors, P. (2005). Attenuation of insulin-stimulated insulin receptor substrate-1 serine 307 phosphorylation in insulin resistance of type 2 diabetes. *J. Biol. Chem.* *280*, 34389-34392.
- Dannhauser, P.N., Camus, S.M., Sakamoto, K., Sadacca, L.A., Torres, J.A., Camus, M.D., Briant, K., Vassilopoulos, S., Rothnie, A., Smith, C.J., et al. (2017). CHC22 and CHC17 clathrins have distinct biochemical properties and display differential regulation and function. *J. Biol. Chem.* *292*, 20834-20844.
- Daugaard, J.R., Nielsen, J.N., Kristiansen, S., Andersen, J.L., Hargreaves, M., and Richter, E.A. (2000). Fiber type-specific expression of GLUT4 in human skeletal muscle: influence of exercise training. *Diabetes* *49*, 1092-1095.
- Davis, I. (2009). The “super-resolution” revolution. *Biochem. Soc. Trans.* *37*, 1042-1044.
- Davis, R.J., Corvera, S., and Czech, M.P. (1986). Insulin stimulates cellular iron uptake and causes the redistribution of intracellular transferrin receptors to the plasma membrane. *J. Biol. Chem.* *261*, 8708-8711.
- Dawson, K., Aviles-Hernandez, A., Cushman, S.W., and Malide, D. (2001). Insulin-regulated trafficking of dual-labeled glucose transporter 4 in primary rat adipose cells. *Biochem. Biophys. Res. Commun.* *287*, 445-454.
- DeBosch, B., Sambandam, N., Weinheimer, C., Courtois, M., and Muslin, A.J. (2006a). Akt2 regulates cardiac metabolism and cardiomyocyte survival. *J. Biol. Chem.* *281*, 32841-32851.
- DeBosch, B., Treskov, I., Lupu, T.S., Weinheimer, C., Kovacs, A., Courtois, M., and Muslin, A.J. (2006b). Akt1 is required for physiological cardiac growth. *Circulation* *113*, 2097-2104.
- DeFronzo, R.A. (2004). Pathogenesis of type 2 diabetes mellitus. *Med Clin North Am* *88*, 787-835, ix.

- DeFronzo, R.A., Gunnarsson, R., Björkman, O., Olsson, M., and Wahren, J. (1985). Effects of insulin on peripheral and splanchnic glucose metabolism in noninsulin-dependent (type II) diabetes mellitus. *J. Clin. Invest.* *76*, 149-155.
- Dempsey, G.T., Vaughan, J.C., Chen, K.H., Bates, M., and Zhuang, X. (2011). Evaluation of fluorophores for optimal performance in localization-based super-resolution imaging. *Nat. Methods* *8*, 1027-1036.
- Dendup, T., Feng, X., Clingan, S., and Astell-Burt, T. (2018). Environmental risk factors for developing type 2 diabetes mellitus: A systematic review. *Int. J. Environ. Res. Public Health* *15*.
- Deng, D., and Yan, N. (2016). GLUT, SGLT, and SWEET: Structural and mechanistic investigations of the glucose transporters. *Protein Sci.* *25*, 546-558.
- Devereux, R.B., Roman, M.J., Paranicas, M., O'Grady, M.J., Lee, E.T., Welty, T.K., Fabsitz, R.R., Robbins, D., Rhoades, E.R., and Howard, B.V. (2000). Impact of diabetes on cardiac structure and function: the strong heart study. *Circulation* *101*, 2271-2276.
- Diabetes UK (2014). *The Cost of Diabetes: Report* (Diabetes UK).
- Dickson, R.M., Cubitt, A.B., Tsien, R.Y., and Moerner, W.E. (1997). On/off blinking and switching behaviour of single molecules of green fluorescent protein. *Nature* *388*, 355-358.
- Dietrich, C., Yang, B., Fujiwara, T., Kusumi, A., and Jacobson, K. (2002). Relationship of lipid rafts to transient confinement zones detected by single particle tracking. *Biophys. J.* *82*, 274-284.
- Dobson, S.P., Livingstone, C., Gould, G.W., and Tavaré, J.M. (1996). Dynamics of insulin-stimulated translocation of GLUT4 in single living cells visualised using green fluorescent protein. *FEBS Lett.* *393*, 179-184.
- Doherty, G.J., and McMahon, H.T. (2009). Mechanisms of endocytosis. *Annu. Rev. Biochem.* *78*, 857-902.
- Dransfeld, O., Uphues, I., Sasson, S., Schürmann, A., Joost, H.G., and Eckel, J. (2000). Regulation of subcellular distribution of GLUT4 in cardiomyocytes: Rab4A reduces basal glucose transport and augments insulin responsiveness. *Exp Clin Endocrinol Diabetes* *108*, 26-36.
- Drawnel, F.M., Boccardo, S., Prummer, M., Delobel, F., Graff, A., Weber, M., Gérard, R., Badi, L., Kam-Thong, T., Bu, L., et al. (2014). Disease modeling and phenotypic drug screening for diabetic cardiomyopathy using human induced pluripotent stem cells. *Cell Rep.* *9*, 810-821.
- Dresner, A., Laurent, D., Marcucci, M., Griffin, M.E., Dufour, S., Cline, G.W., Slezak, L.A., Andersen, D.K., Hundal, R.S., Rothman, D.L., et al. (1999). Effects of free fatty acids on glucose transport and IRS-1-associated phosphatidylinositol 3-kinase activity. *J. Clin. Invest.* *103*, 253-259.

- Duelli, R., and Kuschinsky, W. (2001). Brain glucose transporters: relationship to local energy demand. *News Physiol. Sci.* 16, 71-76.
- Duh, E.J., Sun, J.K., and Stitt, A.W. (2017). Diabetic retinopathy: current understanding, mechanisms, and treatment strategies. *JCI Insight* 2.
- Dutka, D.P., Pitt, M., Pagano, D., Mongillo, M., Gathercole, D., Bonser, R.S., and Camici, P.G. (2006). Myocardial glucose transport and utilization in patients with type 2 diabetes mellitus, left ventricular dysfunction, and coronary artery disease. *J. Am. Coll. Cardiol.* 48, 2225-2231.
- Egert, S., Nguyen, N., Brosius, F.C., and Schwaiger, M. (1997). Effects of wortmannin on insulin- and ischemia-induced stimulation of GLUT4 translocation and FDG uptake in perfused rat hearts. *Cardiovasc. Res.* 35, 283-293.
- Egert, S., Nguyen, N., and Schwaiger, M. (1999). Contribution of alpha-adrenergic and beta-adrenergic stimulation to ischemia-induced glucose transporter (GLUT) 4 and GLUT1 translocation in the isolated perfused rat heart. *Circ. Res.* 84, 1407-1415.
- Ehler, E., Moore-Morris, T., and Lange, S. (2013). Isolation and culture of neonatal mouse cardiomyocytes. *J. Vis. Exp.*
- Erdmann, J., Kallabis, B., Oppel, U., Sypchenko, O., Wagenpfeil, S., and Schusdziarra, V. (2008). Development of hyperinsulinemia and insulin resistance during the early stage of weight gain. *Am. J. Physiol. Endocrinol. Metab.* 294, E568-75.
- Eriksson, J., Koranyi, L., Bourey, R., Schalin-Jäntti, C., Widén, E., Mueckler, M., Permutt, A.M., and Groop, L.C. (1992). Insulin resistance in type 2 (non-insulin-dependent) diabetic patients and their relatives is not associated with a defect in the expression of the insulin-responsive glucose transporter (GLUT-4) gene in human skeletal muscle. *Diabetologia* 35, 143-147.
- Everitt, B.S., Landau, S., Leese, M., and Stahl, D. (2011). *Cluster Analysis* (Chichester, UK: John Wiley & Sons, Ltd).
- Falkenburger, B.H., Jensen, J.B., Dickson, E.J., Suh, B.-C., and Hille, B. (2010). Phosphoinositides: lipid regulators of membrane proteins. *J. Physiol. (Lond.)* 588, 3179-3185.
- Fazakerley, D.J., Lawrence, S.P., Lizunov, V.A., Cushman, S.W., and Holman, G.D. (2009). A common trafficking route for GLUT4 in cardiomyocytes in response to insulin, contraction and energy-status signalling. *J. Cell Sci.* 122, 727-734.
- Fearon, I.M., Gaça, M.D., and Nordskog, B.K. (2013). In vitro models for assessing the potential cardiovascular disease risk associated with cigarette smoking. *Toxicol. In Vitro* 27, 513-522.
- Feldman, E.L., Callaghan, B.C., Pop-Busui, R., Zochodne, D.W., Wright, D.E., Bennett, D.L., Bril, V., Russell, J.W., and Viswanathan, V. (2019). Diabetic neuropathy. *Nat. Rev. Dis. Primers* 5, 41.

- Feng, B., Ng, J.-H., Heng, J.-C.D., and Ng, H.-H. (2009). Molecules that promote or enhance reprogramming of somatic cells to induced pluripotent stem cells. *Cell Stem Cell* 4, 301-312.
- Fernández-Real, J.M., Moreno, J.M., López-Bermejo, A., Chico, B., Vendrell, J., and Ricart, W. (2007). Circulating soluble transferrin receptor according to glucose tolerance status and insulin sensitivity. *Diabetes Care* 30, 604-608.
- Fischer, Y., Thomas, J., Holman, G.D., Rose, H., and Kammermeier, H. (1996). Contraction-independent effects of catecholamines on glucose transport in isolated rat cardiomyocytes. *Am. J. Physiol.* 270, C1204-10.
- Fischer, Y., Thomas, J., Sevilla, L., Muñoz, P., Becker, C., Holman, G., Kozka, I.J., Palacín, M., Testar, X., Kammermeier, H., et al. (1997). Insulin-induced recruitment of glucose transporter 4 (GLUT4) and GLUT1 in isolated rat cardiac myocytes. Evidence of the existence of different intracellular GLUT4 vesicle populations. *J. Biol. Chem.* 272, 7085-7092.
- Florez, J.C., Hirschhorn, J., and Altshuler, D. (2003). The inherited basis of diabetes mellitus: implications for the genetic analysis of complex traits. *Annu. Rev. Genomics. Hum. Genet.* 4, 257-291.
- Florian, M., Jankowski, M., and Gutkowska, J. (2010). Oxytocin increases glucose uptake in neonatal rat cardiomyocytes. *Endocrinology* 151, 482-491.
- Franck, N., Stenkula, K.G., Ost, A., Lindström, T., Strålfors, P., and Nystrom, F.H. (2007). Insulin-induced GLUT4 translocation to the plasma membrane is blunted in large compared with small primary fat cells isolated from the same individual. *Diabetologia* 50, 1716-1722.
- Franz, M.J., Boucher, J.L., Rutten-Ramos, S., and VanWormer, J.J. (2015). Lifestyle weight-loss intervention outcomes in overweight and obese adults with type 2 diabetes: a systematic review and meta-analysis of randomized clinical trials. *J Acad Nutr Diet* 115, 1447-1463.
- Freidenberg, G.R., Henry, R.R., Klein, H.H., Reichart, D.R., and Olefsky, J.M. (1987). Decreased kinase activity of insulin receptors from adipocytes of non-insulin-dependent diabetic subjects. *J. Clin. Invest.* 79, 240-250.
- Fröjdö, S., Vidal, H., and Pirola, L. (2009). Alterations of insulin signaling in type 2 diabetes: a review of the current evidence from humans. *Biochim. Biophys. Acta* 1792, 83-92.
- Fujita, H., Hatakeyama, H., Watanabe, T.M., Sato, M., Higuchi, H., and Kanzaki, M. (2010). Identification of three distinct functional sites of insulin-mediated GLUT4 trafficking in adipocytes using quantitative single molecule imaging. *Mol. Biol. Cell* 21, 2721-2731.

- Fujiwara, T., Ritchie, K., Murakoshi, H., Jacobson, K., and Kusumi, A. (2002). Phospholipids undergo hop diffusion in compartmentalized cell membrane. *J. Cell Biol.* *157*, 1071-1081.
- Fujiwara, T.K., Iwasawa, K., Kalay, Z., Tsunoyama, T.A., Watanabe, Y., Umemura, Y.M., Murakoshi, H., Suzuki, K.G.N., Nemoto, Y.L., Morone, N., et al. (2016). Confined diffusion of transmembrane proteins and lipids induced by the same actin meshwork lining the plasma membrane. *Mol. Biol. Cell* *27*, 1101-1119.
- Fumeron, F., Péan, F., Driss, F., Balkau, B., Tichet, J., Marre, M., Grandchamp, B., and Insulin Resistance Syndrome (DESIR) Study Group (2006). Ferritin and transferrin are both predictive of the onset of hyperglycemia in men and women over 3 years: the data from an epidemiological study on the Insulin Resistance Syndrome (DESIR) study. *Diabetes Care* *29*, 2090-2094.
- Ganji, E., Chan, C.S., Ward, C.W., and Killian, M.L. (2021). Optogenetic activation of muscle contraction in vivo. *Connect Tissue Res* *62*, 15-23.
- Gao, L., Chen, J., Gao, J., Wang, H., and Xiong, W. (2017). Super-resolution microscopy reveals the insulin-resistance-regulated reorganization of GLUT4 on plasma membranes. *J. Cell Sci.* *130*, 396-405.
- Garvey, W.T., Maianu, L., Hancock, J.A., Golichowski, A.M., and Baron, A. (1992). Gene expression of GLUT4 in skeletal muscle from insulin-resistant patients with obesity, IGT, GDM, and NIDDM. *Diabetes* *41*, 465-475.
- Garvey, W.T., Maianu, L., Zhu, J.H., Hancock, J.A., and Golichowski, A.M. (1993). Multiple defects in the adipocyte glucose transport system cause cellular insulin resistance in gestational diabetes. Heterogeneity in the number and a novel abnormality in subcellular localization of GLUT4 glucose transporters. *Diabetes* *42*, 1773-1785.
- Gerich, J.E. (1998). The genetic basis of type 2 diabetes mellitus: impaired insulin secretion versus impaired insulin sensitivity. *Endocr. Rev.* *19*, 491-503.
- Giannone, G., Hossy, E., Levet, F., Constals, A., Schulze, K., Sobolevsky, A.I., Rosconi, M.P., Gouaux, E., Tampé, R., Choquet, D., et al. (2010). Dynamic superresolution imaging of endogenous proteins on living cells at ultra-high density. *Biophys. J.* *99*, 1303-1310.
- Godin, A.G., Lounis, B., and Cognet, L. (2014). Super-resolution microscopy approaches for live cell imaging. *Biophys. J.* *107*, 1777-1784.
- Goldstein, M.S., Mullick, V., Huddlestun, B., and Levine, R. (1953). Action of muscular work on transfer of sugars across cell barriers; comparison with action of insulin. *Am. J. Physiol.* *173*, 212-216.
- Goodyear, L.J., and Kahn, B.B. (1998). Exercise, glucose transport, and insulin sensitivity. *Annu. Rev. Med.* *49*, 235-261.

- Goodyear, L.J., Giorgino, F., Sherman, L.A., Carey, J., Smith, R.J., and Dohm, G.L. (1995). Insulin receptor phosphorylation, insulin receptor substrate-1 phosphorylation, and phosphatidylinositol 3-kinase activity are decreased in intact skeletal muscle strips from obese subjects. *J. Clin. Invest.* *95*, 2195-2204.
- Goodyear, L.J., Hirshman, M.F., Napoli, R., Calles, J., Markuns, J.F., Ljungqvist, O., and Horton, E.S. (1996). Glucose ingestion causes GLUT4 translocation in human skeletal muscle. *Diabetes* *45*, 1051-1056.
- Gormal, R.S., Padmanabhan, P., Kasula, R., Bademosi, A.T., Coakley, S., Giacomotto, J., Blum, A., Joensuu, M., Wallis, T.P., Lo, H.P., et al. (2020). Modular transient nanoclustering of activated β 2-adrenergic receptors revealed by single-molecule tracking of conformation-specific nanobodies. *Proc. Natl. Acad. Sci. USA* *117*, 30476-30487.
- Gosteli-Peter, M.A., Schmid, C., and Zapf, J. (1996). Triiodothyronine increases glucose transporter isotype 4 mRNA expression, glucose transport, and glycogen synthesis in adult rat cardiomyocytes in long-term culture. *Biochem. Biophys. Res. Commun.* *221*, 521-524.
- Gould, G.W., Brodsky, F.M., and Bryant, N.J. (2020). Building GLUT4 vesicles: CHC22 clathrin's human touch. *Trends Cell Biol.* *30*, 705-719.
- Granéli, C., Hicks, R., Brolén, G., Synnergren, J., and Sartipy, P. (2019). Diabetic cardiomyopathy modelling using induced pluripotent stem cell derived cardiomyocytes: recent advances and emerging models. *Stem Cell Rev and Rep* *15*, 13-22.
- Green, H., and Kehinde, O. (1975). An established preadipose cell line and its differentiation in culture. II. Factors affecting the adipose conversion. *Cell* *5*, 19-27.
- Green, H., and Meuth, M. (1974). An established pre-adipose cell line and its differentiation in culture. *Cell* *3*, 127-133.
- Griffié, J., Shannon, M., Bromley, C.L., Boelen, L., Burn, G.L., Williamson, D.J., Heard, N.A., Cope, A.P., Owen, D.M., and Rubin-Delanchy, P. (2016). A Bayesian cluster analysis method for single-molecule localization microscopy data. *Nat. Protoc.* *11*, 2499-2514.
- Griffié, J., Shlomovich, L., Williamson, D.J., Shannon, M., Aaron, J., Khuon, S., L Burn, G., Boelen, L., Peters, R., Cope, A.P., et al. (2017). 3D Bayesian cluster analysis of super-resolution data reveals LAT recruitment to the T cell synapse. *Sci. Rep.* *7*, 4077.
- Griffié, J., Burn, G.L., Williamson, D.J., Peters, R., Rubin-Delanchy, P., and Owen, D.M. (2018). Dynamic Bayesian Cluster Analysis of Live-Cell Single Molecule Localization Microscopy Datasets. *Small Methods* 1800008.
- Gronnier, J., Crowet, J.-M., Habenstein, B., Nasir, M.N., Bayle, V., Hosy, E., Platre, M.P., Gouguet, P., Raffaele, S., Martinez, D., et al. (2017). Structural basis for plant

plasma membrane protein dynamics and organization into functional nanodomains. *Elife* 6.

Gruzman, A., Babai, G., and Sasson, S. (2009). Adenosine Monophosphate-Activated Protein Kinase (AMPK) as a New Target for Antidiabetic Drugs: A Review on Metabolic, Pharmacological and Chemical Considerations. *Rev. Diabet. Stud.* 6, 13-36.

Guan, F., Yu, B., Qi, G., Hu, J., Zeng, D., and Luo, J. (2008). Chemical hypoxia-induced glucose transporter-4 translocation in neonatal rat cardiomyocytes. *Arch Med Res* 39, 52-60.

Gumà, A., Zierath, J.R., Wallberg-Henriksson, H., and Klip, A. (1995). Insulin induces translocation of GLUT-4 glucose transporters in human skeletal muscle. *Am. J. Physiol.* 268, E613-22.

Gustavsson, J., Parpal, S., and Strålfors, P. (1996). Insulin-stimulated glucose uptake involves the transition of glucose transporters to a caveolae-rich fraction within the plasma membrane: implications for type II diabetes. *Mol Med* 2, 367-372.

Gustavsson, J., Parpal, S., Karlsson, M., Ramsing, C., Thorn, H., Borg, M., Lindroth, M., Peterson, K.H., Magnusson, K.E., and Strålfors, P. (1999). Localization of the insulin receptor in caveolae of adipocyte plasma membrane. *FASEB J.* 13, 1961-1971.

Haga, Y., Ishii, K., and Suzuki, T. (2011). N-glycosylation is critical for the stability and intracellular trafficking of glucose transporter GLUT4. *J. Biol. Chem.* 286, 31320-31327.

Hailstones, D., Sleer, L.S., Parton, R.G., and Stanley, K.K. (1998). Regulation of caveolin and caveolae by cholesterol in MDCK cells. *J. Lipid Res.* 39, 369-379.

Haller, H., Leonhardt, W., Hanefeld, M., and Julius, U. (1979). Relationship between adipocyte hypertrophy and metabolic disturbances. *Endokrinologie* 74, 63-72.

Haller, H., Ji, L., Stahl, K., Bertram, A., and Menne, J. (2017). Molecular Mechanisms and Treatment Strategies in Diabetic Nephropathy: New Avenues for Calcium Dobesilate-Free Radical Scavenger and Growth Factor Inhibition. *Biomed Res. Int.* 2017, 1909258.

Hamers-Casterman, C., Atarhouch, T., Muyldermans, S., Robinson, G., Hamers, C., Songa, E.B., Bendahman, N., and Hamers, R. (1993). Naturally occurring antibodies devoid of light chains. *Nature* 363, 446-448.

Hansen, P.A., Gulve, E.A., Marshall, B.A., Gao, J., Pessin, J.E., Holloszy, J.O., and Mueckler, M. (1995). Skeletal muscle glucose transport and metabolism are enhanced in transgenic mice overexpressing the Glut4 glucose transporter. *J. Biol. Chem.* 270, 1679-1684.

Hansson, B., Morén, B., Fryklund, C., Vliex, L., Wasserstrom, S., Albinsson, S., Berger, K., and Stenkula, K.G. (2019). Adipose cell size changes are associated with a drastic actin remodeling. *Sci. Rep.* 9, 12941.

- Harary, I., and Farley, B. (1963). In vitro studies on single beating rat heart cells. I. Growth and organization. *Exp. Cell Res.* 29, 451-465.
- Hardie, D.G., Carling, D., and Carlson, M. (1998). The AMP-activated/SNF1 protein kinase subfamily: metabolic sensors of the eukaryotic cell? *Annu. Rev. Biochem.* 67, 821-855.
- Hatakeyama, H., and Kanzaki, M. (2011). Molecular basis of insulin-responsive GLUT4 trafficking systems revealed by single molecule imaging. *Traffic* 12, 1805-1820.
- Haw, J.S., Galaviz, K.I., Straus, A.N., Kowalski, A.J., Magee, M.J., Weber, M.B., Wei, J., Narayan, K.M.V., and Ali, M.K. (2017). Long-term Sustainability of Diabetes Prevention Approaches: A Systematic Review and Meta-analysis of Randomized Clinical Trials. *JAMA Intern. Med.* 177, 1808-1817.
- Hawley, S.A., Davison, M., Woods, A., Davies, S.P., Beri, R.K., Carling, D., and Hardie, D.G. (1996). Characterization of the AMP-activated protein kinase kinase from rat liver and identification of threonine 172 as the major site at which it phosphorylates AMP-activated protein kinase. *J. Biol. Chem.* 271, 27879-27887.
- Hayashi, T., Wojtaszewski, J.F., and Goodyear, L.J. (1997). Exercise regulation of glucose transport in skeletal muscle. *Am. J. Physiol.* 273, E1039-51.
- Hayashi, T., Hirshman, M.F., Kurth, E.J., Winder, W.W., and Goodyear, L.J. (1998). Evidence for 5' AMP-activated protein kinase mediation of the effect of muscle contraction on glucose transport. *Diabetes* 47, 1369-1373.
- Hearse, D.J., and Sutherland, F.J. (2000). Experimental models for the study of cardiovascular function and disease. *Pharmacol. Res.* 41, 597-603.
- Heilemann, M., van de Linde, S., Schüttelpelz, M., Kasper, R., Seefeldt, B., Mukherjee, A., Tinnefeld, P., and Sauer, M. (2008). Subdiffraction-resolution fluorescence imaging with conventional fluorescent probes. *Angew. Chem. Int. Ed. Engl.* 47, 6172-6176.
- Heim, P., Morandi, C., Brouwer, G.R., Xu, L., Montessuit, C., and Brink, M. (2020). Neuregulin-1 triggers GLUT4 translocation and enhances glucose uptake independently of insulin receptor substrate and ErbB3 in neonatal rat cardiomyocytes. *Biochim. Biophys. Acta Mol. Cell Res.* 1867, 118562.
- Hell, S.W., and Wichmann, J. (1994). Breaking the diffraction resolution limit by stimulated emission: stimulated-emission-depletion fluorescence microscopy. *Opt. Lett.* 19, 780-782.
- Henriques, R., Lelek, M., Fornasiero, E.F., Valtorta, F., Zimmer, C., and Mhlanga, M.M. (2010). QuickPALM: 3D real-time photoactivation nanoscopy image processing in ImageJ. *Nat. Methods* 7, 339-340.
- Herman, G.A., Bonzelius, F., Cieutat, A.M., and Kelly, R.B. (1994). A distinct class of intracellular storage vesicles, identified by expression of the glucose transporter GLUT4. *Proc. Natl. Acad. Sci. USA* 91, 12750-12754.

- Hess, S.T., Girirajan, T.P.K., and Mason, M.D. (2006). Ultra-high resolution imaging by fluorescence photoactivation localization microscopy. *Biophys. J.* *91*, 4258-4272.
- Hex, N., Bartlett, C., Wright, D., Taylor, M., and Varley, D. (2012). Estimating the current and future costs of Type 1 and Type 2 diabetes in the UK, including direct health costs and indirect societal and productivity costs. *Diabet. Med.* *29*, 855-862.
- Holman, G.D. (2020). Structure, function and regulation of mammalian glucose transporters of the SLC2 family. *Pflugers Arch.* *472*, 1155-1175.
- Houmard, J.A., Weidner, M.D., Dolan, P.L., Leggett-Frazier, N., Gavigan, K.E., Hickey, M.S., Tyndall, G.L., Zheng, D., Alshami, A., and Dohm, G.L. (1995). Skeletal muscle GLUT4 protein concentration and aging in humans. *Diabetes* *44*, 555-560.
- Hsieh, T.-S., Chen, Y.-J., Chang, C.-L., Lee, W.-R., and Liou, J. (2017). Cortical actin contributes to spatial organization of ER-PM junctions. *Mol. Biol. Cell* *28*, 3171-3180.
- Hu, H., Wei, Y., Wang, D., Su, N., Chen, X., Zhao, Y., Liu, G., and Yang, Y. (2018a). Glucose monitoring in living cells with single fluorescent protein-based sensors. *RSC Adv.* *8*, 2485-2489.
- Hu, L., Qiu, C., Wang, X., Xu, M., Shao, X., and Wang, Y. (2018b). The association between diabetes mellitus and reduction in myocardial glucose uptake: a population-based 18F-FDG PET/CT study. *BMC Cardiovasc. Disord.* *18*, 203.
- Huang, S., and Czech, M.P. (2007). The GLUT4 glucose transporter. *Cell Metab.* *5*, 237-252.
- Huang, B., Bates, M., and Zhuang, X. (2009). Super-resolution fluorescence microscopy. *Annu. Rev. Biochem.* *78*, 993-1016.
- Huang, B., Babcock, H., and Zhuang, X. (2010). Breaking the diffraction barrier: super-resolution imaging of cells. *Cell* *143*, 1047-1058.
- Huang, S., Lifshitz, L.M., Jones, C., Bellve, K.D., Standley, C., Fonseca, S., Corvera, S., Fogarty, K.E., and Czech, M.P. (2007). Insulin stimulates membrane fusion and GLUT4 accumulation in clathrin coats on adipocyte plasma membranes. *Mol. Cell. Biol.* *27*, 3456-3469.
- Huycke, E.J., and Kruhoffer, P. (1955). Effects of insulin and muscular exercise upon the uptake of hexoses by muscle cells. *Acta Physiol Scand* *34*, 232-249.
- IDF (2019). *IDF Diabetes Atlas (International Diabetes Federation)*.
- Ingram, J.R., Schmidt, F.I., and Ploegh, H.L. (2018). Exploiting nanobodies' singular traits. *Annu. Rev. Immunol.* *36*, 695-715.
- Isakoff, S.J., Taha, C., Rose, E., Marcusohn, J., Klip, A., and Skolnik, E.Y. (1995). The inability of phosphatidylinositol 3-kinase activation to stimulate GLUT4 translocation indicates additional signaling pathways are required for insulin-stimulated glucose uptake. *Proc. Natl. Acad. Sci. USA* *92*, 10247-10251.

- Ishikura, S., Bilan, P.J., and Klip, A. (2007). Rabs 8A and 14 are targets of the insulin-regulated Rab-GAP AS160 regulating GLUT4 traffic in muscle cells. *Biochem. Biophys. Res. Commun.* 353, 1074-1079.
- Itzhaki, I., Maizels, L., Huber, I., Zwi-Dantsis, L., Caspi, O., Winterstern, A., Feldman, O., Gepstein, A., Arbel, G., Hammerman, H., et al. (2011). Modelling the long QT syndrome with induced pluripotent stem cells. *Nature* 471, 225-229.
- James, D.E., Brown, R., Navarro, J., and Pilch, P.F. (1988). Insulin-regulatable tissues express a unique insulin-sensitive glucose transport protein. *Nature* 333, 183-185.
- James, D.E., Strube, M., and Mueckler, M. (1989). Molecular cloning and characterization of an insulin-regulatable glucose transporter. *Nature* 338, 83-87.
- James, G., Witten, D., Hastie, T., and Tibshirani, R. (2013). *An Introduction to Statistical Learning* (New York, NY: Springer New York).
- Jayasinghe, I., Crossman, D., Soeller, C., and Cannell, M. (2012). Comparison of the organization of T-tubules, sarcoplasmic reticulum and ryanodine receptors in rat and human ventricular myocardium. *Clin. Exp. Pharmacol. Physiol.* 39, 469-476.
- JeBailey, L., Rudich, A., Huang, X., Di Ciano-Oliveira, C., Kapus, A., and Klip, A. (2004). Skeletal muscle cells and adipocytes differ in their reliance on TC10 and Rac for insulin-induced actin remodeling. *Mol. Endocrinol.* 18, 359-372.
- Jedrychowski, M.P., Gartner, C.A., Gygi, S.P., Zhou, L., Herz, J., Kandror, K.V., and Pilch, P.F. (2010). Proteomic analysis of GLUT4 storage vesicles reveals LRP1 to be an important vesicle component and target of insulin signaling. *J. Biol. Chem.* 285, 104-114.
- Jia, G., Hill, M.A., and Sowers, J.R. (2018). Diabetic cardiomyopathy: an update of mechanisms contributing to this clinical entity. *Circ. Res.* 122, 624-638.
- Jiang, L., Fan, J., Bai, L., Wang, Y., Chen, Y., Yang, L., Chen, L., and Xu, T. (2008). Direct quantification of fusion rate reveals a distal role for AS160 in insulin-stimulated fusion of GLUT4 storage vesicles. *J. Biol. Chem.* 283, 8508-8516.
- Jones, S.A., Shim, S.-H., He, J., and Zhuang, X. (2011). Fast, three-dimensional super-resolution imaging of live cells. *Nat. Methods* 8, 499-508.
- Joost, H.-G., and Thorens, B. (2001). The extended GLUT-family of sugar/polyol transport facilitators: nomenclature, sequence characteristics, and potential function of its novel members. *Mol Membr Biol* 18, 247-256.
- Jorand, R., Biswas, S., Wakefield, D.L., Tobin, S.J., Golfetto, O., Hilton, K., Ko, M., Ramos, J.W., Small, A.R., Chu, P., et al. (2016). Molecular signatures of mu opioid receptor and somatostatin receptor 2 in pancreatic cancer. *Mol. Biol. Cell* 27, 3659-3672.

- Josowitz, R., Carvajal-Vergara, X., Lemischka, I.R., and Gelb, B.D. (2011). Induced pluripotent stem cell-derived cardiomyocytes as models for genetic cardiovascular disorders. *Curr. Opin. Cardiol.* 26, 223-229.
- Ju, L., Ringler, T., and Gunzburger, M. (2011). Voronoi tessellations and their application to climate and global modeling. In *Numerical techniques for global atmospheric models*, P. Lauritzen, C. Jablonowski, M. Taylor, and R. Nair, eds. (Berlin, Heidelberg: Springer Berlin Heidelberg), pp. 313-342.
- Kabouridis, P.S., Janzen, J., Magee, A.L., and Ley, S.C. (2000). Cholesterol depletion disrupts lipid rafts and modulates the activity of multiple signaling pathways in T lymphocytes. *Eur. J. Immunol.* 30, 954-963.
- Kaddai, V., Jager, J., Gonzalez, T., Najem-Lendom, R., Bonnafous, S., Tran, A., Le Marchand-Brustel, Y., Gual, P., Tanti, J.F., and Cormont, M. (2009). Involvement of TNF-alpha in abnormal adipocyte and muscle sortilin expression in obese mice and humans. *Diabetologia* 52, 932-940.
- Kadowaki, T., Kasuga, M., Akanuma, Y., Ezaki, O., and Takaku, F. (1984). Decreased autophosphorylation of the insulin receptor-kinase in streptozotocin-diabetic rats. *J. Biol. Chem.* 259, 14208-14216.
- Kahn, B.B. (1992). Alterations in glucose transporter expression and function in diabetes: mechanisms for insulin resistance. *J. Cell Biochem.* 48, 122-128.
- Kahn, B.B., Rosen, A.S., Bak, J.F., Andersen, P.H., Damsbo, P., Lund, S., and Pedersen, O. (1992). Expression of GLUT1 and GLUT4 glucose transporters in skeletal muscle of humans with insulin-dependent diabetes mellitus: regulatory effects of metabolic factors. *J. Clin. Endocrinol. Metab.* 74, 1101-1109.
- Kandror, K., and Pilch, P.F. (1994). Identification and isolation of glycoproteins that translocate to the cell surface from GLUT4-enriched vesicles in an insulin-dependent fashion. *J. Biol. Chem.* 269, 138-142.
- Kannel, W.B., and McGee, D.L. (1979). Diabetes and glucose tolerance as risk factors for cardiovascular disease: the Framingham study. *Diabetes Care* 2, 120-126.
- Kannel, W.B., Hjortland, M., and Castelli, W.P. (1974). Role of diabetes in congestive heart failure: the Framingham study. *Am. J. Cardiol.* 34, 29-34.
- Karbassi, E., Fenix, A., Marchiano, S., Muraoka, N., Nakamura, K., Yang, X., and Murry, C.E. (2020). Cardiomyocyte maturation: advances in knowledge and implications for regenerative medicine. *Nat. Rev. Cardiol.*
- Karlsson, H.K.R., Zierath, J.R., Kane, S., Krook, A., Lienhard, G.E., and Wallberg-Henriksson, H. (2005). Insulin-stimulated phosphorylation of the Akt substrate AS160 is impaired in skeletal muscle of type 2 diabetic subjects. *Diabetes* 54, 1692-1697.
- Kasahara, M., and Hinkle, P.C. (1977). Reconstitution and purification of the D-glucose transporter from human erythrocytes. *J. Biol. Chem.* 252, 7384-7390.

- Kasahara, T., and Kasahara, M. (1997). Characterization of rat Glut4 glucose transporter expressed in the yeast *Saccharomyces cerevisiae*: comparison with Glut1 glucose transporter. *Biochim. Biophys. Acta* 1324, 111-119.
- Kashiwagi, A., Verso, M.A., Andrews, J., Vasquez, B., Reaven, G., and Foley, J.E. (1983). In vitro insulin resistance of human adipocytes isolated from subjects with noninsulin-dependent diabetes mellitus. *J. Clin. Invest.* 72, 1246-1254.
- Kasula, R., Chai, Y.J., Bademosi, A.T., Harper, C.B., Gormal, R.S., Morrow, I.C., Hosy, E., Collins, B.M., Choquet, D., Papadopulos, A., et al. (2016). The Munc18-1 domain 3a hinge-loop controls syntaxin-1A nanodomain assembly and engagement with the SNARE complex during secretory vesicle priming. *J. Cell Biol.* 214, 847-858.
- Katz, E.B., Stenbit, A.E., Hatton, K., DePinho, R., and Charron, M.J. (1995). Cardiac and adipose tissue abnormalities but not diabetes in mice deficient in GLUT4. *Nature* 377, 151-155.
- Keller, J.P., Marvin, J.S., Lacin, H., Lemon, W.C., Shea, J., Kim, S., Lee, R.T., Koyama, M., Keller, P.J., and Looger, L.L. (2019). *In vivo* glucose imaging in multiple model organisms with an engineered single-wavelength sensor. *BioRxiv*.
- Kennedy, J.W., Hirshman, M.F., Gervino, E.V., Ocel, J.V., Forse, R.A., Hoenig, S.J., Aronson, D., Goodyear, L.J., and Horton, E.S. (1999). Acute exercise induces GLUT4 translocation in skeletal muscle of normal human subjects and subjects with type 2 diabetes. *Diabetes* 48, 1192-1197.
- Kessler, A., Tomas, E., Immler, D., Meyer, H.E., Zorzano, A., and Eckel, J. (2000). Rab11 is associated with GLUT4-containing vesicles and redistributes in response to insulin. *Diabetologia* 43, 1518-1527.
- Kettlewell, S., Seidler, T., and Smith, G.L. (2009). The effects of over-expression of the FK506-binding protein FKBP12.6 on K(+) currents in adult rabbit ventricular myocytes. *Pflugers Arch.* 458, 653-660.
- Kim, J., Yang, G., Kim, Y., Kim, J., and Ha, J. (2016). AMPK activators: mechanisms of action and physiological activities. *Exp Mol Med* 48, e224.
- Kim, J.D., Lim, D.-M., Park, K.-Y., Park, S.E., Rhee, E.J., Park, C.-Y., Lee, W.-Y., and Oh, K.W. (2020). Serum Transferrin Predicts New-Onset Type 2 Diabetes in Koreans: A 4-Year Retrospective Longitudinal Study. *Endocrinol Metab (Seoul)* 35, 610-617.
- Kim, Y.B., Nikoulina, S.E., Ciaraldi, T.P., Henry, R.R., and Kahn, B.B. (1999). Normal insulin-dependent activation of Akt/protein kinase B, with diminished activation of phosphoinositide 3-kinase, in muscle in type 2 diabetes. *J. Clin. Invest.* 104, 733-741.
- Kim, Y.-B., Kotani, K., Ciaraldi, T.P., Henry, R.R., and Kahn, B.B. (2003). Insulin-stimulated protein kinase C lambda/zeta activity is reduced in skeletal muscle of humans with obesity and type 2 diabetes: reversal with weight reduction. *Diabetes* 52, 1935-1942.

- Kiskowski, M.A., Hancock, J.F., and Kenworthy, A.K. (2009). On the use of Ripley's K-function and its derivatives to analyze domain size. *Biophys. J.* *97*, 1095-1103.
- Klip, A., McGraw, T.E., and James, D.E. (2019). Thirty sweet years of GLUT4. *J. Biol. Chem.* *294*, 11369-11381.
- Kobayashi, H., and Fukuda, M. (2013). Arf6, Rab11 and transferrin receptor define distinct populations of recycling endosomes. *Commun Integr Biol* *6*, e25036.
- Kolb, H., and Martin, S. (2017). Environmental/lifestyle factors in the pathogenesis and prevention of type 2 diabetes. *BMC Med.* *15*, 131.
- Kolterman, O.G., Gray, R.S., Griffin, J., Burstein, P., Insel, J., Scarlett, J.A., and Olefsky, J.M. (1981). Receptor and postreceptor defects contribute to the insulin resistance in noninsulin-dependent diabetes mellitus. *J. Clin. Invest.* *68*, 957-969.
- Kozka, I.J., Clark, A.E., and Holman, G.D. (1991). Chronic treatment with insulin selectively down-regulates cell-surface GLUT4 glucose transporters in 3T3-L1 adipocytes. *J. Biol. Chem.* *266*, 11726-11731.
- Kozka, I.J., Clark, A.E., Reckless, J.P., Cushman, S.W., Gould, G.W., and Holman, G.D. (1995). The effects of insulin on the level and activity of the GLUT4 present in human adipose cells. *Diabetologia* *38*, 661-666.
- Kraegen, E.W., Sowden, J.A., Halstead, M.B., Clark, P.W., Rodnick, K.J., Chisholm, D.J., and James, D.E. (1993). Glucose transporters and in vivo glucose uptake in skeletal and cardiac muscle: fasting, insulin stimulation and immunoisolation studies of GLUT1 and GLUT4. *Biochem. J.* *295 (Pt 1)*, 287-293.
- Krapf, D. (2018). Compartmentalization of the plasma membrane. *Curr. Opin. Cell Biol.* *53*, 15-21.
- Kriegel, H.-P., Kröger, P., Sander, J., and Zimek, A. (2011). Density-based clustering. *WIREs Data Mining Knowl Discov* *1*, 231-240.
- Krook, A., Roth, R.A., Jiang, X.J., Zierath, J.R., and Wallberg-Henriksson, H. (1998). Insulin-stimulated Akt kinase activity is reduced in skeletal muscle from NIDDM subjects. *Diabetes* *47*, 1281-1286.
- Krook, A., Björnholm, M., Galuska, D., Jiang, X.J., Fahlman, R., Myers, M.G., Wallberg-Henriksson, H., and Zierath, J.R. (2000). Characterization of signal transduction and glucose transport in skeletal muscle from type 2 diabetic patients. *Diabetes* *49*, 284-292.
- Kudo, N., Barr, A.J., Barr, R.L., Desai, S., and Lopaschuk, G.D. (1995). High rates of fatty acid oxidation during reperfusion of ischemic hearts are associated with a decrease in malonyl-CoA levels due to an increase in 5'-AMP-activated protein kinase inhibition of acetyl-CoA carboxylase. *J. Biol. Chem.* *270*, 17513-17520.

- Kurth-Kraczek, E.J., Hirshman, M.F., Goodyear, L.J., and Winder, W.W. (1999). 5' AMP-activated protein kinase activation causes GLUT4 translocation in skeletal muscle. *Diabetes* 48, 1667-1671.
- Kusumi, A., Tsunoyama, T.A., Hirose, K.M., Kasai, R.S., and Fujiwara, T.K. (2014). Tracking single molecules at work in living cells. *Nat. Chem. Biol.* 10, 524-532.
- Laforest, S., Labrecque, J., Michaud, A., Cianflone, K., and Tchernof, A. (2015). Adipocyte size as a determinant of metabolic disease and adipose tissue dysfunction. *Crit Rev Clin Lab Sci* 52, 301-313.
- Lagache, T., Lang, G., Sauvonnnet, N., and Olivo-Marin, J.-C. (2013). Analysis of the spatial organization of molecules with robust statistics. *PLoS One* 8, e80914.
- Laidlaw, K.M.E. (2018). A role for EFR3A during insulin stimulated dispersal of GLUT4 at the plasma membrane. Doctoral dissertation.
- Lampson, M.A., Racz, A., Cushman, S.W., and McGraw, T.E. (2000). Demonstration of insulin-responsive trafficking of GLUT4 and vptR in fibroblasts. *J. Cell Sci.* 113 (Pt 22), 4065-4076.
- Lampson, M.A., Schmoranzler, J., Zeigerer, A., Simon, S.M., and McGraw, T.E. (2001). Insulin-regulated release from the endosomal recycling compartment is regulated by budding of specialized vesicles. *Mol. Biol. Cell* 12, 3489-3501.
- Lauritzen, H.P.M.M., Ploug, T., Prats, C., Tavaré, J.M., and Galbo, H. (2006). Imaging of insulin signaling in skeletal muscle of living mice shows major role of T-tubules. *Diabetes* 55, 1300-1306.
- Lauritzen, H.P.M.M., Galbo, H., Brandauer, J., Goodyear, L.J., and Ploug, T. (2008). Large GLUT4 vesicles are stationary while locally and reversibly depleted during transient insulin stimulation of skeletal muscle of living mice: imaging analysis of GLUT4-enhanced green fluorescent protein vesicle dynamics. *Diabetes* 57, 315-324.
- Lauritzen, H.P.M.M., Galbo, H., Toyoda, T., and Goodyear, L.J. (2010). Kinetics of contraction-induced GLUT4 translocation in skeletal muscle fibers from living mice. *Diabetes* 59, 2134-2144.
- Lee, J., and Pilch, P.F. (1994). The insulin receptor: structure, function, and signaling. *Am. J. Physiol.* 266, C319-34.
- Lee, M., Gardin, J.M., Lynch, J.C., Smith, V.E., Tracy, R.P., Savage, P.J., Szklo, M., and Ward, B.J. (1997). Diabetes mellitus and echocardiographic left ventricular function in free-living elderly men and women: The Cardiovascular Health Study. *Am. Heart J.* 133, 36-43.
- Lemay, A., Turcot, L., Déchéne, F., Dodin, S., and Forest, J.-C. (2010). Hyperinsulinemia in nonobese women reporting a moderate weight gain at the beginning of menopause: a useful early measure of susceptibility to insulin resistance. *Menopause* 17, 321-325.

- Lemieux, K., Han, X.X., Dombrowski, L., Bonen, A., and Marette, A. (2000). The transferrin receptor defines two distinct contraction-responsive GLUT4 vesicle populations in skeletal muscle. *Diabetes* 49, 183-189.
- Leon, B.M., and Maddox, T.M. (2015). Diabetes and cardiovascular disease: Epidemiology, biological mechanisms, treatment recommendations and future research. *World J. Diabetes* 6, 1246-1258.
- Leto, D., and Saltiel, A.R. (2012). Regulation of glucose transport by insulin: traffic control of GLUT4. *Nat. Rev. Mol. Cell Biol.* 13, 383-396.
- Levet, F., Hosity, E., Kechkar, A., Butler, C., Beghin, A., Choquet, D., and Sibarita, J.-B. (2015). SR-Tesseler: a method to segment and quantify localization-based super-resolution microscopy data. *Nat. Methods* 12, 1065-1071.
- Levine, R., and Goldstein, M.S. (1958). On the mechanism of action of insulin. *Hormoner* 11, 2-22.
- Leyton Puig, D., Leyton Puig, D., Kedziora *, K.M., Isogai *, T., van den Broek, B., Jalink, K., and Innocenti, M. (2016). Tips and tricks for artifact-free PFA-based fixation of the actin cytoskeleton and its regulatory proteins for single molecule localization super-resolution microscopy. *Protoc. exch.*
- Li, L.V., and Kandror, K.V. (2005). Golgi-localized, gamma-ear-containing, Arf-binding protein adaptors mediate insulin-responsive trafficking of glucose transporter 4 in 3T3-L1 adipocytes. *Mol. Endocrinol.* 19, 2145-2153.
- Li, C.H., Bai, L., Li, D.D., Xia, S., and Xu, T. (2004). Dynamic tracking and mobility analysis of single GLUT4 storage vesicle in live 3T3-L1 cells. *Cell Res.* 14, 480-486.
- Lim, S.N., Bonzelius, F., Low, S.H., Wille, H., Weimbs, T., and Herman, G.A. (2001). Identification of discrete classes of endosome-derived small vesicles as a major cellular pool for recycling membrane proteins. *Mol. Biol. Cell* 12, 981-995.
- Liu, J., Kimura, A., Baumann, C.A., and Saltiel, A.R. (2002). APS facilitates c-Cbl tyrosine phosphorylation and GLUT4 translocation in response to insulin in 3T3-L1 adipocytes. *Mol. Cell. Biol.* 22, 3599-3609.
- Liu, J., DeYoung, S.M., Hwang, J.B., O'Leary, E.E., and Saltiel, A.R. (2003). The roles of Cbl-b and c-Cbl in insulin-stimulated glucose transport. *J. Biol. Chem.* 278, 36754-36762.
- Liu, P., Leffler, B.J., Weeks, L.K., Chen, G., Bouchard, C.M., Strawbridge, A.B., and Elmendorf, J.S. (2004). Sphingomyelinase activates GLUT4 translocation via a cholesterol-dependent mechanism. *Am. J. Physiol. Cell Physiol.* 286, C317-29.
- Liu, Y., Wang, H.-Y., Shao, J., Zaro, J.L., and Shen, W.-C. (2020). Enhanced insulin receptor interaction by a bifunctional insulin-transferrin fusion protein: an approach to overcome insulin resistance. *Sci. Rep.* 10, 7724.

- Livingstone, C., James, D.E., Rice, J.E., Hanpeter, D., and Gould, G.W. (1996). Compartment ablation analysis of the insulin-responsive glucose transporter (GLUT4) in 3T3-L1 adipocytes. *Biochem. J.* 315 (Pt 2), 487-495.
- Lizunov, V.A., Matsumoto, H., Zimmerberg, J., Cushman, S.W., and Frolov, V.A. (2005). Insulin stimulates the halting, tethering, and fusion of mobile GLUT4 vesicles in rat adipose cells. *J. Cell Biol.* 169, 481-489.
- Lizunov, V.A., Lisinski, I., Stenkula, K., Zimmerberg, J., and Cushman, S.W. (2009). Insulin regulates fusion of GLUT4 vesicles independent of Exo70-mediated tethering. *J. Biol. Chem.* 284, 7914-7919.
- Lizunov, V.A., Stenkula, K.G., Lisinski, I., Gavrilova, O., Yver, D.R., Chadt, A., Al-Hasani, H., Zimmerberg, J., and Cushman, S.W. (2012). Insulin stimulates fusion, but not tethering, of GLUT4 vesicles in skeletal muscle of HA-GLUT4-GFP transgenic mice. *Am. J. Physiol. Endocrinol. Metab.* 302, E950-60.
- Lizunov, V.A., Stenkula, K., Troy, A., Cushman, S.W., and Zimmerberg, J. (2013a). Insulin regulates Glut4 confinement in plasma membrane clusters in adipose cells. *PLoS One* 8, e57559.
- Lizunov, V.A., Lee, J.-P., Skarulis, M.C., Zimmerberg, J., Cushman, S.W., and Stenkula, K.G. (2013b). Impaired tethering and fusion of GLUT4 vesicles in insulin-resistant human adipose cells. *Diabetes* 62, 3114-3119.
- Lorenzo-Almorós, A., Tuñón, J., Orejas, M., Cortés, M., Egido, J., and Lorenzo, Ó. (2017). Diagnostic approaches for diabetic cardiomyopathy. *Cardiovasc Diabetol* 16, 28.
- Louch, W.E., Sheehan, K.A., and Wolska, B.M. (2011). Methods in cardiomyocyte isolation, culture, and gene transfer. *J. Mol. Cell Cardiol.* 51, 288-298.
- Madonna, R., Pieragostino, D., Balistreri, C.R., Rossi, C., Geng, Y.-J., Del Boccio, P., and De Caterina, R. (2018). Diabetic macroangiopathy: Pathogenetic insights and novel therapeutic approaches with focus on high glucose-mediated vascular damage. *Vascul. Pharmacol.*
- Maegawa, H., Shigeta, Y., Egawa, K., and Kobayashi, M. (1991). Impaired autophosphorylation of insulin receptors from abdominal skeletal muscles in nonobese subjects with NIDDM. *Diabetes* 40, 815-819.
- Maier, V.H., and Gould, G.W. (2000). Long-term insulin treatment of 3T3-L1 adipocytes results in mis-targeting of GLUT4: implications for insulin-stimulated glucose transport. *Diabetologia* 43, 1273-1281.
- Malhotra, R., and Brosius, F.C. (1999). Glucose uptake and glycolysis reduce hypoxia-induced apoptosis in cultured neonatal rat cardiac myocytes. *J. Biol. Chem.* 274, 12567-12575.

- Mangmool, S., Denkaew, T., Phosri, S., Pinthong, D., Parichatikanond, W., Shimauchi, T., and Nishida, M. (2016). Sustained BAR Stimulation Mediates Cardiac Insulin Resistance in a PKA-Dependent Manner. *Mol. Endocrinol.* 30, 118-132.
- Manley, S., Gillette, J.M., Patterson, G.H., Shroff, H., Hess, H.F., Betzig, E., and Lippincott-Schwartz, J. (2008). High-density mapping of single-molecule trajectories with photoactivated localization microscopy. *Nat. Methods* 5, 155-157.
- Le Marchand-Brustel, Y., Grémeaux, T., Ballotti, R., and Van Obberghen, E. (1985). Insulin receptor tyrosine kinase is defective in skeletal muscle of insulin-resistant obese mice. *Nature* 315, 676-679.
- Marette, A., Richardson, J.M., Ramlal, T., Balon, T.W., Vranic, M., Pessin, J.E., and Klip, A. (1992). Abundance, localization, and insulin-induced translocation of glucose transporters in red and white muscle. *Am. J. Physiol.* 263, C443-52.
- Marsh, R.J., Pfisterer, K., Bennett, P., Hirvonen, L.M., Gautel, M., Jones, G.E., and Cox, S. (2018). Artifact-free high-density localization microscopy analysis. *Nat. Methods* 15, 689-692.
- Martin, L.B., Shewan, A., Millar, C.A., Gould, G.W., and James, D.E. (1998). Vesicle-associated membrane protein 2 plays a specific role in the insulin-dependent trafficking of the facilitative glucose transporter GLUT4 in 3T3-L1 adipocytes. *J. Biol. Chem.* 273, 1444-1452.
- Martin, S., Tellam, J., Livingstone, C., Slot, J.W., Gould, G.W., and James, D.E. (1996). The glucose transporter (GLUT-4) and vesicle-associated membrane protein-2 (VAMP-2) are segregated from recycling endosomes in insulin-sensitive cells. *J. Cell Biol.* 134, 625-635.
- Masters, J.R. (2002). HeLa cells 50 years on: the good, the bad and the ugly. *Nat. Rev. Cancer* 2, 315-319.
- Mathur, A., Ma, Z., Loskill, P., Jeeawoody, S., and Healy, K.E. (2016). In vitro cardiac tissue models: Current status and future prospects. *Adv. Drug Deliv. Rev.* 96, 203-213.
- Matsa, E., Rajamohan, D., Dick, E., Young, L., Mellor, I., Staniforth, A., and Denning, C. (2011). Drug evaluation in cardiomyocytes derived from human induced pluripotent stem cells carrying a long QT syndrome type 2 mutation. *Eur. Heart J.* 32, 952-962.
- Mattheyses, A.L., Simon, S.M., and Rappoport, J.Z. (2010). Imaging with total internal reflection fluorescence microscopy for the cell biologist. *J. Cell Sci.* 123, 3621-3628.
- Mayle, K.M., Le, A.M., and Kamei, D.T. (2012). The intracellular trafficking pathway of transferrin. *Biochim. Biophys. Acta* 1820, 264-281.
- McClain, D.A., Sharma, N.K., Jain, S., Harrison, A., Salaye, L.N., Comeau, M.E., Langefeld, C.D., Lorenzo, F.R., and Das, S.K. (2018). Adipose tissue transferrin and insulin resistance. *J. Clin. Endocrinol. Metab.* 103, 4197-4208.

- McIntyre, H.D., Catalano, P., Zhang, C., Desoye, G., Mathiesen, E.R., and Damm, P. (2019). Gestational diabetes mellitus. *Nat. Rev. Dis. Primers* 5, 47.
- McLaughlin, T., Sherman, A., Tsao, P., Gonzalez, O., Yee, G., Lamendola, C., Reaven, G.M., and Cushman, S.W. (2007). Enhanced proportion of small adipose cells in insulin-resistant vs insulin-sensitive obese individuals implicates impaired adipogenesis. *Diabetologia* 50, 1707-1715.
- Melan, M.A. (1994). Overview of cell fixation and permeabilization. *Methods Mol. Biol.* 34, 55-66.
- Merrill, G.F., Kurth, E.J., Hardie, D.G., and Winder, W.W. (1997). AICA riboside increases AMP-activated protein kinase, fatty acid oxidation, and glucose uptake in rat muscle. *Am. J. Physiol.* 273, E1107-12.
- Meyer, M.M., Levin, K., Grimmsmann, T., Beck-Nielsen, H., and Klein, H.H. (2002). Insulin signalling in skeletal muscle of subjects with or without Type II-diabetes and first degree relatives of patients with the disease. *Diabetologia* 45, 813-822.
- De Meyts, P. (2000). The Insulin Receptor and Its Signal Transduction Network. In *Endotext*, L.J. De Groot, G. Chrousos, K. Dungan, A. Grossman, J.M. Hershman, C. Koch, M. Korbonits, R. McLachlan, M. New, J. Purnell, et al., eds. (South Dartmouth (MA): MDText.com, Inc.),.
- Mitrakou, A., Kelley, D., Veneman, T., Jenssen, T., Pangburn, T., Reilly, J., and Gerich, J. (1990). Contribution of abnormal muscle and liver glucose metabolism to postprandial hyperglycemia in NIDDM. *Diabetes* 39, 1381-1390.
- Montessuit, C., and Lerch, R. (2013). Regulation and dysregulation of glucose transport in cardiomyocytes. *Biochim. Biophys. Acta* 1833, 848-856.
- Montessuit, C., Rosenblatt-Velin, N., Papageorgiou, I., Campos, L., Pellieux, C., Palma, T., and Lerch, R. (2004). Regulation of glucose transporter expression in cardiac myocytes: p38 MAPK is a strong inducer of GLUT4. *Cardiovasc. Res.* 64, 94-104.
- Montessuit, C., Papageorgiou, I., Campos, L., and Lerch, R. (2006). Retinoic acids increase expression of GLUT4 in dedifferentiated and hypertrophied cardiac myocytes. *Basic Res. Cardiol.* 101, 27-35.
- Moretti, A., Bellin, M., Welling, A., Jung, C.B., Lam, J.T., Bott-Flügel, L., Dorn, T., Goedel, A., Höhnke, C., Hofmann, F., et al. (2010). Patient-specific induced pluripotent stem-cell models for long-QT syndrome. *N. Engl. J. Med.* 363, 1397-1409.
- Morisco, C., Condorelli, G., Trimarco, V., Bellis, A., Marrone, C., Condorelli, G., Sadoshima, J., and Trimarco, B. (2005). Akt mediates the cross-talk between beta-adrenergic and insulin receptors in neonatal cardiomyocytes. *Circ. Res.* 96, 180-188.
- Morishima, M., Horikawa, K., and Funaki, M. (2018). Cardiomyocytes cultured on mechanically compliant substrates, but not on conventional culture devices, exhibit

- prominent mitochondrial dysfunction due to reactive oxygen species and insulin resistance under high glucose. *PLoS One* 13, e0201891.
- Morris, S. (2020). Dynamics of the plasma membrane transporter GLUT4. Doctoral dissertation. MCSB.
- Morris, N.J., Ross, S.A., Lane, W.S., Moestrup, S.K., Petersen, C.M., Keller, S.R., and Lienhard, G.E. (1998). Sortilin is the major 110-kDa protein in GLUT4 vesicles from adipocytes. *J. Biol. Chem.* 273, 3582-3587.
- Morris, S., Geoghegan, N.D., Sadler, J.B.A., Koester, A.M., Black, H.L., Laub, M., Miller, L., Heffernan, L., Simpson, J.C., Mastick, C.C., et al. (2020). Characterisation of GLUT4 trafficking in HeLa cells: comparable kinetics and orthologous trafficking mechanisms to 3T3-L1 adipocytes. *PeerJ* 8, e8751.
- Mueckler, M. (2001). Insulin resistance and the disruption of Glut4 trafficking in skeletal muscle. *J. Clin. Invest.* 107, 1211-1213.
- Mueckler, M., and Thorens, B. (2013). The SLC2 (GLUT) family of membrane transporters. *Mol. Aspects Med.* 34, 121-138.
- Mueckler, M., Caruso, C., Baldwin, S.A., Panico, M., Blench, I., Morris, H.R., Allard, W.J., Lienhard, G.E., and Lodish, H.F. (1985). Sequence and structure of a human glucose transporter. *Science* 229, 941-945.
- Muyldermans, S. (2013). Nanobodies: natural single-domain antibodies. *Annu. Rev. Biochem.* 82, 775-797.
- Nakatsu, F., Baskin, J.M., Chung, J., Tanner, L.B., Shui, G., Lee, S.Y., Pirruccello, M., Hao, M., Ingolia, N.T., Wenk, M.R., et al. (2012). PtdIns4P synthesis by PI4KIII α at the plasma membrane and its impact on plasma membrane identity. *J. Cell Biol.* 199, 1003-1016.
- Ng, Y., Ramm, G., Lopez, J.A., and James, D.E. (2008). Rapid activation of Akt2 is sufficient to stimulate GLUT4 translocation in 3T3-L1 adipocytes. *Cell Metab.* 7, 348-356.
- Nolan, J.J., Freidenberg, G., Henry, R., Reichart, D., and Olefsky, J.M. (1994). Role of human skeletal muscle insulin receptor kinase in the in vivo insulin resistance of noninsulin-dependent diabetes mellitus and obesity. *J. Clin. Endocrinol. Metab.* 78, 471-477.
- Nollmann, M., and Georgieva, M. (2015). Superresolution microscopy for bioimaging at the nanoscale: from concepts to applications in the nucleus. *Res. Rep. Biol.* 157.
- Nystrom, F.H., Chen, H., Cong, L.N., Li, Y., and Quon, M.J. (1999). Caveolin-1 interacts with the insulin receptor and can differentially modulate insulin signaling in transfected Cos-7 cells and rat adipose cells. *Mol. Endocrinol.* 13, 2013-2024.
- Ogurtsova, K., da Rocha Fernandes, J.D., Huang, Y., Linnenkamp, U., Guariguata, L., Cho, N.H., Cavan, D., Shaw, J.E., and Makaroff, L.E. (2017). IDF Diabetes Atlas: Global

- estimates for the prevalence of diabetes for 2015 and 2040. *Diabetes Res. Clin. Pract.* **128**, 40-50.
- Olivier, N., Keller, D., Gönczy, P., and Manley, S. (2013). Resolution doubling in 3D-STORM imaging through improved buffers. *PLoS One* **8**, e69004.
- Orban, E., Schwab, S., Thorand, B., and Huth, C. (2014). Association of iron indices and type 2 diabetes: a meta-analysis of observational studies. *Diabetes Metab Res Rev* **30**, 372-394.
- Ovesný, M., Křížek, P., Borkovec, J., Svindrych, Z., and Hagen, G.M. (2014). ThunderSTORM: a comprehensive ImageJ plug-in for PALM and STORM data analysis and super-resolution imaging. *Bioinformatics* **30**, 2389-2390.
- Owens, J., Moreira, K., and Bain, G. (2013). Characterization of primary human skeletal muscle cells from multiple commercial sources. *In Vitro Cell Dev Biol Anim* **49**, 695-705.
- Padlan, E.A. (1994). Anatomy of the antibody molecule. *Mol. Immunol.* **31**, 169-217.
- Palacios, S., Lalioti, V., Martinez-Arca, S., Chattopadhyay, S., and Sandoval, I.V. (2001). Recycling of the insulin-sensitive glucose transporter GLUT4. Access of surface internalized GLUT4 molecules to the perinuclear storage compartment is mediated by the Phe5-Gln6-Gln7-Ile8 motif. *J. Biol. Chem.* **276**, 3371-3383.
- Pan, D.A., Lillioja, S., Kriketos, A.D., Milner, M.R., Baur, L.A., Bogardus, C., Jenkins, A.B., and Storlien, L.H. (1997). Skeletal muscle triglyceride levels are inversely related to insulin action. *Diabetes* **46**, 983-988.
- Pan, X., Zaarur, N., Singh, M., Morin, P., and Kandror, K.V. (2017). Sortilin and retromer mediate retrograde transport of Glut4 in 3T3-L1 adipocytes. *Mol. Biol. Cell* **28**, 1667-1675.
- Parameswaran, S., Kumar, S., Verma, R.S., and Sharma, R.K. (2013). Cardiomyocyte culture - an update on the in vitro cardiovascular model and future challenges. *Can. J. Physiol. Pharmacol.* **91**, 985-998.
- Park, C.R., and Johnson, L.H. (1955). Effect of insulin on transport of glucose and galactose into cells of rat muscle and brain. *Am. J. Physiol.* **182**, 17-23.
- Parpal, S., Karlsson, M., Thorn, H., and Strålfors, P. (2001). Cholesterol depletion disrupts caveolae and insulin receptor signaling for metabolic control via insulin receptor substrate-1, but not for mitogen-activated protein kinase control. *J. Biol. Chem.* **276**, 9670-9678.
- Parton, R.G., Molero, J.C., Floetenmeyer, M., Green, K.M., and James, D.E. (2002). Characterization of a distinct plasma membrane macrodomain in differentiated adipocytes. *J. Biol. Chem.* **277**, 46769-46778.
- Pattar, G.R., Tackett, L., Liu, P., and Elmendorf, J.S. (2006). Chromium picolinate positively influences the glucose transporter system via affecting cholesterol

- homeostasis in adipocytes cultured under hyperglycemic diabetic conditions. *Mutat. Res.* 610, 93-100.
- Patterson, G.H., and Lippincott-Schwartz, J. (2002). A photoactivatable GFP for selective photolabeling of proteins and cells. *Science* 297, 1873-1877.
- Pearse, B.M. (1976). Clathrin: a unique protein associated with intracellular transfer of membrane by coated vesicles. *Proc. Natl. Acad. Sci. USA* 73, 1255-1259.
- Pendsey, S.P. (2010). Understanding diabetic foot. *Int. J. Diabetes Dev. Ctries.* 30, 75-79.
- Pentassuglia, L., Heim, P., Lebboukh, S., Morandi, C., Xu, L., and Brink, M. (2016). Neuregulin-1B promotes glucose uptake via PI3K/Akt in neonatal rat cardiomyocytes. *Am. J. Physiol. Endocrinol. Metab.* 310, E782-94.
- Peter, A.K., Bjerke, M.A., and Leinwand, L.A. (2016). Biology of the cardiac myocyte in heart disease. *Mol. Biol. Cell* 27, 2149-2160.
- Phillips, D.I., Caddy, S., Ilic, V., Fielding, B.A., Frayn, K.N., Borthwick, A.C., and Taylor, R. (1996). Intramuscular triglyceride and muscle insulin sensitivity: evidence for a relationship in nondiabetic subjects. *Metab. Clin. Exp.* 45, 947-950.
- Pike, L.J. (2009). The challenge of lipid rafts. *J. Lipid Res.* 50 Suppl, S323-8.
- Platonova, E., Winterflood, C.M., Junemann, A., Albrecht, D., Faix, J., and Ewers, H. (2015). Single-molecule microscopy of molecules tagged with GFP or RFP derivatives in mammalian cells using nanobody binders. *Methods* 88, 89-97.
- Ploug, T., van Deurs, B., Ai, H., Cushman, S.W., and Ralston, E. (1998). Analysis of GLUT4 distribution in whole skeletal muscle fibers: identification of distinct storage compartments that are recruited by insulin and muscle contractions. *J. Cell Biol.* 142, 1429-1446.
- Popp, M.W., Antos, J.M., Grotenbreg, G.M., Spooner, E., and Ploegh, H.L. (2007). Sortagging: a versatile method for protein labeling. *Nat. Chem. Biol.* 3, 707-708.
- Poulsen, M.K., Henriksen, J.E., Dahl, J., Johansen, A., Gerke, O., Vach, W., Haghfelt, T., Høilund-Carlsen, P.F., Beck-Nielsen, H., and Møller, J.E. (2010). Left ventricular diastolic function in type 2 diabetes mellitus: prevalence and association with myocardial and vascular disease. *Circ Cardiovasc Imaging* 3, 24-31.
- Powell, T., and Twist, V.W. (1976). A rapid technique for the isolation and purification of adult cardiac muscle cells having respiratory control and a tolerance to calcium. *Biochem. Biophys. Res. Commun.* 72, 327-333.
- Powell, K.A., Campbell, L.C., Tavaré, J.M., Leader, D.P., Wakefield, J.A., and Gould, G.W. (1999). Trafficking of Glut4-green fluorescent protein chimaeras in 3T3-L1 adipocytes suggests distinct internalization mechanisms regulating cell surface glut4 levels. *Biochem. J.* 344 Pt 2, 535-543.

- Qi, Y., Xu, Z., Zhu, Q., Thomas, C., Kumar, R., Feng, H., Dostal, D.E., White, M.F., Baker, K.M., and Guo, S. (2013). Myocardial loss of IRS1 and IRS2 causes heart failure and is controlled by p38 α MAPK during insulin resistance. *Diabetes* 62, 3887-3900.
- Qu, F., Wang, X., Chen, Z., Liang, T., and Qu, A. (2010). Labeling GLUT4 with quantum dots for 3D tracking in live L6 cells. In *World Congress on Medical Physics and Biomedical Engineering*, September 7 - 12, 2009, Munich, Germany, O. Dössel, and W.C. Schlegel, eds. (Berlin, Heidelberg: Springer Berlin Heidelberg), pp. 514-517.
- Quon, M.J., Butte, A.J., Zarnowski, M.J., Sesti, G., Cushman, S.W., and Taylor, S.I. (1994). Insulin receptor substrate 1 mediates the stimulatory effect of insulin on GLUT4 translocation in transfected rat adipose cells. *J. Biol. Chem.* 269, 27920-27924.
- Rea, S., and James, D.E. (1997). Moving GLUT4: the biogenesis and trafficking of GLUT4 storage vesicles. *Diabetes* 46, 1667-1677.
- Richter, E.A., and Hargreaves, M. (2013). Exercise, GLUT4, and skeletal muscle glucose uptake. *Physiol. Rev.* 93, 993-1017.
- Richter, K.N., Revelo, N.H., Seitz, K.J., Helm, M.S., Sarkar, D., Saleeb, R.S., D'Este, E., Eberle, J., Wagner, E., Vogl, C., et al. (2018). Glyoxal as an alternative fixative to formaldehyde in immunostaining and super-resolution microscopy. *EMBO J.* 37, 139-159.
- Riehle, C., and Abel, E.D. (2016). Insulin signaling and heart failure. *Circ. Res.* 118, 1151-1169.
- Ries, J., Kaplan, C., Platonova, E., Eghlidi, H., and Ewers, H. (2012). A simple, versatile method for GFP-based super-resolution microscopy via nanobodies. *Nat. Methods* 9, 582-584.
- Ripley, B.D. (1976). The second-order analysis of stationary point processes. *J Appl Probab* 13, 255-266.
- Ripsin, C.M., Kang, H., and Urban, R.J. (2009). Management of blood glucose in type 2 diabetes mellitus. *Am. Fam. Physician* 79, 29-36.
- Robinson, L.J., Pang, S., Harris, D.S., Heuser, J., and James, D.E. (1992). Translocation of the glucose transporter (GLUT4) to the cell surface in permeabilized 3T3-L1 adipocytes: effects of ATP insulin, and GTP gamma S and localization of GLUT4 to clathrin lattices. *J. Cell Biol.* 117, 1181-1196.
- Rondinone, C.M., Carvalho, E., Wesslau, C., and Smith, U.P. (1999). Impaired glucose transport and protein kinase B activation by insulin, but not okadaic acid, in adipocytes from subjects with Type II diabetes mellitus. *Diabetologia* 42, 819-825.
- Ros-Baro, A., Lopez-Iglesias, C., Peiro, S., Bellido, D., Palacin, M., Zorzano, A., and Camps, M. (2001). Lipid rafts are required for GLUT4 internalization in adipose cells. *Proc. Natl. Acad. Sci. USA* 98, 12050-12055.

- Rothbauer, U., Zolghadr, K., Tillib, S., Nowak, D., Schermelleh, L., Gahl, A., Backmann, N., Conrath, K., Muyldermans, S., Cardoso, M.C., et al. (2006). Targeting and tracing antigens in live cells with fluorescent nanobodies. *Nat. Methods* 3, 887-889.
- Ruan, Y., Yin, P., Li, F., Li, D., Lin, Q., and Li, K. (2019). The accuracy of determining cluster size by analyzing ripley's K function in single molecule localization microscopy. *Appl. Sci.* 9, 3271.
- Rubin-Delanchy, P., Burn, G.L., Griffié, J., Williamson, D.J., Heard, N.A., Cope, A.P., and Owen, D.M. (2015). Bayesian cluster identification in single-molecule localization microscopy data. *Nat. Methods* 12, 1072-1076.
- Rubler, S., Dlugash, J., Yuceoglu, Y.Z., Kumral, T., Branwood, A.W., and Grishman, A. (1972). New type of cardiomyopathy associated with diabetic glomerulosclerosis. *Am. J. Cardiol.* 30, 595-602.
- Russell, R.R., Bergeron, R., Shulman, G.I., and Young, L.H. (1999). Translocation of myocardial GLUT-4 and increased glucose uptake through activation of AMPK by AICAR. *Am. J. Physiol.* 277, H643-9.
- Rust, M.J., Bates, M., and Zhuang, X. (2006). Sub-diffraction-limit imaging by stochastic optical reconstruction microscopy (STORM). *Nat. Methods* 3, 793-795.
- Rydén, L., Armstrong, P.W., Cleland, J.G., Horowitz, J.D., Massie, B.M., Packer, M., and Poole-Wilson, P.A. (2000). Efficacy and safety of high-dose lisinopril in chronic heart failure patients at high cardiovascular risk, including those with diabetes mellitus. Results from the ATLAS trial. *Eur. Heart J.* 21, 1967-1978.
- Ryder, J.W., Kawano, Y., Galuska, D., Fahlman, R., Wallberg-Henriksson, H., Charron, M.J., and Zierath, J.R. (1999). Postexercise glucose uptake and glycogen synthesis in skeletal muscle from GLUT4-deficient mice. *FASEB J.* 13, 2246-2256.
- Ryder, J.W., Yang, J., Galuska, D., Rincón, J., Björnholm, M., Krook, A., Lund, S., Pedersen, O., Wallberg-Henriksson, H., Zierath, J.R., et al. (2000). Use of a novel impermeable biotinylated photolabeling reagent to assess insulin- and hypoxia-stimulated cell surface GLUT4 content in skeletal muscle from type 2 diabetic patients. *Diabetes* 49, 647-654.
- Saddik, M., Gamble, J., Witters, L.A., and Lopaschuk, G.D. (1993). Acetyl-CoA carboxylase regulation of fatty acid oxidation in the heart. *J. Biol. Chem.* 268, 25836-25845.
- Sage, D., Pham, T.-A., Babcock, H., Lukes, T., Pengo, T., Chao, J., Velmurugan, R., Herbert, A., Agrawal, A., Colabrese, S., et al. (2019). Super-resolution fight club: assessment of 2D and 3D single-molecule localization microscopy software. *Nat. Methods* 16, 387-395.

- Salans, L.B., Knittle, J.L., and Hirsch, J. (1968). The role of adipose cell size and adipose tissue insulin sensitivity in the carbohydrate intolerance of human obesity. *J. Clin. Invest.* *47*, 153-165.
- Salt, I.P., Connell, J.M., and Gould, G.W. (2000). 5-aminoimidazole-4-carboxamide ribonucleoside (AICAR) inhibits insulin-stimulated glucose transport in 3T3-L1 adipocytes. *Diabetes* *49*, 1649-1656.
- Samuel, V.T., and Shulman, G.I. (2016). The pathogenesis of insulin resistance: integrating signaling pathways and substrate flux. *J. Clin. Invest.* *126*, 12-22.
- Santalucía, T., Camps, M., Castelló, A., Muñoz, P., Nuel, A., Testar, X., Palacin, M., and Zorzano, A. (1992). Developmental regulation of GLUT-1 (erythroid/Hep G2) and GLUT-4 (muscle/fat) glucose transporter expression in rat heart, skeletal muscle, and brown adipose tissue. *Endocrinology* *130*, 837-846.
- Santi, P.A. (2011). Light sheet fluorescence microscopy: a review. *J. Histochem. Cytochem.* *59*, 129-138.
- Sargeant, R.J., and Pâquet, M.R. (1993). Effect of insulin on the rates of synthesis and degradation of GLUT1 and GLUT4 glucose transporters in 3T3-L1 adipocytes. *Biochem. J.* *290 (Pt 3)*, 913-919.
- Satoh, S., Nishimura, H., Clark, A.E., Kozka, I.J., Vannucci, S.J., Simpson, I.A., Quon, M.J., Cushman, S.W., and Holman, G.D. (1993). Use of bismannose photolabel to elucidate insulin-regulated GLUT4 subcellular trafficking kinetics in rat adipose cells. Evidence that exocytosis is a critical site of hormone action. *J. Biol. Chem.* *268*, 17820-17829.
- Schneider, C.A., Rasband, W.S., and Eliceiri, K.W. (2012). NIH Image to ImageJ: 25 years of image analysis. *Nat. Methods* *9*, 671-675.
- Schnell, U., Dijk, F., Sjollem, K.A., and Giepmans, B.N.G. (2012). Immunolabeling artifacts and the need for live-cell imaging. *Nat. Methods* *9*, 152-158.
- Schrauwen, P. (2007). High-fat diet, muscular lipotoxicity and insulin resistance. *Proc Nutr Soc* *66*, 33-41.
- Shang, Y., Zhang, X., Chen, L., Leng, W., Lei, X., Yang, Q., Liang, Z., and Wang, J. (2016). Assessment of Left Ventricular Structural Remodelling in Patients with Diabetic Cardiomyopathy by Cardiovascular Magnetic Resonance. *J. Diabetes Res.* *2016*, 4786925.
- Shao, D., and Tian, R. (2015). Glucose transporters in cardiac metabolism and hypertrophy. *Compr. Physiol.* *6*, 331-351.
- Shapira, K.E., Ehrlich, M., and Henis, Y.I. (2018). Cholesterol depletion enhances TGF- β Smad signaling by increasing c-Jun expression through a PKR-dependent mechanism. *Mol. Biol. Cell* *29*, 2494-2507.
- Sharonov, A., and Hochstrasser, R.M. (2006). Wide-field subdiffraction imaging by accumulated binding of diffusing probes. *Proc. Natl. Acad. Sci. USA* *103*, 18911-18916.

- Shepherd, P.R., Gnudi, L., Tozzo, E., Yang, H., Leach, F., and Kahn, B.B. (1993). Adipose cell hyperplasia and enhanced glucose disposal in transgenic mice overexpressing GLUT4 selectively in adipose tissue. *J. Biol. Chem.* 268, 22243-22246.
- Shewan, A.M., Marsh, B.J., Melvin, D.R., Martin, S., Gould, G.W., and James, D.E. (2000). The cytosolic C-terminus of the glucose transporter GLUT4 contains an acidic cluster endosomal targeting motif distal to the dileucine signal. *Biochem. J.* 350 Pt 1, 99-107.
- Shewan, A.M., McCann, R.K., Lamb, C.A., Stirrat, L., Kioumourtzoglou, D., Adamson, I.S., Verma, S., James, D.E., and Bryant, N.J. (2013). Endosomal sorting of GLUT4 and Gap1 is conserved between yeast and insulin-sensitive cells. *J. Cell Sci.* 126, 1576-1582.
- Shi, J., and Kandror, K.V. (2005). Sortilin is essential and sufficient for the formation of Glut4 storage vesicles in 3T3-L1 adipocytes. *Dev. Cell* 9, 99-108.
- Shi, J., and Kandror, K.V. (2007). The luminal Vps10p domain of sortilin plays the predominant role in targeting to insulin-responsive Glut4-containing vesicles. *J. Biol. Chem.* 282, 9008-9016.
- Shigematsu, S., Watson, R.T., Khan, A.H., and Pessin, J.E. (2003). The adipocyte plasma membrane caveolin functional/structural organization is necessary for the efficient endocytosis of GLUT4. *J. Biol. Chem.* 278, 10683-10690.
- Shindler, D.M., Kostis, J.B., Yusuf, S., Quinones, M.A., Pitt, B., Stewart, D., Pinkett, T., Ghali, J.K., and Wilson, A.C. (1996). Diabetes mellitus, a predictor of morbidity and mortality in the Studies of Left Ventricular Dysfunction (SOLVD) Trials and Registry. *Am. J. Cardiol.* 77, 1017-1020.
- Sinha, M.K., Pories, W.J., Flickinger, E.G., Meelheim, D., and Caro, J.F. (1987). Insulin-receptor kinase activity of adipose tissue from morbidly obese humans with and without NIDDM. *Diabetes* 36, 620-625.
- Sivitz, W.I., Lund, D.D., Yorek, B., Grover-McKay, M., and Schmid, P.G. (1992). Pretranslational regulation of two cardiac glucose transporters in rats exposed to hypobaric hypoxia. *Am. J. Physiol.* 263, E562-9.
- Slot, J.W., Geuze, H.J., Gigengack, S., Lienhard, G.E., and James, D.E. (1991a). Immuno-localization of the insulin regulatable glucose transporter in brown adipose tissue of the rat. *J. Cell Biol.* 113, 123-135.
- Slot, J.W., Geuze, H.J., Gigengack, S., James, D.E., and Lienhard, G.E. (1991b). Translocation of the glucose transporter GLUT4 in cardiac myocytes of the rat. *Proc. Natl. Acad. Sci. USA* 88, 7815-7819.
- Smith, J.E., and Reese, T.S. (1980). Use of aldehyde fixatives to determine the rate of synaptic transmitter release. *J. Exp. Biol.* 89, 19-29.
- Stadtfeld, M., and Hochedlinger, K. (2009). Without a trace? PiggyBac-ing toward pluripotency. *Nat. Methods* 6, 329-330.

- Stadtfield, M., Nagaya, M., Utikal, J., Weir, G., and Hochedlinger, K. (2008a). Induced pluripotent stem cells generated without viral integration. *Science* 322, 945-949.
- Stadtfield, M., Maherali, N., Breault, D.T., and Hochedlinger, K. (2008b). Defining molecular cornerstones during fibroblast to iPS cell reprogramming in mouse. *Cell Stem Cell* 2, 230-240.
- Stanly, T.A., Fritzsche, M., Banerji, S., García, E., Bernardino de la Serna, J., Jackson, D.G., and Eggeling, C. (2016). Critical importance of appropriate fixation conditions for faithful imaging of receptor microclusters. *Biol. Open* 5, 1343-1350.
- Steinbusch, L.K.M., Schwenk, R.W., Ouwens, D.M., Diamant, M., Glatz, J.F.C., and Luiken, J.J.F.P. (2011). Subcellular trafficking of the substrate transporters GLUT4 and CD36 in cardiomyocytes. *Cell Mol. Life Sci.* 68, 2525-2538.
- Stenbit, A.E., Tsao, T.S., Li, J., Burcelin, R., Geenen, D.L., Factor, S.M., Houseknecht, K., Katz, E.B., and Charron, M.J. (1997). GLUT4 heterozygous knockout mice develop muscle insulin resistance and diabetes. *Nat. Med.* 3, 1096-1101.
- Stenkula, K.G., and Erlanson-Albertsson, C. (2018). Adipose cell size: importance in health and disease. *Am. J. Physiol. Regul. Integr. Comp. Physiol.* 315, R284-R295.
- Stenkula, K.G., Lizunov, V.A., Cushman, S.W., and Zimmerberg, J. (2010). Insulin controls the spatial distribution of GLUT4 on the cell surface through regulation of its postfusion dispersal. *Cell Metab.* 12, 250-259.
- Stuart, C.A., Yin, D., Howell, M.E.A., Dykes, R.J., Laffan, J.J., and Ferrando, A.A. (2006). Hexose transporter mRNAs for GLUT4, GLUT5, and GLUT12 predominate in human muscle. *Am. J. Physiol. Endocrinol. Metab.* 291, E1067-73.
- Suárez-Ortegón, M.F., McLachlan, S., Wild, S.H., Fernández-Real, J.M., Hayward, C., and Polašek, O. (2016). Soluble transferrin receptor levels are positively associated with insulin resistance but not with the metabolic syndrome or its individual components. *Br. J. Nutr.* 116, 1165-1174.
- Subtil, A., Lampson, M.A., Keller, S.R., and McGraw, T.E. (2000). Characterization of the insulin-regulated endocytic recycling mechanism in 3T3-L1 adipocytes using a novel reporter molecule. *J. Biol. Chem.* 275, 4787-4795.
- Sun, Y., Bilan, P.J., Liu, Z., and Klip, A. (2010). Rab8A and Rab13 are activated by insulin and regulate GLUT4 translocation in muscle cells. *Proc. Natl. Acad. Sci. USA* 107, 19909-19914.
- Suzuki, K., and Kono, T. (1980). Evidence that insulin causes translocation of glucose transport activity to the plasma membrane from an intracellular storage site. *Proc. Natl. Acad. Sci. USA* 77, 2542-2545.
- Szablewski, L. (2017). Glucose transporters in healthy heart and in cardiac disease. *Int. J. Cardiol.* 230, 70-75.

- Takahashi, K., and Yamanaka, S. (2006). Induction of pluripotent stem cells from mouse embryonic and adult fibroblast cultures by defined factors. *Cell* 126, 663-676.
- Takahashi, K., and Yamanaka, S. (2013). Induced pluripotent stem cells in medicine and biology. *Development* 140, 2457-2461.
- Tan, J., and Brill, J.A. (2014). Cinderella story: PI4P goes from precursor to key signaling molecule. *Crit Rev Biochem Mol Biol* 49, 33-58.
- Tan, S.-X., Fisher-Wellman, K.H., Fazakerley, D.J., Ng, Y., Pant, H., Li, J., Meoli, C.C., Coster, A.C.F., Stöckli, J., and James, D.E. (2015). Selective insulin resistance in adipocytes. *J. Biol. Chem.* 290, 11337-11348.
- Tanaka, K.A.K., Suzuki, K.G.N., Shirai, Y.M., Shibutani, S.T., Miyahara, M.S.H., Tsuboi, H., Yahara, M., Yoshimura, A., Mayor, S., Fujiwara, T.K., et al. (2010). Membrane molecules mobile even after chemical fixation. *Nat. Methods* 7, 865-866.
- Taniguchi, C.M., Emanuelli, B., and Kahn, C.R. (2006). Critical nodes in signalling pathways: insights into insulin action. *Nat. Rev. Mol. Cell Biol.* 7, 85-96.
- Taylor, E.B., An, D., Kramer, H.F., Yu, H., Fujii, N.L., Roeckl, K.S.C., Bowles, N., Hirshman, M.F., Xie, J., Feener, E.P., et al. (2008). Discovery of TBC1D1 as an insulin-, AICAR-, and contraction-stimulated signaling nexus in mouse skeletal muscle. *J. Biol. Chem.* 283, 9787-9796.
- Thillaiappan, N.B., Chavda, A.P., Tovey, S.C., Prole, D.L., and Taylor, C.W. (2017). Ca²⁺ signals initiate at immobile IP3 receptors adjacent to ER-plasma membrane junctions. *Nat. Commun.* 8, 1505.
- Thorens, B., and Mueckler, M. (2010). Glucose transporters in the 21st Century. *Am. J. Physiol. Endocrinol. Metab.* 298, E141-5.
- Thorley, J.A., Pike, J., and Rappoport, J.Z. (2014). Super-resolution Microscopy. In *Fluorescence Microscopy*, (Elsevier), pp. 199-212.
- Thrainsdottir, I.S., Aspelund, T., Thorgeirsson, G., Gudnason, V., Hardarson, T., Malmberg, K., Sigurdsson, G., and Rydén, L. (2005). The association between glucose abnormalities and heart failure in the population-based Reykjavik study. *Diabetes Care* 28, 612-616.
- Todd, J.A., Walker, N.M., Cooper, J.D., Smyth, D.J., Downes, K., Plagnol, V., Bailey, R., Nejentsev, S., Field, S.F., Payne, F., et al. (2007). Robust associations of four new chromosome regions from genome-wide analyses of type 1 diabetes. *Nat. Genet.* 39, 857-864.
- Tokunaga, M., Imamoto, N., and Sakata-Sogawa, K. (2008). Highly inclined thin illumination enables clear single-molecule imaging in cells. *Nat. Methods* 5, 159-161.
- Tordjman, K.M., Leingang, K.A., James, D.E., and Mueckler, M.M. (1989). Differential regulation of two distinct glucose transporter species expressed in 3T3-L1 adipocytes:

- effect of chronic insulin and tolbutamide treatment. *Proc. Natl. Acad. Sci. USA* 86, 7761-7765.
- Trachanas, K., Sideris, S., Aggeli, C., Poulidakis, E., Gatzoulis, K., Tousoulis, D., and Kallikazaros, I. (2014). Diabetic cardiomyopathy: from pathophysiology to treatment. *Hellenic J Cardiol* 55, 411-21.
- Tsao, T.S., Burcelin, R., Katz, E.B., Huang, L., and Charron, M.J. (1996). Enhanced insulin action due to targeted GLUT4 overexpression exclusively in muscle. *Diabetes* 45, 28-36.
- Tsao, T.S., Stenbit, A.E., Factor, S.M., Chen, W., Rossetti, L., and Charron, M.J. (1999). Prevention of insulin resistance and diabetes in mice heterozygous for GLUT4 ablation by transgenic complementation of GLUT4 in skeletal muscle. *Diabetes* 48, 775-782.
- Tsien, R.Y. (1998). The green fluorescent protein. *Annu. Rev. Biochem.* 67, 509-544.
- Tsuchiya, Y., Hatakeyama, H., Emoto, N., Wagatsuma, F., Matsushita, S., and Kanzaki, M. (2010). Palmitate-induced down-regulation of sortilin and impaired GLUT4 trafficking in C2C12 myotubes. *J. Biol. Chem.* 285, 34371-34381.
- Ueda, S., Kitazawa, S., Ishida, K., Nishikawa, Y., Matsui, M., Matsumoto, H., Aoki, T., Nozaki, S., Takeda, T., Tamori, Y., et al. (2010). Crucial role of the small GTPase Rac1 in insulin-stimulated translocation of glucose transporter 4 to the mouse skeletal muscle sarcolemma. *FASEB J.* 24, 2254-2261.
- Uhlig, M., Passlack, W., and Eckel, J. (2005). Functional role of Rab11 in GLUT4 trafficking in cardiomyocytes. *Mol. Cell. Endocrinol.* 235, 1-9.
- Urry, L.A., College, M., Oakland, California, Cain, M.L., College, B., Brunswick, Maine, Wasserman, S.A., California, U. of, et al. (2017). *Campbell Biology (11th Edition)* (New York, NY: Pearson).
- Uusitupa, M. (2002). Lifestyles matter in the prevention of type 2 diabetes. *Diabetes Care* 25, 1650-1651.
- van de Linde, S. (2019). Single-molecule localization microscopy analysis with ImageJ. *J. Phys. D, Appl. Phys.* 52, 203002.
- van Deventer, S., Arp, A.B., and van Sptiel, A.B. (2020). Dynamic plasma membrane organization: A complex symphony. *Trends Cell Biol.*
- van Varik, B.J., Rennenberg, R.J.M.W., Reutelingsperger, C.P., Kroon, A.A., de Leeuw, P.W., and Schurgers, L.J. (2012). Mechanisms of arterial remodeling: lessons from genetic diseases. *Front. Genet.* 3, 290.
- Verboven, K., Wouters, K., Gaens, K., Hansen, D., Bijnen, M., Wetzels, S., Stehouwer, C.D., Goossens, G.H., Schalkwijk, C.G., Blaak, E.E., et al. (2018). Abdominal subcutaneous and visceral adipocyte size, lipolysis and inflammation relate to insulin resistance in male obese humans. *Sci. Rep.* 8, 4677.

- Verhey, K.J., and Birnbaum, M.J. (1994). A Leu-Leu sequence is essential for COOH-terminal targeting signal of GLUT4 glucose transporter in fibroblasts. *J. Biol. Chem.* **269**, 2353-2356.
- Vettor, R., Fabris, R., Serra, R., Lombardi, A.M., Tonello, C., Granzotto, M., Marzolo, M.O., Carruba, M.O., Ricquier, D., Federspil, G., et al. (2002). Changes in FAT/CD36, UCP2, UCP3 and GLUT4 gene expression during lipid infusion in rat skeletal and heart muscle. *Int J Obes Relat Metab Disord* **26**, 838-847.
- Wakioka, T., Sasaki, A., Mitsui, K., Yokouchi, M., Inoue, A., Komiya, S., and Yoshimura, A. (1999). APS, an adaptor protein containing Pleckstrin homology (PH) and Src homology-2 (SH2) domains inhibits the JAK-STAT pathway in collaboration with c-Cbl. *Leukemia* **13**, 760-767.
- Walker, A.M., Patel, P.A., Rajwani, A., Groves, D., Denby, C., Kearney, L., Sapsford, R.J., Witte, K.K., Kearney, M.T., and Cubbon, R.M. (2016). Diabetes mellitus is associated with adverse structural and functional cardiac remodelling in chronic heart failure with reduced ejection fraction. *Diab. Vasc. Dis. Res.* **13**, 331-340.
- Wang, W., Hansen, P.A., Marshall, B.A., Holloszy, J.O., and Mueckler, M. (1996). Insulin unmasks a COOH-terminal Glut4 epitope and increases glucose transport across T-tubules in skeletal muscle. *J. Cell Biol.* **135**, 415-430.
- Wardzala, L.J., and Jeanrenaud, B. (1981). Potential mechanism of insulin action on glucose transport in the isolated rat diaphragm. Apparent translocation of intracellular transport units to the plasma membrane. *J. Biol. Chem.* **256**, 7090-7093.
- Wasserman, D.H., and Halseth, A.E. (1998). An overview of muscle glucose uptake during exercise. Sites of regulation. *Adv. Exp. Med. Biol.* **441**, 1-16.
- Watson, R.T., Hou, J.C., and Pessin, J.E. (2008). Recycling of IRAP from the plasma membrane back to the insulin-responsive compartment requires the Q-SNARE syntaxin 6 but not the GGA clathrin adaptors. *J. Cell Sci.* **121**, 1243-1251.
- Wedick, N.M., Snijder, M.B., Dekker, J.M., Heine, R.J., Stehouwer, C.D.A., Nijpels, G., and van Dam, R.M. (2009). Prospective investigation of metabolic characteristics in relation to weight gain in older adults: the Hoorn Study. *Obesity (Silver Spring)* **17**, 1609-1614.
- Westermeier, F., Riquelme, J.A., Pavez, M., Garrido, V., Díaz, A., Verdejo, H.E., Castro, P.F., García, L., and Lavandero, S. (2016). New molecular insights of insulin in diabetic cardiomyopathy. *Front. Physiol.* **7**, 125.
- Weyer, C., Foley, J.E., Bogardus, C., Tataranni, P.A., and Pratley, R.E. (2000). Enlarged subcutaneous abdominal adipocyte size, but not obesity itself, predicts type II diabetes independent of insulin resistance. *Diabetologia* **43**, 1498-1506.

- Wheeler, T.J., Fell, R.D., and Hauck, M.A. (1994). Translocation of two glucose transporters in heart: effects of rotenone, uncouplers, workload, palmitate, insulin and anoxia. *Biochim. Biophys. Acta* 1196, 191-200.
- Whelan, D.R., and Bell, T.D.M. (2015). Image artifacts in single molecule localization microscopy: why optimization of sample preparation protocols matters. *Sci. Rep.* 5, 7924.
- WHO (2013). Diabetes Fact Sheet N° 312.
- WHO (2016). Global Report on Diabetes (France: World Health Organization).
- Wieczorke, R., Dlugai, S., Krampe, S., and Boles, E. (2003). Characterisation of mammalian GLUT glucose transporters in a heterologous yeast expression system. *Cell Physiol. Biochem.* 13, 123-134.
- Wiese, R.J., Mastick, C.C., Lazar, D.F., and Saltiel, A.R. (1995). Activation of mitogen-activated protein kinase and phosphatidylinositol 3'-kinase is not sufficient for the hormonal stimulation of glucose uptake, lipogenesis, or glycogen synthesis in 3T3-L1 adipocytes. *J. Biol. Chem.* 270, 3442-3446.
- Williamson, D.J., Burn, G.L., Simoncelli, S., Griffié, J., Peters, R., Davis, D.M., and Owen, D.M. (2020). Machine learning for cluster analysis of localization microscopy data. *Nat. Commun.* 11, 1493.
- Winder, W.W., and Hardie, D.G. (1999). AMP-activated protein kinase, a metabolic master switch: possible roles in type 2 diabetes. *Am. J. Physiol.* 277, E1-10.
- Wu, X., Chi, R.J., Baskin, J.M., Lucast, L., Burd, C.G., De Camilli, P., and Reinisch, K.M. (2014). Structural insights into assembly and regulation of the plasma membrane phosphatidylinositol 4-kinase complex. *Dev. Cell* 28, 19-29.
- Xu, X. (1996). A density-based algorithm for discovering clusters in large spatial databases with noise. 226-231.
- Xu, Y., Rubin, B.R., Orme, C.M., Karpikov, A., Yu, C., Bogan, J.S., and Toomre, D.K. (2011). Dual-mode of insulin action controls GLUT4 vesicle exocytosis. *J. Cell Biol.* 193, 643-653.
- Yamamoto, M., Toya, Y., Schwencke, C., Lisanti, M.P., Myers, M.G., and Ishikawa, Y. (1998). Caveolin is an activator of insulin receptor signaling. *J. Biol. Chem.* 273, 26962-26968.
- Yan, Q., Lu, Y., Zhou, L., Chen, J., Xu, H., Cai, M., Shi, Y., Jiang, J., Xiong, W., Gao, J., et al. (2018). Mechanistic insights into GLUT1 activation and clustering revealed by super-resolution imaging. *Proc. Natl. Acad. Sci. USA* 115, 7033-7038.
- Yang, J., and Holman, G.D. (1993). Comparison of GLUT4 and GLUT1 subcellular trafficking in basal and insulin-stimulated 3T3-L1 cells. *J. Biol. Chem.* 268, 4600-4603.

- Yang, J., Clarke, J.F., Ester, C.J., Young, P.W., Kasuga, M., and Holman, G.D. (1996). Phosphatidylinositol 3-kinase acts at an intracellular membrane site to enhance GLUT4 exocytosis in 3T3-L1 cells. *Biochem. J.* 313 (Pt 1), 125-131.
- Yu, C., Cresswell, J., Löffler, M.G., and Bogan, J.S. (2007). The glucose transporter 4-regulating protein TUG is essential for highly insulin-responsive glucose uptake in 3T3-L1 adipocytes. *J. Biol. Chem.* 282, 7710-7722.
- Zahiti, B.F., Gorani, D.R., Gashi, F.B., Gjoka, S.B., Zahiti, L.B., Haxhiu, B.S., and Kamberi, L.S. (2013). Left ventricular diastolic dysfunction in asymptomatic type 2 diabetic patients: detection and evaluation by tissue Doppler imaging. *Acta Inform. Med.* 21, 120-123.
- Zammit, P.S., Partridge, T.A., and Yablonka-Reuveni, Z. (2006). The skeletal muscle satellite cell: the stem cell that came in from the cold. *J. Histochem. Cytochem.* 54, 1177-1191.
- Zeigerer, A., Lampson, M.A., Karylowski, O., Sabatini, D.D., Adesnik, M., Ren, M., and McGraw, T.E. (2002). GLUT4 retention in adipocytes requires two intracellular insulin-regulated transport steps. *Mol. Biol. Cell* 13, 2421-2435.
- Zisman, A., Peroni, O.D., Abel, E.D., Michael, M.D., Mauvais-Jarvis, F., Lowell, B.B., Wojtaszewski, J.F., Hirshman, M.F., Virkamaki, A., Goodyear, L.J., et al. (2000). Targeted disruption of the glucose transporter 4 selectively in muscle causes insulin resistance and glucose intolerance. *Nat. Med.* 6, 924-928.
- Zottola, R.J., Cloherty, E.K., Coderre, P.E., Hansen, A., Hebert, D.N., and Carruthers, A. (1995). Glucose transporter function is controlled by transporter oligomeric structure. A single, intramolecular disulfide promotes GLUT1 tetramerization. *Biochemistry* 34, 9734-9747.
- Zuppinger, C. (2019). 3D cardiac cell culture: A critical review of current technologies and applications. *Front. Cardiovasc. Med.* 6, 87.
- Zwi, L., Caspi, O., Arbel, G., Huber, I., Gepstein, A., Park, I.-H., and Gepstein, L. (2009). Cardiomyocyte differentiation of human induced pluripotent stem cells. *Circulation* 120, 1513-1523.